THE JOURNAL OF

PHYSICAL
CHEMISTRY

THE JOURNAL OF
PHYSICAL CHEMISTRY

1A

COMMUNICATIONS TO THE EDITOR

■ Supplementary material for this paper is available separately, in photocopy or micro-
fiche form. Ordering information is given in the paper.

* In papers with more than one author, the asterisk indicates the name of the author to
whom inquiries about the paper should be addressed.

AUTHOR INDEX

Radiolysis of 1,1-Difluoroethane

Halbert Carmichael* and Yan K. Lau

Department of Chemistry, North Carolina State University, Raleigh, North Carolina 27607   (Received May 1, 1974)

1,1-Difluoroethane has been irradiated in the gas phase both in the presence and absence of NO, and those products eluting from a Porapak Q column before 1,1-difluoroethane were identified and measured. Hydrogen is formed by at least two processes. Trifluoromethane and 1,1,1-trifluoroethane are formed by fluoride ion transfer reactions of fragment ions. Methane and ethane are formed from methyl radicals resulting from fragmentation of the parent ion. Ethene, fluoroethene, and 1,1-difluoroethene are all formed in significant amounts. In the absence of radical scavengers all unsaturated products reach limiting concentrations of less than 100 ppm.

Introduction

Extensive studies of the radiolysis of simple hydrocarbons have shown that radical, ionic, and molecular elimination reactions all occur leading to a variety of products.[1] For some compounds the relative importance of the various reaction pathways has been established.[2] Both photolysis[3] and radiolysis[4] of partially halogenated alkanes cause the breaking of the carbon–halogen bonds for chloro-, bromo-, and iodoalkanes. This study was undertaken to see if the radiolysis of partially fluorinated alkanes would more closely parallel that of the other haloalkanes which are similar in their polarity or that of the alkanes which are similar in their relative bond strengths.

The many studies of the decomposition of vibrationally excited haloalkanes have been reviewed by Maccoll.[5] In general the fluoroalkanes react like many of the chloroalkanes in showing unimolecular elimination of hydrogen halide. On the other hand, vacuum ultraviolet photolysis of ethyl fluoride results in the elimination of both hydrogen and hydrogen fluoride.[6] The vacuum ultraviolet photolysis of vinyl fluoride shows elimination of molecular hydrogen and hydrogen fluoride as well as fluorine atoms.[7] The radiation chemistry of perfluoroalkanes is dominated by the breaking of carbon–fluorine bonds by mechanisms that are not yet completely elucidated.[8] The mercury photosensitized decomposition of 1,1-difluoroethane occurs mostly through reactions of the 1,1-difluoroethyl radical.[9]

1,1-Difluoroethane was chosen for this work because its lack of symmetry will lead to readily distinguishable products for many of the possible decomposition modes. Studies of the pyrolysis of this compound have shown that it is stable at room temperature and that the decomposition of the electronic ground state of the molecule is simple.[10]

Experimental Section

All reactant gases were obtained from the Matheson Co. The 1,1-difluoroethane was bulb-to-bulb distilled at −196°. Analysis showed that the resulting material contained less than 1 ppm each of methane, acetylene, and *trans*-CHFCHF, no propane, and about 0.1% carbon dioxide. The nitric oxide and nitrous oxide were both degassed at −196° then distilled off at −80°.

The irradiation vessels were spherical 500-ml Pyrex flasks with cold fingers and breakseals. Vessels were flamed out under vacuum prior to reuse. Irradiations were carried out at a total pressures of 86 or 94 Torr. Gases or gas mixtures were introduced into the bulbs, frozen down in liquid nitrogen, and pumped on prior to sealing the inlet tube. Samples were irradiated in the North Carolina State University cobalt-60 irradiation facility. Nitrous oxide dosimetry (using $G(N_2) = 10.0$)[11a] showed that the absorbed dose rate was 1.09×10^{17} eV/sec per mole of difluoroethane, assuming that difluoroethane and nitrous oxide absorb radiation in proportion to their electron content.

Hydrogen was identified from mass spectra of the fraction of the reaction products volatile at −196°. It was measured quantitatively by adding small measured quantities of helium to the gas or gas mixture to be irradiated. After irradiation the gases volatile at −196° were separated and their mass spectrum run. The relative amounts of hydrogen

and helium in the separated fractions were determined by comparison of the mass 2 and mass 4 peaks with those for mixtures of known composition run under identical conditions.

Other products were identified both by matching gas chromatographic retention times with authentic samples and by running mass spectra on the separated peaks from the gas chromatograph. Table I[11b] lists the retention times for a number of products. All quantitative results reported here were obtained using a 6-m Porapak Q column at 65° and a flame ionization detector. The product yields were determined using the areas of product peaks relative to the area of the difluoroethane peak. With the exception of CHF_3 the sensitivities of all compounds were proportional to the number of carbons in the compound to within 5%. A special calibration for CHF_3 showed that mole for mole its peak area is 0.055 that of CH_2CF_2. Qualitative observations regarding N_2, SiF_4, N_2O, and CO_2 were all made on special runs using a thermal conductivity detector and Porapak Q columns.

Results

Radiolysis of pure 1,1-difluoroethane resulted in the production of hydrogen, methane, ethane, ethene, trifluoromethane, 1,1,1-trifluoroethane, 1,1-difluoroethene, and fluoroethene in significant quantities. Fluoromethane, difluoromethane, fluoroethane, trifluoroethene, cis- and trans-1,2-difluoroethene, and ethyne were all formed in small quantities. Another product which came off the chromatograph between trifluoromethane and fluoromethane and had a mass spectrum consistent with CHCF was formed in small quantities. 1,2-Difluoroethane and 1,1,2-trifluoroethane were not major products. HF was not observed directly, but the fact that SiF_4 was not observed in samples irradiated in a Monel vessel until the sample had been in contact with glass indicates that HF is a significant product. In the absence of radical scavengers a significant mass of material was contained in products which came off the chromatograph column after the 1,1-difluoroethane. Of these only cis-CHFCHF and propane were positively identified.

Figure 1 shows the amounts of methane and ethane observed for various lengths of radiolysis. The amount of methane was greatly diminished in the presence of 1% NO and ethane was completely absent. Only one of the products of long retention time was seen in presence of NO. In 1,1-difluoroethane–NO mixtures irradiated for 15 days both N_2 and N_2O were produced in significant amounts, but no SiF_4 was observed.

Figure 2 shows the amount of CH_2CF_2 produced for various irradiation times in the presence and absence of NO. The curved line fitted to the data in the absence of NO is that corresponding to a product produced with an initial G value of 0.59 and a maximum concentration of 66 ppm. Figures 3 and 4[11b] show similar behavior for C_2H_4 and C_2H_3F. Results for these products are subject to a larger uncertainty than are those for CH_2CF_2. C_2H_4 was not completely resolved from C_2H_2. C_2H_3F is the product of pyrolysis of CH_3CHF_2, and small quantities might be formed on sealing the vessel prior to irradiation. Figure 5 shows that the production of both CHF_3 and CH_3CF_3 was linear with time and was unaffected by the presence of NO. Figures 6 and 7[11b] depict the much smaller yields of CH_3F, CH_2F_2, and t-CHFCHF which were also unaffected by the addition of NO.
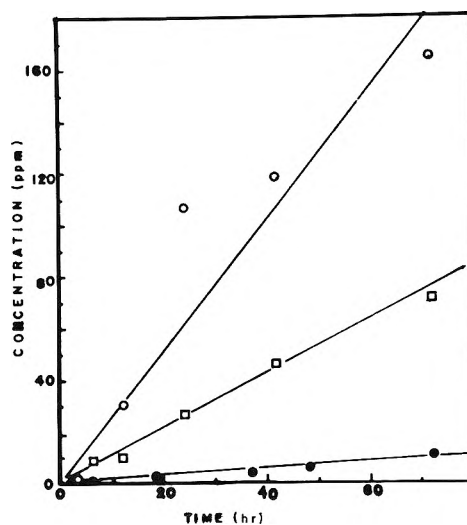
Figure 1. Methane and ethane produced in the radiolysis of 1,1-difluoroethane: (O) methane without NO added, (●) methane with NO added, (□) ethane without NO added.
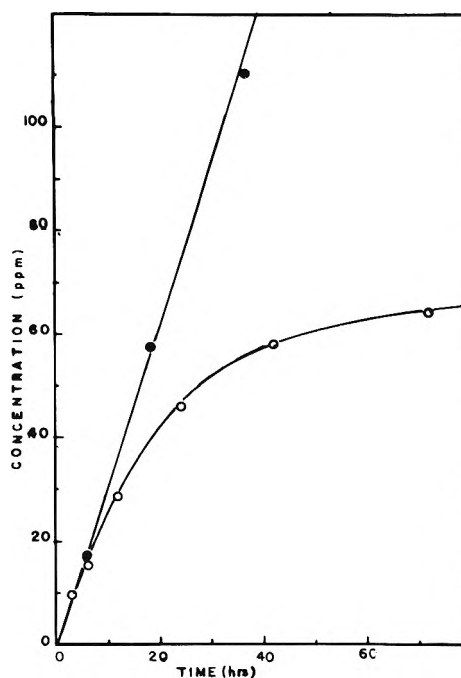
Figure 2. 1,2-Difluoroethene produced in the radiolysis of 1,1-difluoroethane: (O) without NO, (●) with NO.

Table II summarizes the products observed in the radiolysis of CH_3CHF_2 and gives the G values for all the products measured quantitatively. The G values for CH_3CHF_2 are initial values and do not account for secondary reactions which would consume these products. Most of the products with approximate values given were not completely resolved from more important products in most chromatograph runs. Several experiments using 3.5% SF_6 added to the CH_3CHF_2 gave results that were experimentally indistinguishable from those with neat CH_3CHF_2.

Discussion

1,1-Difluoroethane was chosen partly because of the large number of reaction pathways available, and the large number of different products indicates that many decomposition pathways are followed. Methane and ethane are
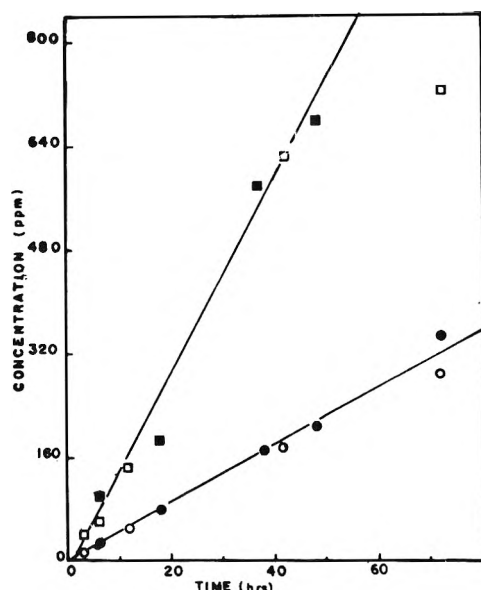
Figure 5. Trifluoromethane and 1,1,1-trifluoroethane produced in the radiolysis of 1,1-difluoroethane: (O) trifluoromethane, (□) 1,1,1-trifluoroethane. Filled figures indicate experiments with NO added.

TABLE II: G Values for Products from the Radiolysis of CH_3CHF_2

	Neat	With NO
H_2	2.5	1.1
CH_4	1.4	0.043
CH_3F	0.06	0.064
CH_2F_2	0.018	0.012
CHF_3	2.3	2.3
C_2H_2	<0.1	<0.1
C_2H_4	0.43	0.34
C_2H_3F	0.72	0.58
CH_2CF_2	0.59	0.47
t-CHFCHF	0.012	0.015
C_2HF_3	0.004	0.004
C_2H_6	0.15	<0.003
CH_3CF_3	0.66	0.68
C_2H_5F	0.06	0.06

formed *via* a scavengeable precurser, the methyl radical. The relative amounts are consistent with ethane being formed by methyl radical combination and methane being formed *via* hydrogen abstraction from 1,1-difluoroethane by methyl radicals with a rate constant 0.19 times that for abstraction from ethane. It is clear that the methyl radicals do not come from a simple carbon–carbon bond breaking in the parent compound. Such a break would produce equal numbers of methyl and difluoromethyl radicals. The latter would be as reactive toward hydrogen abstraction as methyl radicals[12] yet very little difluoromethane is observed. Even the difluoromethane that is seen does not come from radicals since it also forms in the presence of NO.

Two of the major products come from a similar set of reactions. Trifluoromethane can be formed by a fluoride ion transfer reaction involving the difluoromethyl ion.

$$CHF_2^+ + CH_3CHF_2 \longrightarrow CHF_3 + C_2H_4F^+$$
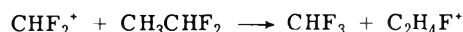
This reaction has been seen in ion cyclotron resonance experiments,[13] and the difluoromethyl ion is the major ion in the mass spectrum of 1,1-difluoroethane. The presence of methyl radicals without difluoromethyl radicals could be explained by fragmentation of the parent ion.

$$CH_3CHF_2 \rightsquigarrow CH_3 + CHF_2^+ + e^-$$

The sum of the methane yield and twice the ethane yield is equal to about two-thirds the trifluoromethane yield giving a rough material balance for these processes. Trifluoroethane can be formed by an analogous ion–molecule reaction, also seen by Dawson, *et al.*[13]

$$C_2H_3F_2^+ + CH_3CHF_2 \longrightarrow CH_3CF_3 + C_2H_4F^+$$
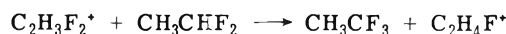
The difluoroethyl ion is the second most important ion in the mass spectrum of 1,1-difluoroethane. The third most important ion in the cracking pattern, $C_2H_4F^+$, would not lead to any new products by undergoing a fluoride ion transfer reaction with the parent molecule.

All three major olefinic products formed in radiolysis are subject to attack by species generated during subsequent radiolysis so G values for formation must be found from very short runs or by extrapolation. In the absence of scavengers all reach steady-state concentrations of less than 100 ppm. 1,1-Difluoroethene could be formed by molecular hydrogen elimination, a major reaction in hydrocarbon radiolysis.

$$CH_3CHF_2 \rightsquigarrow CH_2CF_2 + H_2$$
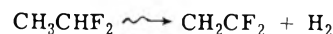
More than enough unscavenged hydrogen is found to account for all the difluoroethene by this reaction. Radiolysis of difluoroethane in the presence of SF_6 yielded as much CH_2CF_2 as in neat difluoroethane. This implies that those excited molecules which eliminate hydrogen are not the result of neutralization of the parent ion by electrons. The possibility that the electrons were being attached by the parent compound in the radiolysis of neat 1,1-difluoroethane is unlikely in light of Fessenden's results on electron attachment to partially fluorinated alkanes.[14] Another interesting pathway for the formation of olefins is through an acid–base reaction involving ethyl ions.

$$C_2H_3F_2^+ + base \longrightarrow CH_2CF_2 + conjugate \ acid$$

If the base is the parent molecule, this reaction is probably endothermic, but other bases such as water and HF are also present and might well take part in such reactions as has been shown by Munson and Field.[15] The fact that all three olefins showed lower yields in the presence of NO hints at the possibility of radical–radical disproportion reactions making some contribution to the olefin products. Such a disproportionation reaction has been seen in mercury photosensitization of 1,1-difluoroethane.[9] If NO were affecting the system by scavenging positive charges it would affect the yields of CHF_3 and CH_3CF_3 which are unchanged by the addition of NO.

The small but easily measured amounts of *trans*-CHFCHF are interesting. This compound is an impurity in the starting material but in quantities smaller than those measured after radiolysis. *cis*-CHFCHF was identified among the products of long retention time, but no attempts to measure it quantitatively were made. Since neither 1,2-difluoroethane nor 1,1,2-trifluoroethane are important products, and Figure 7[11] shows that the yield of 1,2-difluoroethene is linear with time, it is reasonable to argue that it is not a secondary product. Therefore it is necessary to propose a path for its formation directly from the parent compound. If the fluorines of the difluoroethyl ion scramble as the hydrogens in the ethyl ion are known to do,[16] two interconverting ions could be formed, $CH_3CF_2^+$ and CH_2FCHF^+. The tendency for fluorine atoms to congregate on the same carbon atom would make the former more im-

portant and would mean that the amount of CH_2CF_2 formed by ionic pathways would be much larger than the amount of CHFCHF actually seen.

The small yields of CH_2F_2 and CH_3F as well as the small yield of methane in the presence of NO seem to be the only indications of any molecular elimination of carbenes during the radiolysis of 1,1-difluoroethane. No products resulting from the reaction of these carbenes were identified. What is clear is that this is a much less important path in the radiolysis of 1,1-difluoroethane than it is in the radiolysis of ethane itself.[2a]

Summary

The radiolysis of 1,1-difluoroethane produces CHF_3 and CH_3CF_3 by fluoride ion transfer reactions involving fragment ions. Methyl radicals formed in the fragmentation of the parent ion eventually form methane and ethane. Of lesser importance are the formation of C_2H_4, C_2H_3F, and CH_2CF_2 via processes that are not completely identified, but lead to large yields of both hydrogen atoms and molecular hydrogen. Of minor importance are processes which produce CH_4, CH_3F, and CH_2F_2 by direct elimination. The production of CHFCHF hints at the possibility of scrambling among the fluorines and hydrogens of ethyl ions.

Supplementary Material Available. Table I and Figures 3, 4, 6, and 7 will appear following these pages in the microfilm edition of this volume of the journal. Photocopies of the supplementary material from this paper only or microfiche (105 × 148 mm, 24X reduction, negatives) containing all of the supplementary material for the papers in this issue may be obtained from the Journals Department, American Chemical Society, 1155 16th St., N.W., Washington, D. C. 20036. Remit check or money order for $3.00 for photocopy or $2.00 for microfiche, referring to code number JPC-74-2183.

References and Notes

(1) P. Ausloos, *Annu. Rev. Phys. Chem.,* **17,** 205 (1966).
(2) (a) H. H. Carmichael, R. Gordon, Jr., and P. Ausloos, *J. Chem. Phys.,* **42,** 343 (1965); (b) R. E. Rebbert and P. Ausloos, *J. Res. Nat. Bur. Stand., Sect. A,* **76,** 329 (1972).
(3) J. G. Calvert and J. N. Pitts, "Photochemistry," Wiley, New York, N.Y., 1966.
(4) R. F. Claridge and J. E. Willard, *J. Amer. Chem. Soc.,* **87,** 4992 (1965); D. W. Skelly, R. G. Hayes, and W. H. Hamill, *J. Chem. Phys.,* **43,** 2795 (1965); T. I. Balkas, J. H. Fendler, and R. H. Schuler, *J. Phys. Chem.,* **75,** 455 (1971).
(5) A. Maccoll, *Chem. Rev.,* **69,** 33 (1969); G. E. Millward and E. Tschuikow-Roux, *J. Phys. Chem.,* **76,** 292 (1972).
(6) S. C. Chau, Y. Inel, and E. Tschuikow-Roux, *Can. J. Chem.,* **50,** 1443 (1972).
(7) A. W. Kirk and E. Tschuikow-Roux, *J. Chem. Phys.,* **53,** 1924 (1970).
(8) N. H. Sagert and A. S. Blair, *Can. J. Chem.,* **46,** 3284 (1968); M. B. Fallgatter and R. J. Hanrahan, *J. Phys. Chem.,* **74,** 2806 (1970); E. Heckel and R. J. Hanrahan, *Int. J. Radiat. Phys. Chem,* **5,** 287 (1973); G. A. Kennedy and R. J. Hanrahan, *J. Phys. Chem.,* **78,** 366 (1974).
(9) P. M. Scott and K. R. Jennings, *J. Phys. Chem.,* **73,** 1513 (1969).
(10) E. Tschuikow-Roux, W. J. Quiring, and J. M. Simmie, *J. Phys. Chem.,* **74,** 2449 (1970); B. Noble, H. H. Carmichael, and C. L. Bumgardner, *ibid.,* **76,** 1680 (1972).
(11) (a) F. T. Jones and T. J. Sworski, *J. Phys. Chem.,* **70,** 1546 (1966). (b) See paragraph at end of text regarding supplementary material.
(12) J. T. Bryant and G. O. Pritchard, *J. Phys. Chem.,* **71,** 3439 (1967).
(13) J. H. J. Dawson, W. G. Henderson, R. M. O'Malley, and K. R. Jennings, *Int. J. Mass Spectrom. Ion Phys.,* **11,** 61 (1973).
(14) R. W. Fessenden and K. M. Bansal, *J. Chem. Phys.,* **59,** 1760 (1973).
(15) M. S. B. Munson and F. H. Field, *J. Amer. Chem. Soc.,* **87,** 4242 (1965).
(16) P. Ausloos, S. G. Lias, and I. B. Sandoval, *Discuss. Faraday Soc.,* **67** (1963).

Consecutive Unimolecular Decomposition Following Recoil Tritium Activation of 1,1-Difluoroethane[1]

W. S. Smith and Y. -N. Tang*

Department of Chemistry, Texas A & M University, College Station, Texas 77843

Excited $C_2H_3TF_2$ formed by T*-for-H substitution in CH_3CHF_2 gives C_2H_2TF and C_2HT as the secondary and tertiary decomposition products, respectively. The observed trends demonstrate that the $C_2H_3TF_2$ yield increases, the C_2HT yield decreases, while the C_2H_2TF yield exhibits a maximum with increasing pressure. These trends are consistent with a mechanism of consecutive unimolecular decomposition in which all the excitation energy is introduced during the initial substitution.

Introduction

Although consecutive reactions in thermal systems are discussed in every kinetics textbook,[2] the consecutive decomposition initiated by hot atom activation has scarcely been investigated.[3-5] Previously, Krohn and coworkers have presented some good evidence in a series of recoil ^{18}F studies for the consecutive decomposition of $CF_3^{18}F$ to give $CF^{18}F$ and $CH_2^{18}FCF_3$ to give $CH^{18}F$.[3] However, in order

to provide a better quantitative basis for future theoretical treatment, a system which yields nonradical species as decomposition products should be more appropriate.

From the pressure studies of recoil tritium reactions with cyclobutane, Lee and Rowland have obtained a broad energy distribution with a "median" energy of 5 eV following the T*-for-H substitution.[6] Subsequent studies with CH$_3$NC demonstrated that the substitution products are *always* left in a high state of internal excitation.[7] This quantity of excitation energy should be enough to initiate consecutive unimolecular processes in some suitable system.

In the present work, we wish to report an experimental study of a consecutive decomposition following the T*-for-H substitution in CH$_3$CHF$_2$. In hot atom systems, if the excitation energy arising from the primary substitution is high enough, it is possible that the secondary decomposition product may undergo a tertiary reaction. In the CH$_3$CHF$_2$ case, the secondary product, vinyl fluoride, may further decompose by HF elimination to give acetylene.[8,9]

$$T^* + C_2H_4F_2 \longrightarrow (C_2H_3TF_2)^* + H \quad (1)$$

$$(C_2H_3TF_2)^* \longrightarrow (C_2H_2TF)^* + HF \quad (2)$$

$$(C_2H_2TF)^* \longrightarrow C_2HT + HF \quad (3)$$
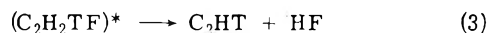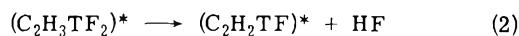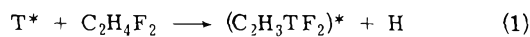
Experimental Section

The standard techniques for recoil tritium studies were adopted. Samples containing CH$_3$CHF$_2$ with a small amount of ^{3}He and O$_2$ were sealed by high vacuum techniques in Pyrex 1720 bulbs at pressures ranging from 100 to 900 Torr. Energetic tritium atoms were produced by the nuclear reaction ^{3}He(n,p)^{3}H. All irradiations were carried out at the Texas A & M University Nuclear Science Center Reactor, where samples were subjected to a thermal neutron flux of 1×10^{13} neutrons/cm^2 sec for 5 min.

The usual procedure for radio-gas chromatography was followed.[10] A 50-ft dimethylsulfclane column (35%) at 25° was used for the separation of the major products, C$_2$H$_3$TF$_2$, C$_2$H$_2$TF, and C$_2$HT. HT and CH$_3$T were resolved with a 50-ft column of 10% propylene carbonate coated on alumina which was operated at 0°. Quantitative yields of each tritium labeled product were obtained by means of a gas proportional counter.

Helium-3 with a tritium content of less than 2×10^{-11} % was obtained from the Monsanto Research Corp. 1,1-Difluoroethane was obtained from Matheson Co. in >98% purity. Oxygen with a minimum purity of 99% was obtained from Airco.

Results and Discussion

Pressure Dependence of Reaction Products. Besides the T*-for-H substitution as shown in (1), other primary processes from recoil tritium reactions with CH$_3$CHF$_2$ include H abstraction, F abstraction, T*-for-F substitution, and T*-for-R displacements

$$T^* + C_2H_4F_2 \longrightarrow HT + C_2H_3F_2 \quad (4)$$

$$T^* + CH_3CHF_2 \longrightarrow TF + CH_3CHF \quad (5)$$

$$T^* + CH_3CHF_2 \longrightarrow CH_3CHTF + F \quad (6)$$

$$T^* + CH_3CHF_2 \longrightarrow CH_3T + CHF_2 \quad (7)$$

$$ \longrightarrow CHTF_2 + CH_3 \quad (8)$$
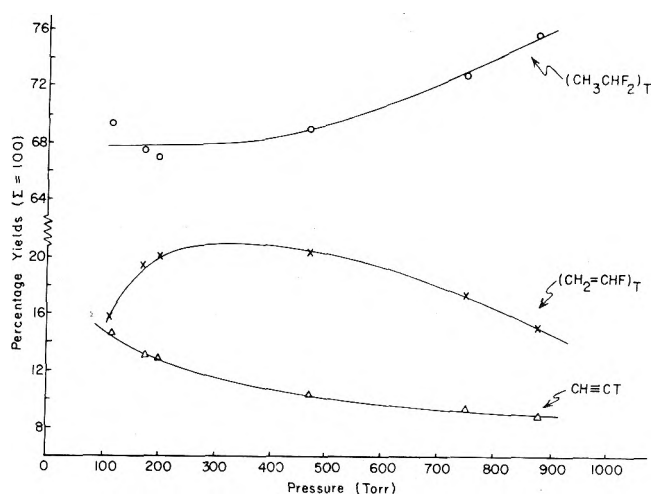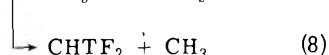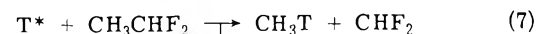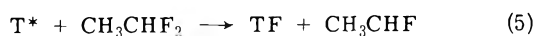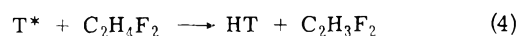
Figure 1. Percentage yields of stabilization and decomposition products from recoil tritium reactions with CH$_3$CHF$_2$ as a function of pressure.

All of the expected primary products with the exception of TF have been experimentally observed. At a pressure of 1 atm, the yields of these products (with reference to the yield of HT as 1000) are CH$_3$CHTF (3), CH$_3$T (57), CHTF$_2$ (12), and C$_2$H$_3$TF$_2$ (520).

Products expected from the consecutive HF-elimination processes, (2) and (3), are also observed. At 1 atm, their yields relative to that of HT as 1000 are C$_2$H$_2$TF (72) and C$_2$HT (30). The pressure dependence of the yields for these two products and that for the stabilization product, C$_2$H$_3$TF$_2$, is shown in Figure 1. They are expressed as percentages of the initial amount of excited C$_2$H$_3$TF$_2$. It is obvious from the figure that when the pressure increases from 100 to 900 Torr, the yield of C$_2$H$_3$TF$_2$ increases, the yield of C$_2$HT decreases, and the yield of C$_2$H$_2$TF goes through a maximum.

In reactions 2 and 3, TF may be eliminated instead of HF to give nonlabeled products. In order to account for the undetected TF, the observed yield of vinyl fluoride must be multiplied by 4/3 and the observed yield of acetylene must be multiplied by 2. A tritium isotope effect of unity is assumed here. All of the data shown in Figure 1 have already been corrected for these factors.

Other decomposition paths for excited C$_2$H$_3$TF$_2$ such as H$_2$ and F$_2$ elimination are also possible.

$$(C_2H_3TF_2)^* \longrightarrow C_2H_3T + F_2 \quad (9)$$

$$(C_2H_3TF_2)^* \longrightarrow CHT{=}CF_2 + H_2 \quad (10)$$
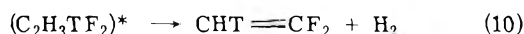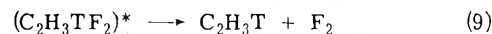
However, at 1 atm, the observed yields of C$_2$H$_3$T and CHT=CF$_2$ are only 4 and 6, respectively, relative to HT as 1000. These small yields indicate that both (9) and (10) are relatively unimportant decomposition routes when in competition with (2).

In order to show the complementary nature of the stabilization and decomposition products for the T*-for-H substitution route, the *corrected* yields of C$_2$H$_3$TF$_2$, C$_2$H$_2$TF, and C$_2$HT (expressed relative to HT as 1000) are summed up. An assumption that the HT yield is pressure independent has been made here. The sum of the three yields at various pressures is roughly a constant with a value of 670 ± 10. This also confirms that the product contributions from other decomposition routes such as (9) and (10) are very minor.

Consecutive Decomposition Following Hot Atom Activation. There are some significant differences between the consecutive decomposition initiated by hot atom activation and that by conventional thermal activation. In the thermal activation case, the excitation energy is introduced into the activated molecule in two separate steps since the molecules receive the internal energy as a result of bimolecular collisions. Whenever the parent molecule has accumulated enough energy, it will undergo the first decomposition process. The resulting product will only undergo further decomposition when enough excitation energy is again accumulated. This means that another collisional excitation is in general a requirement between the two decomposition steps.

On the other hand, in the case of hot atom activation, all the required excitation energy is introduced into the parent molecule during the primary substitution process. Bimolecular collisions with other species will have a negative effect. Instead of supplying energy and causing the second decomposition, a collision will normally deactivate the excited species. As a result, an increased collisional frequency will enhance the stabilization and not the consecutive decomposition.

Theoretically, consecutive decomposition similar to that of the hot atom activation system can also be initiated by other nonthermal processes such as photolysis and chemical activation. However, there is essentially no report in the literature which is *solely* devoted to the study of consecutive reactions initiated by these methods.[3]

Scheme of Stabilization and Consecutive Decomposition in Recoil Tritium Activation of CH_3CHF_2. The thermal decomposition of CH_3CHF_2 has been studied by Tschuikow-Roux, Quiring, and Simmie with shock tube techniques.[8] The HF elimination from CH_3CHF_2 has an activation energy of 61.9 ± 1.8 kcal/mol while the decomposition of vinyl fluoride has an activation energy of 70.8 ± 3.6 kcal/mol.[9] The heat of reaction for the former process is 20 kcal/mol while that of the latter is 17 kcal/mol.[8,9] This means that during the first consecutive decomposition step the total excitation energy of the two products, vinyl fluoride and HF, will be decreased by an additional 24 kcal/mol due to the thermodynamic requirement.

The full scheme of stabilization and consecutive decomposition of recoil tritium activation of CH_3CHF_2 is shown in Figure 2. According to the amount of excitation energy, we have divided the primary substitution product, $C_2H_3TF_2$, into three categories. The first type includes those with energy below 62 kcal/mol, the activation energy for reaction 2. These molecules, which are represented by one asterisk, have only one reaction path available to them, *i.e.*, collisional stabilization to yield the labeled parent.

The second group of excited molecules, which are marked with two asterisks, possess energy between 62 and 91 kcal/mol. The latter quantity, which represents the minimum energy requirement to initiate the consecutive decomposition, is evaluated by adding the heat of reaction of (2) to the activation energy for HF elimination from vinyl fluoride neglecting the amount of energy carried away by the HF in reaction 2. Excited molecules in this category may either decompose to vinyl fluoride or be stabilized to give the tritiated parent. The stabilization process may be carried out by either strong or weak collisions. In other words, the excited molecule may either lose all its excitation in a single encounter, or it may cascade down in energy by multiple collisions.
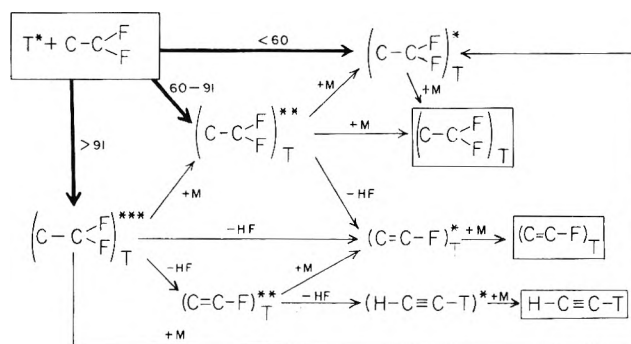
Figure 2. Possible stabilization and decomposition modes of excited $C_2H_3TF_2$ subsequent to hot atom excitation.
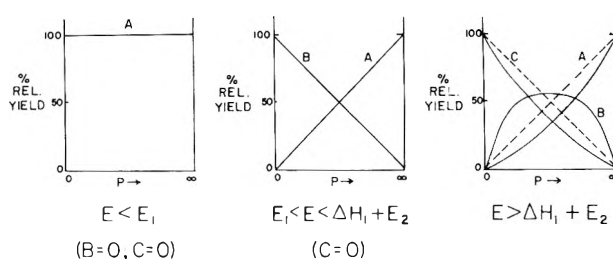
Figure 3. Three fundamental types of pressure dependence curves for the hypothetical system A $(E_1, \Delta H_1) \rightarrow$ B $(E_2, \Delta H_2) \rightarrow$ C.

The third type of excited molecules, which are represented by three asterisks, possess energies greater than 91 kcal/mol. These molecules are capable of giving C_2HT as their consecutive decomposition product. However, they also may be stabilized or partially stabilized by strong or weak collisions to give $C_2H_3TF_2$ and C_2H_2TF as final products.

Qualitative Confirmation of the Pressure Dependence of the Products. The unimolecular nature of the consecutive decomposition can be confirmed by analyzing the pressure effect on the stabilization and the decomposition products. In particular, it is constructive to demonstrate that a maximum is actually expected for the intermediate compound (C_2H_2TF, in this case) for its pressure dependence. Since the excitation distribution is expected to be broad, the pressure dependence of products excited according to the three categories described in the previous section has been employed for this illustration.

Figure 3 shows the pressure dependence of products for the three categories of excitation. A hypothetical consecutive decomposition is used here for illustration

$$A \xrightarrow[\Delta H_1]{E_1} B \xrightarrow[\Delta H_2]{E_2} C$$
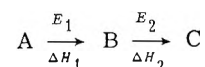
where E_1, E_2 and ΔH_1, ΔH_2 are activation energies and heats of reaction for the two respective decomposition steps. For the group with excitation energy less than E_1, the stabilized parent compound, which is the only possible final product, should be invariant with pressure. For the second type of excited molecules, which are capable of undergoing the first decomposition but not the consecutive one, A and B are the only expected products. The former should increase while the latter should decrease with increasing pressure although the variations are not necessarily linear. For the third type of molecules with excitation energy in excess of that needed to undergo both the first and second decomposition, all three products are possible.
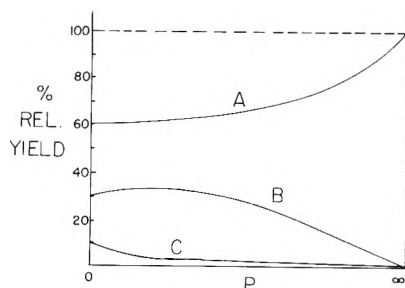
Figure 4. Pressure dependent product curves for a hypothetical energy distribution assuming the following: 60%, $E < E_1$; 30%, $E_1 < E < \Delta H_1 + E_2$; 10%, $E > \Delta H_1 + E_2$.

The pressure dependence is such that A increases with pressure, C decreases with pressure, while B exhibits a maximum (B has a zero yield at both zero and infinite pressure, and a finite yield at intermediate pressures).

In the actual recoil tritium activated systems, a broad spectrum involving contributions from all three of these categories should exist. For qualitative comparison with the experimental results, a hypothetical distribution of these three groups is assumed: 60% group 1, 30% group 2, and 10% group 3. The combined result is shown in Figure 4. It is seen that this distribution reproduces the trends expressed by the experimental results.

In this work a simple qualitative picture has been obtained which confirms that T*-for-H substitution gives a broad excitation distribution with a median energy of several electron volts of energy. The limiting values for the three energy ranges mentioned in the previous section (62

and 91 kcal/mol) can only be treated as extreme lower limits. These theoretical parameters could easily be 20 or 30 kcal/mol lower in energy than the more realistic energies where decomposition and consecutive decomposition become *significant*. Moreover, the necessary inclusion of the amount of energy partitioned to HF during the first decomposition step tends to push the energy limit for molecules which are capable of undergoing consecutive decomposition to a value somewhat beyond the 110- or 120-kcal/mol range.

References and Notes

(1) Part of this work was presented at the 161st National Meeting of the American Chemical Society, Los Angeles, Calif., April, 1971.
(2) See, for example, S. W. Benson, "Foundations of Chemical Kinetics," McGraw-Hill, New York, N Y., 1960.
(3) K. A. Krohn, N. J. Parks, and J. W. Root, *J. Chem. Phys.*, **55**, 5771, 5785 (1971).
(4) F. S. Rowland, "Proceedings of the International School of Physics, 'Enrico Fermi' Course XLIV—Molecular Beam and Reaction Kinetics," Ch. Schlier, Ed., Academic Press, New York, N.Y., 1970.
(5) R. Wolfgang, *Progr. React. Kinet.*, **3**, 97 (1965); *Annu. Rev. Phys. Chem.*, **16**, 15 (1965).
(6) E. K. C. Lee and F. S. Rowland, *J. Amer. Chem. Soc.*, **85**, 897 (1963).
(7) C. T. Ting and F. S. Rowland, *J. Phys. Chem.*, **72**, 763 (1968); **74**, 4080 (1970).
(8) E. Tschuikow-Roux, W. J. Quiring, and J. M. Simmie, *J. Phys. Chem.*, **74**, 2449 (1970).
(9) J. M. Simmie, W. J. Quiring, and E. Tschuikow-Roux, *J. Phys. Chem.*, **74**, 992 (1970).
(10) J. K. Lee, E. K. C. Lee, B. Musgrave, Y.-N. Tang, J. W. Root, and F. S. Rowland, *Anal. Chem.*, **34**, 641 (1962).

Kinetics of Gas-Phase Thermal Decomposition of Tris(difluoroamino)methyl Compounds

Francis C. Rauch and Anthony J. Fanelli*[1]

American Cyanamid Company, Chemical Research Division, Stamford, Connecticut 06904

Gas-phase thermal decomposition kinetics are reported for tris(difluoroamino)methyl chloride, $(NF_2)_3C-Cl$, tris(difluoroaminomethylamine, $(NF_2)_3C-NH_2$, and tris(difluoroamino)methyl methyl ether, $(NF_2)_3C-O-CH_3$, over the temperature range 184.5–230° in static reactors. The reactions in each case are first order with activation energies of 36.1, 29.6, and 36.2 kcal/mol, respectively. A correlation was found between the order of stability and electronegativity of the group attached to the tris(difluoroamino) functionality.

Introduction

Recently several reports[2-5] have appeared concerning the synthesis and chemistry of difloroamino (NF_2) compounds. In a study of the decomposition behavior of a series of poly-(difluoroamino)fluoromethanes[4] attention was drawn to the similarity in rate parameters to those of polynitro com-

pounds. As a result the rate-determining step was postulated as homolytic cleavage of the C–N bond as had been previously proposed for the polynitro compounds.[6]

Herein thermal decomposition results are reported for three compounds having the general structure $(NF_2)_3C-Z$ with Z = Cl, NH_2, OCH_3, not previously reported. A similar study of related compounds with Z = NF_2 or F has already

appeared.[4] In contrast to the mechanism proposed for the latter two compounds only one of the compounds, $(NF_2)_3C-Cl$, is proposed to decompose by simple C–N bond rupture, the remaining two having more complex mechanisms.

Experimental Section

Caution. The NF compounds discussed in this paper are extremely dangerous and frequently explode without warning. They are especially sensitive to impact, friction, and changes of state. They are also strong oxidizing agents. Even 1 mmol quantities are dangerous and should be handled with adequate shielding, remote handling equipment, and protective clothing.

Gas-phase decomposition studies were carried out using a 22-ml spherical reactor (s/v = 0.85 cm^{-1}) constructed from Monel metal and capped with a Hoke M440 bellows seal valve. All connections were made with Swagelok fittings. The bulb was prepassivated with surplus NF compounds or sacrifice runs of starting material. At most eight to ten runs were found necessary to achieve reproducible data. To ensure that homogeneous rather than heterogeneous catalyzed decomposition was being observed, it was found convenient to make runs employing packed and unpacked vessels simultaneously. Both vessels were identical except that one was packed with nickel wire, increasing the surface-to-volume ratio by a factor of about 3.

A sampling procedure was used in the kinetics runs. The bulb was charged to the appropriate pressure on a vacuum line and an initial sample removed for analysis. The bulb was then immersed in the hot bath, either fluidized sand or silicone oil, for the selected time interval, quickly removed, and the reaction quenched by immersion in an ice bath. Calibration with a bulb specially equipped with a thermocouple at its center showed that the temperature rise and fall times on entering and leaving the bath were negligible provided reasonably long time intervals were used between samples. This was also demonstrated by the reproducibility of the results for successive runs using different time intervals.

The concentrations of starting material and products were followed by vpc using an Aerograph Model 202 chromatograph equipped with a 7-ft column of FX-45 on GC/CLA. Isolation of products was accomplished using a Hamilton Co. fraction collector cooled to −196°. Starting materials were supplied by a separate synthesis group at the American Cyanamid research laboratories under government contract.

Methods for synthesizing the tris(difluoroamino)methyl compounds described in this paper as well as others have appeared elsewhere.[2,3] The compounds herein were prepared by reaction of the appropriate compound (HCl, NH$_3$, CH$_3$OH) with perfluoroguanidine followed by fluorination to convert the bis(difluoroamino)fluoramino adducts to the corresponding tris(difluoroamino) compound.

Purity was generally 99% as judged by vpc and appropriate spectroscopic methods. These same methods were used for isolation and identification of intermediates, principally ir, uv, nmr, and mass spectroscopy. Comparisons with known compounds appearing in the open or classified literature were made where possible.

Kinetic Results

Decomposition studies for $(NF_2)_3C-Cl$, $(NF_2)_3C-NH_2$, and $(NF_2)_3C-OCH_3$ were carried out over the temperature
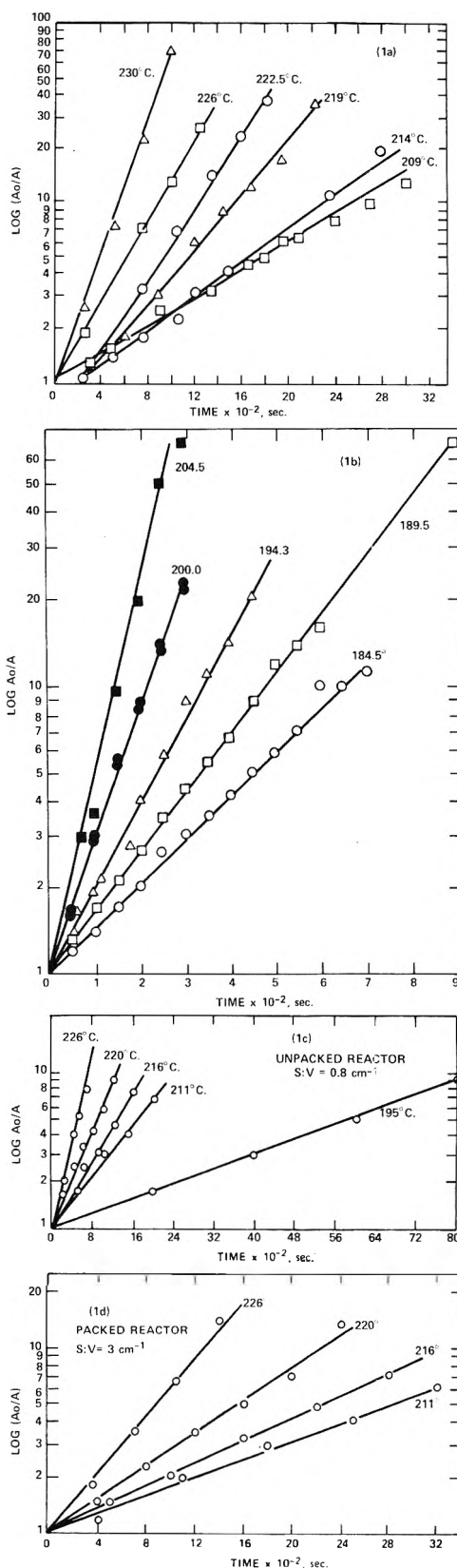
Figure 1. Rate plots for decomposition of tris(difluoroamino)methyl compounds: (a) $(NF_2)_3C-Cl$, (b) $(NF_2)_3C-NH_2$, (c) and (d) $(NF_2)_3C-O-CH_3$.

range 184.5–230°. In all cases first-order kinetics were followed quite well to conversion ratios in excess of 90%. The first-order rate law was established from measurements of the partial pressure of starting compound as a function of

TABLE I: Thermal Decomposition First-Order Rate Constants for Tris(difluoroamino)methyl Compounds

				Compound			
					$(NH_2)_3C\text{-}O\text{-}CH_3$		
$(NF2)_3C\text{-}Cl$		$(NH_2)_3C\text{-}NH_2$		Unpacked		Packed	
$k \times 10^3$, sec^{-1}	t, °C	$k \times 10^3$, sec^{-1}	t, °C	$k \times 10^4$ sec^{-1}	t, °C	$k \times 10^4$, sec^{-1}	k(unpacked)/ k(packed)
0.86	209.0	3.54	184.5	2.68	195.0		
1.05	214.0	5.23	189.5	9.48	211.0	5.76	1.6
1.73	219.0	6.81	194.3	12.40	216.0	7.15	1.7
2.48	222.5	10.34	200.0	18.28	220.0	10.37	1.8
2.60	226.0	14.04	204.5	31.30	226.0	17.45	1.8
4.04	230.0						

TABLE II: Activation Parameters For Tris(difluoroamino)methyl Compounds

Compound		A, sec^{-1}	E_a, kcal/mol
$(NF_2)_3C\text{-}Cl$		13.24 ± 3.54	36.05 ± 3.16
$(NH_2)_3C\text{-}NH_2$		11.68 ± 0.41	29.58 ± 0.88
$(NH_2)_3C\text{-}O\text{-}CH_3$	(unpacked)	13.25 ± 0.80	36.07 ± 1.77
	(packed)	13.10 ± 2.30	36.28 ± 5.23
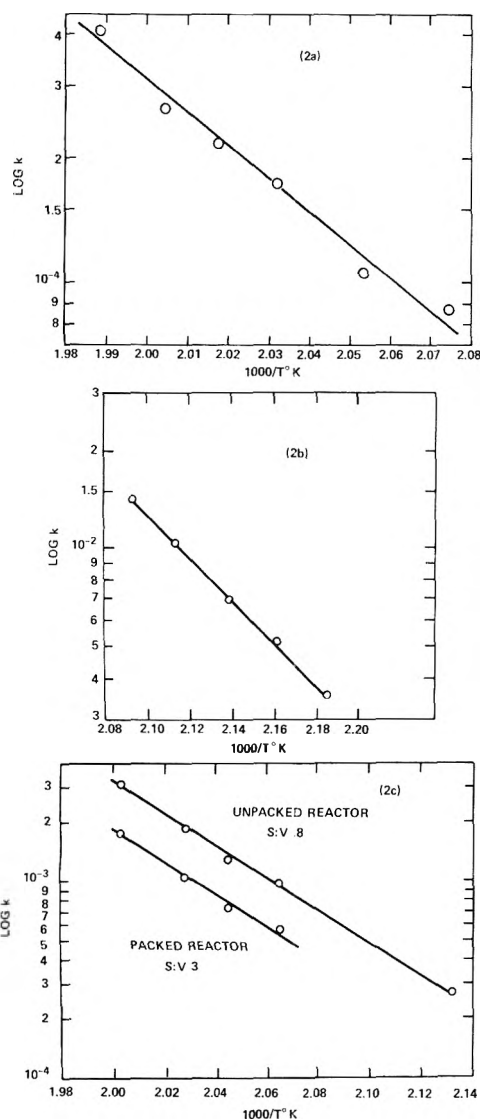
Figure 2. Arrhenius plots for tris(difluoroamino)methyl compounds: (a) $(NF_2)_3C\text{-}Cl$, (b) $(NF_2)_3C\text{-}NH_2$, (c) $(NF_2)_3C\text{-}O\text{-}CH_3$.

time by gas chromatography. Fitting of the data to rate laws having $n = \frac{1}{2}$, 2 gave significantly poorer results. Results for all three compounds are shown in Figure 1. For $(NF_2)_3C\text{-}OCH_3$ results for the packed reactor are included explicitly because in this case the rate was actually found to be lower than in the unpacked reactor. The consequence of this on the proposed mechanism of decomposition will be discussed later.

Arrhenius plots are presented in Figure 2. Rate constants and kinetic parameters calculated from the data are summarized in Tables I and II. Data were computed by least squares. Standard errors are given.

Mechanism

A. Tris(difluoroamino)methyl Chloride, $(NF_2)_3C\text{-}Cl$. The induction period noted at three of the temperatures in Figure 1 is probably an artifact. The absence of an induction period in such similar compounds as $(NF_2)_3C\text{-}NF_2$ and $(NF_2)_3C\text{-}F$,[4] and the fact that it was observed in only three of the runs, suggest that it was due to some experimental fault in detection. The rapid growth of the principal intermediate from the beginning of pyrolysis (Figure 3) also lends support to this contention. The rather meager supply of starting material prevented further investigation of this point.

The value of the activation energy is comparable with those obtained for other tris(difluoroamino)methyl compounds which have no active hydrogen atoms.[4] Whereas the A factor is in the range expected for homogeneous decomposition it is somewhat lower than those for the poly-(difluoroamino)fluoromethanes.[4] The reason for this discrepancy is unclear. That the decomposition rate was not affected by a threefold increase in surface-to-volume ratio excludes heterogeneous catalysis as the cause. It is noteworthy that A factors for gas-phase decomposition of polyatomic molecules into two large fragments cover a wide range. Values of log A from 13.22 to 17.45 are given for 16 examples of such reactions.[7]

The following intermediates and products have been identified, principally by infrared spectroscopy: $F_2N\text{-}C(=NF)Cl$, CF_3Cl, CF_4, N_2F_4, NF_3, and N_2. The species, $F_2NC(F_2)Cl$ and $F\text{-}C(=NF)Cl$, have not been unambiguously identified but were suggested by a composite infrared spectrum. N,N'-Trifluorochloroformamidine, $F_2N\text{-}C(=NF)Cl$, is the principal decomposition intermediate. The concentration-time profiles shown in Figure 3 for six temperatures indicate rapid initial growth, passage through a maximum, and, finally, exponential decay. In order to gain a semiquantitative idea of its stability, the ex-
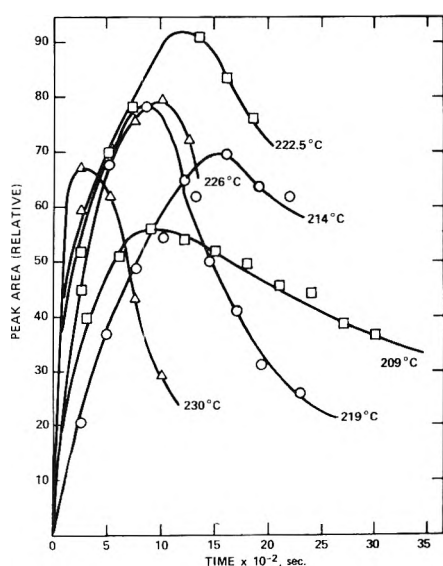
Figure 3. Concentration–time profiles for $F_2N-C(=NF)Cl$.

Figure 4. $(NF_2)_3C-NH_2$ decomposition products identified and their distribution with contact time at $184.5°$.

Figure 5. $(NF_2)_2C(F)NH_2$ concentration–time profile.

perimental profile at 219° was curve fitted using a first-order growth–decay equation

$$(F_2NC-Cl)_t = ((NF_2)_3C-Cl)_0 \frac{k_1}{k_1 - k_2} (e^{-k_1 t} - e^{-k_2 t})$$

(with NF double-bonded to the C of F_2NC-Cl)

where k_1 and k_2 refer to the formation and decay rate constants of the intermediate. From this analysis it is estimated that the first-order rate constant for decomposition of $F_2N-C(=NF)Cl$ is about 9.6×10^{-4} sec^{-1}, a value about half that of $(NF_2)_3C-Cl$ at the same temperature.

From the nature of the principal intermediate and the similarity in the values of the kinetic parameters to those found for compounds $(NF_2)_3C-NF_2$ and $(NF_2)_3C-F$,[4] it is concluded that the first and rate-controlling step in these three cases is the same, i.e., homolytic cleavage of a C–N bond. The initial steps in this mechanism are visualized as follows

$$(NF_2)_3C-Cl \xrightarrow{k_1} (NF_2)_2C-Cl + \cdot NF_2$$

$$(NF_2)_2\dot{C}-Cl \xrightarrow{k_2} F_2N-C(=NF)-Cl + \cdot F$$
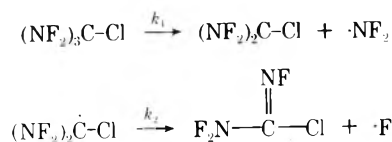
This path parallels the routes proposed for the formation of $(NF_2)_2C=NF$ from $(NF_2)_3CNF_2$ and of $F_2N-C(=NF)F$ from $(NF_2)_3C-F$.[4] Ejection of a fluorine atom from the methyl radical produced in the first step is considered to be extremely rapid. From the limited data on the nature and distribution of the other products which was not easily obtainable from our experimental procedure due to extensive overlapping of the chromatographic peaks, further speculation on the details of the mechanism beyond the two steps above seems unwarranted. It is likely, however, that a scheme analogous to those proposed for the compounds $(NF_2)_3C-NF_2$, $(NF_2)_3C-F$, and $(NF_2)_2C(F)-F$[4] could be followed by $(NF_2)_3C-Cl$ also.

B. Tris(difluoroamino)methylamine, $(NF_2)_3C-NH_2$.
The following significant compounds were identified as intermediates during decomposition: N_2, CF_4, N_2F_4, HF, $F_2C=NF$, and $(NF_2)_2C(F)NH_2$. The ultimate decomposition products corresponding to infinite time are N_2, CF_4, and HF. Figure 4 shows the distribution of the resolvable
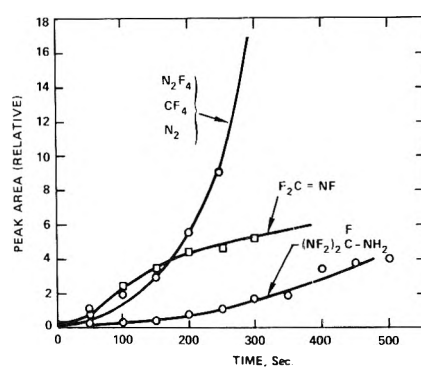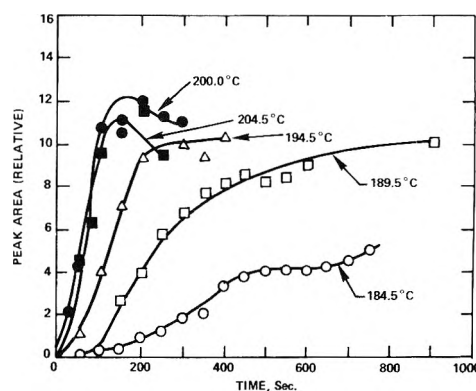
chromatographic peaks of the products with contact time at a temperature of $184.4°$. The most interesting product profile in Figure 4 from the point of view of mechanism is the compound $(NF_2)_2C(F)NH_2$. Figure 5 shows concentration–time profiles for this compound at five temperatures. The plots indicate that bis(difluoroamino)fluoromethylamine has considerable stability up to about 200° since no maxima are found for the lower three temperatures up to the time at which the runs were terminated.

The Arrhenius A factor (Table II) is lower than normal for poly(difluoroamino)methyl compounds, giving rise to a negative entropy of activation, -5.92 ± 1.33 eu. From the low energy of activation and the negative entropy of activation, it would seem that homolytic bond cleavage of, e.g., a C–NF$_2$ bond can be eliminated from consideration as the rate-controlling step. The energy of activation for such processes are generally about 40 kcal/mol, being approximately equal to the dissociation energy of the bond broken. Such a process should also have a positive entropy of activation.

Failure to observe $F_2N-C(=NF)NH_2$ among the products also suggests that C–N bond breaking is not the first step in the decomposition since for all other tris(difluoroamino)methyl compounds investigated, where it is the first step, trifluoroguanyl compounds have been found as principal intermediates.

A negative entropy of activation generally implies that rotational degrees of freedom in the starting material are replaced by vibrational modes in the transition state, e.g., a cyclic intermediate. Two possibilities for the rate-controlling step can be conceived almost immediately.

Scheme I: HF Elimination
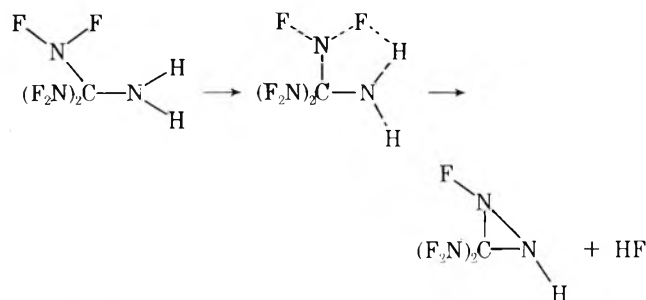
Scheme II: HNF$_2$ Elimination

$$HNF_2 + (F_2N)_2C=NH$$
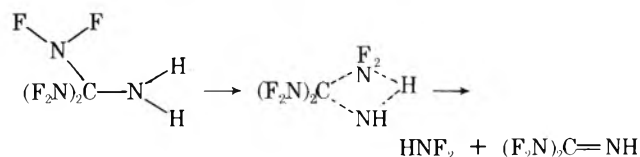
From our data one scheme cannot be favored over the other; however, Scheme II provides a ready path for formation of bis(difluoroamino)fluoromethylamine in a secondary process, e.g.

$$HNF_2 \longrightarrow \cdot NF + HF$$

$$HF + (NF_2)_2C=NH \longrightarrow (NF_2)_2C(F)NH_2$$
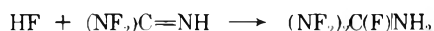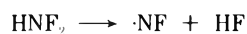
C.   Tris(difluoroamino)methyl   Methyl   Ether, $(NF_2)_3C\text{-}O\text{-}CH_3$. As noted above the rate constants for the packed reactor are smaller by a constant factor of 1.7 ± 0.1 than the corresponding rate constants observed for the unpacked reactor (Figure 1). This factor is approximately one-half of the value by which the surface-to-volume ratio of the two reactors differ. The slopes of the respective Arrhenius plots are the same within experimental error. The apparent activation energy (taking the average of the values calculated for each line, 36.1 and 36.3) is considerably higher than those expected for a simple heterogeneous decomposition process. The high frequency factor and an activation energy within the range of the first C–N bond dissociation energy found for other tris(difluoroamino)methyl compounds[4] suggests that homolytic bond rupture is involved in some manner in the rate-controlling step(s).

Fifteen intermediates were indicated by product isolation. The most interesting compound identified is $(F_2N)_3C\text{-}O\text{-}CH_2\text{-}NF_2$. This compound has greater NF content than the parent, yet is more stable. The remaining intermediates together with their time distribution at 226° (unpacked reactor) are given in Figure 6. The curves were constructed from chromatographic data and are labelled according to the relative retention time of their corresponding peaks.

The intermediates can be divided into two distinct categories: those retaining the CH$_3$–O–C configuration and those having a –CH$_2$–O–C structure. Compounds in the first category are regarded as deriving from the unimolecular decomposition of CH$_3$–O–C(NF$_2$)$_3$, in which the tris portion of the molecule, –C(NF$_2$)$_3$, suffers a series of degradative steps giving rise to CH$_3$–O–C(=NF)NF$_2$, CH$_3$–O–CF(=NF), and CH$_3$–O–CF$_3$. The compounds in the second category derive from CH$_3$–O–C(NF$_2$)$_3$ by replacement of a hydrogen of the methyl group with either NF$_2$ or F.
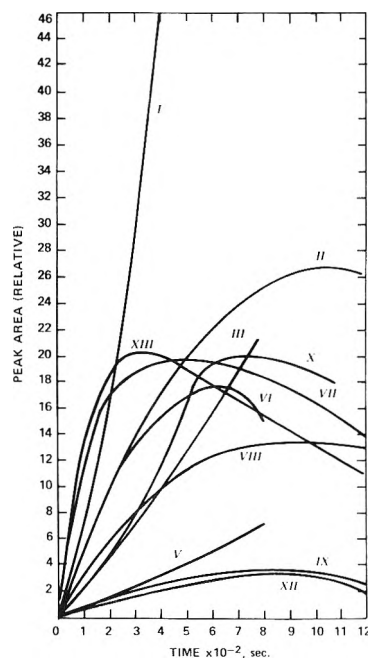
Figure 6. Product distribution from decomposition of CH$_3$–O–C(NF$_2$)$_3$ at 226°: I, N$_2$,COF$_2$,HF; II, N$_2$F$_4$; III, CH$_3$–O–CF$_3$; IV, F$_2$N–CH$_2$–O–CF$_3$; V, CH$_3$–O–C(=NF)F; VI, CH$_3$–O–C(=NF)NF$_2$; VII, F$_2$N–CH$_2$–O–C(=NF)F; VIII, F–CH$_2$–O–C(=NF)F; X, F$_2$N–CH$_2$–O–C(=NF)NF$_2$; XII, F–CH$_2$–O–C(NF$_2$)$_3$; XIII, F$_2$N–CH$_2$–O–C(NF$_2$)$_3$.

Thus, this category can be subdivided into two further classes: one containing F$_2$N–CH$_2$–O–C(NF$_2$)$_3$ and its decomposition products, and one containing F–CH$_2$–O–C(NF$_2$)$_3$ and its decomposition products. The nature of the products clearly demonstrates that the disappearance of CH$_3$–O–C(NF$_2$)$_3$ is related to at least two reactive steps. Absence of such compounds as F–C(=NF)F, CH$_3$F, and CH$_3$NF$_2$ indicates that the C–O–C backbone remains intact throughout much of the decomposition. To examine different possible mechanisms, especially the role of the surface, the decomposition at 226° was examined in the presence of additives. Three additives were tested: helium, nitric oxide, and N$_2$F$_4$. None was found to have any noticeable effect on the rate. The experiments with helium as an additive in large excess (250 mm of He:10 mm of (NF$_2$)$_3$C–O–CH$_3$) were carried out in order to determine whether the surface was merely acting as a third body in the chain-breaking step. The nitric oxide (1 mm of NO:10 mm of (NF$_2$)$_3$C–O–CH$_3$) was incorporated as a radical scavenger. The N$_2$F$_4$ (3 mm of N$_2$F$_4$:10 mm of (NF$_2$)$_3$C–O–CH$_3$) was used to determine whether the reaction scheme involved both C–NF$_2$ bond rupture and back reaction between the radicals thus formed. Although this list of experiments with additives is far from exhaustive, they do seem to indicate that the surface is playing some role other than just a third body.

Any proposed mechanism must account for several significant observations. The rate of decomposition is first order in CH$_3$–O–C(NF$_2$)$_3$. The kinetic parameters suggest that homolytic C–N bond scission is involved in the rate-determining step(s). The rate of disappearance of CH$_3$–O–C(NF$_2$)$_3$ is decreased when the surface-to-volume ratio is increased. The nature of the intermediates suggests that the disappearance of CH$_3$–O–C(NF$_2$)$_3$ is related to two distinct processes: one involving reaction at the tris group and another involving reaction at the methyl group. The C–O–

C backbone remains intact throughout much of the decomposition. The surface plays some role other than just a third body.

To explain these observations the following mechanism is proposed

$$CH_3-O-C(NF_2)_3 \xrightarrow{k} \cdot NF_2 + CH_3\dot{O}C(NF_2)_2 \xrightarrow{-F}$$

$$\begin{array}{c} NF \\ \parallel \\ CH_3OC-NF_2 \end{array} \text{ etc. (1)}$$

$$\cdot NF_2 + M \underset{}{\overset{K}{\rightleftharpoons}} M \cdot NF_2 \qquad (2)$$

$$\cdot NF_2 + CH_3-\dot{O}-C(NF_2)_3 \xrightarrow{k_2} HNF_2 + \cdot CH_2-O-(NF_2)_3 \quad (3)$$

$$CH_2-O-C(NF_2)_3 + \cdot NF_2 \longrightarrow F_2N-CH_2-O-C(NF_2)_3 \xrightarrow{-NF_2}$$

$$F_2NCH_2O\dot{C}(NF_2)_2 \xrightarrow{-F} \text{ etc. (4)}$$

$$+ \cdot F \longrightarrow F-CH_2-O-C(NF_2)_3 \xrightarrow{-NF_2}$$

$$FCH_2O\dot{C}(NF_2)_2 \xrightarrow{-F} \text{ etc. (4')}$$
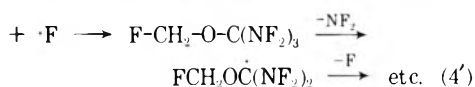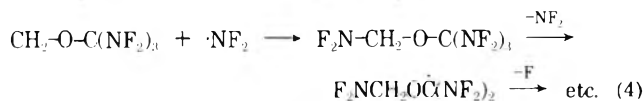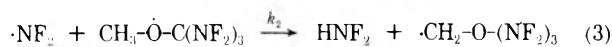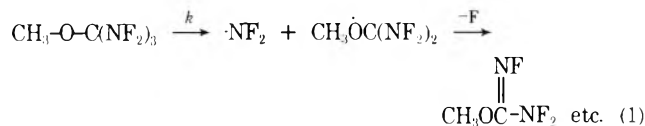
If it is assumed that the equilibrium reaction between $\cdot NF_2$ and the surface is rapidly established, this scheme leads to first-order kinetics with the observed inverse dependence of the rate on the surface-to-volume ratio.

$$-d(CH_3-O-C(NF_2)_3/dt = k_1(CH_3-O-C(NF_2)_3 + k_2(\cdot NF_2)(CH_3-O-C(NF_2)_3)$$

From the assumed rapid equilibrium reaction

$$(NF_2 \cdot) = (M \cdot NF_2)/KM$$

For low surface coverage and/or weak bonding, M may be replaced by M_0.

$$\frac{-d((NF_2)_3C-O-CH_3)}{dt} = \left[k_1 + k_2\frac{M \cdot NF_2}{KM_0}\right] \times$$

$$(NF_2)_3C-O-CH_3 = k'((NF_2)_3C-O-CH_3)$$

Note also that the basic form of the rate law is not changed even if the stoichiometry of the equilibrium reaction is different. For example, if it is assumed that the equilibrium may be written

$$2NF_2 \cdot M \rightleftharpoons M \cdot N_2F_4$$

it may be shown that the rate law is as follows

$$\frac{-d((NF_2)_3C-O-CH_3)}{dt} = \left\{k_1 + k_2\left[\frac{M \cdot N_2F_4}{KM_0}\right]^{1/2}\right\} \times (NF_2)_3C-O-CH_3$$

Since there are several unknowns in the expression for the observed rate constant the order with which the surface appears cannot be determined from our experimental data.

Exactly what the nature of the active surface sites is has not been determined. That it is not a "typical" passivated Monel surface seems clear, since for the reactors employed conditioning of the surface by several sacrifice runs of $(NF_2)_3C-O-CH_3$ was required to yield reproducible kinetics and to produce the compound, $F_2N-CH_2OC(NF_2)_3$, even though the reactors were prepassivated with other NF compounds. It should also be noted that exposure of the conditioned surface to the atmosphere effectively destroys the activity of the sites which function in this reaction.

The proposed mechanism considers $\cdot NF_2$ rather than $\cdot F$ to be the predominant reacting species in step 3 in order to account for the retardation effect of the surface. If the reaction

$$\cdot F + CH_3OC(NF_2)_3 \longrightarrow HF + \cdot CH_2OC(NF_2)_3$$
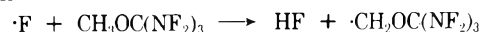
predominated, no such effect would be expected, since a surface equilibrium involving fluorine radicals is not easily visualized. Inspection of the product profiles in Figure 6 supports this hypothesis, in that the relative buildup of $F_2N-CH_2OC(NF_2)_3$ (peak XIII) is considerably greater than that of $FCH_2OC(NF_2)_3$ (peak XII). Presuming that these two species form according to steps 4 and 4', there is no reason to believe that one should be favored over the other, since the activation energies for both reactions should be about zero. The conclusion, then, is that NF_2 radicals are present in much greater concentration than F radicals. Absence of NF_3 among the reaction products is, perhaps, more striking evidence that the concentration of F atoms does not build up to any appreciable extent, their effective removal probably accomplished by some very rapid reaction. One such reaction could be

$$F \cdot + HNF_2 \longrightarrow HF + \cdot NF_2$$
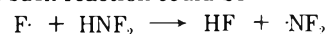
The results of the single experiment in which the pyrolysis was carried out in the presence of N_2F_4 are difficult to assess in terms of the proposed mechanism. Since the concentration of NF_2 radicals builds up very rapidly, the amount added might not have been sufficient to cause an appreciable effect.

References and Notes

(1) To whom correspondence should be addressed at The Lummus Company, 1515 Broad Street, Bloomfield, N.J. 07003.
(2) J. F. Zollinger, C. D. Wright, J. J. McBrady, D. H. Dybvig, F. A. Fleming, G. A. Kurhajeo, R. A. Mitsch, and E. W. Neuvar, *J. Org. Chem.*, **38**, 1065 (1973), and previous papers in this series.
(3) W. C. Firth, Jr., and S. Frank, *J. Org. Chem.*, **38**, 1083 (1973).
(4) J. M. Sullivan, A. E. Axworthy, and T. J. Houser, *J. Phys. Chem.*, **74**, 2611 (1970).
(5) R. A. Mitsch and W. E. Neuvar, *J. Phys. Chem.*, **70**, 546 (1966).
(6) J. M. Sullivan and A. E. Axworth, *J. Phys. Chem.*, **70**, 3366 (1966).
(7) S. W. Benson, "Thermochemical Kinetics," Wiley, New York, N.Y., 1968.

Kinematics of Hydride-Ion and Hydrogen-Atom Transfer Reactions in Monosilane[1]

T. M. Mayer and F. W. Lampe*

Davey Laboratory, Department of Chemistry, The Pennsylvania State University, University Park, Pennsylvania 16802

(Received February 25, 1974; Revised Manuscript Received July 22, 1974)

The kinematics of ion–molecule reactions in monosilane that represent the net transfer of a hydride ion or hydrogen atom have been investigated by isotopic distribution measurements and kinetic energy analysis of product ions in a tandem mass spectrometer. Reactions involving a net hydride-ion transfer proceed *via* a direct, stripping-type process, yielding an ion with very little kinetic energy, and by a complex-formation mechanism that is particularly prominent at low collision energies and leads to scrambling of H and D atoms. Direct H-atom transfer processes, observed in those cases in which it is energetically favorable, approach the spectator stripping model at higher collision energies. For those cases in which direct processes and the complex-formation process yield the same product ion, it was found that the two channels proceed with nearly equal cross sections at low-collision energies. At higher collision energies the direct processes completely dominate the mechanism.

Introduction

The importance of reactions involving the net transfer of a hydride ion or hydrogen atom from one particle to another in ion–molecule chemistry is well recognized. Reactions whose overall chemistry can be described as the transfer of an H^- ion have been reported to be of particular importance in such organic systems as propane and cyclobutane,[2] in the silanes,[3-8] in mixtures of silane and simple organic molecules,[9-13] and in mixtures of silane and water.[14] However little detailed evidence to elucidate the nature of a H^- transfer mechanism has been presented. Isotope distributions of products in general support the H^- transfer mechanism but the actual kinematic aspects of the mechanism remains unclear. Given the great variety of dynamical situations found in ion–molecule chemistry, it is reasonable to suppose that the mechanisms associated with these net H^- transfer reactions may be quite diversified. For example, reaction 1, which has previously been reported to occur in

$$SiH_2^+ + SiH_4 \longrightarrow SiH_3^+ + SiH_3 \qquad (1)$$

monosilane,[3,6,7] can be described as involving the net transfer of H^- from the neutral molecule to the projectile ion but the same products may also arise from H-atom transfer from the target to projectile ion, or *via* a complex formation mechanism, with dissociation of a randomized complex giving the observed products.

In previous work it was not possible to assign unambiguously a mechanism for this reaction.

We have studied the dynamics of a number of reactions involving the net transfer of H^- or H in monosilane. These studies were carried out in a tandem mass spectrometer using kinetic energy analysis of product ions scattered in the forward direction. The results are interpreted in terms of two kinematic models of ion–molecule reactions.

Experimental Section

The tandem mass spectrometer used in this study has been described previously.[7] The apparatus permits the injection of mass selected ions having kinetic energies variable down to about 1 eV, with an energy spread of 1–2 eV, FWHM, into a collision chamber containing the neutral

target gas. The instrument is in the "in-line" configuration, such that product ions scattered into the forward direction are collected with an acceptance angle of $\sim 10°$. The kinetic energy of the product ions is measured with a retarding field analyzer placed immediately after the collision cell. The analyzer is similar to one described previously.[15] The integral ion current is measured as a function of retarding potential, and the first derivative of this curve yields the kinetic energy distribution. As was noted previously[15] with this type apparatus, collection efficiency is dependent on ion kinetic energy, particularly for very low energy ions (<2 eV), and in this range an extracting potential must be used to collect ions emerging from the collision chamber. It was found that this extracting potential has a slight broadening effect on the measured kinetic energy distribution.

Performance of the energy analyzer was tested by comparison with published results[16-18] for the reactions

$$CH_3^+ + CH_4 \longrightarrow C_2H_5^+ + H_2$$

$$C_2H_4^+ + C_2H_4 \longrightarrow C_3H_3^+ + CH_3 + H_2$$

$$C_2H_4^+ + C_2H_4 \longrightarrow C_3H_5^+ + CH_3$$
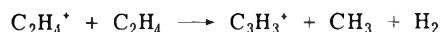
The results obtained are in general agreement with the published data; however, the observed product ions have a larger energy spread, reflecting the larger energy spread of our primary beam.

Monosilane gas was obtained from J. T. Baker Chemical Co. It was fractionated on the vacuum line and checked mass spectrometrically for purity. Monosilane-d_4 was synthesized by the reduction of $SiCl_4$ with $LiAlD_4$ in di-n-butyl ether solution.[19] It was purified in the same manner as monosilane.

All relevant data were corrected for the presence of ^{29}Si and ^{30}Si isotopes in both the primary beam and the product ions.

Results and Discussion

In the studies reported here, ions formed by electron impact on SiH_4 were injected into the collision chamber containing SiD_4 as target gas. The overall chemical

TABLE I: The Chemistry of Light Particle Transfer
Reactions in Monosilane

Reaction no.		$\Delta H°$, kcal/mol
2	$SiH_3^+ + SiH_4 \rightarrow SiH_3^+ + SiH_4$	0
1	$SiH_2^+ + SiH_4 \rightarrow SiH_3^+ + SiH_3$	-1
3	$SiH^+ + SiH_4 \rightarrow SiH_2^+ + SiH_3$	$+16$ to $+41^a$
4	$SiH^+ + SiH_4 \rightarrow SiH_3^+ + SiH_2$	-18 to $+7^a$
5	$Si^+ + SiH_4 \rightarrow SiH^+ + SiH_3$	$+28$ to $+53^a$
6	$Si^+ + SiH_4 \rightarrow SiH_3^+ + SiH$	$+21$

^{a} Range of $\Delta H°$ due to uncertainty in the heat of formation of SiH^+.

reactions studied, irrespective of the actual isotopic distribution of H and D atoms, are shown in Table I. Also shown are the standard enthalpy changes calculated from existing thermochemical data.[20-22]

The kinetic energies of the product ions can be interpreted in terms of two simple models that have been developed in the last several years to describe the kinematics of ion–molecule reactions. Most discussions of ion–molecule kinematics have been concerned with the distinction between "direct" and "complex formation" mechanisms with the simplest model for describing direct mechanisms being the "spectator stripping" model developed by Henglein and coworkers.[23,24] This type of reaction generally involves the transfer of a small particle from the target molecule to the projectile ion in a time short enough so that there is little or no energy redistribution or momentum transfer to the remaining "spectator" particle(s). In this approximation one can predict easily the kinetic energy that the product ion should have. For example, in a stripping process involving the transfer of a neutral particle, consider m_1, v_1, and E_1 to be the mass, velocity, and kinetic energy, respectively, of the primary ion; m_2, v_2, and E_2 those of the target; m_3, v_3, and E_3 those of the product ion; m_4, v_4, and E_4 those of the neutral product. Then for negligible kinetic energy of the target molecule and no momentum transfer to the spectator during reaction, conservation of momentum requires

$$v_3 = (m_1/m_3)v_1$$

or

$$E_3'(\text{s}) = (m_1/m_3)E_1 \qquad (I)$$

where $E_3(\text{s})$ denotes the expected kinetic energy of the ion formed in stripping processes. The neutral spectator would be left with only the thermal energy (~ 0.04 eV) it originally possessed.

It should be kept in mind that the term "direct process" does not always imply a spectator-stripping mechanism. While the stripping model approximates a very common type of direct mechanism, there are many instances of direct interactions involving concerted motion of many nuclei and extensive rearrangement and redistribution of energy. In this paper the stripping model will serve as an ideal direct mechanism to which comparisons will be made.

The "complex formation" model[23,25,26] involves the formation of a persistent intermediate that stays together for a sufficient period of time such that the relative energy of the system may be distributed throughout the complex. This time is usually interpreted as being of the order of a few periods of rotation ($\sim 10^{-12}$ sec), hence the breakup of
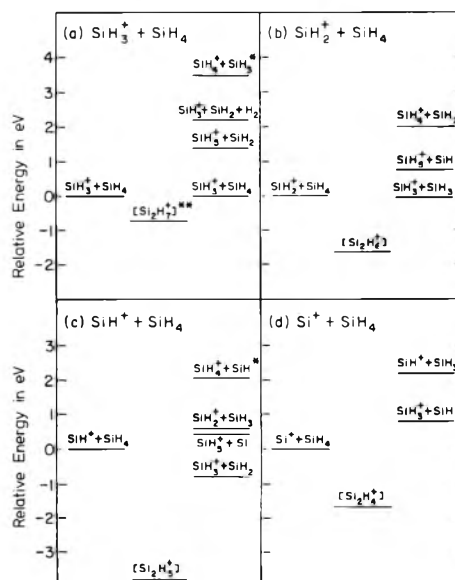
Figure 1. Energy level diagrams in eV for light particle transfer reactions in SiH_4: *$\Delta H_f°$ of SiH_4^+ taken from ref 27; **energy of $Si_2H_7^+$ based on an estimated proton affinity for Si_2H_6 of 6.5 eV.

the complex is treated as a unimolecular decay which may be considered separately from the initial collision. For this type of mechanism, the complex contains the relative energy of the system as internal energy, and moves with the velocity

$$v_\ddagger = \frac{m_1}{m_1 + m_2} v_1$$

The subsequent dissociation of the complex will yield products whose angular and kinetic energy distributions are symmetric around the center of mass of the system. In such a case the velocities of products collected from a wide angle in the forward direction are expected to lie in a broad band centered around the velocity of the center of mass, viz.

$$v_3 = v_\ddagger$$

or

$$E_3(\ddagger) = \frac{m_1 m_3}{(m_1 + m_2)^2} E_1 \qquad (II)$$

where $E_3(\ddagger)$ denotes the energy of the product ion formed from the dissociation of a complex. Thus eq I and II provide a means of distinguishing between reactions proceeding via a stripping or complex formation mechanism.

It is usually the case, particularly in systems containing a large number of degrees of freedom, that a mechanism will fit no model exactly, but will fall somewhere in between the predictions of two different models. As will be seen, this is the present case, with these two models forming the framework for the discussion of the individual reactions that follows.

(a) $SiH_3^+ + SiH_4$. In accord with the energy level diagram shown in Figure 1a, the only monosilicon product ion resulting from collision of low-energy SiH_3^+ ions on SiH_4 is SiH_3^+ itself, the overall reaction yielding products identical with the reactants.[6,7] Even at higher kinetic energies of the reactant SiH_3^+ ions, for which SiH_5^+ and SiH_4^+ formation are energetically possible, only SiH_3^+ ions have been observed as products in pure monosilane.[6,7]

Hence, the net reaction can be described as involving H^- transfer, as shown by (2) in Table I. Above a relative energy of 2.2 eV dissociation of the neutral SiH_4 product to SiH_2 + H_2 may occur.

In this study the injection of SiH_3^+ ions into SiD_4 yields the monosilicon ion products SiH_2D^+, $SiHD_2^+$, and SiD_3^+. Presumably SiH_3^+ is also formed, but this product is obscured by the primary beam. The previous observation in this laboratory[7] that only SiD_3^+ ions are observed t 90° to the reactant ion beam suggests that at least part of the total reaction proceeds via a direct D^- transfer mechanism resulting in no isotopic scrambling in the product ion. The observation of isotopically mixed products in the forward direction suggests a complex mechanism. Hence, below a relative kinetic energy of 2.2 eV (4.1 eV lab), we may describe the reaction as occurring via the direct D^- transfer (7) and by the complex formation mechanism (8), viz.

$$SiH_3^+ + SiD_4 \longrightarrow SiD_3^+ + SiH_3D \qquad (7)$$

$$SiH_3^+ + SiD_4 \longrightarrow [Si_2H_3D_4^+] \begin{cases} \longrightarrow SiD_3^+ + SiH_3D & (8a) \\ \longrightarrow SiD_2H^+ + SiH_2D_2 & (8b) \\ \longrightarrow SiDH_2^+ + SiHD_3 & (8c) \\ \longrightarrow SiH_3^+ + SiD_4 & (8d) \end{cases}$$

Further evidence supporting the complex formation mechanism is the observation of $Si_2H_7^+$ as a collision-stabilized product at higher pressures.[7]

A statistical break up of the complex in (8) into the products shown predicts the intensity ratios a:b:c:d to be 4:18:12:1. The relative intensities of SiD_3^+ and SiD_2H^+ at several different collision energies are shown in Table II, SiD_3^+ formation is significantly greater than that of SiD_2H^+ formation. Since statistical breakup of the complex predicts that SiD_2H^+ formation should be 4.5 times more probable than SiD_3^+ formation, we conclude that the direct D^- transfer (7) is the predominant mode of reaction at all energies.

The direct nature of (7) may be established by a consideration of the kinetic energy of the SiD_3^+ ions formed. If (7) proceeds via a spectator-stripping reaction, in which D^- is the particle transferred, the product observed from the reaction is the ionized spectator, SiD_3^+. The spectator-stripping model predicts that SiD_3^+ should possess only the thermal kinetic energy of the SiD_4 target molecule. Thus the SiD_3^+ energy should be near zero and independent of the collision energy. The prediction is confirmed by Figure 2, in which the kinetic energy distributions of the SiD_3^+ product ions and SiH_3^+ primary ions are shown for several collision energies. While the peak of the SiD_3^+ distribution is observed to be near 0.5 eV, we believe that it's true value is nearer to zero, due to the difficulties and uncertainties in the collection of very low-energy ions from the collision chamber. We, therefore, place no emphasis on the position of the peak in the distributions of very low energy ions, but rather on the position of the band as a whole. The point marked C in Figure 2 represents the energy of SiD_3^+ to be expected (cf. eq II) if the reaction proceeds via a complex mechanism.

It is clear from Figure 2 that SiD_3^+ ions are formed with very little kinetic energy and that this energy is independent of the collision energy. This is perhaps most strikingly apparent for the largest collision energy shown in Figure 2, in which the SiD_3^+ energy band lies well below the C point.

TABLE II: Relative Intensities of SiD_3^+ and SiD_2H^+ from Reactions 7 and 8

Product	Collision energy, eV					Statistical prediction
	0.54	1.07	2.15	3.22	4.30	
SiD_3^+	100	100	100	100	100	100
SiD_2H^+	47	31	16	20	13	450
$SiDH_2^+$						300
SiH_3^+						25

Figure 2. Kinetic energy distributions of SiD_3^+ product ions at several collision energies of SiH_3^+ + SiD_4.

We do not expect to see SiD_3^+ formation by the complex mechanism reflected in the energy distribution measurement, since, at most, this represents less than 10% of he total SiD_3^+ production.

We may conclude that the hydride transfer reaction 7 is predominantly a direct reaction that approaches the spectator-stripping model, in the energy range investigated. The reaction is thermoneutral so that any energy observed in SiD_3^+ must arise from the relative kinetic energy of the reactants. Therefore, the fact that the energy band of the SiD_3^+ ions extends considerably above zero indicates that there is some momentum transfer to the SiD_3^+ spectator. This means, of course, that (7) is not a pure spectator-stripping reaction but one that closely approaches it.

Assuming that SiD_2H^+ is formed solely by the complex mechanism 8 and that the breakdown of the complex is statistical, we may, from the observed intensities in Table II estimate the fractions of total product formation that arise via the complex and direct mechanisms. At the lowest energy studied ($\sim$0.5 eV CM) the contribution from the direct mechanism comprises about 66% of the total reaction and this contribution from the direct mechanism increases with increasing collision energy, until at a relative kinetic energy of 4 eV it comprises over 85% of the reaction. This transition from a complex to direct mechanism at increased colli-

TABLE III: Relative Intensities of SiD_3^+, SiD_2H^+, and $SiDH_2^+$ from Reactions 10, 11, and 12

Product	Collision energy, eV					Statistical prediction
	0.54	1.09	2.18	3.27	4.36	
SiD_3^+	100	98	100	100	100	100
SiD_2H^+	52	40	16	4		300
$SiDH_2^+$	100	100	75	48	64	100

sion energies is a rather common occurrence in ion–molecule reactions,[23,28] and is due to the fact that products formed *via* a complex formation may have considerably more internal excitation than products arising *via* a direct mechanism. The complex that is formed contains the relative energy of the system as internal energy, which may be deposited as internal energy of the product ions. Thus a complex mechanism will yield a given product in stable form only up to a certain energy, beyond which the product will have so much internal excitation that it will decompose. The same product in stable form can be produced at higher energies *via* a direct mechanism, since these processes tend to leave more energy in relative translation, than in internal excitation of the products.[28]

(b) $SiH_2^+ + SiH_4$. Inspection of Figure 1b indicates that below a collision energy of 0.74 eV, SiH_3^+ is the only monosilicon ion produced in collisions of SiH_2^+ and SiH_4. The overall reaction is illustrated by (1) in Table I. Above a collision energy of 0.74 eV SiH_5^+ formation becomes energetically feasible, and above 2.0-eV collision energy SiH_4^+ formation is possible. However, neither of these latter two ions has been observed in pure monosilane.[3,6,7] Thus under our conditions only SiH_3^+ formation need be considered.

Previous authors[3,6,7] have not been able to assign a mechanism for this reaction, but as noted in the Introduction, several processes here will lead to the same product ion. In the present study by using SiD_4 as target gas, we may distinguish between these dynamical processes as shown by

$$SiH_2^+ + SiD_4 \longrightarrow SiD_3^+ + SiH_2D \qquad (10)$$

$$SiH_2^+ + SiD_4 \longrightarrow SiH_2D^+ + SiD_3 \qquad (11)$$

$$SiH_2^+ + SiD_4 \longrightarrow [Si_2H_2D_4^+] \left\{ \begin{array}{l} \longrightarrow SiD_3^+ + SiH_2D \quad (12a) \\ \longrightarrow SiHD_2^+ + SiHD_2 \quad (12b) \\ \longrightarrow SiH_2D^+ + SiD_3 \quad (12c) \end{array} \right.$$
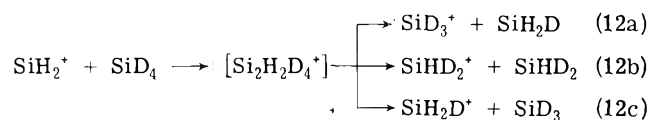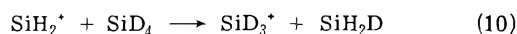
where (10) is a direct D^- transfer reaction producing the low-energy SiD_3^+ product, (11) is a direct D-atom transfer resulting in an energetic SiH_2D^+ ion, and (12a–c) represents the complex formation mechanism. We observe all three of these products when SiH_2^+ is injected into SiD_4. The relative intensities for formation of SiD_3^+, SiH_2D^+, and $SiHD_2^+$ at a number of collision energies are shown in Table III. A statistical breakup of the complex predicts that the ratio a:b:c should be 1:3:1. As is seen from Table III the SiD_3^+ and SiH_2D^+ ions are formed in much greater abundance than $SiHD_2^+$ and therefore we can conclude that the direct mechanisms indicated by (10) and (11) are the predominant channels of reaction.

If one examines the kinetic energy distribution of the SiD_3^+ ion, similar behavior to that noted for (7) is expected. Thus, if (10) proceeds *via* a direct D^- transfer mechanism, the SiD_3^+ should be formed with very little
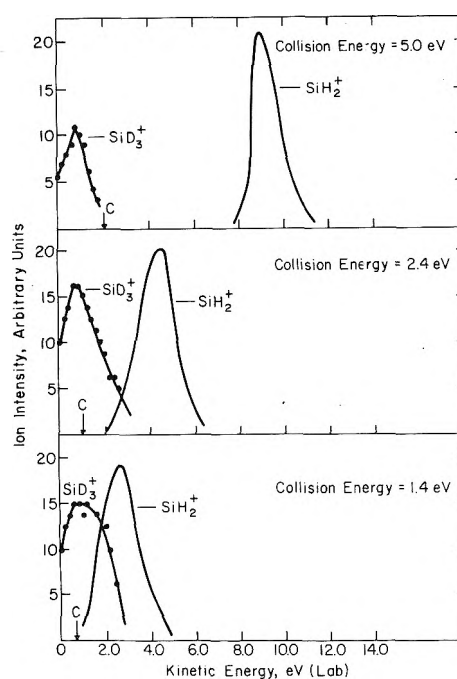
Figure 3. Kinetic energy distributions of SiD_3^+ product ions at several collision energies of $SiH_2^+ + SiD_4$.

energy and its energy should be independent of collision energy. This is confirmed by Figure 3 and thus it is established that (10) is a direct D^- transfer reaction similar to (7). Again the fact that the energy band of the SiD_3^+ extends considerably above zero indicates that this is not a pure stripping process, but that some of the available energy of the collision is acquired by the spectator SiD_3^+ ion.

On the other hand, (11) is a direct reaction where the particle transferred is a neutral D atom and the product ion should contain most of the relative energy of the system as kinetic energy. The spectator-stripping model predicts that the SiH_2D^+ ion should have 0.938 times the energy of the primary ion (*cf.* eq II). Figure 4 shows the kinetic energy distributions of SiH_2D^+ ion at several collision energies, and it can immediately be seen that the product ion carries appreciable kinetic energy, which increases with increasing primary ion energy. The C and S points marked in Figure 4 indicate the product ion energies expected from the complex and stripping models, respectively. It can be seen that the peak of the SiH_2D^+ energy distribution lies considerably above the C point in all cases and approaches closer to the S point as the collision energy is increased. It is clear from Figure 4 that (11) is a direct D-atom transfer reaction that closely approaches the ideal spectator-stripping model at higher energies.

The $SiHD_2^+$ ion is presumed to be formed only through the complex formation mechanism indicated in (12b), leading to scrambling of H and D atoms. Due to the low observed intensities, the kinetic energy of this product was measured at only one collision energy. The energy distribution at a collision energy of 2.5 eV yielded a broad band centered on the energy one would expect from the complex formation model calculated from eq I. It is thus concluded that this ion, along with those of (12a) and (12c), is formed *via* a complex formation mechanism.

The relative contributions of the complex and direct mechanisms to the total product production can be derived
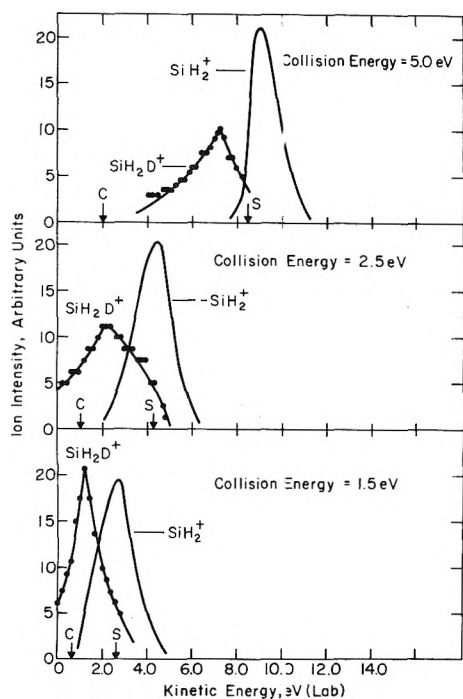
Figure 4. Kinetic energy distributions of SiH_2D^+ product ions at several collision energies of $SiH_2^+ + SiD_4$.
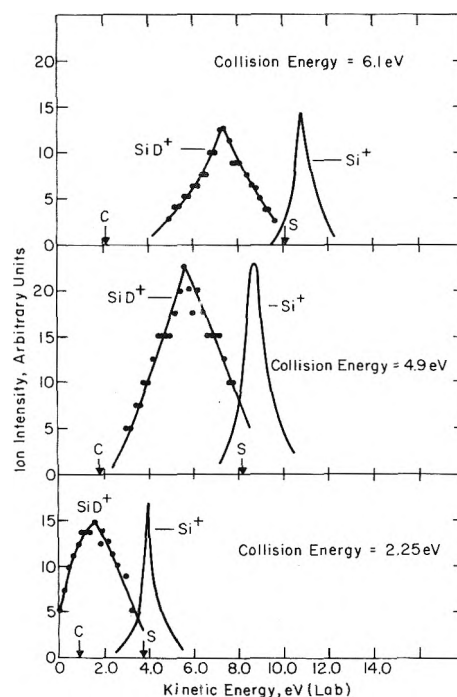
Figure 6. Kinetic energy distributions of SiD^+ product ions at several collision energies of $Si^+ + SiD_4$.
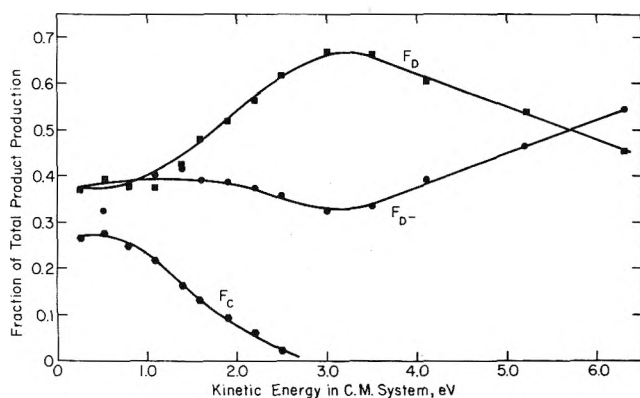
Figure 5. Relative contributions of direct and complex mechanisms for the reaction $SiH_2^+ + SiD_4$: F_D (■), fraction due to direct D atom transfer; F_{D-} (●), fraction due to direct D^- ion transfer; F_C (●), fraction due to complex formation.

from the relative intensities; the fractional contibutions of (10), (11), and (12) as a function of collision energy are shown in Figure 5. It can be seen that at low energies the products formed by the complex mechanism account for less than a third of the total product production. This low efficiency of the complex mechanism can be accounted for in part by the competing channels for dissociation of the complex that lead to product ions containing two silicon atoms,[3,6,7] and to reactant ions, including those undergoing isotopic exchange. The contribution due to a complex mechanism decreases with increasing collision energy and is negligible above 3.0 eV.

The relative contributions of the two stripping processes is a more interesting matter. Reactions 10 and 11 are formally similar, both involving a direct transfer of a small particle, except that the product ion in (10) is the spectator and is therefore formed with very little kinetic energy,

while the product in (11) is formed with the greater portion of the available collision energy. While we do not understand why one process should be favored over the other in the range of 1–5 eV, as indicated in Figure 5, at higher energies we would expect the atom transfer reaction to decrease relative to the hydride ion transfer reaction. Because the ionic product from the atom transfer contains most of the relative energy of the system, it will reach the point where it is sufficiently excited internally to decompose. The D^- transfer product contains relatively little of the available collision energy, and it should be stable to much higher energies. While the highest energy we have measured is considerably below the energy needed to dissociate the SiH_2D^+ product, as predicted by the spectator-stripping model,[23] Figure 5 shows qualitative agreement with this prediction.

(c) $SiH^+ + SiH_4$. Reaction 4 in Table I, although probably exothermic, was reported to occur with only a small cross section in previous studies.[6,7] Reaction 3 is endothermic by at least 10 kcal/mol and has not been previously reported. As can be seen from the energy level diagram in Figure 1c, all other channels for monosilicon ion products are endothermic and indeed have not been observed. When SiH^+ ions were injected into SiD_4 in this study, small amounts of SiD_3^+ were observed, and at higher energies, endothermic reaction 3 was observed, yielding $SiHD^+$. Because of the small intensities encountered, kinetic energy analysis of these products was not feasible. However, in light of the earlier discussion, it is suggested that (3) and (4) proceed through the direct D atom and D^- ion transfer mechanism. Very small amounts of ions at masses 32 (SiD_2^+) and 33 (SiD_2H^+) were observed, but because of the relative unimportance of these products and lack of further information, speculation about the mechanism of their formation is not warranted.

(d) $Si^+ + SiH_4$. As indicated in Figure 1d all reactions of Si^+ and SiH_4 leading to monosilicon product ions are en-

dothermic. In this study we have observed reactions 5 and 6 to occur with cross sections whose energy dependence is typical of endothermic reactions.[29] However (5) was observed to occur at energies below the threshold for ground state reactants of 2.2 eV, indicating an appreciable amount of excitation in the Si^+ beam. The SiD^+ and SiD_3^+ products were observed in the approximate intensity ratio of 4:1, respectively. Because of the lack of H atoms in the reactant ion, scrambling of H and D atoms in the product due to complex formation is of course not possible, and interpretation of the dynamical situation is less clear. However in view of the fact that these products are observed for the most part at higher energies, we would expect that they are formed predominantly *via* the direct D atom and D^- ion transfer mechanisms. When we consider the product energy distributions of the SiD^+ product ion, shown in Figure 6, we see that this reaction is definitely a direct D atom transfer. The product energy bands lie considerably above the complex model prediction (C) and, as in the case of reaction 11, move closer to the stripping-model prediction (S) at higher energies. This indicates that the reaction is making a transition from complex in character at low energies to stripping in character at higher energies.

Conclusions

Observations of product-ion energies in H^- transfer reactions have shown that these products in monosilane are formed *via* a *direct* H^- ion transfer mechanism, with the resulting SiH_3^+ ion formed with very little kinetic energy. Reactions leading to the same product as the direct H^- transfer mechanism may occur *via* a complex formation mechanism particularly at lower collision energies, with a transition to the direct mechanism at higher energies. It has also been demonstrated that in monosilane a direct H atom transfer reaction which approaches the spectator stripping model at higher energies, occurs with SiH_2^+, SiH^+, and Si^+ primary ions.

References and Notes

(1) U. S. Atomic Energy Commission Document No. COO-3416-11.
(2) J. H. Futrell and T. O. Tiernan, "Ion-Molecule Reactions," J. L. Franklin, Ed., Plenum Press, New York, N. Y., 1972.
(3) G. G. Hess and F. W. Lampe, J. Chem. Phys., **44**, 2257 (1966).
(4) P. Potzinger and F. W. Lampe, J. Phys. Chem., **74**, 587 (1970).
(5) P. Potzinger and F. W. Lampe, J. Phys. Chem., **75**, 13 (1971).
(6) J. M. S. Henis, G. W. Stewart, M. K. Tripodi, and P. P. Gaspar, J. Chem. Phys., **57**, 389 (1972).
(7) T-Y. Yu, T. M. H. Cheng, V. Kempter, and F. W. Lampe, J. Phys. Chem., **76**, 3321 (1972).
(8) T-Y. Yu, T. M. H. Cheng, and F. W. Lampe, J. Phys. Chem., **78**, 1184 (1974).
(9) D. P. Beggs and F. W. Lampe, J. Phys. Chem., **73**, 4194 (1969).
(10) D. P. Beggs and F. W. Lampe, J. Phys. Chem., **73**, 3307 (1969).
(11) D. P. Beggs and F. W. Lampe, J. Phys. Chem., **73**, 3315 (1969).
(12) T-Y. Yu, T. M. H. Cheng, and F. W. Lampe, J. Phys. Chem., **77**, 2587 (1973).
(13) G. W. Stewart, J. M. S. Henis, and P. P. Gaspar, J. Chem. Phys., **57**, 1990, 2247 (1972).
(14) T. M. H. Cheng and F. W. Lampe, J. Phys. Chem., **77**, 2841 (1973).
(15) A. Ding, A. Henglein, and K. Lacmann, Z. Naturforsch. A, **23**, 779 (1968).
(16) A. Ding, A. Henglein, and K. Lacmann, Z. Naturforsch. A, **23**, 780 (1968).
(17) Z. Herman, P. Hierl, A. Lee, and R. Wolfgang, J. Chem. Phys., **51**, 454 (1969).
(18) Z. Herman, A. Lee and R. Wolfgang, J. Chem. Phys., **51**, 452 (1969).
(19) A. E. Finholt, A. C. Bond, K. E. Wilzbach, and H. I. Schlesinger, J. Amer. Chem. Soc., **69**, 2692 (1947).
(20) J. L. Franklin, J. G. Dillard, H. M. Rosenstock, J. T. Herron, K. Drexel, and F. H. Field, Nat. Stand. Ref. Data Ser., Nat. Bur. Stand., **No. 26**, (June 1969).
(21) P. Potzinger and F. W. Lampe, J. Phys. Chem., **73**, 3912 (1969).
(22) P. John and J. H. Purnell, J. Chem. Soc., Faraday Trans. 1, **69**, 1455 (1973).
(23) A. Henglein, Estratto da Rendiconti della Scuola Internationale di Fisica "Enrico Fermi.," XLIV Corso, Ch. Schlier, Ed., 1969.
(24) A. Henglein, J. Phys. Chem., **76**, 3883 (1972).
(25) W. B. Miller, S. A. Safron, and D. R. Herschbach, Discuss. Faraday Soc., **44**, 108 (1967).
(26) R. Wolfgang, Accounts Chem. Res., **3**, 48 (1970).
(27) B. P. Pollen, T. A. Carlson, W. E. Modeman, G. K. Schweitzer, W. E. Bull, and F. A. Grimm, J. Chem. Phys., **53**, 768 (1970).
(28) Z. Herman and R. Wolfgang, "Ion-Molecule Reactions," J. L. Franklin, Ed., Plenum Press, New York, N. Y., 1972.
(29) T. M. H. Cheng and F. W. Lampe, Chem. Phys. Lett., **19**, 532 (1973).

Reactions of Chemically Activated Pentenyl Radicals. Kinetic Parameters of 1,4 H Shifts and the Cis-Trans Isomerization of Homoallylic Radicals[1]

W. P. L. Carter and D. C. Tardy*

Department of Chemistry, University of Iowa, Iowa City, Iowa 52242

(Received December 21, 1973; Revised Manuscript Received June 17, 1974)

The reactions resulting from adding H atoms to 2-pentyne in the gas phase have been studied using several deactivating gases. Measured decomposition products are propyne, 1-butyne, and 1,2-butadiene, resulting from decompositions of initially formed radicals at rates consistent with thermal results. 1,3-Butadiene, resulting from isomerization of initially formed 2-penten-2-yl first *via* a 1,4 H shift and then *via* a cis-trans isomerization of homoallylic 2-penten-5-yl, was also formed. Information about the rates of these isomerizations was obtained. 1,4 H shift activated complex models could be tested using this work and literature results, and the use of looser activated complex models is supported. Using loose 1,4 H shift activated complex frequencies and a 0°K primary vinylic C-H bond dissociation energy of 110.2 kcal/mol, a 1,4 H shift critical energy of 18.9 kcal/mol, and a cis-trans homoallylic isomerization critical energy of 23.4 kcal/mol are obtained. In addition, there is evidence of a possible 1,3 H shift of 2-penten-3-yl occurring with a critical energy of about 30 kcal/mol.

Introduction

Vibrationally excited hydrocarbon free radicals have been observed to undergo extensive isomerization in the gas phase.[2-12] Recently, it has been pointed out that forming excited C_6 or larger alkyl radicals can result in quite complex systems of interacting isomers just because of the possibility of 1,4 or higher hydrogen shifts.[2a] Although such hydrogen shifts are the only type of isomerization that appears to be important in saturated radicals,[2] unsaturated radicals can in addition undergo skeletal rearrangements[3,4,13] and cyclizations[4-7,12] resulting from the interaction of the radical center with the double bond. As a result, even pentenyl systems can become quite complex. An example of such systems is that generated by the addition of H atoms to 2-pentyne, where the possible hydrogen shifts, "homoallylic" rearrangements,[3,4,13,14] and internal addition reactions are shown in Figures 1 and 2.

It would be of interest to obtain a qualitative idea of the critical energy and of the nature of the activated complex of 1,4 hydrogen shifts in unsaturated radicals. Such information can be used with the RRKM theory[15] to obtain rate constants for these processes. There is some uncertainty on how to assign the vibrational frequencies of such cyclic activated complexes as XIII and XV which are needed in RRKM calculations, and previously reported assignments[2a,8,9,16] are mainly based on intuition. What is needed is a way to test models for these activated complexes. Thermal studies could be useful in this regard, but previously reported work has given unreasonably low A factors,[10] though corrections have been suggested.[11] The 1,4 hydrogen shift in chemically activated 3-methyl-1-buten-1-yl radical (XII) shown in Figure 3 has been quantitatively studied by Watkins and O'Deen.[8] Though that study is probably more reliable than thermal work, two parameters (the critical energy and the complex model) cannot be tested with one rate constant. However, the 1,4 hydrogen shift can be reasonably assumed to have a similar critical energy and activated complex as in this work; its rate is measured at about 10 kcal/mol higher energy. Therefore, if quantitative information can be obtained on the 1,4 H shift occur-

ring in the H + 2-pentyne system, this work would complement Watkins' result and test these activated complex models. In addition, more reliable critical energies could be obtained.

Another type of isomerization undergone by unsaturated free radicals that has been previously observed is the so-called homoallylic rearrangement.[3,4,13,14] An example of this which is well known[3,4] is the interconversion of IX and XI shown on Figures 1 and 2. There is evidence that this skeletal rearrangement is fast even when the radicals are thermalized at 0°,[4] suggesting a maximum critical energy of about 15 kcal/mol. Another version of this reaction may be the cis-trans isomerization involving III and V (Figures 1 and 2). Without the involvement of a relatively stable intermediate, one would not expect the chemically activated radicals in this system to be able to undergo cis-trans isomerizations, as normally such reactions require about 60 kcal/mol,[17] and the radicals here have only 40-50 kcal/mol. However, if a cyclopropyl form is a long lived enough intermediate in the homoallylic rearrangement, as calculations imply,[14] it would be reasonable to expect the cis-trans isomerization of homoallylic radicals such as III and V to occur with the same sort of extreme rapidity. Evidence for this has been obtained in studies of liquid-phase systems,[13] but this is the first examination of this in the gas phase.

Another possible isomerization that may be important in this system is the isomerization of III to IX *via* a cyclobutyl radical (VIII) in an example of cyclization-decyclization reaction.[5,12] An activation energy for the ring opening of cyclobutyl has been reported to be around 18 kcal/mol (relative to cyclobutyl) in a thermal system,[6] but that work is considered unreliable[5,12,17] and its results appear unreasonable. Examination of models will reveal that for significant overlap for the partial bonds in the transition state a system with at least as much strain as cyclobutene is required. A more reasonable critical energy of about 32 kcal/mol has been obtained in a recent study of the ring opening of chemically activated methylcyclobutyl-1.[12] Corrections suggested on the earlier work of cyclobutyl give a very similar energy.[5] Nevertheless, even when the critical energy is
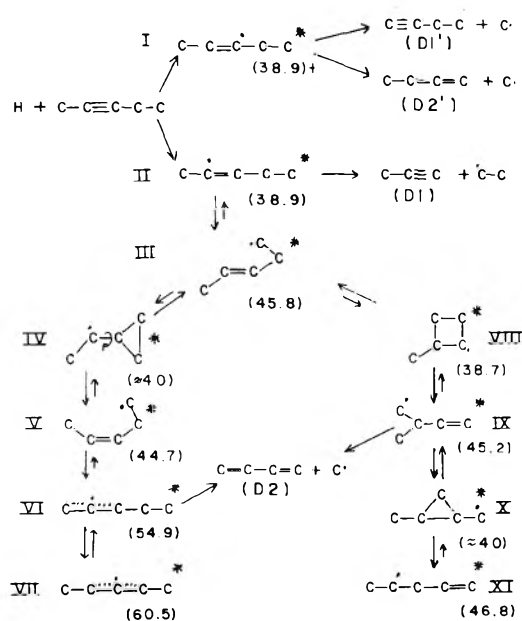
Figure 1. Reaction scheme for H + 2-pentyne reported in this work. Numbers in parentheses represent the internal energy (kcal/mol) of the radical relative to its zero-point energy.

Figure 2. Energy profile for the scheme depicted in Figure 1. The minimum energies of excitation are represented with the point of the arrow. The path designated with a solid line is the one suggested by the experimental data.

Figure 3. Reaction scheme for isopropyl + acetylene as reported by Watkins.[8] Numbers in parentheses represent the internal energy (kcal/mol) of the radical relative to its zero-point energy.

0.04–0.14% 2-pentyne, 3–10% hydrogen in nitrogen; (3) 2% 2-pentyne in heptane vapor; (4) 0.5–1% 2-pentyne, 0.5–1% oxygen in hydrogen; and (5) 0.5–1% 2-pentyne, 0.5–1% ethylene in hydrogen. The mixture ratios of the quantitative runs are shown on Table I. The hydrogen gas was passed from the tank through a liquid nitrogen cooled silica gel trap before use. Ethylene (Matheson, CP), nitrogen, and oxygen were transferred directly from the tank in a way to prevent contamination from the air. The 2-pentyne (Chemical Samples Co., 99.9%) was used without further purification, as it was found to have no major interfering impurities. The heptane (Matheson Coleman and Bell, bp 98–99°) also did not need purification, as, when photolyzed by itself, it gave no products interfering with the 2-pentyne products of interest at pressures above 2.5 Torr. However, this may not be true of lower pressure runs.

Hydrogen atoms were generated by the mercury ($^3P_1$) photosensitized decomposition of hydrogen molecules or heptane[18] resulting from irradiation (through a 90–99% opaque filter) by a G8T5 germicidal lamp in a quartz well in the Pyrex reaction vessels. For the nitrogen runs or runs at pressures below about 0.5 mm, a 200-l. vessel was used; otherwise, a 20-l. vessel was sufficient. Photolysis times varied from 15 sec to 45 min to obtain about 5% reaction of the 2-pentyne. The reaction vessels were part of a standard Pyrex mercury-saturated vacuum system with grease-free stopcocks. Pressures were measured using a McLeod gauge or a Barocel Electronic manometer.

After each run the condensable products were trapped by pumping out the reaction vessel through a glass wool filled trap cooled with liquid nitrogen. The reaction vessel was then closed and the trap pressured up with hydrogen or helium and warmed, then the condensable gases were retrapped in a similar manner in a glass wool filled injection system to the gas-phase chromatography (vpc) column. For the runs with heptane, it was necessary to separate the large amounts of heptane from the lower boiling substances for product analysis. This was done by injecting the reaction mixture in a preparative squalane vpc column and by trapping all the products coming off before heptane for the analytical injection. Analyses was not made for noncondensable products or C_{10} products (resulting from the combination of the stabilized C_5 radicals).

All analyses were done by vpc using squalane, 2,4-dimethylsulfolane, or hexamethylphosphoramide columns at room temperature or 0° with a flame ionization detector. Quantitative measurements were made of the decomposition products propyne, 1,2-butadiene, 1,3-butadiene, and 1-butyne by measuring the areas under the vpc peaks using

that high, radical III still has about 8 kcal/mol more energy than is necessary to undergo this reaction.

As 1,3-butadiene is definitely observed in large yield as a decomposition product in the H + 2-pentyne system, and can be reasonably expected to be formed only from decomposition of VI or IX, either a cis–trans isomerization of a homoallylic radical or a cyclization–decyclization reaction involving a cyclobutyl radical must be important in this system. Even if the latter can occur, it could only be important if it occurs much faster than the cis–trans isomerization because as soon as radical V is formed, it would immediately be converted by a very rapid 1,5 H shift[2a,7] to much more stable allylic forms (VI and VII). Therefore, if the cis–trans isomerization is fast, practically all of the 1,3-butadiene would be coming from radical VI.

Experimental Section

Photolysis were done at room temperature with five different mixtures: (1) 0.4–1% 2-pentyne in hydrogen; (2)

TABLE I: H + 2-Pentyne Experimental Data

Pressure, Torr	Propyne/ C=C-C=C	C=C=C—C/ propyne	C=C=C—C/ 1-butyne	% reactants[a]			
				2P	H	N	C$_7$
0.016	0.0281	13.46	1.79	0.5	99.5		
0.11	0.0265	7.88	1.70	0.5	99.5		
0.88	0.0290	2.76	1.22	0.5	99.5		
0.93	0.0264			0.5	99.5		
1.50	0.0282	1.95	1.36	0.5	99.5		
1.98	0.0266	1.70		0.5	99.5		
1.99	0.0371			0.5	99.5		
2.04	0.0275	1.61		0.5	99.5		
2.48	0.0338			0.5	99.5		
3.00	0.0393	1.09		0.5	99.5		
4.60	0.0453	0.930	1.25	0.5	99.5		
5.27	0.0514	0.795		1	99		
8.50	0.0719	0.680	1.31	0.5	99.5		
13.0	0.0971			0.5	99.5		
20.0	0.166	0.428	1.19	2	98		
20.5	0.170	0.407		2	98		
57.0	0.604	0.354	1.35	0.4	99.6		
86.0	1.18	0.270		0.5	99.5		
108	1.72	0.271		0.4	99.6		
1.35	0.0279	1.97		0.067	4.6	95	
2.22	0.0281	1.61		0.14	9.7	90	
5.55	0.0447	0.840		0.13	9.2	91	
5.70	0.0452	0.893		0.046	3.2	97	
9.60	0.0618	0.601		0.046	3.2	97	
20.0	0.123	0.420		0.038	2.6	97	
30.00	0.168	0.390		0.042	2.9	97	
0.69	0.0686	0.693		2.0			98
1.00	0.0713	0.548	1.37	2.0			98
1.01	0.0724	0.583	1.26	2.0			98
1.33	0.0907	0.516		2.2			98
2.05	0.1127	0.406		2.0			98
2.10	0.0997	0.577		2.2			98
3.10	0.140	0.435	1.27	2.2			98
5.39	0.245	0.277		2.0			98
7.00	0.301	0.273	1.18	2.0			98
10.0	0.419	0.341		2.2			98

[a] Reactants: 2P = 2-pentyne, H = hydrogen, N = nitrogen, C$_7$ = heptane.

TABLE II: Relative Yields of H + 2-Pentyne Disproportionation Products

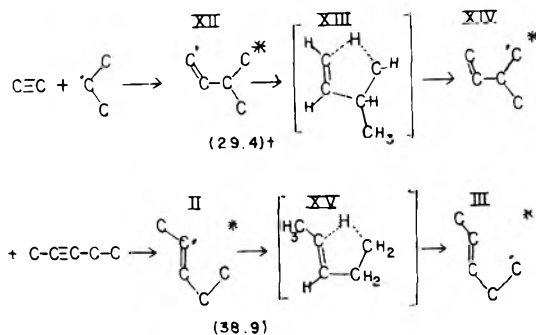|	Pressure, mm[a]			
	0.0115	0.170	1.73	14.4
trans-2-Pentene	100	100	100	100
cis-2-Pentene	50	53.1	47.9	45.1
1-Pentene	8.3	3.1	10.6	14.7
1,3-Pentadiene	10.4	4.7	3.1	3.7
2,3-Pentadiene	6.3	10.9	12.5	7.8

[a] All runs with hydrogen as the deactivator.

a planimeter. A correction factor of 1.31 was used to correct for the reduced sensitivity of the flame detector to the C$_3$ propyne relative to the C$_4$ products. This factor was determined by injection of known ratio mixtures of propyne and 1,3-butadiene, and agrees with the expected factor of 1.33. Qualitative analysis of the stabilization products was generally done with separate runs and shorter columns.

The identification of propyne, 1,2-butadiene, 1,3-butadiene, 1-butyne, 1-pentene, cis- and trans-2-pentene, 1,2-pentadiene, cis- and trans-1,3-pentadiene, 1,4-pentadiene, 3-methyl-1-butene, cis- and trans-2-heptene, 3-ethyl-2-pentene, and cis- and trans-3-methyl-3-hexene were made by comparing the vpc retention times of the reaction products (or lack of products) with known samples. In the case

of propyne and 1,3-butadiene this was done with more than one type of column.

Results

2-Pentyne–Hydrogen Runs. The relative yield ratios of the various decomposition products are listed in Table I. Also observed were peaks corresponding to ethane, ethylene, and methane resulting from the methyl and ethyl radicals formed. Another peak, corresponding to some C$_3$ product (probably propane), was observed with variable yield, usually roughly equal to that of propyne. Minor products observed were various butenes and perhaps butane. Runs with oxygen in the mixture at about the same concentration as 2-pentyne resulted in no major alteration in the relative yields of propyne, 1,2-butadiene, 1,3-butadiene, or 1-butyne, supporting the belief that those are indeed decomposition products, along with the fact that the total absolute yields of these compounds decreased in the expected manner with increasing pressure.

The disproportionation products of the stabilized pentenyl radicals were analyzed in the pressure range of 0.01–15 mm. Table II lists the approximate relative yields of the most important of these products. The absolute yields of all of these increased with pressure in the expected manner. Adding oxygen to the mixture caused a decrease in the yields of these products, as expected, though they were not completely inhibited. The higher relative 1,3-pentadiene

yields at lower pressure may be due to the fact that it can also result from the decomposition of III, V, VI, and VII. A minor product was a compound with a retention time similar to that of 3-methyl-1-butene and which behaved like a decomposition product in its pressure dependence. 1,2-Pentadiene may have been formed, but, if so, it was buried under the 1,3-pentadiene peaks. Very little, if any, 1,4-pentadiene was observed at any pressure.

2-Pentyne–Hydrogen–Nitrogen Runs. The quantitative results of these runs are shown in Table I. Qualitatively, these runs appeared no different than the hydrogen runs with respect to the C_2–C_4 products. Stabilization products were not analyzed in the systems with nitrogen.

2-Pentyne–n-Heptane Runs. n-Heptane was chosen for the strong collider runs because it could also serve as a hydrogen atom source as a result of its mercury photosensitized decomposition.[18] Of the compounds tested, heptane appeared to be the cleanest when photolyzed by itself, giving very little C_3 products and a single C_4 product in a small yield whose vpc peak did not interfere with those of the compounds of interest. Stabilization products were not examined in the heptane runs. The relative yields of the decomposition products are shown in Table I.

2-Pentyne–Ethylene–Hydrogen Runs. In order to obtain an additional test of the assumptions concerning the mechanism of this system, runs were done when ethyl radicals, generated by the addition of H to ethylene, were present to trap the various stabilized pentenyl radicals. These runs were done in the pressure range of 1–20 mm and the C_7 products were analyzed. Unfortunately, unambiguous identification of these products was not possible. Two peaks were observed (on a squalane column) in the region of interest. The first consisted of at least two unresolved peaks with retention times about the same as that of the higher boiling isomer of 3-methyl-3-hexene. The second peak had nearly the same retention time as both *trans*-2-heptene and 3-ethyl-2-pentene. Neither the lower boiling isomer of 3-methyl-3-hexene nor *cis*-2-heptene were observed. At 20 mm pressure, the two peaks were about equal in size, while the first peak decreased relative to the second at lower pressures.

Discussion

The mechanism shown in Figures 1 and 2 is based on the assumption that only 1,4 or 1,5 H shifts occur *via* relatively unstrained intermediates. The "homoallylic" isomerizations and the cyclization–decyclization reactions shown are possible important isomerizations in this system. The only other reasonable possibilities are 1,3 or 1,2 H shifts, presumably occurring *via* four- or three-member ring cyclic transition states. Such isomerizations may have been observed recently in the pentyl radical system at very low pressures,[19] but the critical energies for these processes determined from that study are too high for it to be important in this system. Earlier studies of the thermal reactions of deuterium-substituted radicals also indicate that these isomerizations generally compete unfavorably with decompositions; even the H splitoff decomposition (analogous to the reverse of the formation reaction in the H + 2-pentyne system) was found to be much faster than the 1,2 H shift,[20] while the C–C rupture decompositions were found to be much faster than either the 1,2 or the 1,3 H shifts.[21]

Despite this, it can be argued that I might still undergo a 1,2 H shift to VII at a significant rate, the reaction some-how being aided by VII's allylic stabilization. Likewise I could isomerize to VI, or I could isomerize to III and V. If either of these reactions were important, a significant amount of the 1,3-butadiene would be expected to result after the formation of I, instead of it all coming from II as indicated by Figures 1 and 2. The decomposition yields of the lowest pressure runs are a test of this. In the 0.016-mm (hydrogen) run (collision rate = 5.7×10^5 sec^{-1}) the total yield of the direct decomposition products of I, 1-butyne and 1,2-butadiene, is 0.58 of the total yield of the other decomposition products, propyne and 1,3-butadiene. Results of RRKM[15] calculations indicate that even at 0.016 mm pressure some of I is collisionally stabilized and that the 0.58 should be increased to 0.70 to obtain an estimate of the zero pressure ratio. This ratio is similarly found to be 0.83 for the hydrogen run at 0.11 mm. If one assumes that 50% I and 50% II are formed upon the addition of H to 2-pentyne, the mechanism of Figures 1 and 2 predicts the (1,2-butadiene + 1-butyne)/(propyne + 1,3-butadiene) ratio should be 1.0 at zero pressure; the first two products coming from the formation of I and the second two coming from II. It appears that a maximum of 30% of radical I is undergoing some isomerization process at the lowest pressures. However, this would not be significant at moderate pressures where the isomerization of I, like its decomposition, would compete unfavorably with stabilization.

The results of the experiments where the stabilized isomers are trapped with ethyl radicals can also be interpreted as supporting the assumed mechanism. The second vpc peak can be identified with 3-ethyl-2-pentene, the only ethyl trapping product of stabilized I, while the first (multiple) peak can reasonably be assumed to be ethyl trapping products resulting after the formation and perhaps isomerization of II. This is consistent with the fact that each peak is approximately equal in size at higher pressures. At lower pressures, decomposition becomes important in decreasing the concentrations of some of the radicals, and, since the decomposition forming 1,3-butadiene is faster than the decompositions of I by either path, one would expect the total concentration of radicals II–XI to decrease relative to the concentration of I. This is indeed what is observed if the assignments of the vpc peaks are accepted. The data give a crude estimate of the rate constant of the decomposition of II–XI to 1,3-butadiene to be around 5×10^7 to 10^8 sec^{-1}, which is the right order of magnitude.

In order to completely characterize the mechanism, it is necessary to determine whether most of the 1,3-butadiene is coming from VI or IX. As mentioned before, this is the same as determining whether the cis–trans isomerization of a homoallylic radical is rapid. The data support, in several ways, the belief that most of the 1,3-butadiene is coming from VI, *i.e.*, that the cis–trans isomerization is fast. This is consistent with earlier work in the liquid phase,[13] where cis–trans isomerization of a homoallylic radical was found to be competitive with the rapid skeletal rearrangement. In the H + 2-pentyne system, evidence concerning this comes from examination of the disproportionation products of the stabilized radicals found in Table II. If IX is formed, it would interconvert rapidly with XI, and, as the latter is thermodynamically favored, it is reasonable to expect its stabilization products, 1-pentene and 1,4-pentadiene. However, little or no 1,4-pentadiene is observed. In addition, the fact that the yields of 1-pentene relative to the 2-pentenes are small is further evidence that the IV–VII path is favored over the VIII–XI path. This is because the VIII–XI

path has no 2-pentene precursors and the thermodynamically favored radical (XI) can form 1-pentene, while all radicals in the IV–VII path are 2-pentene precursors and the thermodynamically favored radical (VII) cannot form 1-pentene.

It can be argued that the apparent difference in pressure dependence of the formation of 1-pentene relative to 2-pentene constitutes evidence that these products are coming from different pathways. However, the stabilization yields tend to show larger scatter from run-to-run, and the "trend" in Table II may not be as significant as they appear. Even if it were, however, it can be explained by the assumption that 1-pentene comes from VI, while most of the 2-pentenes come from VII. The larger relative amounts of 1-pentene observed at higher pressures would be due to stabilization of some of the VI before it isomerizes.

Further evidence that radical IX is not the major source of 1,3-butadiene is the observation that the ring opening reaction of cyclobutyl radicals has a critical energy of around 32 kcal/mol.[5,12] This gives the isomerization of III to VIII a minimum excess energy of only around 7 kcal/mol. Using this energy and reasonable activated complex models and a critical energy for the ethyl + propyne addition reaction (the reverse of the decomposition forming propyne) of about 8 kcal/mol,[3] RRKM[15] steady-state estimates of the propyne/1,3-butadiene yield ratios are several orders of magnitude higher than what is observed. Therefore, the observed large 1,3-butadiene yield is evidence that the cis–trans isomerization must not be slow, and that the formation of VI is important.

Plots of the observed propyne/1,3-butadiene yields vs. the collision rate and of 1,2-butadiene/propyne vs. 1/collision rate are shown in Figures 4–7. The shapes of these plots are consistent with the assumed mechanism. The fact that the slopes depend on the diluent gas in the reaction mixture can be explained by the observation that hydrogen, nitrogen, and heptane are not equally efficient in removing vibrational energy via collision. Relative to a strong collider (a species which upon collision with an excited molecule removes enough energy so that molecule cannot undergo further unimolecular reaction) hydrogen has been found to be roughly 0.22 times as efficient and nitrogen 0.55 times as efficient in removing energy on a collision number basis.[22] Generally, larger molecules such as heptane behave as strong colliders.[23,24] If one assumes that a weak collider can be treated like a strong collider whose collision rate is reduced roughly by a factor of its efficiency, one would expect the slopes of the plots of propyne/1,3-butadiene in Figures 4 and 5 to increase with increasing efficiency and the slopes of the plots of 1,2-butadiene/propyne on Figures 6 and 7 to decrease with increasing efficiency. This is what is found, and the relative collisional efficiencies obtained from the differences in the slopes are, except for the 1,2-butadiene/propyne yields obtained in heptane, approximately what are to be expected.[22] The poor fit for the 1,2-butadiene/propyne yield ratios, predominately at low pressures, is probably due to some low-pressure heptane photolysis product causing the observed "propyne" vpc peak to be larger than appropriate. It is reasonable to expect the heptane–mercury photosensitized photolysis to be less clean at lower pressures. This would also explain the less conspicuous (but almost equally significant) deviation of the propyne/1,3-butadiene yield ratios observed in the low-pressure heptane runs shown in Figure 4. The quantitative reliability of the heptane runs may not
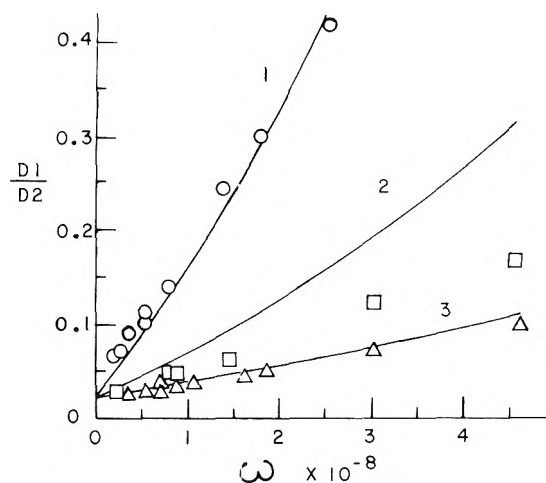
Figure 4. Plots of D1/D2 (propyne/1,3-butadiene) vs. ω, the collision frequency, for heptane (O), nitrogen (□), and hydrogen (△) bath molecules. The lines 1, 2, and 3 are calculated from the optimized critical energies for a strong collider: 800-cm^{-1} SL (step ladder) and 400-cm^{-1} SL models.
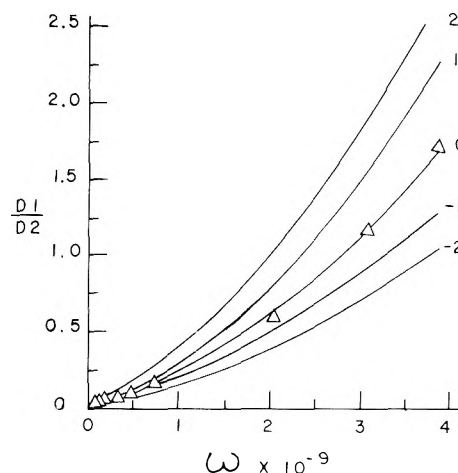
Figure 5. Plots of D1/D2 (propyne/1,3-butadiene) vs. ω for various critical energy changes with hydrogen (400-cm^{-1} SL) as the deactivator. Experimental values are represented by △; line 0 results from the optimized energies (set A of Table III). Lines 1 and −1 result when the cis–trans isomerization critical energy changes by ±1 kcal/mol, while lines 2 and −2 result when the 1,4 H shift critical energy changes by ±1 kcal/mol.

be as great as the others because generating H atoms by the mercury-photosensitized decomposition of an alkane has not been as extensively studied as that of generating H from hydrogen molecules, and because heptane does not have a high vapor pressure at 300°K, and thus may not be behaving enough like an ideal gas in calculating the collision rates. Nevertheless, the yield ratios in the heptane runs are qualitatively reasonable at higher pressures, and both plots indicate that heptane is indeed more efficient in inhibiting decomposition than either hydrogen or nitrogen.

Assumed Mechanism

The mechanism shown in Figures 1 and 2 can be simplified for the purposes of data analysis. As discussed above, the formation of radicals VIII–XI can be neglected. It is safe to assume that the 1,5 H shift of V forming VI is very fast relative to collisional stabilization, as such isomeriza-

Figure 6. Plots of D2'/D1 (1,2-butadiene/propyne) vs. ω^{-1} for heptane (O), nitrogen (□), and hydrogen (Δ) bath molecules. The lines 1, 2, and 3 are calculated from the optimized critical energies for a strong collider: 800-cm^{-1} SL and 400-cm^{-1} SL models.
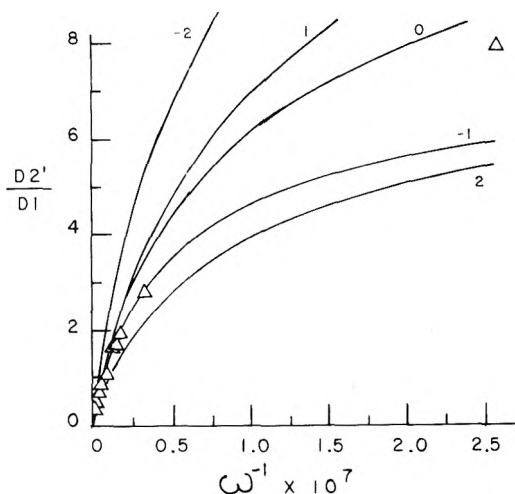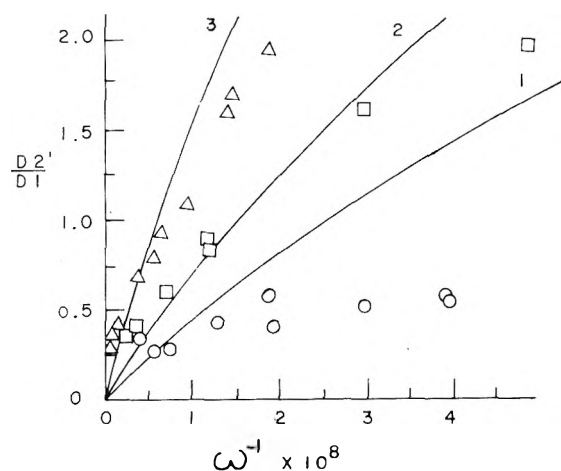

Figure 7. Plots of D2'/D1 (1,2-butadiene/propyne) vs. ω^{-1} for various critical energy changes with hydrogen (400-cm^{-1} SL) as the deactivator. Experimental values are represented by Δ; line 0 results from the optimized energies (set A of Table III). Lines 1 and −1 result when the 1,3 H shift critical energy changes by ±1 kcal/mol, while lines 2 and −2 result when the 1,4 H shift critical energy changes by ±1 kcal/mol.

tions have been observed to be too fast to measure in a similar system with less energy and higher pressures.[7] It is assumed that the interconversion of VI and VII is also very fast because of the high vibrational energy of these radicals. Consequently, the rapidly interconverting radicals V–VII can be thought of as being the same species for the purposes of RRKM[15] calculations. An additional assumption made is that radical IV does not last long enough for a significant amount of it to be collisionally stabilized, so the cis–trans isomerization of III to V is treated as a single process. Radical I is assumed to undergo three processes: decomposition to 1,2-butadiene, decomposition to 1-butyne, and isomerization to either V, VI, or VII. The yield of 1-butyne was assumed to be about 0.56 that of 1,2-butadiene; the low pressure ratio (1/1.8) being used because 1-butyne is important in influencing the yields of other products only at low pressures.

Although the isomerization of I to VI has somewhat

lower excess energy than the neglected isomerization of III to VIII, the former process cannot be ignored because a significant fraction (~50%) of I which is not stabilized will react via this pathway. Thus this isomerization will affect the steady-state concentration of I, and therefore the yield of 1,2-butadiene, especially at lower pressures. On the other hand, the isomerization of III to VIII does not significantly affect the steady-state concentration of III because the experimental evidence indicates that the competitive process III to IV is much faster. The relatively rapid isomerization of III to V via IV tends to decrease the steady-state concentration of III relative to I, so the *rate* of the isomerization of III to VIII is much slower than the rate of the isomerization I, although the rate *constant* is probably higher.

Nevertheless, a certain amount of 1,3-butadiene is expected to be formed from the decomposition of IX following isomerization of III to VIII. However, the importance of this should be small relative to the decomposition of VI even at low pressures; and, because it occurs via a higher critical energy pathway, it should become even less important at higher pressures. Therefore, ignoring this process should not affect calculations of the critical energy of the III to V isomerization, because, as seen on Figure 5 (discussed below), that process affects the yield ratios most significantly at the higher pressures.

Calculation of Energy Parameters

In order to obtain estimates of isomerization critical energies and to test the 1,4 H shift activated complex models, steady-state[25] RRKM[15] calculations were done. The relative decomposition yields of propyne, 1,3-butadiene, and 1,2-butadiene were calculated for the H + 2-pentyne system assuming the mechanism discussed above. The stabilization yields of XII and XIV (Figure 3) in the system studied by Watkins and O'Deen[8] were also calculated. Back isomerization of XIV to XII was neglected because of thermodynamic considerations and the fact that the study[8] was done at relatively high pressures.

The principles of calculating decomposition and stabilization yields in systems with multiple isomerizations and inefficient collisional stabilizations as well as decompositions are described elsewhere.[25] Required for such calculations are the following.

(1) The heat of formation at $0°K$ of the radicals and the activated complexes of the important reactions. Heats of formation of radicals are obtained from the appropriate C–H bond dissociation energies and the $0°K$ heats of formation of the appropriate hydrocarbon. All heats of formation used are those given in the API tables.[26] Alkyl C–H bond dissociation energies used are 102.7, 96.2, and 92.8 kcal/mol for methane, primary, and secondary bonds, respectively.[27] Allylic C–H bond dissociation energies used are 87.1 and 81.5 kcal/mol for primary and secondary bonds, respectively.[28] As a result of the uncertainty of the vinylic C–H bond dissociation energy,[28] the heats of formation of radicals I, II, and XII had to be treated as an adjustable energy parameter. (I is given the same heat of formation as II, while that of XII was linked to that of I and II by assuming the difference between the bond dissociation energies of primary and secondary vinylic C–H bonds is the same as that of alkyl C–H bonds, about 3.5 kcal/mol.[27]) The heats of formation of the decomposition and formation complexes could be estimated from the reported thermal activation energies[3,8,29-31] for their reverse reactions. Nev-

ertheless, some decomposition critical energies had to be considered adjustable parameters because of the sensitivity of the calculated ratios to some of these energies. The critical energy for the addition of H to 2-pentyne was assumed to be 2.0 kcal/mol,[27] and was not considered adjustable. The heats of formation of the 1,4 H shift isomerization complexes (the critical energy of the isomerization of XII was assumed to be equal to that of II), the homoallylic cis-trans isomerization, and the isomerization of I were all treated as adjustable parameters.

(2) The sums of states of the activated complexes and the quantum densities of states of the radicals are needed in the RRKM calculations of the rate constants.[15] These are obtained from the vibrational frequencies assigned for the compound or complex. The frequency assignments of the radicals and decomposition and formation complexes are given and rationalized in Appendix B, and generally follow the usual methods for obtaining such frequency assignments.[2a,32]

Two methods of assigning frequencies for the two 1,4 H shift complexes (XIII and XV, Figure 3) were used, giving the "tight" models and the "loose" models. The tight assignments are based on the assignments used by Watkins, et al.,[8,9] which are similar to those used by Rabinovitch, et al.[2b] The frequencies of the loose assignments were obtained using normal mode calculations[33,34] on the activated complex models where the valence force constants[34-36] involving stretching or bending of the C $\cdots$ H bond of the transferring hydrogen were taken as half normal.[37] These calculations are described elsewhere.[36] The designations loose and tight come from the fact that Watkins's assignments give ring mode frequencies much higher than did the normal mode calculations.[36]

The isomerization of I is assumed to be a 1,3 H shift, so that complex was given frequencies appropriate to a four-member cyclic structure. The ring and skeletal frequencies used are those obtained from normal mode calculations of the 1,3 H shifts of pentyl-2 to pentyl-1.[36] The III to V isomerization complex was given frequencies appropriate to a compound with a cyclopropyl like structure (IV). All frequency assignments used in the calculations are given in Appendix B.

(3) The following reaction path degeneracies were used.

Reaction	Path degeneracy
all decompositions	1
isomers of I	3
II to III	3
III to II	1
III to V	1
V to III	1
XII to XIV	6

(4) The energy transfer model for the collisional stabilization of the excited radicals is also needed in the calculation.[25] Heptane was assumed to be a strong collider. Energy transfer involving weak colliders is specified by probabilities of the excited species going from one energy state to another upon collision.[22,38] In these calculations, collision with hydrogen was assumed to be described by a step ladder model with a step size of 400 cm^{-1} (1.144 kcal/mol), and nitrogen by a step ladder model with a step size of 800 cm^{-1} (2.29 kcal/mol).[22] (A step ladder model assumes that upon collision the amount of energy transferred is always equal to the step size.) It was found that if energy transfer in hydrogen was described by an exponential model with

average transferred energy = 525 cm^{-1} (1.50 kcal/mol) exactly the same ratios were obtained as with the step ladder model, despite the significantly different energy transfer probabilities obtained by the two models.[24,38] The manner the detailed energy transfer probabilities are obtained for the step ladder or exponential models is described elsewhere.[38]

Watkins and O'Deen's studies[8] were done with acetylene as the bath gas. Unfortunately, the collisional efficiency of acetylene in chemical activation systems has not been determined. As thermal studies suggest acetylene may have an efficiency of 0.52-0.86,[23] corrections for the inefficiency of acetylene were approximated by multiplying Watkins and O'Deen's[8] collision rates by 0.75. The uncertainty of the efficiency of acetylene probably does not cause an uncertainty in the energies greater than 0.5 kcal/mol.[12]

The calculated decomposition and stabilization yields are compared with experimental, and the adjustable energy parameters are varied until an optimized set of energy parameters has been obtained. Any change in an energy parameter of an optimized set causes the square of the per cent deviation of the calculated yield ratio relative to the experimental yield ratio to increase. Although the energy levels used in the calculations[25] are spaced at 400 cm^{-1} (1.144 kcal/mol), the energy parameters could be changed in increments of 100 cm^{-1} (0.29 kcal/mol).

Results of Calculations

Several optimized sets of energy parameters obtained in calculations done simultaneously on the H + 2-pentyne system and the isopropyl + acetylene system[8] are shown in Table III. The optimized energy sets depend on the 1,4 H shift activated complex vibrational frequencies and, to a smaller extent, on whether the calculated ratios were fit to experiments done in hydrogen or nitrogen. An idea of the quality of the fit of calculated to experiment is shown in Figures 4 and 6, where the lines are the calculated yield ratios for hydrogen, nitrogen, or heptane as the bath gas using energy set A of Table III. (The fits obtained from sets B, C, or D are quite similar, except that in Figure 4 the fit to nitrogen is somewhat better and the fit to heptane somewhat worse.) Comparing energy sets A and E, it is seen that no optimized energy parameter is significantly different whether obtained from optimizing on hydrogen runs or nitrogen runs, despite significant differences in the quality of the fits.

Because of the uncertainty of the 1,4 H shift complex model and of the vinylic C-H bond dissociation energy,[28] there is no unique set of energy parameters which fit the data. Judgements, however, can be made on the basis of reasonableness of the individual critical energies or bond dissociation energies obtained. When the vinylic C-H bond dissociation energies are held fixed at what is believed to be their minimum value,[28] the critical energy for the isopropyl + acetylene addition reaction obtained is significantly different than what thermal work[8,29] indicates; energy sets B and D are unreasonable on that basis. It should also be noted that the critical energies for the other addition reactions (the reverse of the various decompositions) are in much closer agreement with thermal results[3,29-31] with energy sets A and E than with B, C, or D. Additional evidence against the reasonableness of set C is the fact that the vinylic C-H bond dissociation energy is less than the reported minimum.[28] The high bond dissociation energies of sets A and E are not unreasonable in view of the fact that the C–

TABLE III: Optimized Energy Parameters

Calcd fit to 1,4 H shift complex model	Expected	Calculated critical energies[a]				
		A	B	C	D	E Nitrogen Loose
		Hydrogen runs				
		Loose	Loose	Tight	Tight	Loose
C-C·-C + C≡C	7.6[c]	7.6[b]	9.3	7.6[b]	5.3	7.6[b]
C· + C=C=C-C	8.1[d]	7.9	7.1	6.2	6.8	8.2
C-C· + C≡C-C	7.8[e]	7.8	6.7	6.9	6.7	8.1
C· + C=C-C=C	4-5[f]	4.7	4.7	4.7	4.4	4.1
1,4 H shifts		18.9	20.9	18.0	17.2	18.9
cis-trans-C—C=C—C—C·		23.4		23.4		
Isomers of C-C=C··-C-C		30.0		32.3		
D(=C-H), 0°K						
Primary	≥106.5[g]	110.2	106.5[b]	105.9	106.5[k]	110.2
Secondary	≥103.0	106.7	103.0[b]	102.4	103.0[h]	106.7

[a] Kcal/mol. [b] Parameter held fixed in calculation. [c] Reference 8. [d] Reference 31. [e] Reference 3. [f] Reference 30. [g] Reference 28.

H bond dissociation energy of benzene (at 0°K) is 109.5 kcal/mol.[28] Therefore, it appears that energy set A (or E, which is not very different) and the loose activated complex model[36] are supported by the data.

In such multiparameter calculations, it is important to consider the sensitivity of the calculated results to the energy parameters, and whether there are more variable parameters than are appropriate. Because the decomposition energy parameters obtained in sets A and E agree with the thermal results[3,30,31] we can think of them as being fixed while the unknown isomerization critical energies are to be determined. An idea of how each of the three isomerization critical energies affect the calculated ratios can be obtained by examining Figures 5 and 7, where the lines indicate calculated ratios using energy set A and with one of the isomerization critical energies increased or decreased by 1 kcal/mol from its optimized value. From Figure 5 we see that the 1,4 H shift critical energy affects the ratios significantly at all pressures, while the cis–trans isomerization energy is mainly important at higher pressures (ω's). Though the isomerization energy of I (not shown on Figure 5) has no significant effect on the propyne/1,3-butadiene ratios, we can see from Figure 7 that it has a significant effect on the 1,2-butadiene/propyne ratio at low pressures (high ω⁻¹), as expected. On Figure 7, the 1,4 H shift energy is important at all pressures; both ratios are quite sensitive to this parameter. The cis–trans isomerization energy has little effect on the ratios of Figure 7, so is not shown. An important observation is that each of the three isomerization energy parameters affects the two ratios differently, so all three parameters must be adjusted to obtain a fit to the data. These results suggest that if we do not consider the effect of the uncertainty of the vinylic C–H bond dissociation energy the maximum uncertainty of the critical energies should be about ±0.5 kcal/mol for the 1,4 H shift, about ±1.0 kcal/mol for the cis–trans isomerization, and about ±1.5 for the isomerization of I.

Conclusion

A qualitative study of the rather complex system of isomerizations resulting from the exothermic addition of H atoms to 2-pentyne has given information about three different isomerization processes. Though 1,4 H shifts have been studied previously,[2,8-11] it is now possible to test its activated complex model, using this and previously reported[8] studies. The results are somewhat clouded by the unfortunate uncertainty of the vinylic C–H bond dissocia-

tion energy,[28] but it appears that the data suggest the use of an isomerization complex model obtained from normal mode calculations[36] using force constant–bond number correlations[37] which have much lower ring frequencies than previously assumed.[2a,8,9] The activated complex used for the isomerization of 2-penten-2-yl (II) corresponds to a 300°K thermal A factor of $10^{13.07}$ (including a reaction path degeneracy of 3) and gives an isomerization critical energy of 18.9 ± 0.5 kcal/mol if a secondary vinylic C–H bond dissociation energy of 106.7 kcal/mol is used.

Additional information obtained concerns the cis–trans isomerization of homoallylic radicals, which this work suggests occurs with a critical energy of about 23.4 ± 1 kcal/mol. Although much lower than the usual 60 kcal/mol for cis–trans isomerizations of olefins,[17] it is suprisingly high in view of the fact that the skeletal rearrangement in homoallylic radicals (for example, the interconversion of IX and XI in Figures 1 and 2) probably occurs with a critical energy of less than 16 kcal/mol[4,14] and is believed to occur via a similar intermediate.[13]

In order to explain the low pressure data, it is necessary to assume that 2-pentene-3-yl (I) is undergoing some slow isomerization process. The only reasonable isomerization that species can undergo is a 1,3 H shift, and the data indicate that it occurs at about 30 ± 1.5 kcal/mol, which agrees with the expected value.[19,21]

Appendix A. Calculation of Collision Rates

Collision rates were calculated using the following relation

$$\omega = 4.415 \times 10^7 \, (s_{AM}^2/\sqrt{T_\mu})P$$

where ω is the collision rate in sec⁻¹, s_{AM} is the effective collision diameter, T is the temperature (°K), μ is the reduced mass in AMU, and P is the pressure in mm. s_{AM} is related to the Lennard-Jones parameters σ_M and ϵ/k.[39,40] For hydrogen, nitrogen, all C_5 hydrocarbons, and heptane, cross sections of 2.97, 3.71, 5.70, and 6.80 Å, respectively,[39,40] and ϵ/k values of 33.3, 85, 310, and 325°K, respectively, were used.[39,41]

TABLE IV: Frequencies Used in Estimating Frequency Assignments

Type		Frequencies, cm⁻¹				
Stretches						
C–H	C–H	2950				
C–C	C–C	950				
C=C	C=C	1650				
C–C		1300				
CCH, HCH bends						
Primary C						
CH3	CHB CH3	1462	1462	1374	1168	950
·CH2ᵃ	CHB ·CH2	1462	1168	950		
=CH2ᵇ	CHB =CH2	1440	978	907		
·=CH	CHB ·=CH	907				
Secondary C						
CH2	CHB CH2	1450	1310	1260	768	
·CH	CHB ·CH	1260	768			
=CH	CHB =CH	1300	920			
Tertiary C						
CH	CHB CH	1346	1346			
Torsions						
Single bond						
C_1–C_3ᶜ	SBT METH	212				
C_2–C_2ᵈ	SBT ETHY	95				
Double bond						
C_1–C_3	DBT 1	650				
C_2–C_2	DBT 2	350				
Allylic		375	175			
skeletal bends						
n-pentane skel.	SKL N-PE	403	403	188		
i-pentane skel.	SKL I-PE	403	352	352	352	
methyl on ring	CCC R ME	400	350			

ᵃ · refers to C next to radical center. ᵇ = refers to C next to double bond. ᶜ One C on one side of bond, three on other. ᵈ Two C's on both sides of bond.

Appendix B. Assignment of Vibrational Frequencies

The useful general frequency assignment technique used by Larson, Chua, and Rabinovitch[2b] (LCB) for alkyl radicals has been extended to alkenyl radicals. The frequencies used are given in Table IV and are those of LCB plus estimates of olefin-type frequencies obtained from examining frequencies of propylene,[42] cis- and trans-2-butene,[43] 1-butene,[44] isobutene,[42] and 1,3-butadiene.[45] Frequency assignments are made using Table IV by taking the appropriate frequency for each stretch and torsion (the notation "C_1-C_3" means that there is one C on one side of the bond, and three on the other) possible in the molecule, by taking the appropriate set of frequencies for the CCH or HCH bends associated with each carbon atom which has H's bonded to it, and by taking the set of CCC bend frequencies appropriate to the type of carbon skeleton the molecule has. The skeletal (CCC) bends for the unsaturated hydrocarbons were assumed to be the same as for alkanes. This is suggested by comparing such frequencies in saturated[34,46] and unsaturated[42–44,45] C_4 hydrocarbons; this assumption has to be made because of the scarcity of vibrational assignments for larger alkenes.

All vinylic radicals were assumed to be in the bent configuration,[47] so they were given torsional and skeletal frequencies appropriate to olefins given in Table IV. The two partial double bonds of allylic radicals were given frequencies of 1300 cm⁻¹.

For the H + 2-pentyne addition complex, the C–C, C–H stretches and the HCH, HCC bends were assigned using Table IV. The partial triple bond was given a stretch frequency of 1950 cm⁻¹. The skeletal bends of 475, 360, 300, 200, and 120 cm⁻¹ used were believed appropriate to 2-pentyne and were based on analogies drawn from the published frequencies of 1-halo-2-butynes,[48] allyl halides,[49] and 1-butene.[44] One methyl torsion was assumed to be free, the other methyl and the ethyl torsions were given the usual 212, 95 cm⁻¹ assignment. Two partial CC ⋯ H bend frequencies of 150 cm⁻¹ were added.[32]

The frequencies of the activated complexes involving the decompositions of 1-penten-3-yl to 1,3-butadiene + methyl and 2-penten-2-yl to 1,2-butadiene + methyl were assigned in a way analogous to the technique used for similar alkyl radical decompositions.[32] The forming double bond was given increased stretching and torsion frequencies (950 → 1300 cm⁻¹ and 212 → 431 or 95 → 223 cm⁻¹), while the breaking bond stretch (950 cm⁻¹) was taken as the reaction coordinate and its torsion frequency was halved (212 → 106 or 95 → 48 cm⁻¹). In addition, four bending frequencies were halved, two for each side of the breaking bond. For leaving methyl groups, two CCH bends were reduced (1168, 920 → 584, 475 cm⁻¹). If a C next to the breaking bond was secondary in the radical, one CCH bend (1260 → 630 cm⁻¹) and one CC ⋯ C bend (403 → 201 or 188 → 94 cm⁻¹) frequency was halved. If a C next to the breaking bond was tertiary, two skeletal bends were reduced (352(2) → 176(2) cm⁻¹). No additional changes were made even in the case of the decomposition of 2-penten-3-yl to methylallyl + methyl, despite the fact that a C=C torsion in the radical becomes a C=C=C bend in methylallyl, because examination of the frequencies of methylallyl[50] shows that there is no significant change in the magnitude of that frequency.

For the frequency assignments of the activated complexes of the decomposition of 2-penten-2-yl to propyne + methyl, and of the formation of 3-methyl-1-butene-1-yl from acetylene + isopropyl, the rules given above are not sufficient. The following rules are based on those given above and on the results of comparing the frequencies in

the radicals with corresponding frequencies in the fragments. The frequency changes associated with the stretch and torsion of the breaking bond and with the radical fragment are the same as those described above. The stretching frequencies of the partial triple bond was set at 1925 cm^{-1}. The skeletal bend corresponding to C::C $\cdot\cdot$ C was halved (403 $\rightarrow$ 201 or 188 $\rightarrow$ 94 cm^{-1}). For the decomposition forming propyne, rotation about what becomes the C–C bond in propyne was assumed to be free. The following alterations were also made because the frequencies of the radicals were significantly different in kind or magnitude from corresponding frequencies in the fragments. For the activated complex, averages of the differing corresponding frequencies were used. The CCH bends of the C between the breaking bond and the partial triple bond (1300, 920 cm^{-1}) corresponded to acetylenic CCH bends of 650(2) cm^{-1},[51] so these modes were assigned 975, 785 cm^{-1} in the complexes. In the complexes involving addition to acetylene, double bond torsion (650 cm^{-1}) and the C=C $\cdot$ –H bend (907 cm^{-1}) also corresponded to acetylenic CCH bends (650(2) cm^{-1}), so these frequencies were 778, 650 cm^{-1} in the complexes. For the decomposition forming propyne, a skeletal bend (403 cm^{-1}) and the double bond torsion (350 cm^{-1}) of the radical corresponded to C–C≡C bends of about 374, 201 cm^{-1},[51] so the complex was given frequencies of 388, 275 cm^{-1}.

The cis–trans isomerization complex of 2-penten-5-yl was given a skeleton of ethylcyclopropane, with the radical center on the secondary ethyl carbon. The ethyl group was given CCC bend frequencies of 403, 250, and 188 cm^{-1}. All other modes consisted of stretches and HCH, CCH bends and were assigned using Table IV. For the reaction coordinate, one C–C stretch frequency (950 cm^{-1}) corresponding to a ring mode was deleted.

The isomerization of 2-penten-3-yl is assumed to occur via a 1,3 H shift via an activated complex

$$
\begin{array}{ccccc}
 & & \overset{\displaystyle\lceil\!-\!\text{H}\!-\!\rceil}{} & & \\
\text{C} & \!\!-\!\! & \text{C}\!=\!\text{C} & \!\!-\!\!\text{C}\!-\! & \text{C} \\
1 & & 2\quad3 & 4 & 5
\end{array}
$$
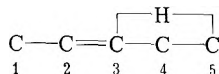
The C–C, C=C, and C–H stretches and the HCH, CCH bends were assigned using Table IV, where carbons 5 and 3 were assumed to be secondary and tertiary, respectively. A C $\cdots$ H stretch of 2380 cm^{-1} [52] was used; the other such stretch is assumed to be the reaction coordinate. Skeletal (CCC) bends and ring bend frequencies (583, 485, 409, 269, and 111 cm^{-1}) used were those taken from the results of the normal mode calculation on the isomerization complex of pentyl-1 to pentyl-3.[36]

The method of assigning the frequency assignments of the tight 1,4 H shift isomerization complexes is exactly analogous to that described for the 1,3 H shift above, only the ring bend and C $\cdots$ H stretch frequencies used (1100(2), 1013, 870, 290 cm^{-1}) were those of Watkins and coworkers.[3]

Assigned frequencies are given elsewhere.[52]

In addition to being dependent on the vibrational quantum sums and densities, the RRKM calculated rate constants also depend on the overall rotational degrees of freedom of the reactants and activated complexes. An approximate correction for this[53] is made by multiplying all the sums and densities by the square root of the product of the moments of inertia, a quantity which is proportional to the partition function.[54] These quantities, in units of AMU$^{3/2}$ Å^3, are listed in Table V for all radicals and complexes used.

TABLE V: Correction Factors for Overall Rotation

Radical	Factor[a]
C—C=C·—C—C	1201
C—·C=C—C—C	1201
trans-C—C=C—C—C·	1200
cis-C—C=C—C—C·	1200
C÷C÷C—C—C	1222
C—C÷C÷C—C	1222
$\overset{\displaystyle\text{C}}{\underset{\displaystyle|}{\cdot\text{C}=\text{C}-\text{C}-\text{C}}}$	1249
Activated complexes	
C—C=C·—C—C → C—C—C=C=C + C·	1368
C—·C=C—C—C → C—C≡C + ·C—C	1423
C÷C÷C—C—C → C=C—C—C=C + C·	1300
C—·C=C—C—C → C—C=C—C—C·	1147
trans- → cis-C—C=C—C—C .	1150
$\cdot\text{C}=\overset{\displaystyle\text{C}}{\underset{\displaystyle|}{\text{C}}}-\text{C}-\text{C} \rightarrow \text{C}=\text{C}-\overset{\displaystyle\text{C}}{\underset{\displaystyle|}{\text{C}}}-\text{C}\cdot$	1050

[a] Square root of the product of the moments of inertia units: mass = AMU, distance = Å.

TABLE VI: Vibrational Entropies[a] for Pertinent Radicals and Complexes

Radical	s^a	Complex	$s^{a,b}$
I	3.55	H addition	4.24
II	3.55	I → D2	4.01
III	3.58	I →VI	2.97
V	3.58	II → D1	4.10
VI	3.69	II → III	2.05
VII	3.32	III → V	3.10
VIII	2.06	III → VIII	2.60
IX	3.43	V → VI	2.44
XI	3.78	VI → VII	2.05
		VI → D2	4.24
		VIII → IX	2.60
		IX → XI	2.54
		IX → D2	4.18

[a] s is defined as $S/2.303R$ and is calculated at 300°K using only the vibrational contributions. [b] The translation along the reaction coordinate is not included.

The A factors for pertinent reactions can be calculated from the entropies listed in Table VI by the equation

$$A = \frac{ekT}{h}e^{\Delta s^*}$$

References and Notes

(1) Taken in part from the Ph.D. Thesis of W. P. L. Carter, University of Iowa.
(2) (a) C. W. Larson, P. T. Chua, and B. S. Rabinovitch, J. Phys. Chem., 76, 2507 (1972); (b) E. A. Hardwidge, C. W. Larson, and B. S. Rabinovitch, J. Amer. Chem. Soc., 92, 3278 (1970).
(3) R. R. Getty, J. A. Kerr, A. F. Trotman-Dickenson, J. Chem. Soc. A, 1360 (1967).
(4) W. P. L. Carter and D. C. Tardy, J. Phys. Chem., 78, 1245 (1974).
(5) R. Walsh, Int. J. Chem. Kinet., 2, 71 (1970).
(6) A. S. Gordon, S. R. Smith, and C. M. Drew, J. Chem. Phys., 36, 824 (1962); A. S. Gordon, Int. J. Chem. Kinet., 2, 75 (1970).
(7) K. W. Watkins and D. K. Olsen, J. Phys. Chem., 76, 1089 (1972).
(8) K. W. Watkins and L. A. O'Deen, J. Phys. Chem., 75, 2665 (1971).
(9) K. W. Watkins and D. R. Lawson, J. Phys. Chem., 75, 1632 (1971).
(10) L. Endrenyi and D. J. LeRoy, J. Phys. Chem., 70, 4081 (1966).
(11) K. W. Watkins, Can. J. Chem., 50, 3738 (1972).
(12) W. P. L. Carter and D. C. Tardy, J. Phys. Chem., 78, 1573 (1974).
(13) L. K. Montgomery, J. W. Matt, and J. K. Webster, J. Amer. Chem. Soc., 89, 923 (1967); L. K. Montgomery, J. W. Matt ibid., 89, 934 (1967).
(14) W. J. Heare, J. Amer. Chem. Soc., 95, 2643 (1973).
(15) R. A. Marcus and O. K. Rice, J. Phys. Colloid Chem., 55, 894 (1951); R. A. Marcus, J. Chem. Phys., 20, 359 (1952).
(16) H. E. O'Neal and S. W. Benson, J. Phys. Chem., 71, 2903 (1967).

(17) S. W. Benson and H. E. O'Neal, *Nat. Stand. Ref. Data Ser., Nat. Bur. Stand.*, **No. 21** (1970).

(18) R. J. Cvetanovic, *Progr. React. Kinet.*, **2**, 39 (1964).

(19) D. C. Tardy, *Int. J. Chem. Kinet.*, **6**, 291 (1974).

(20) W. M. Jackson and J. R. McNesby, *J. Chem. Phys.*, **36**, 2272 (1962).

(21) A. S. Gordon and J. R. McNesby, *J. Chem. Phys.*, **33**, 1882 (1960).

(22) D. C. Tardy and B. S. Rabinovitch, *J. Chem. Phys.*, **48**, 5194 (1968).

(23) S. P. Pavlou and B. S. Rabinovitch, *J. Phys. Chem.*, **75**, 3037 (1971).

(24) Y. N. Lin and B. S. Rabinovitch, *J. Phys. Chem.*, **74**, 3151 (1968).

(25) W. P. L. Carter and D. C. Tardy, *J. Phys. Chem.*, **78**, 1579 (1974).

(26) F. D. Rossini, "Selected Values of Physical and Thermodynamic Properties of Hydrocarbons and Related Compounds," Carnagie Press, Pittsburgh, Pa., 1953.

(27) C. W. Larson and B. S. Rabinovitch, *J. Chem. Phys.*, **50**, 871 (1969).

(28) D. M. Golden and S. W. Benson, *Chem. Rev.*, **69**, 125 (1969).

(29) J. A. Dominguez and A. F. Trotman-Dickenson, *J. Chem. Soc.*, 940 (1962).

(30) R. J. Cvetanovic and R. S. Irwin, *J. Chem. Phys.*, **46**, 1694 (1967).

(31) R. R. Getty, J. A. Kerr, and A. F. Trotman-Dickenson, *J. Chem. Soc. A*, 979 (1967).

(32) C. W. Larson, B. S. Rabinovitch, and D. C. Tardy, *J. Chem. Phys.*, **47**, 4570 (1967).

(33) E. B. Wilson, J. C. Decius, and P. C. Cross, "Molecular Vibrations," McGraw-Hill, New York, N.Y., 1955.

(34) J. H. Schachtschnider and R. G. Snyder, *Spectrochim. Acta*, **19**, 117 (1963).

(35) N. Neto, C. DiLauro, E. Castellucci, and S. Califano, *Spectrochim. Acta, Sect. A*, **23**, 1763 (1967); N. Neto, C. DiLauro, and S. Califano, *ibid.*, **26**, 1489 (1970).

(36) W. P. L. Carter and D. C. Tardy, *J. Phys. Chem.*, submitted for publication.

(37) H. S. Johnston, "Gas Phase Reaction Rate Theory," Ronald Press, New York, N.Y., 1966, pp 80–83.

(38) D. C. Tardy and B. S. Rabinovitch, *J. Chem. Phys.*, **45**, 3720 (1966).

(39) J. O. Hirschfelder, C. F. Curtis, and R. B. Bird, "Molecular Theory of Gases and Liquids," Wiley, New York, N.Y., 1954.

(40) F. J. Fletcher, B. S. Rabinovitch, K. W. Watkins, and D. J. Locker, *J. Phys. Chem.*, **70**, 2823 (1966).

(41) Y. N. Lin, S. C. Chan, and B. S. Rabinovitch, *J. Phys. Chem.*, **72**, 1932 (1968).

(42) M. G. Borisov and L. M. Sverdlov, *Opt. Spectrosc.*, **19**, 33 (1965).

(43) J. E. Kilpatrick and K. S. Pitzer, *J. Res. Nat. Bur. Stand.*, **38**, 191 (1947).

(44) F. H. Dorer and B. S. Rabinovitch, *J. Phys. Chem.*, **69**, 1952 (1965).

(45) L. M. Sverdlov and N. V. Tarsova, *Opt. Spectrosc.*, **9**, 155 (1960).

(46) R. G. Snyder and J. H. Schachtschnider, *Spectrochim. Acta*, **21**, 169 (1965).

(47) W. C. Bentrude, *Annu. Rev. Phys. Chem.*, **18**, 283 (1967).

(48) R. D. McLachlan, *Spectrochim. Acta*, **23**, 1793 (1967).

(49) R. D. McLachlan and R. A. Nyquist, *Spectrochim. Acta Sect. A*, **24**, 103 (1968).

(50) L. M. Sverdlov and G. M. Borsov, *Opt. Spectrosc.*, **9**, 227 (1960).

(51) G. Herzberg, "Infrared and Raman Spectra of Polyatomic Molecules," Van Nostrand, Princeton, N.J., 1945.

(52) W. P. L. Carter, Ph.D. Thesis, University of Iowa, Iowa City Iowa, 1973.

(53) P. J. Robinson and K. A. Holbrook, "Unimolecular Reactions," Wiley-Interscience, London, 1972.

(54) D. F. Eggers, L. W. Gregory, G. D. Halsey, and B. S. Rabinovitch, "Physical Chemistry," Wiley, New York, N.Y., 1964, p 313.

Substituted Pyridinyl Radicals in Aqueous Solutions. Formation, Reactivity, and Acid–Base Equilibria[1]

P. Neta* and L. K. Patterson

Radiation Research Laboratories and Center for Special Studies, Mellon Institute of Science, Carnegie-Mellon University, Pittsburgh, Pennsylvania 15213 (Received May 6, 1974)

Pyridinyl radicals have been produced from various pyridines as well as pyridinium cations by reduction with e_{aq}^- and, where reactivity allows, by electron transfer. Both meta- and para-substituted carboxy and carbamoyl compounds were investigated. These radicals all exhibit a strong optical absorption band in the region of 300 nm (ϵ 4000–13,000 M^{-1} cm^{-1}) and another moderately intense band (ϵ 2000–7000 M^{-1} cm^{-1}) at about 400 nm. In all cases the separation between bands was greater for meta radicals than for their para counterparts. Radical–radical reaction rate constants were measured by monitoring transient decay. Dissociation constants for these intermediates were determined from pH dependent alterations in transient spectra. Two dissociation constants were observed for the carboxypyridinyl radicals ($pK_1 \sim 0$; $pK_2 \sim 6$) and one for the carbamoyl substituted radicals ($pK = 1.3$–2.1). It was found that pyridinyl radical disproportionation is enhanced by increased degrees of protonation. Previously reported increase in radical reactivity with decreasing pH may be fully explained by this effect. Comparisons of electron transfer and disproportionation rate constants reveal greater stability for para-substituted pyridinyl radicals than for their meta counterparts. This stability may be due largely to increased conjugation between the ring and para substituent as compared with the meta analog. Results of INDO calculations involving the carboxypyridinyl radicals support this view.

Introduction

One-electron reduction of pyridines yields pyridinyl radicals. Possible participation of such radicals in biochemical redox reaction involving NAD (nicotinamide adenine dinucleotide) has stimulated considerable interest in these species. Optical spectra of radicals generated in aqueous solution from reduction of NAD^+, nicotinamide, and related pyridines have been measured by pulse radiolysis; associated kinetics of growth and decay have also been examined.[2,3] Further, an esr study of *in situ* irradiated solutions has shown that one-electron reduction of pyridine and its carboxy derivatives is followed by rapid protonation on the ring nitrogen even at very high pH.[4]
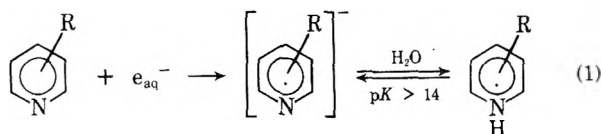
In aqueous solutions these radicals disappear by second-order processes. By contrast, however, several derivative radicals such as N-ethyl-4-carbethoxypyridinyl have been prepared in certain organic solvents and found to be stable.[5] This pronounced solvent related difference in radical stability has been interpreted in terms of polarity effects on an equilibrium between the radicals and ionic intermediates produced from their disproportionation.[6] The effect of pH on pyridinyl radical decay rates in aqueous solution has been explained in terms of such an equilibrium.

In the present paper, we show that this equilibrium need not be invoked and that changes in decay rate with changing pH *merely result from radical protonation in acid*. We have also made a detailed comparison of meta and para isomeric radicals by measuring their adsorption spectra, acid-base equilibria, and stabilities as reflected in electron transfer rate constants.

Experimental Section

All solutions were prepared in triply distilled water and deoxygenated with prepurified nitrogen. Pyridine derivatives were obtained from Aldrich Chemical Co. and from Eastman Organic Chemicals. The computer-controlled pulse radiolysis system developed in these laboratories has previously been described.[7] Irradiations were carried out with 0.1–1-μsec pulses of 2.8-MeV electrons from a Van de Graaff accelerator, and time-dependent optical absorption spectra were measured for each compound as a function of pH. Extinction coefficients, ϵ, were determined by thiocyanate dosimetry assuming $\epsilon^{480}_{(CNS)_2^-}$ 7600 M^{-1} cm^{-1}. Dissociation constants were determined from variations in extinction coefficients with changing pH. Titration curves were plotted for best fit with these experimental data using a Hewlett-Packard 9100A calculator and plotter and the equation

$$\epsilon_{obsd} = (\epsilon_{H_2A} + \epsilon_{HA}K_1/[H^+] + \epsilon_A K_1 K_2/[H^+]^2)/(1 + K_1/[H^+] + K_1 K_2/[H^+]^2)$$

where H_2A, HA, and A represent three acid–base forms and K_1 and K_2 are the dissociation constants. Decay kinetics were determined over a tenfold range of radical concentrations and electron transfer kinetics over a fivefold range of solute concentrations.

Formation of Pyridinyl Radicals

Pyridine derivatives can be reduced in aqueous solution by e_{aq}^- (reaction 1). While the reaction of e_{aq}^- with pyridine itself is only moderately rapid ($k = 1 \times 10^9$ M^{-1} sec^{-1}) the presence of carboxy and carbamoyl substituents on the ring increases the rate to the diffusion-controlled limit. Nicotinic and isonicotinic acid, the associated amides, and NAD$^+$ all react with e_{aq}^- at rate constant $>10^{10}$ M^{-1} sec^{-1}.[2,3] In order to properly study radicals produced from e_{aq}^- reactions it is necessary to eliminate interference from OH reaction with the pyridines. This can be achieved by adding an OH scavenger whose intermediate has no absorption which overlaps that of the radical under study. t-BuOH is especially suitable because it produces an intermediate which is essentially transparent in the wavelength

region above 250 nm. However, this intermediate becomes involved in cross reactions with pyridinyl radicals and affects the decay kinetics. This difficulty can be avoided if a scavenger is used which reacts with H and OH to yield an intermediate which also reduces the pyridine by electron transfer. One may thus produce a one-radical system. Formate, for example, yields CO_2^- radicals upon reaction with OH and H, and these in turn efficiently reduce NAD$^+$ and other pyridinium compounds.[2,4,6] However, the use of formate is limited to solutions at pH $> \sim 5.5$ because in the acid region e_{aq}^- is converted to H by reaction with H$^+$ and formic acid (pK = 3.7) reacts with H very slowly. i-PrOH, however, reacts efficiently with both OH and H to produce an intermediate which exhibits little absorption at wavelengths greater than 300 nm and is known to transfer electrons efficiently in many systems (see, $e.g.$, ref 8). It was decided, therefore, to examine rates of electron transfer from the $(CH_3)_2\dot{C}OH$ radical to pyridine derivatives in order to determine the proper conditions for producing a one-radical system.

For these experiments, solutions were prepared with i-PrOH concentrations of 0.5 M and were saturated with N$_2$O. The pyridine concentration was limited to $<10^{-3}$ M. At neutral pH all e_{aq}^- is converted to OH by N$_2$O while in the acid region e_{aq}^- is converted to H by reaction with H$^+$. Both OH and H react efficiently with i-PrOH to yield $(CH_3)_2\dot{C}OH$. The pyridinyl radicals (Pyr$\cdot$) absorb strongly around 400 nm and it is, therefore, possible to monitor without interference the formation of pyridinyl by the reduction of pyridinium cation (Pyr$^+$)

$$(CH_3)_2\dot{C}OH + Pyr^+ \longrightarrow (CH_3)_2CO + H^+ + \dot{Pyr} \quad (2)$$
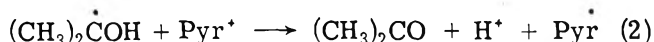
The hydroxyisopropoyl radical dissociates into $(CH_3)_2\dot{C}O^-$ (pK = 12.2) which is known to be a stronger reducing agent. By adjusting the pH to ≥ 13 one can measure the rate for the reaction

$$(CH_3)_2\dot{C}O^- + Pyr^+ \longrightarrow (CH_3)_2CO + \dot{Pyr} \quad (3)$$
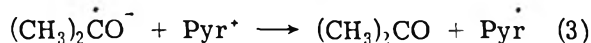
In order to correlate structure with rate constant, studies were carried out at several pH values with pyridines having carboxyl and carbamoyl substituents either meta or para to the nitrogen. With each compound a series of solute concentrations between 1×10^{-5} and 1×10^{-3} M were used. Both the formation kinetics and the maximum optical density after formation were observed. At lower concentrations complete electron transfer was not achieved because part of the $(CH)_2\dot{C}OH$ radicals disappeared by radical-radical reactions. This competing process also causes the formation kinetics to appear to be too rapid. At the higher solute concentrations reaction 2 or 3 becomes quantitative, and the same rate constants were determined over a fivefold range of concentrations.

The results, summarized in Table I, show a clear distinction between the reactivities of $(CH_3)_2\dot{C}OH$ and $(CH_3)_2\dot{C}O^-$ and suggest several trends in reactivity. Pyridine derivatives *in which the nitrogen is neutral, i.e.,* nonsubstituted and nonprotonated, are not reduced by $(CH_3)_2\dot{C}OH$, i.e., $k < 1 \times 10^6$ M^{-1} sec^{-1}, but can be reduced by $(CH_3)_2\dot{C}O^-$ at moderate rates, $k \sim 10^8$ M^{-1} sec^{-1}. When the nitrogen is positively charged, through protonation or methylation, the reduction by $(CH_3)_2\dot{C}OH$ becomes efficient. The rate constants are again increased, although only slightly, upon protonation of a carboxyl group on the ring. In all cases, however, the para isomer

**TABLE I: Rate Constants for Electron Transfer from
$(CH_3)_2\dot{C}OH$ or $(CH_3)_2\dot{C}O^-$ to Pyridine Derivatives**

Compound	pH	k, M^{-1} sec^{-1}
p-HN $^+C_5H_4CO_2H$	0.4	2.0×10^9
p-HN $^+C_5H_4CO_2^-$	3.2	8.5×10^8
p-NC$_5$H$_4$CO$_2^-$	9.0	$<1 \times 10^6$
p-NC$_5$H$_4$CO$_2^-$	13.3	2.0×10^8
m-HN $^+C_5H_4CO_2H$	0.0	3.5×10^8
m-HN $^+C_5H_4CO_2^-$	3.4	1.8×10^8
m-NC$_5$H$_4$CO$_2^-$	8.2	$<1 \times 10^6$
m-NC$_5$H$_4$CO$_2^-$	13.1	$\geq 1 \times 10^8$
p-CH$_3$N $^+C_5H_4CO_2^-$	8.6	1.5×10^9
m-CH$_3$N $^+C_5H_4CO_2^-$	9.2	1.0×10^8
m-HN $^+C_5H_4CONH_2$	1.9	4.0×10^8
m-NC$_5$H$_4$CONH$_2$	9.2	$<1 \times 10^6$

accepts an electron ~5–10 times more rapidly than the meta isomer. This behavior correlates with the difference in redox potentials for the two isomers, e.g., as determined for nicotinic and isonicotinic acid. At pH 1 the polarographic half-wave potentials for the reduction of nicotinic and isonicotinic acid are -1.08 and -0.80 V (vs. standard calomel electrode), respectively.[9] Pulse polarographic experiments[10] with $(CH_3)_2\dot{C}OH$ yielded a value of $E_{1/2} = -1.30$ V, which indicates that both acids should be efficiently reduced by this radical. In neutral solutions, on the other hand, the $E_{1/2}$ values for nicotinic and isonicotinic acid are -1.66 and -1.56 V, respectively, and thus no electron transfer can be expected. The $E_{1/2}$ for $(CH_3)_2\dot{C}O^-$ is -2.2 V, and again reduction becomes possible.

The half-wave potential for $\dot{C}O_2^-$ is comparable[10] to that for $(CH_3)_2\dot{C}OH$ and, therefore, a similar behavior in the electron transfer reactions is expected. Indeed, a qualitative observation has been made which suggests that $\dot{C}O_2^-$ can transfer electron efficiently to pyridinium ions but not to pyridines.[4] A rate constant of 1.6×10^9 M^{-1} sec^{-1} for the electron transfer to NAD$^+$ has been reported.[2]

Spectral Characteristics and Dissociation Constants

Pyridinyl radicals were produced in irradiated aqueous solutions by reaction of pyridine derivatives with e_{aq}^- and, whenever possible, also by their reactions with $(CH_3)_2\dot{C}OH$. Transient absorption spectra were monitored at various pH values in order to detect related shifts in absorbance and these shifts were then used for the determination of dissociation constants. After the pK values had been established spectra were recorded at the pH regions where one form of the radical predominates.

The spectra observed with solutions of isonicotinic acid are shown in Figure 1. In the acid region electron transfer from $(CH_3)_2\dot{C}OH$ is rapid and all primary radicals ultimately yield pyridinyl. In neutral solutions the electron transfer does not take place, and the absorbance observed in the presence of either i-PrOH or t-BuOH was identical. At pH ≥ 12.7 where $(CH_3)_2\dot{C}O^-$ predominates transfer is again rapid and the optical density increases accordingly, although no shift in the spectrum could be detected between pH 8 and pH 14. The spectrum in this region is in good agreement with that reported previously.[3] Changes in the absorbance at 405 and 425 nm with pH were used to determine the pK values as shown in the bottom part of Figure 1. The pK of 6.3 had to be determined in the presence of t-BuOH, because with i-PrOH as the pH decreases and the isonicotinate ion protonates on the nitrogen (p$K = 4.86$), electron transfer begins to take place; and the ab-

Figure 1. (Top) Transient absorption spectra of the acid–base forms of the 4-carboxypyridinyl radical. Observed with 0.2–1×10^{-3} M solutions of isonicotinic acid. (O) Spectrum observed at pH 8.8 in the presence of 0.5 M t-BuOH. An identical spectrum was obtained at pH 8.0 in the presence of 0.5 M i-PrOH. In both cases only the e_{aq}^- reacted with the isonicotinic acid and no electron transfer from the alcohol radicals took place. At pH 12.7 with i-PrOH electron transfer was rapid and an identical spectrum was obtained with the same extinction coefficients (i.e., optical densities 2.3 times higher). At pH 13 and 14 the spectra were also identical. (●) Spectrum at pH 2.9 in the presence of 0.5 M i-PrOH. Electron transfer from the alcohol radical was rapid in this case. (△) Spectrum at $H_0 = -0.8$ with perchloric acid and 0.5 M i-PrOH. Again the electron transfer was rapid. (Bottom) Effect of pH on the transient absorption. (O) Determined at 405 nm with solutions containing 1×10^{-3} M isonicotinic acid and 0.5 M t-BuOH. The titration curve was calculated from the plateau values using p$K = 6.3$. (●) determined at 425 nm with solutions containing 1×10^{-3} M isonicotinic acid and 0.5 M i-PrOH. The curve was calculated using p$K = -0.17$. For pH <0.5 the H_0 scale for perchloric acid has been used (C. H. Rochester, "Acidity Functions," Academic Press, New York, N. Y., 1970, p 43).

sorbance increases gradually in a way that masks the increase due to radical protonation. The pK in the acid region was obtained in the presence of i-PrOH because electron transfer was complete at all pH values below 4. The data in Figure 1 suggest the following equilibria in the 4-carboxypyridinyl radical
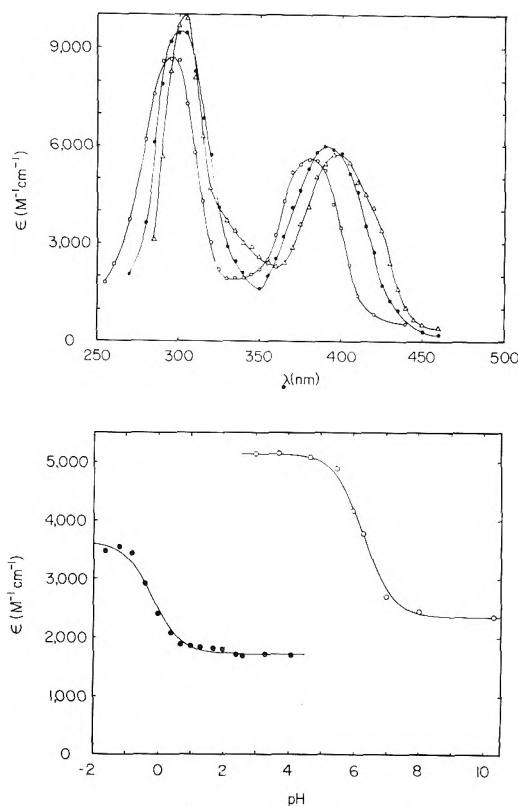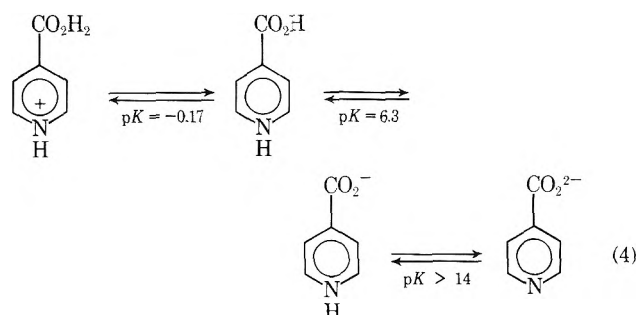

$$\tag{4}$$
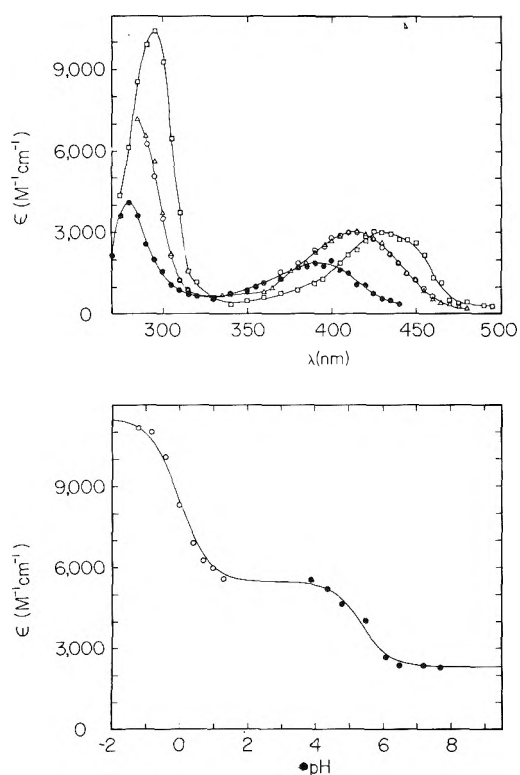
Figure 2. (Top) Transient absorption spectra of the acid–base forms of the 3-carboxypyridinyl radical. Observed with 0.2–1×10^{-3} M solutions of nicotinic acid. (●) Spectrum observed at pH 9.2 in the presence of 0.5 M t-BuOH. Identical spectra were obtained at pH 7 and 11 in the presence of 0.5 M i-PrOH and no electron transfer from the alcohol radical took place. At pH 13.1 the optical density increased because of electron transfer from the alcohol radical anion. (O) Spectrum observed at pH 4.25 in the presence of t-BuOH. (△) An identical spectrum observed at pH 1.3 in the presence of i-PrOH. The optical density was 2.3 times higher in this case because electron transfer from the alcohol radical is rapid. (□) Spectrum observed at $H_0 = -1.6$ in the presence of i-PrOH. (Bottom) Effect of pH on the transient absorption. Determined at 295 nm with 1×10^{-3} M solution of nicotinic acid containing 0.5 M i-PrOH. At the low pH region (O) electron transfer from the alcohol radical was rapid. At the higher region (●) electron transfer did not take place and the optical densities were normalized to the same ϵ scale. The titration curve was calculated using the indicated plateau values and pK values of 0.0 and 5.4.

Corresponding results for nicotinic acid are shown in Figure 2. Shifts in the absorption maxima follow the same pattern as with isonicotinic acid, although the higher wavelength maxima are considerably less intense for nicotinic acid. Also, separation between the two absorption bands is more pronounced with nicotinic than with isonicotinic acid. The pK values for both cases are very similar in the acid region but differ slightly in the neutral region. In order to facilitate comparison pK values and spectral parameters are summarized in Table II.

Results for the N-methyl derivatives of the two radicals discussed above are shown in Figures 3 and 4.[11] It can be seen from the figures and the summary in Table II that the same trends for the para and meta isomers hold for the N-methyl derivatives as well. In fact, the presence of the methyl group has a very small effect on spectral parameters and pK values as compared with the effect of the carboxyl group position.

Results for the amides studied are included in Table II, and spectral data for 4-carbamoyl-1-hexylpyridinyl are also shown in Figure 5. The spectra for the amides resem-

ble those for the corresponding acids and again a considerable difference is observed between the para and meta isomer and a smaller difference upon alkylation of the nitrogen. The pK values for the carbamoylpyridinyl radicals are, however, different from those of the carboxy analogs. Instead of p$K \approx 0.0$ for all carboxypyridinyl radicals, pK values of ~ 1.3 and 2.1 are observed for the meta and para carbamoyl derivatives, respectively. Similarly higher pK values have previously been observed for benzamide electron adduct (p$K = 7.7$)[12a] as compared with the benzoic acid adduct (p$K = 5.3$).[12b] This trend may be assigned to the higher electronegativity of the OH group as compared to NH_2. The site of protonation is the oxygen, as suggested previously for electron adducts of aliphatic and aromatic amides.[12a]

$$\text{(5)}$$
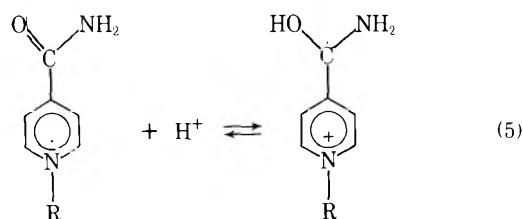
Reactions of Pyridinyl Radicals

Pyridinyl radicals react with each other by second-order processes to either combine or disproportionate. Although combination to form dimers has been suggested by several authors (see, e.g., ref 2) the disproportionation mechanism appears now to be more favorable. Moreover, recently such a mechanism has been suggested to take place via electron transfer.[6]

$$\text{(6)}$$
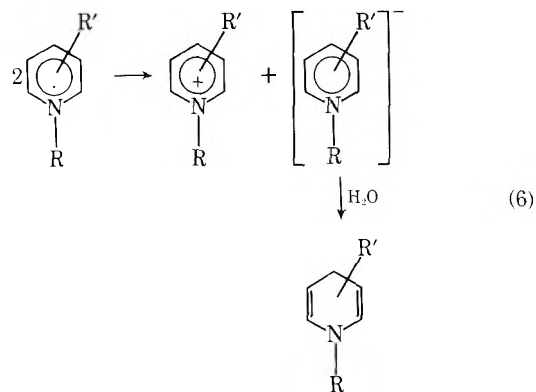
The rate of bimolecular disappearance of pyridinyl radicals in aqueous solutions has been followed by kinetic spectrophotometry at the absorption maxima around 400 nm. Decay of the $\sim$300-nm absorption was sometimes complicated by the formation of stable products which absorb in the 300–370-nm region. Second-order decay kinetics have been monitored under conditions such that only the pyridinyl radical was present in the solution. The radical from t-BuOH has been found to react with pyridinyl moderately rapidly ($k \sim 2 \times 10^8$ M^{-1} sec^{-1}) even when the pyridinyl decayed biomolecularly very slowly (see below). Therefore, decay rates of the radicals from nicotinic and isonicotinic acid were not determined in neutral solution, because electron transfer from $(CH_3)_2\dot{C}OH$ does not take place under these conditions and cross reactions result in rapid decay. At pH 13 transfer from $(CH_3)_2\dot{C}O^-$ was efficient and low decay rates were observed.

It can be seen from Table II that in neutral solutions all

TABLE II: Dissocation Constants and Spectral Parameters of Substituted Pyridinyl Radicals

Radical	pK	λ_{max}^1	ϵ_{max}^1	λ_{max}^2	ϵ_{max}^2	Second-order decay $2k$, M^{-1} sec^{-1}
p-HN $^+C_5H_4CO_2H_2$	−0.17	303	10,000	397	5700	1×10^9
p-HNC$_5$H$_4$CO$_2$H	6.3	302	9,500	391	6000	4×10^8
p-HNC$_5$H$_4$CO$_2^-$	>14	295	8,700	380	5600	$\sim$7 $\times 10^6$
p-NC$_5$H$_4$CO$_2^{2-}$						
m-HN $^+C_5H_4CO_2H_2$	0.0	295	10,500	430	3000	1×10^9
m-HNC$_5$H$_4$CO$_2$H	5.4	≤285	≥7,200	415	3000	4×10^8
m-HNC$_5$H$_4$CO$_2^-$		280	4,100	395	2000	
p-CH$_3$N $^+C_5H_4CO_2H_2$	0.1	310	12,600	410	5500	1×10^9
p-CH$_3$NC$_5$H$_4$CO$_2$H	6.8	310	10,400	400	6300	1×10^8
p-CH$_3$NC$_5$H$_4$CO$_2^-$		307	11,800	395	7000	$<2 \times 10^5$
m-CH$_3$N $^+C_5H_4CO_2H_2$	0.16	300	11,000	440	3200	$\sim$2 $\times 10^9$
m-CH$_3$NC$_5$H$_4$CO$_2$H	5.0	297	6,600	420	3700	$\sim$4 $\times 10^8$
m-CH$_3$NC$_5$H$_4$CO$_2^-$		≤290	≥3,200	400	2300	$\sim$6 $\times 10^7$
m-HN $^+C_5H_4C(OH)NH_2$	1.4	305	10,000	445	3500	1.5×10^9
m-HNC$_5$H$_4$CONH$_2$		287	5,000	410	2800	
p-C$_6$H$_{13}$N $^+C_5H_4C(OH)NH_2$	2.1	329	11,400	420	6100	1×10^9
p-C$_6$H$_{13}$NC$_5$H$_4$CONH$_2$		316	10,800	406	6800	$\leq$1 $\times 10^5$
m-C$_6$H$_{13}$N $^+C_5H_4C(OH)NH_2$	1.26	312	9,600	445	3500	
m-C$_6$H$_{13}$NC$_5$H$_4$CONH$_2$		290	4,300	422	2300	$\sim$10^7
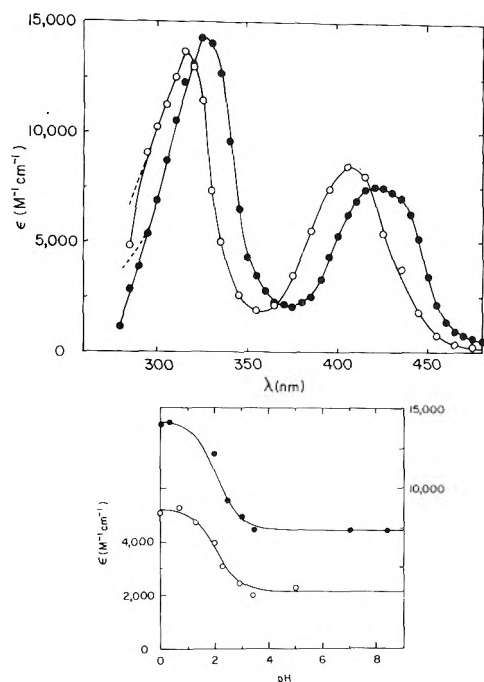
Figure 5. (Top) Transient absorption spectra of the acid–base forms of the 4-carbamoyl-1-hexylpyridinyl radical. Observed with solutions containing 2 × 10⁻⁴ M 4-carbamoyl-1-hexylpyridinium bromide and 0.5 M i-PrOH (O) pH 7.7. Indentical spectra were obtained in the presence of formate or t-BuOH instead of i-PrOH. In the case of t-BuOH the yield was lower by a factor of 2.5 (●) pH 0.9. In the presence of formate instead of i-PrOH the shape of the spectrum was identical but the yield was ~30% lower due to incomplete scavenging (see text). The dashed lines are the absorption corrected for the destruction by radiation of the parent compound. (Bottom) Effect of pH on the transient absorption. Determined at 330 (●) and 440 (O) nm. The curves were calculated using the plateau values and pK = 2.1.

radicals decay more slowly than in acid solution. In strong acid all decay rate constants are ~ 1–2 × 10⁹ M^{-1} sec⁻¹, a value which is characteristic of many radicals with no particular stabilizing features.[13] At moderate acidities some-

what lower rates are observed. In the neutral region, however, very slow decay is found, and it is readily seen that the para isomers decay much more slowly than the meta. The large difference in decay rates between the various acid–base forms cannot be explained by the effect of electrostatic charge, which in this case can only contribute a factor of ~2.[13] Moreover, the large difference between the two isomers indicates that the resonance structures or spin density distribution are more important in determining the radical reactivity. The effects of pH and of isomerism are treated in detail below.

Effect of pH on Decay Rates. In a recent communication[6] Kosower, *et al.*, have reported the measurement, by pulse radiolysis, of the bimolecular disappearance rates of pyridinyl radicals in aqueous solutions. They produced radicals by the reaction of e_{aq}^- and CO_2^- with 4-carbamoyl-1-methlpyridinium ion and observed increasing decay rate constants with decreasing pH. They concluded that the reaction of pyridinyl radicals with each other results in disproportionation by electron transfer, involving an intermediate ion pair in equilibrium with the initial neutral radicals. While there is no reason to doubt that disproportionation involves electron transfer as suggested,[6,14–16] the postulated equilibrium between an ion pair and the initial radicals is open to question. The present study shows that such an equilibrium does not have to be invoked to explain the results of Kosower, *et al.*, and that the pH effects observed by these authors can have an alternative interpretation. This interpretation is based on findings in the present work that 4-carbamoyl-1-alkylpyridinyl radicals protonate on oxygen with pK ~ 2 and that the decay of the protonated form by itself or by reaction with the neutral radical is very rapid.

We have carried out experiments similar to those of Kosower, *et al.*, using 4-carbamoyl-1-hexylpyridinium bromide. The decay rate constant at pH 7 in the presence of either formate or *i*-PrOH was found to be very low (2*k* ≤ 1 × 10⁵ M^{-1} sec⁻¹) while in the presence of t-BuOH the system contains both the pyridinyl radical and $\dot{C}H_2C(CH_3)_2OH$ so that the decay becomes rapid as the re-

sult of a cross reaction between the two radicals ($k = 2 \times 10^8 \ M^{-1} \ \mathrm{sec}^{-1}$). Lowering the pH to 3.5 with either formate or i-PrOH present caused a dramatic increase in the decay rate constant but no detectable change in the optical spectrum, in agreement with the previous report.[6] Measurements at a still lower pH in the presence of formate are complicated by incomplete scavenging as mentioned above. In fact, decreased optical absorbance was observed at lower pH values when formate was used. The decay of the acid form has been monitored in the presence of i-PrOH at pH 0.0 and 0.5 and was found to be $2k = 1 \times 10^9 \ M^{-1} \ \mathrm{sec}^{-1}$. In the intermediate pH region the following values of $2k$ have been measured: pH 1.3, 6×10^8; pH 2.4, 4×10^8; pH 3.3, 1×10^8; and pH 4.7, $3 \times 10^7 \ M^{-1} \ \mathrm{sec}^{-1}$. These values are in agreement with a pK of 2.1 (Figure 5 and Table II) assuming that the cross reaction of the two forms of the radicals is also $\sim 10^9 \ M^{-1} \ \mathrm{sec}^{-1}$. Because the neutral form decays very slowly the effect of protonation on decay rates is large even when the protonated form represents <1% of the radicals and, of course, under these conditions no shift in the spectrum can be observed. It can be, therefore, concluded that the complex decay equilibrium suggested previously[6] does not have to be invoked at all. Instead one finds a large difference in reactivity between the acid and neutral forms (eq 5). In both forms the unpaired spin is delocalized over the ring and the α carbon. The neutral radical is relatively unreactive. On the other hand, the charge on the acid form can be expected to reside predominantly on the nitrogen resulting in what can be schematically described as a pyridinium-substituted alkyl radical, which is more reactive.

By analogy, carboxypyridinyl radicals are unreactive only in their basic form, $RNC_5H_4CO_2{}^-$. Protonation results in partial positive charge on the nitrogen and shift of spin density to the α carbon leading to increased reactivity. The acid form can be formulated mainly as $R^+NC_5H_4\dot{C}O_2H_2$. Because the intermediate form is also reactive, it may be suggested that it exists predominantly as a zwitterion rather than the neutral form.

$$(7)$$
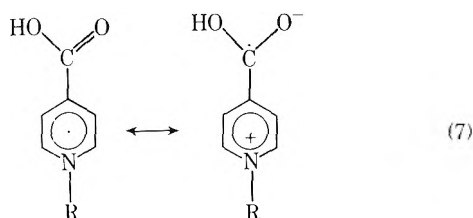
Reactivity of Meta and Para Isomers. Rate constants for electron transfer to pyridine derivatives (Table I) are significantly higher for the para than for the meta isomers. Although not conclusive, this finding may suggest that the radicals produced from the para isomers would be less reactive. The decay rate constants (Table II) clearly indicate this to be the case as far as the radical–radical reaction is concerned. The increased stability of the para isomer can be explained by increased spin interaction between the ring and the substituent. The esr hyperfine constants[4] indicate that a large portion of the spin density on the ring of a pyridinyl radical is concentrated on the para carbon atom while only negligible densities are found at the meta position. It is reasonable to assume, therefore, that carboxy or carbamoyl groups at the para position will have a greater interaction than in the meta position. To examine this possibility in a more quantitative manner, INDO calculations[17] have been carried out on two isomers. The radical

$HNC_5H_4CO_2H$ has been chosen for this calculation because of its relative simplicity and lack of overall charge.[18] The calculated spin densities are as follows.
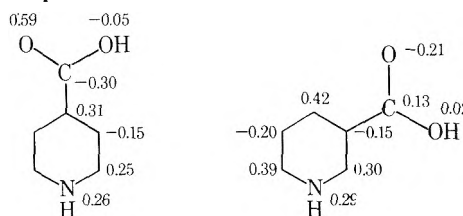
Although these values cannot be considered to represent the true situation with complete accuracy, they indicate marked differences between the isomers. In the meta derivative almost all the unpaired spin density remains on the ring with little conjugation with the carboxyl group. On the other hand, the para isomer shows considerable conjugation, with only 77% overal spin density on the ring and appreciable polarization of the C–O bond. The calculations, therefore, indicate greater resonance stabilization of p-carboxypyridinyl as compared to its meta counterpart. Similar behavior is to be expected for the carbamoyl derivatives. If this difference in stability correlates with electron transfer rates as found with $(CH_3)_2\dot{C}OH$ (Table I) one might expect that the m-carboxypyridinyl radical would transfer an electron to the p-carboxypyridinium ion to produce the more stable p-carboxypyridinyl. This experiment is described below.

Electron Transfer from Pyridinyl to Pyridinium. In order to measure the rate constant for the expected electron transfer from the meta radical to the para compound (see discussion above) experiments were carried out with nicotinic and isonicotinic acids at low pH. Upon irradiation of solutions containing 1 M i-PrOH and $1 \times 10^{-2} \ M$ nicotinic acid at $H_0 = -1.0$ the m-carboxypyridinyl radical was formed within <1 μsec after the pulse. Upon addition of 5×10^{-5} to $2 \times 10^{-4} \ M$ isonicotinic acid the initial spectrum of the m-carboxypyridinyl was found to disappear, while a corresponding growth of the p-carboxypyridinyl spectrum occurred. The rate of this change was best monitored at 395 nm, and a rate constant of $2.0 \times 10^9 \ M^{-1} \ \mathrm{sec}^{-1}$ was derived for the electron transfer (followed by proton equilibration)

$$(m\text{-}H\overset{+}{N}C_5H_4CO_2H_2)\cdot \ + \ p\text{-}H\overset{+}{N}C_5H_4CO_2H \ \longrightarrow$$

$$m\text{-}H\overset{+}{N}C_5H_4CO_2H \ + \ (p\text{-}H\overset{+}{N}C_5H_4CO_2H_2)\cdot \qquad (8)$$
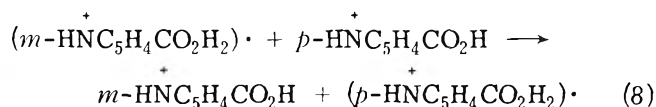
Summary and Conclusions

Both pyridines and pyridinium ions can be reduced efficiently by $e_{aq}{}^-$ to produce pyridinyl radicals. However, pyridinium ions can also undergo one-electron reduction by $\dot{C}O_2{}^-$ and $(CH_3)_2\dot{C}OH$ ($k \sim 1$–$2 \times 10^9 \ M^{-1} \ \mathrm{sec}^{-1}$). Pyridines, on the other hand, cannot be reduced by $(CH_3)_2\dot{C}OH$ but are reduced by $(CH_3)_2\dot{C}O^-$ ($k \sim 1$–$2 \times 10^8 \ M^{-1} \ \mathrm{sec}^{-1}$). Electron transfer reactions to p-carboxy- or p-carbamoylpyridinium ions were found to be 5–10 times more rapid than those to the meta isomers. It was further found that the radical produced from the meta isomer can transfer an electron to the corresponding para compound ($k \sim 2 \times 10^9 \ M^{-1} \ \mathrm{sec}^{-1}$). These findings correlate with the greater tendency of the para isomers toward reduction, as reflected by their redox potentials, compared with the meta isomers. Moreover, they demonstrate the greater stability of the para-substituted pyridinyl radical as compared with the meta-substituted radical. This characteristic is also reflect-

ed by the slower radical–radical reactions observed for the para isomers (in neutral solutions). The resonance stabilization of the two isomers should be related to conjugation between the ring and the substituent. INDO calculations show that in p-carboxypyridinyl a considerable portion of the unpaired spin is distributed over both the heterocyclic ring and the carboxyl group, while in the meta isomer the electron density is almost completely located on the ring, and little conjugation exists with the carboxyl group.

Pyridinyl radicals show intense absorption with maxima around 300 and 400 nm. Most para-substituted radicals have extinction coefficients of the order of 10,000 and 5000 M^{-1} cm^{-1} at the two maxima, respectively. The meta isomers have somewhat lower extinction coefficients and larger separation between the maxima.

Spectral shifts with pH were used to determine dissociation constants for these radicals. Carboxyl groups on the ring of pyridinyl undergo two acid–base equilibria with the first pK value around 0 for both meta and para isomers, and the second pK value ~5 for *m*- and ~6.5 for *p*-carboxypyridinyl. Carbamoylpyridinyl radicals show one pK value only, ~1.3 for the meta and 2.1 for the para isomer studied. This difference in the pK between the meta and the para isomers reflects the higher electron density on the para substituent as compared with the meta analog. These pK values can be compared to those observed previously for the electron adducts to benzoic acid (pK$_1$ = 5.3, pK$_2$ = 12.0)[12b] and benzamide (pK = 7.7).[12a] This comparison indicates that a decrease of 5 pK units may occur as a result of the combined effect of the additional positive charge and of electron withdrawal by the ring nitrogen. The difference in pK between COOH and CONH$_2$ is comparable in both the benzene and pyridine derived radicals, and reflects the greater electronegativity of OH as compared with NH$_2$. Similar comparisons of OH with NH$_2$ and similar effects on pK by the ring nitrogen have been observed in various other systems.[19] The ring NH proton does not dissociate even at pH 14, in agreement with the esr observation.[4]

Pyridinyl radicals react by second-order processes to disproportionate by electron transfer and to produce a pyridinium ion and a dihydropyridine. N-Alkylpyridinyl bearing a conjugating para substituent decay in neutral solutions very slowly, <10^5 M^{-1} sec^{-1}. Protonation of the carboxy or carbamoyl substituent results in higher decay rates of the order of 10^9 M^{-1} sec^{-1}. The higher reactivity of the protonated forms probably results from resonance structures with a positive charge on the nitrogen and unpaired spin on the α carbon, i.e., structures that can be formally defined as the unstable pyridinium substituted alkyl radicals. The effect of pH on decay rate constants can be principally explained by the difference in reactivities between the various acid–base forms of the radicals. The effect of electrostatic charge on these rates is small by comparison to the effect of resonance stabilization.

The slower decay rates previously observed[6] in less polar solvents can be explained by the effect of polarity on the kinetics of the disproportionation reaction which involves the conversion of two neutral species into a positive and negative ion.

References and Notes

(1) Supported in part by the U. S. Atomic Energy Commission.
(2) E. J. Land and A. J. Swallow, *Biochim. Biophys. Acta*, 162, 327 (1968).
(3) M. Simic and M. Ebert, *Int. J. Radiat. Phys. Chem.*, 3, 259 (1971).
(4) P. Neta, *Radiat. Res.*, 52, 471 (1972).
(5) E. M. Kosower and E. J. Poziomek, *J. Amer. Chem. Soc.*, 86, 5515 (1964).
(6) E. M. Kosower, A. Teuerstein, and A. J. Swallow, *J. Amer. Chem. Soc.*, 95, 6127 (1973).
(7) L. K. Patterson and J. Lilie, *Int. J. Radiat. Phys. Chem.*, 6, 129 (1974).
(8) R. L. Willson, *Trans. Faraday Soc.*, 67, 3020 (1971).
(9) L. Meites, "Polarographic Techniques," Interscience, New York, N.Y., 1965, p 706.
(10) J. Lilie, G. Beck, and A. Henglein, *Ber. Bunsenges. Phys. Chem.*, 75, 458 (1971).
(11) See paragraph at end of text regarding supplementary material.
(12) (a) E. Hayon, T. Ibata, N. N. Lichtin, and M. Simic, *J. Phys. Chem.*, 76, 2072 (1972); (b) M. Simic and M. Z. Hoffman, *ibid.*, 76, 1398 (1972).
(13) See, *e.g.*, P. Neta, M. Simic, and E. Hayon, *J. Phys. Chem.*, 73, 4207 (1969); R. Wander, P. Neta, and L. M. Dorfman, *ibid.*, 72, 2946 (1968).
(14) H. R. Haysom, J. M. Phillips, and G. Scholes, *J. Chem. Soc., Chem. Commun.*, 1082 (1972).
(15) H. Zemel and P. Neta, *Radiat. Res.*, 55, 393 (1973).
(16) P. Neta and R. W. Fessenden, *J. Phys. Chem.*, 78, 523 (1974).
(17) J. A. Pople, D. L. Beveridge, and P. A. Dobosh, *J. Amer. Chem. Soc.*, 90, 4201 (1968).
(18) Experience in this laboratory (R. W. Fessenden, private communication) has shown that agreement between calculated and experimental hyperfine constants is less satisfactory for charged radicals than for the neutral species.
(19) See review by P. Neta, *Advan. Phys. Org. Chem.*, in press.

Growth of Calcium Phosphate on Hydroxyapatite Crystals. Effect of Supersaturation and Ionic Medium

G. H. Nancollas* and B. Tomažič[1]

Chemistry Department, State University of New York at Buffalo, Buffalo, New York 14214 (Received April 3, 1974)

The kinetics of growth of hydroxyapatite seed crystals has been studied at 25° and at constant physiological pH in stable supersaturated solutions of calcium phosphate. The grown material was characterized chemically and by infrared and X-ray powder diffraction methods. The pH was maintained by means of the pH-Stat-controlled addition of base and the growth was followed by analyzing the solutions for calcium and phosphate. Experiments have been made over a wide range of initial supersaturation in order to obtain information about the nature of the calcium phosphate phases formed. The overall precipitation reaction involves not only the formation of different calcium phosphate phases but also the concomitant dissolution of the thermodynamically unstable phase octacalcium phosphate formed rapidly in the initial stages of the reaction. Dissolution of the solid material formed in the crystallization experiments indicated a stoichiometry corresponding to OCP. The results of growth experiments at low supersaturation and in the presence of neutral electrolytes are discussed in relation to the calcium phosphate phases formed under these conditions.

Introduction

Although the precipitation of calcium phosphates and in particular hydroxyapatite [$Ca_5(PO_4)_3OH$, hereafter HAP] has been extensively studied, there remains considerable uncertainty as to the nature of the phases formed during the early stages of the precipitation reaction.[2-5] The eventual transformation of these phases into the thermodynamically stable HAP phase is also little understood. Since the process of HAP formation is very slow, thermodynamic data such as solubilities are not readily accessible since the attainment of true equilibrium is not easily ensured. A major difficulty is that different workers have used very different experimental methods both in the preparation of the calcium phosphate phases and in studying the course of the precipitation reactions. Thus crystalline materials prepared under conditions of high temperature are sometimes studied in aqueous systems at room temperatures and behave quite differently from the calcium phosphates prepared at ambient temperatures. It will be apparent from the results of the present work that the nature of the initially precipitated phases and the course of the subsequent crystal growth reaction is markedly dependent not only upon the degree of supersaturation of the solution, but also on the ionic strength of the solution and the type of neutral or inert electrolyte present. The wide range of conditions used by other workers makes it very difficult to compare their results and this has contributed a great deal to the present unsatisfactory state of knowledge.

The solubility product, K_{sp}, of well-defined crystalline HAP has been determined from the results of dissolution experiments but the reported values of K_{sp} range from $10^{-55.6}$[6] to 10^{-60}.[7] The dissolution of HAP is a moderately fast process and, as an example of a weathering reaction, the congruent dissolution is probably straightforward. Many published data, however, reveal that in the process of HAP crystal growth, equilibrium conditions cannot be attained in experimentally reasonable times.[8] For this reason, analysis of solid–solution experimental data solely on the basis of thermodynamic solubility products is an oversimplification. Kinetic considerations may be of paramount importance in controlling the formation of the calcium phosphate phases during the precipitation reactions. Thus in the case of calcium phosphate precipitation at physiological pH, the initial rapidly formed amorphous precursor undergoes a slow transformation to HAP and significant changes, with time, are observed in such factors as chemical composition, the degree of crystallinity,[9] and the specific surface area[10] of the solid phases.

The spontaneous precipitation of calcium phosphate from its supersaturated solutions has been extensively studied. The critical precipitation point is usually determined by the slow mixing of solutions containing calcium and phosphate ions and observing the first appearance of solid phase. This procedure suffers from the disadvantage that a considerable amount of precipitation has already taken place before the precipitate is visible in the solution. The usual assumption of homogeneous nucleation is also open to question since it is doubtful if any medium is sufficiently free from foreign nucleating sites to preclude the possibility of heterogeneous nucleation. For these reasons, it is very difficult to reproduce the results of spontaneous nucleation experiments and the present work is concerned with the growth of well-defined seed materials in stable supersaturated solutions of calcium phosphate. Such experiments have been shown to be highly reproducible[11,12] and studies can be made of the effects of factors such as the level of supersaturation, seed morphology, and the presence of foreign ions. Thus at pH values below the physiological level at which dicalcium phosphate dihydrate (hereafter DCPD) is the stable phase, it has been shown that crystal growth of seed crystals from stable supersaturated solutions, under conditions of both variable and constant pH, is controlled by a surface reaction at the crystal–solution interface. The rate of crystal growth is proportional to the square of the supersaturation and is independent of the fluid dynamics within the system.[13] However, the congruent dissolution of DCPD crystals into subsaturated

solutions is diffusion controlled and the rate is directly proportional to the degree of undersaturation.[14]

The present work is concerned with the growth of HAP seed crystals under conditions of physiological pH. This system is considerably more complex than that for DCPD and the simple kinetic equation which applies in the latter can no longer be used. Factors such as solid surface:solution ratio, level of supersaturation, and the presence of neutral electrolyte have been studied in order to throw more light on the precipitation of calcium phosphates under physiological conditions.

Experimental Section

Materials. Reagent grade materials were used in all experiments. Well-crystallized HAP seed material was prepared by the method of Nancollas and Mohan.[8]

Crystal Growth Experiments. The crystal growth experiments were performed in a water-thermostated double-walled vessel using stable supersaturated solutions of known supersaturation. The solution was stirred with a magnetic stirrer at about 250 rpm, and nitrogen gas was bubbled throughout the experiment to exclude carbon dioxide. The pH was measured with a glass electrode–calomel electrode pair connected to the Metrohm Herisau pH-Stat (Model Combititrator 3D). The electrode systems were standardized before and after each experiment with NBS standard buffer solutions prepared according to Bates:[15] 0.025 M potassium dihydrogen phosphate + 0.025 M disodium hydrogen phosphate, pH 6.865 and 0.01 M borax, pH 9.180 at 25°. Calcium chloride and phosphoric acid solutions were mixed at the desired molar ratio (1.66 unless otherwise stated), and the pH was adjusted to 7.40 ± 0.01 by the pH-Stat addition of 0.05 M base. Following the addition of a known amount of seed slurry, crystal growth was monitored by pH-Stat addition of 0.05 M alkali metal hydroxide. At known times, samples of solution were withdrawn from the cell and filtered through Millipore Celotate filters of 0.22-μ pore size. The solution phase was analyzed for total calcium and phosphate. Calcium solution concentration was determined by atomic absorption spectroscopy, using a 303M Perkin-Elmer spectrophotometer; a typical calibration line had the following parameters: $[Ca] \times 10^{-4}$ $(M) = (5.37 \pm 0.07)(\text{absorbance}) - (0.0236 \pm 0.008)$, with the standard deviation of determination of 0.02 ppm in the range of 1–8 ppm Ca. Phosphate solution concentration was determined spectrophotometrically by the phosphomolybdate method.[16] A typical calibration line had the following parameters: $[P] \times 10^{-5}$ $(M) = (4.928 \pm 0.119)(\text{absorbance}) - (0.214 \pm 0.093)$; the standard deviation of determination in the $10 - 50$ μM range was 0.5 μM.

The solid phases after lyophilization were further characterized by X-ray diffraction, infrared spectroscopy (Nujol mulling technique and KBr-pellet method), and dissolution experiments. The X-ray diffraction (Cu Kα radiation) examination of seed material and grown products was performed using a Philips XRG-300 X-ray diffractometer coupled to a recorder. The relative crystallinity of grown samples was estimated semiquantitatively from a linear regression line using known crystalline and amorphous synthetics as standards, measuring the intensity of the unresolved 211 reflection.[17] Amorphous calcium phosphate was prepared by spontaneous precipitation from calcium phosphate solutions at pH 7.40 in the presence of 10^{-4} M pyrophosphate as described by Francis.[18] Mixtures with HAP were prepared by weight (50 mg total) and carefully ho-

mogenized in an agate mortar with 1 drop of mineral oil. The resulting paste was evenly spread on a glass plate in order to avoid the preferential orientation of crystallites, as would be the case if pellets were used. The relative intensities of the 211, 112, and 300 reflections were 100, 60, and 60 as given for mineral hydroxyapatite.[19] The standard deviation of determination was 2.67%.

Results and Discussion

It is first necessary to express the degree of supersaturation in the stable supersaturated solutions with respect to the various possible calcium phosphate phases, DCPD, octacalcium phosphate ($Ca_4H(PO_4)_3$, hereafter written OCP), tricalcium phosphate ($Ca_3(PO_4)_2$, hereafter TCP), and HAP. In addition to the concentration of calcium and phosphate ions in the solution, the supersaturation depends upon the pH, temperature, and the concentration of other "neutral" electrolytes. The degree of supersaturation with respect to each of the calcium phosphate phases can be expressed in terms of the appropriate ionic concentration products (S_{CaP}, eq 1), the calculated free calcium ionic

$$S_{CaP} = \frac{IP - K_{sp}}{K_{sp}} \tag{1}$$

concentration (S_{Ca}, eq 2), or the Gibbs free energy of trans-

$$S_{Ca} = \frac{[Ca^{2+}]_t - [Ca^{2+}]_\infty}{[Ca^{2+}]_\infty} \tag{2}$$

fer from supersaturated to saturated solution (ΔG, eq 3). IP

$$\Delta G = -RT \ln \frac{IP}{K_{sp}} \tag{3}$$

corresponds to the activity product in the supersaturated solution defined, for each calcium phosphate phase, by eq 4–7 where K_{sp} is the value of IP at equilibrium (K_{sp}

$$IP_{DCPD} = [Ca^{2+}][HPO_4^{2-}]f_2^2 \tag{4}$$

$$IP_{OCP} = ([Ca^{2+}]f_2)^4([PO_4^{3-}]f_3)^3[H^+]f_1 \tag{5}$$

$$IP_{TCP} = ([Ca^{2+}]f_2)^3([PO_4^{3-}]f_3)^2 \tag{6}$$

$$IP_{HAP} = ([Ca^{2+}]f_2)^5([PO_4^{3-}]f_3)^3 K_w / [H^+]f_1 \tag{7}$$

(DCPD) = 2.1×10^{-7},[20] K_{sp} (OCP) = 1.25×10^{-47},[21] K_{sp} (TCP) = 1.15×10^{-29},[22] and K_{sp} (HAP) = 1.8×10^{-58},[23]), $[Ca^{2+}]_t$ is the free ionic calcium concentration at time t and $[Ca^{2+}]_\infty$ is its equilibrium value, and $-\Delta G$ represents the affinity of the reaction.[24] Concentrations of the ionic species in the solutions were calculated as described previously[25] from mass balance, electroneutrality, proton dissociation, and calcium phosphate ion-pair association constants[12] by successive approximations for the ionic strength, I. The activity coefficients of z-valent ionic species, f_z, were calculated from the extended form of the Debye–Hückel equation proposed by Davies,[26] $-\log f_z = Az^2(I^{1/2}/(1 + I^{1/2}) - 0.3 I)$.

Growth Experiments of High Supersaturation. In most of the previous spontaneous precipitation work, relatively high concentrations were used and the solutions were considerably supersaturated with respect to all of the calcium phosphate phases. These conditions are, however, far removed from those *in vivo* In the present work, experiments made over a range of supersaturation are summarized in
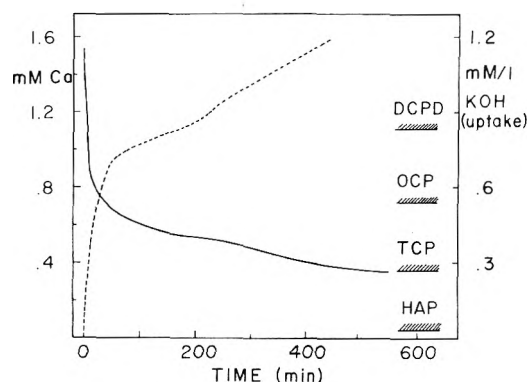
TABLE I: Concentration and Supersaturation Data of Some Typical Calcium Phosphate Supersaturated Solutions Prior to Inoculation (pH 7.40, 25°)

Expt no.	System type	Total [calcium], mM	Total [phosphate], mM	Ionic strength, mM	[NaCl], mM	Phase	S_{CaP} (eq 1)	S_{Ca} (eq 2)	$-\Delta G$ (eq 3), kcal mol^{-1}
46	I	1.562	0.973	6.73		DCPD	0.66	0.24	0.27
						OCP	1.60×10^2	1.1	2.96
						TCP	1.17×10^3	3.4	4.19
						HAP	1.23×10^{11}	43.6	15.07
79	II	0.432	0.287	2.07		DCPD	-0.78	-0.56	-0.91
						OCP	-0.87	-0.33	-1.16
						TCP	5.95	0.53	1.22
						HAP	3.29×10^7	12.0	10.27
25	III	1.576	0.987	157.5	150.0	DCPD	-0.44	-0.12	-0.37
						OCP	2.21	0.18	0.71
						TCP	6.82×10	1.30	2.52
						HAP	1.26×10^9	18.0	12.45

TABLE II: Calcium Phosphate Crystallization Induced by the Addition of HAP Seed (0.2 g of Seed l.$^{-1}$) at 25°, pH 7.4

	Initial concn		Neutral electrolyte	Initial rate, $-\Delta T_{Ca}/\Delta t$, μM min^{-1} g^{-1}	Base
Expt no.	$10^3 T_{Ca}$, M	$10^3 T_P$, M			
46	1.562	0.973		420	KOH
77	1.477	1.041		200	KOH
84	0.934	0.617		112	KOH
72	0.709	0.449		60	KOH
71	0.577	0.377		48	KOH
73	0.501	0.340		57	KOH
74	0.451	0.301		40	KOH
79	0.432	0.287		48	KOH
76	0.371	0.247		43	KOH
28	1.611	0.987		550	NaOH
29	1.616	0.979	0.01 M NaCl	315	NaOH
27	1.620	0.967	0.05 M NaCl	192	NaOH
26	1.583	0.970	0.10 NaCl	195	NaOH
25	1.576	0.987	0.15 NaCl	165	NaOH
24	1.570	0.972	0.40 NaCl	77	NaOH
23	1.616	0.977	0.70 NaCl	77	NaOH
10	1.609	1.013	0.15 M LiCl	193	LiOH
21	1.601	0.921	0.15 M NH$_4$Cl	190	NH$_4$OH
25	1.576	0.987	0.15 M NaCl	165	NaOH
13	1.565	0.968	0.15 M KCl	118	KOH
19	1.672	0.955	0.15 M CsCl	65	CsOH

Figure 1. Crystal growth at high supersaturation. Plots of total calcium concentration (full line) and base uptake (dotted curve) as a function of time for expt 46.

In Figure 1, it can be seen that immediately following inoculation with seed crystals, the very fast growth commences. The initial rate of reaction normalized for seed or solid-phase concentration was estimated to be $-\Delta T_{Ca}/\Delta t \approx$ 420 μM min^{-1} g^{-1}. After about 30 min, the rate decreased $(-\Delta T_{Ca}/\Delta t \approx 5.3$ μM min^{-1} g^{-1}), until almost zero at 200 min following which there is a further increase from 3 to 8 hr characterized by a rate of growth of about 2.5 μM min^{-1} g^{-1}. This discontinuity in the rate curve is paralleled both in the soluble phosphate level and in the potassium hydroxide uptake required to maintain the pH at 7.40. It is interesting to note that the break in the growth curve at 200 min was not noticeable in previous work[8] in which considerably less seed material was employed. The presently studied high solid:solution ratio is certainly of considerable importance since in physiological systems such as the bone-serum interface the mineral surface areas involved are very large.

The observed inflection in the growth curve probably arises through the superposition of a number of kinetic processes which take place at different rates and provides further evidence for the involvement of more than one calcium phosphate phase in the precipitation of HAP. The results may be expressed in terms of the molar ratios of calcium to phosphate $\Delta[Ca]/\Delta[P]$, which have precipitated at any instant. The data are given in Table II where $\Delta[Ca] = T_{Ca}(\text{initial}) - T_{Ca}(\text{time } t)$ and $\Delta[P] = T_p(\text{initial}) - T_p(\text{time } t)$, T_{Ca} and T_p being the total concentrations of calcium and phosphate, respectively; the uncertainty in $\Delta[Ca]/\Delta[P]$ is about ±0.05 or less. It can be seen in Table III that $\Delta[Ca]/\Delta[P]$ decreases from relatively high values during the first 20 min of reaction to the value of 1.45

Tables I and II. Negative values of S_{CaP}, S_{Ca}, and $-\Delta G$ represent undersaturation with respect to the particular phase considered. In systems II and III it was possible to control the driving force to avoid the formation of some of the calcium phosphate phases. HAP is the least soluble phase at pH 7.40 and, in the absence of kinetic complications, it should be the thermodynamically most stable.[27] The results of a typical experiment (expt 46) at relatively high supersaturation are shown in Figure 1 in which the concentration of calcium ion is plotted as a function of time following the addition of 200 mg l.$^{-1}$ of HAP seed crystals to the stable supersaturated solution. On the basis of the calculated concentrations of the calcium and phosphate ions, the ionic products of each of the calcium phosphate phases corresponding to equilibrium are also included in Figure 1. It can be seen in Figure 2 in which the driving force, $-\Delta G$, is plotted against time that the solution became undersaturated with respect to DCPD after a relatively short time (approximately 10 min) while supersaturations of OCP and TCP were maintained for about 40 and 570 min, respectively. At all states of the reaction the solution was highly supersaturated with respect to HAP.

TABLE III: Crystal Growth of Calcium Phosphate on Crystalline HAP Seed (High Supersaturation)[a]

t, min	Amt of 0.05 M KOH, ml	10^3[Ca], M	10^3[P], M	Δ[Ca]/ Δ[P]	% cryst (HAP)
0	0	1.562	0.973		100
5	1.89	1.208	0.764	1.72	
10	3.34	0.996	0.621	1.61	
20	4.64	0.812	0.477	1.51	
30	5.18	0.738	0.408	1.46	89
60	5.75	0.676	0.357	1.44	86
95	6.18	0.610	0.316	1.45	80
150	6.57	0.556	0 281	1.45	
180	6.62	0.543	0 284	1.48	68
210	6.68	0.538	0 282	1.48	77
240	6.85	0.527	0 270	1.47	
300	7.29	0.484	0.232	1.45	
360	7.63	0.427	0.209	1.48	81
420	7.93	0.396	0.197	1.50	
500	9.22	0.368	0.187	1.52	
1200	9.85	0.202	0.815	1.52	
1440	10.17	0.186	0.894	1.56	93

[a] Table I, system I; 0.2 g of speed crystals 1.$^{-1}$; 500-ml initial volume; pH 7.40, 25°; expt 46 and 47.

which remains quite constant up to about 300 min. This value was also found in previous experiments in which a considerably smaller amount of seed material was used.[8] At longer times, the ratio gradually increases but the value of 1.67 required for HAP stoichiometry was not reached even after 3 days of reaction at 25°. It is doubtful if these Δ[Ca]/Δ[P] values are useful indicators of the types of calcium phosphate phases formed since, as will be seen later, the overall precipitation reaction under the conditions of these experiments may involve not only the formation of different calcium phosphate phases but also the concomitant dissolution of a thermodynamically unstable phase formed rapidly in the initial stages of the reaction.

In order to gain more information about the nature of the calcium phosphate phases, X-ray powder diffraction and infrared investigations were made on the solid phases formed at each stage of the precipitation reaction. In Figure 3 X-ray data are shown for the solid phase taken from the crystallization cell at 60 min of reaction (expt 47), taking the precautions described to avoid preferential orientation of the crystallites. It can be seen that the positions of the peaks are identical with those of the HAP seed crystals and in none of the experiments was any X-ray evidence found for the existence of other calcium phosphate phases. The particles of such phases, if formed, were therefore too small to be detected by the X-ray diffraction method. Thus Brown and coworkers[28] have stated that lamellar mixtures of OCP and HAP are undistinguishable when the crystallites are as thin as 25–75 Å. Assuming that the grown material consists of a mixture of crystalline HAP and polymorphic forms which have the same mass absorption coefficients, the percentage crystallinity was calculated using the method of Klug and Alexander[17] on the basis of 100% crystallinity of the original HAP seed material. The data are presented in Table III which shows that the percentage crystallinity decreases for the first ~200 min following the addition of the seed crystals but thereafter increases. In the early stages of growth, the peak width increases which indicates a decrease in average particle size, most probably due to the formation of amorphous or microcrystalline precursors. At later reaction times, the peak width gradually decreases again, indicating an improvement of crystallinity of the

grown product. This is in general agreement with observations made on spontaneously precipitated phases.[4,9]

These results suggest that at the very early stages of HAP seeded growth, an amorphous phase is formed which subsequently undergoes conversion to crystalline material with an apatitic X-ray pattern. Eanes and Posner[29] have studied the spontaneous precipitation reaction and found that the rate of conversion into the crystalline phase was proportonal to the amount of the crystalline phase present; the estimated particle size was ~115 Å which is considerably smaller than in the present work. The conversion of amorphous to crystalline phase may involve an epitaxial matching of the depositing phase onto the HAP crystalline substrate and this explanation is quite consistent with the suggested autocatalytic conversion mechanism.[9,29] Because of the similarities between the structures of OCP and HAP[28] epitaxial overgrowths of these phases will easily occur. It will be particularly likely in systems such as those of the present work where rapid variation in the composition of the liquid phase occurs in the immediate vicinity of the growing crystal. The hydrolysis of OCP crystals to pseudomorphs whose properties progressively approach those of HAP takes place rapidly at temperatures above 50°.[28] At 25°, the hydrolysis reaction will be expected to be slow compared with the formation of the amorphous calcium phosphate phase.

The infrared spectra of calcium phosphate phases have been described by Fowler, Moreno, and Brown.[30] In many cases, the 3570-cm^{-1} OH stretch absorption anticipated for HAP is very weak. A possible explanation for such an effect is that some portion of the OH groups are not detected because of the poor resolution associated with the small size of crystallites of high strain content. On the other hand, the growing material may be deficient in OH since HAP is not the growth product at the early stages. Consequently, the relative intensity of the particular band may be decreasing. However, neither the HAP seed nor any of the grown solids exhibited any absorption in the 1400–1500-cm^{-1} range characteristic of the presence of carbonate. This rules out the possibility of $OH^--CO_3^{2-}$ substitution and demonstrates the effectiveness of the measures taken to exclude carbon dioxide from the system. Fowler, Moreno, and Brown[30] and Termine and Eanes[31] have suggested that the bands at 865 and 910 cm^{-1}, characteristic of OCP, may be useful for identifying OCP in the presence of HAP. In our grown materials the 910-cm^{-1} band was completely absent but there was a diffuse absorption peak at 865 cm^{-1} indicating the presence of some OCP in the samples grown at higher supersaturation (Table I, system I).

Dissolution Experiments. The data presented above (eg., Figure 1) strongly suggest that the precipitation of calcium phosphate onto crystalline HAP seed crystals is made up of a number of parallel processes. Under the conditions of higher supersaturation it is clear (Figure 2) that the formation of up to four different calcium phosphate phases is possible in the very early stages of the reaction. The Δ[Ca]/Δ[P] ratio during the first several hours of growth (~1.45) is very close to the ratio for the freshly precipitated "amorphous" calcium phosphate.[4] In order to obtain further chemical information about the nature of the early developing phases, a number of dissolution experiments have been made under conditions of controlled pH. A 50-ml sample of calcium phosphate slurry was withdrawn from the crystallization cell at a known time and quickly filtered, and the solid 10–12 mg was transferred to another cell con-
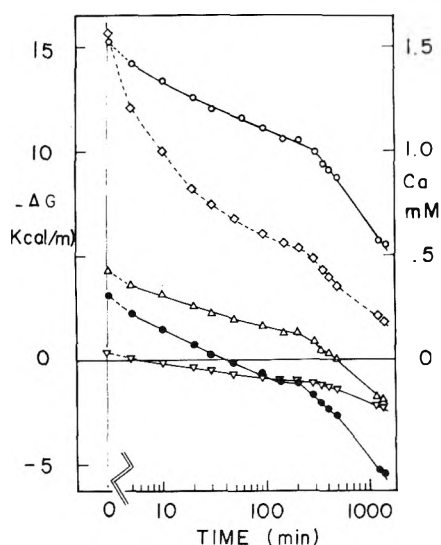
Figure 2. Plot of the driving force $(-\Delta G)$ against time for expt 46: O, total calcium concentration (right-hand ordinate); ◇, HAP; △, TCP; ●, OCP; ▽, DCPD (left-hand ordinate).
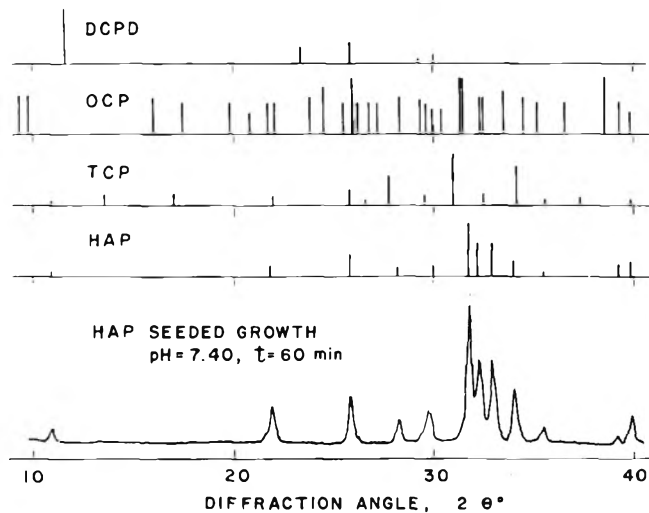
Figure 3. X-Ray powder patterns (Cu Kα radiation) for expt 47.

TABLE IV: Comparison of Precipitation and Dissolution Data (Expt 77)

	Crystal growth		Dissolution		
Time of sample with-drawal, min	10^3[Ca] depos-ited, M	Material depos-ited, Δ[Ca]/Δ[P]	10^3[Ca] after 60 min of dissoln, M	[Ca]^a after 60 min of dissoln	Dis-solved [Ca]/[P] after 60 min
30	0.764	1.53	0.335	44	1.33
70	0.858	1.48	0.276	32	1.33
140	0.947	1.49	0.267	28	1.38
240	0.976	1.48	0.296	30	1.37
300	1.046	1.49	0.200	19	1.32
360	1.088	1.50	0.191	17	1.33
1200	1.331	1.53	0.162	12	1.57

^{a} [Ca] dissolved, expressed as per cent of Ca deposited (column 2).
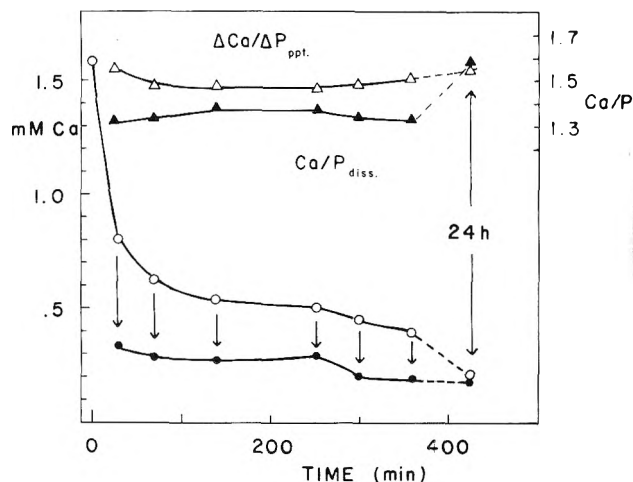
Figure 4. Growth at high supersaturation, plot of total calcium, O, and ΔCa/ΔP, △, as a function of time (expt. 77). Dissolution experiment; ▲, Ca/P in solution after 60 min; ●, T_{Ca} value after 60 min, dissolution of sample taken from growth run (O) at the given time.

taining 50 ml of a sodium chloride solution $(6 \times 10^{-3} M)$ having an ionic strength close to that in the growth cell. The pH was maintained at a value of 7.40 by means of the pH-Stat-controlled addition of $5 \times 10^{-3} M$ hydrochloric acid solution. Dissolution, which proceeded relatively rapidly, was followed for a period of 60 min at the end of which time the solid phases were separated and the solutions analyzed for calcium and phosphate.

In Table IV and Figure 4, the molar ratios of calcium to phosphate dissolved from the grown solids after 60 min are compared with the corresponding Δ[Ca]/Δ[P] growth molar ratios at the given time intervals. The calculated thermodynamic ionic products at the end of the 60-min dissolution period show that the resulting solutions were undersaturated with respect to DCPD, OCP, and TCP but supersaturated in HAP. If the dissolution reaction is allowed to proceed, after some 120 min, the pH begins to fall and a precipitation reaction takes place. However, since the composition of the solution remains undersaturated with respect to DCPD, OCP, and TCP, it follows that if these phases are present, their dissolution generates calcium and phosphate for the formation of the least soluble phase, HAP. It is interesting to note (Table IV) that the stoichi-

ometry of the dissolving phase indicates that OCP may be one of the unstable precursor phases. This is in agreement with experimental evidence that OCP is formed as the first precipitation product in the process of spontaneous precipitation.[32,33] The relative amount of the precipitated phase which dissolves with OCP stoichiometry (Table IV, column 5) decreased with time. It is significant that the corresponding dissolution [Ca]/[P] ratio for later stages of the growth process (1200 min, Table IV) is considerably larger (1.57). This indicates that by that time, OCP or DCPD were no longer available for dissolution from the surface of the grown material, having already been dissolved in the composite growth process at earlier reaction times. Therefore, the anticipated dissolution of TCP and/or HAP would lead to the observed higher dissolution [Ca]/[P] ratio.

Growth Experiments at Low Supersaturation. It is clear from the above, as has been repeatedly stressed by Brown, Moreno, and others,[5,6,27] that in studying the precipitation of calcium phosphate it is important to control the concentrations so that the degree of supersaturation of the solution with respect to the various calcium phosphate phases is defined. Frequently, the results of experiments over a wide range of supersaturations are compared with the expectation that the same calcium phosphate phases will be formed. Recently, Robertson[33] has emphasized the importance of considering the concentrations of calcium and

TABLE V: Crystal Growth of Calcium Phosphate on Crystalline HAP Seed (Low Supersaturation) [a]

t, min	Amt of 0.05 M, KOH, ml	$10^3[Ca]$, M	$10^3[P]$, M	$\Delta[Ca]/\Delta[P]$
0	0	0.432	0.287	
10	0.49	0.351	0.245	1.94
60	0.79	0.312	0.218	1.76
200	1.07	0.279	0.199	1.74
360	1.13	0.254	0.183	1.73
660	1.34	0.216	0.160	1.71
1440	1.70	0.161	0.120	1.65
2040	1.84	0.149	0.115	1.66
2880	2.00	0.132	0.106	1.67
4440	2.11	0.120	0.102	1.69
6240	2.20	0.115	0.097	1.67

[a] Table I, system II; 0.2 g of seed crystals l.$^{-1}$; 500 ml initial volume; pH 7.40, 25°; expt 79.

Figure 6. Crystal growth of calcium phosphate in the presence of sodium chloride. Plots of total calcium concentration as a function of time: $\Diamond$, no NaCl; ∇, 0.01 M NaCl; O, 0.05 M NaCl; $\square$, 0.15 M NaCl; $\triangle$, 0.4 M NaCl; ●, 0.7 M NaCl.

Figure 5. Seeded growth experiments at low supersaturation. Plot of calcium concentration against time under conditions of high supersaturation (curve a, O). Each experiment at low supersaturation (curves b–f, ●) commenced at a concentration given by the points of intersection of the curves with curve a. Curves b, d, and f are plots of total calcium concentration against time for the first 60 min in each case and curve c was continued for 100 min.

phosphate ions in studies of heterogeneous nucleation by crystals of HAP. These experiments were performed in a medium which was still supersaturated with respect to OCP. Therefore his results indicating OCP as the unstable precursor in the induced growth are not surprising and agree with the results of the present study.

The results of growth experiments made in solutions of low supersaturation (Table I, system II, undersaturated in DCPD and OCP and supersaturated with respect to TCP and HAP) are shown in Figure 5 and a typical experiment is summarized in Table V. In Figure 5, curve a (open circles) shows the crystal growth at high supersaturation (system I, Table I). Curves b–f (Figure 5) (solid circles) refer to experiments at low initial supersaturation represented by their intersection with curve a. Thus growth curve f (and Table V) refers to an ex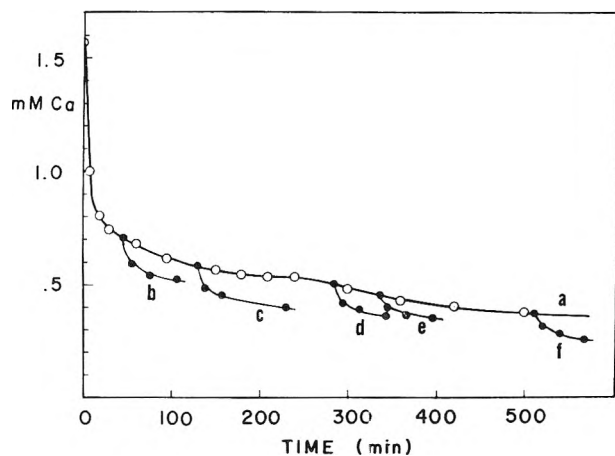periment in which HAP seed crystals were used to inoculate a solution metastable with respect to TCP and HAP (initial $T_{Ca} = 4.32 \times 10^{-4}$ M and $T_P = 2.87 \times 10^{-4}$ M pH 7.40). Crystal growth commences immediately following the addition of seed and the initial rate was estimated as $-\Delta[Ca]/\Delta t = 48$ μM min^{-1} g^{-1}. The $\Delta[Ca]/\Delta[P]$ ratios during the first 100 min for points selected from Figure 5 have an average value of 1.76 with a standard deviation of 0.1. This is considerably higher than the value required for HAP indicating the formation of a phase
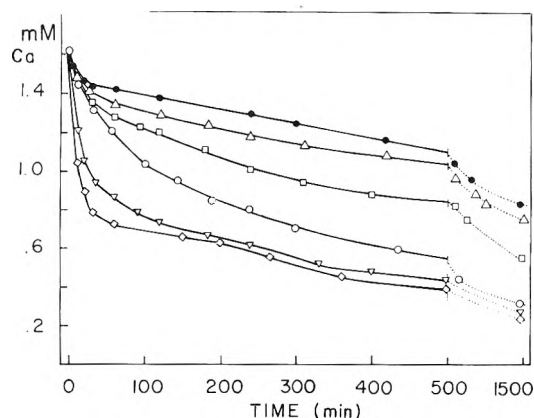
rich in calcium. This contrasts the suggestion of Bell and coworkers[34] that the surface of HAP has a tendency for preferential interaction with phosphate rather than calcium. The data in Table V show that the $\Delta[Ca]/\Delta[P]$ approaches a constant value of 1.66 after several hours of growth indicating the formation of HAP.

Clearly, under these conditions of low supersaturation, the calcium phosphates with lower calcium phosphate molar ratios, DCPD, OCP, and TCP, cannot form. Their subsequent dissolution does not, therefore, contribute to the overall $\Delta[Ca]/\Delta[P]$ values. Striking confirmation of this suggestion was provided by the results of dissolution experiments made, as described above, at a constant pH and ionic strength. The product isolated after 4 days of growth under conditions of low supersaturation, dissolved at a calcium:phosphate molar ratio of 1.69. The dissolution of HAP seed material resulted in a dissolution ratio of 1.72 and both values indicate that the grown material is HAP which undergoes congruent dissolution. The slightly elevated molar ratio as compared with the theoretical value of 1.67 may be attributed to surface phenomena and the presence of minor impurities as suggested by Avnimelech and others.[7]

Seeded Growth in the Presence of Neutral Electrolytes. In the normal crystallization runs, the pH of the supersaturated solution was maintained by the addition of 0.05 M KOH. The results of a series of experiments made using similar concentrations of LiOH, NaOH, CsOH, and NH$_4$OH showed that the kinetic rate curves had the typical shape shown in Figure 1 with the characteristic inflection of about 200 min of growth irrespective of which base was used. The effect of adding "neutral" electrolyte to the system is, however, marked and the results of crystallization experiments in the presence of different concentrations of sodium chloride are shown in Figure 6. A study by Bell and his coworkers[34] has shown that the point of zero change (PZC) of HAP suspensions is dependent upon the composition of the ionic medium. Although the PZC of the amorphous calcium phosphate precursor is not known, it is also likely that it will be dependent upon both the nature of the supporting medium and the history of the sample formation. The added electrolyte may therefore induce coagulation of the particles in a manner analogous to the classical colloid coagulation observed in so many systems.[35] Another influence of the added electrolyte is to decrease the effective supersaturation by reducing the activity coefficients of
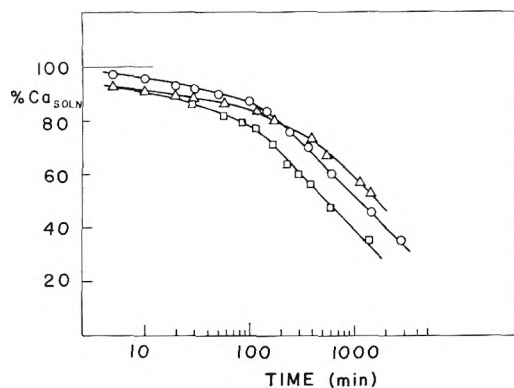
Figure 7. Crystal growth in the presence of 0.15 M potassium ($\triangle$), cesium ($\bigcirc$), and sodium ($\square$) chlorides. Plots of per cent of total calcium concentration against time.

the lattice ions in the solution. This is clearly illustrated in Table I (system III). It can be seen in Figure 6 that the addition of sodium chloride markedly decreases the rate of crystallization and it is interesting to note that the discontinuity characteristic of the high-supersaturation experiments (Figure 1) is absent. This result is consistent with the proposal that the sodium chloride simply reduces the driving force for reaction since at an ionic strength of 0.15 M, DCPD and OCP do not form. It is the concomitant dissolution of such phases in the early stages of reaction which appears to account for the observed inflection in the growth curves.

Crystal growth experiments were made in 0.15 M lithium, potassium, cesium, and ammonium chlorides. The data for potassium, cesium, and sodium chlorides are presented in Figure 7. It can be seen that there is a marked effect on changing the nature of the alkali metal cation. Toward the end of the reaction (1000 min) the extent of crystal growth increases in the order KCl < CsCl < NH_4Cl < LiCl < NaCl. The greatest differences are found between potassium and sodium chlorides which are of particular importance in biological systems. After 1000 min of growth 60% of the calcium is precipitated in the sodium chloride system whereas only 40% has deposited in the presence of potassium chloride. After 24 hr of reaction, $\Delta[Ca]/\Delta[P]$ values are 1.45 and 1.61 for NaCl and KCl, respectively. The precipitated solids at these extended times contained from 5.5 to 6.0 mol % of sodium in the presence of sodium chloride but almost no potassium in the presence of potassium chloride. These results are in good agreement with those of Newman and coworkers,[36] who found that sodium can replace calcium in the calcium phosphate solid whereas potassium is reversibly adsorbed on the surface.

Bell and coworkers[34] have shown that the point of zero change of HAP occurs at pH 7.5 in the presence of sodium chloride and at pH 8.4 in potassium chloride systems. In the present experiments, at pH 7.40 an HAP surface would be appreciably positively charged in the potassium chloride solution leading to a lower rate of crystallization. Unfortunately, no electrokinetic data are yet available for the "amorphous" calcium phosphate phase for which, being more colloidal, different factors may be of importance. It is interesting to note that X-ray powder patterns of solids grown in the presence of 0.15 M sodium or potassium chloride for 120, 240, or 1440 min show no change from that of the HAP seed crystals. This indicates that the formation of the "amorphous" precursor is undetectable under these

conditions in contrast to the results at an effectively higher supersaturation. This finding is in agreement with the results of the growth experiments made at low supersaturation.

It is clear from the results of the present work that the concentrations of lattice ions in supersaturated solutions of calcium phosphate are very important in determining the nature of the calcium phosphate phase which separates on the addition of HAP seed crystals. Indeed, the type of phase formed may be influenced by careful control of the physicochemical conditions. This finding may be important in understanding mineralization in biological systems for which the supersaturation is low and the solid:solution ratio is very appreciable. The matrix of young bone contains a major proportion of an amorphous inorganic component[37] whose formation is frequently attributed to the presence of a variety of potential crystal growth inhibitors in the body fluids. Unfortunately studies of model systems are usually made in media of very high supersaturation in order to provide appreciable measurable concentration changes. In the light of the present results, the reaction path may be markedly altered under such conditions. The use of low concentration levels is certainly more tedious and experimentally demanding but such studies may be closer to those in real biological systems.

References and Notes

(1) On leave of absence from Rudjer Boskovic Institute, Zagreb, Yugoslavia.
(2) (a) M. D. Francis, *Ann. N. Y. Acad. Sci.*, **131**, 694 (1965); (b) H. M. Rootare, V. R. Deitz, and F. Carpenter, *J. Colloid Sci.*, **17**, 179 (1962).
(3) W. F. Newman and M. W. Newman, *Chem. Rev.*, **53**, 1 (1953).
(4) E. D. Eanes, I. H. Gillessen, and A. S. Posner, *Nature (London)*, **298**, 365 (1965).
(5) W. E. Brown, *Clin. Orthop.*, **44**, 5318 (1966).
(6) E. C. Moreno, T. M. Gregory, and W. E. Brown, J. *Res. Nat. Bur. Stand.*, *Sect. A*, **72**, 773 (1968).
(7) Y. Avnimelech, E. C. Moreno, and W. E. Brown, *J. Res. Nat. Bur. Stand., Sect. A*, **77**, 149 (1973).
(8) G. H. Nancollas and M. S. Mohan, *Arch. Oral Biol.*, **15**, 731 (1970).
(9) A. L. Boskey and A. S. Posner, *J. Phys. Chem.*, **77**, 2313 (1973).
(10) J. M. Holmes and R. A. Beebe, *Calcif. Tissue Res.*, **7**, 163 (1971).
(11) G. H. Nancollas and N. Purdie, *Quart. Rev., Chem. Soc.*, **18**, 1 (1964).
(12) R. W. Marshall and G. H. Nancollas, *J. Phys. Chem.*, **73**, 3838 (1969).
(13) G. H. Nancollas and J. S. Wefel, *J. Crystal Growth*, in press.
(14) G. H. Nancollas and R. W. Marshall, *J. Dent. Res.*, **50**, 1268 (1971).
(15) R. G. Bates, "Determination of pH," Wiley, New York, N. Y., 1963.
(16) D. N. Fogg and N. T. Wilkinson, *Analyst (London)*, **83**, 403 (1958).
(17) H. P. Klug and L. E. Alexander, "X-Ray Diffraction Procedures," Wiley, New York, N. Y., 1962.
(18) M. D. Francis, *Calcif. Tissue Res.*, **3**, 151 (1969).
(19) Powder Diffraction File No. 9-432, Joint Committee of Powder Diffraction Standards, Philadelphia, Pa., 1967.
(20) E. C. Moreno, T. M. Gregory, and W. E. Brown, *J. Res. Nat. Bur. Stand., Sect. A*, **70**, 545 (1966).
(21) E. C. Moreno, W. E. Brown, and G. Osborn, *Soil Sci. Soc. Amer.*, **24**, 99 (1960).
(22) E. C. Moreno in "Structural Properties of Hydroxyapatite and Related Compounds," W. E. Brown and R. A. Young, Ed., Gordon and Breach, New York, N. Y., Chapter 14, in press.
(23) J. S. Clark, *Can. J. Chem.*, **33**, 1696 (1955).
(24) W. Stumm and J. J. Morgan, "Aquatic Chemistry," Wiley-Interscience, New York, N. Y., 1970.
(25) G. H. Nancollas, "Interactions in Electrolyte Solutions," Elsevier, Amsterdam, 1966.
(26) C. W. Davies, "Ion Association," Butterworths, London, 1962.
(27) W. E. Brown in "Environmental Phosphorus Handbook," E. J. Griffith, A. Beeton, J. M. Spencer, and D. T. Mitchell, Ed., Wiley, New York, N. Y., 1973.
(28) W. E. Brown, J. P. Smith, J. R. Lehr, and A. W. Frazier, *Nature (London)*, **196**, 1048 (1962).
(29) E. D. Eanes and A. S. Posner, *Trans. N. Y. Acad Sci.*, **28**, 233 (1965).
(30) B. O. Fowler, E. C. Moreno, and W. E. Brown, *Arch. Oral Biol.*, **11**, 477 (1966).

(31) J. D. Termine and E. D. Eanes, *Calcif. Tissue Res.*, **10**, 171 (1972).
(32) H. Furedi-Milhofer, B. Purgaric, L. Brecevic, and N. Pavkovic, *Calcif. Tissue Res.*, **8**, 142 (1971).
(33) W. G. Robertson, *Calcif. Tissue Res.*, **11**, 311 (1973).
(34) J. C. Bell, A. M. Posner, and J. P. Quirk, *J. Colloid Interface Sci.*, **42**, 250 (1973).

(35) B. Tezak, E. Matijevic, and K. Schulz, *J. Phys. Colloid Chem.*, **55**, 1567 (1951).
(36) W. F. Newman, T. Y. Toribara, and B. J. Mulryan, *Arch. Biochem. Biophys.*, **98**, 384 (1962).
(37) R. A. Robinson and M. L. Watson, *Ann. N. Y. Acad. Sci.*, **60**, 596 (1955).

Kinetics of the Reaction between Triplet Benzophenone and Diphenylamine. An Electron Spin Resonance Study

James H. Marshall

Bell Laboratories, Murray Hill, New Jersey 07974 (Received January 30, 1974; Revised Manuscript Received June 13, 1974)

Publication costs assisted by Bell Laboratories

Well-resolved esr spectra of the diphenylamino radical are detected upon the uv irradiation of benzene solutions of benzophenone and diphenylamine. The diphenylamino radicals are presumed to arise from hydrogen atom abstraction by triplet benzophenone. Using naphthalene as a triplet quencher, the rate of this initial reaction is found to be $2.3 \times 10^9 \ M^{-1}$ sec^{-1} or nearly diffusion controlled. Because substantial overall reversible character is apparent during steady photolysis, while the initial reaction appears to be irreversible, a series of reactions is proposed in order to regenerate the starting materials.

Introduction

Although the esr spectra of many related radicals have been reported,[1-3] until recently the spectrum of the diphenylamino radical (Ph$_2$N·)[4] had not been clearly identified. Hoskins[5] heated solutions of tetraphenylhydrazine (Ph$_2$NNPh$_2$), but observed only diphenyl nitroxide and another spectrum which he attributed to a hydrazyl radical. Das, *et al.*,[6] made an extensive esr study of Ph$_2$NNPh$_2$ derived radicals but apparently did not detect Ph$_2$N·. Pannell,[7] although initially reporting Ph$_2$N·, later realized he had observed only diphenyl nitroxide upon the photolysis of diphenylamine (Ph$_2$NH) in *tert*-butyl peroxide. Finally Neugebauer and Fischer[2] recorded the isotropic esr spectra of a series of diarylamino radicals, and subsequently Neugebauer and Bamberger[4] detected the Ph$_2$N· spectrum during the photolysis of Ph$_2$NNPh$_2$ in benzene solution.

Tetraarylhydrazines thermally dissociate into diarylamino radicals in solution, and they are slowly destroyed by disproportionation and polymerization.[8] The photolytic dissociation products of Ph$_2$NNPh$_2$ yield spectra with maxima at 450 and 720 nm.[9-12] By flash photolyzing benzene solutions of Ph$_2$NNPh$_2$ at room temperature, Shida and Kira[9] observed that both absorptions decay by second-order kinetics with a rate constant estimated to be $2.5 \times 10^7 \ M^{-1}$ sec^{-1}.

Benzophenone (Ph$_2$CO) is efficiently photoexcited to a highly reactive n–π* triplet state (Ph$_2$CO(T$_1$))[13,14] which can disappear by various processes including chemical reaction.[15] Naphthalene (C$_{10}$H$_8$), with a triplet energy level substantially lower than that of Ph$_2$CO(T$_1$), quenches Ph$_2$CO(T$_1$) at a diffusion-controlled rate and thereby measurably inhibits most chemical reactions involving Ph$_2$CO(T$_1$).[19]

Reactions between photoexcited ketones and amines have been recently reviewed by Cohen, *et al.*[20] Results suggest efficient quenching of Ph$_2$CO(T$_1$) by amines facilitated by some initial degree of charge-transfer between Ph$_2$CO(T$_1$) and amine.[21-26] Accompanying this high quenching rate is a low quantum yield for photoreduction of Ph$_2$CO.

The rate of Ph$_2$CO(T$_1$) quenching by Ph$_2$NH in 2-propanol is nearly diffusion controlled ($k = 4.3 \times 10^9 \ M^{-1}$ sec^{-1}),[23] and Ph$_2$CO's photoreduction in 2-methyl-2-propanol and acetonitrile by Ph$_2$NH is slow, although producing a high percentage of 4-(*N*-phenylamino)phenyldiphenylmethanol and little 1,1,2,2-tetraphenyl-1,2-ethanediol. In benzene solution no photoproducts were detected.[24] Reversible charge-transfer was invoked to account for the apparent high degree of reversibility in 2-methyl-2-propanol and acetonitrile.

Davidson, *et al.*,[25] confirmed the low yield of isolatable products from the photolysis of Ph$_2$CO and Ph$_2$NH. By flash techniques they determined that the hydroxydiphenylmethyl radical (Ph$_2$ĊOH) was produced, and that at low concentrations of Ph$_2$CO ($5 \times 10^{-3} \ M$) and of aniline, *o*-toluidine, or Ph$_2$NH (*ca.* $10^{-2} \ M$), Ph$_2$ĊOH decayed by a first-order mechanism. They postulated that Ph$_2$ĊOH was reacting with Ph$_2$NH. Although unable to determine if Ph$_2$N· was produced along with Ph$_2$ĊOH, they did report that when benzene, 2-methyl-2-propanol, and acetonitrile solutions of Ph$_2$CO and aniline were flashed, only Ph$_2$ĊOH and anilino radicals, and no radical ions, were detected. The anilino radical decay was second order.

Experimental Section

The esr spectrometer is a Varian X-band system using

100-kHz field modulation. A Fieldial regulator, a Nicolet 1072 signal averager, a Hewlett-Packard 2590A microwave frequency converter and 5245L electronic counter, and a field tracking nmr fluxmeter comprise the major assessories.

Benzophenone (reagent grade) was used as supplied and diphenylamine was recrystallized from H_2O–ethanol. 4-Hydroxy-2,2,6,6-tetramethylpiperidinooxy was prepared from the amine (Aldrich Chemical Co., Inc.) by H_2O_2 oxidation.[27] Tetraphenylhydrazine[28] was recrystallized from ethanol–toluene yielding colorless crystals, and solvents were purified by standard procedures.

Most of the measurements required monitoring the centerline of the $Ph_2N\cdot$ esr spectrum and can be divided into two categories, the long-term (hours) and short-term photolysis (minutes) of individual samples. For all experiments solutions were placed in 9 in. 3 mm i.d. quartz sample tubes. Nitrogen was blown through the quartz dewar insert in the microwave cavity to minimize sample heating during illumination, and sample temperatures were 23 ± 1°. The output of an Osram HBO 200W mercury lamp was focused on the cavity with quartz lenses, and the microwave power was maintained well below the saturation level for $Ph_2N\cdot$.

In order to study the rate of long-term photolytic decomposition, tubes were filled with 1 in. of solution (about 10^{-2} M in either Ph_2NNPh_2 or Ph_2CO and Ph_2NH), degassed by freeze–thaw cycles on a vacuum line, sealed in vacuo, and photolyzed in situ for periods up to 4 hr. During this period the peak-to-peak height of the centerline was determined at appropriate intervals by recording the central 2.5 G of the $Ph_2N\cdot$ spectrum.

For the short-term photolyses, tubes were filled with 3 in. of argon degassed solution, stoppered, and immediately photolyzed. In order to obtain decay curves, the magnetic field was stabilized at the positive peak of the centerline, and trigger pulses for the signal averager sweep were generated by a photodetector which recorded each revolution of a rotating sector situated between the uv source and the cavity. Although the decay curves thus obtained were decidedly more second order than first order, the method relied upon for determination of the order of decay was variation of the peak-to-peak height of the centerline with light intensity. Calibrated wire mesh screens were used for this purpose. Radical concentrations were determined by comparison with a 2.3×10^{-6} M benzene solution of 4-hydroxy-2,2,6,6-tetramethylpiperidinooxy.

For the remaining short-term experiments, i.e., those involving benzene solutions of Ph_2CO, Ph_2NH, and $C_{10}H_8$, tubes were similarly filled with 3 in. of argon degassed solution, stoppered, and immediately photolyzed. The central 2.5 G of the spectrum was recorded to determine the peak-to-peak height of the centerline. In addition a Corning 4-69 glass filter, with negligible transmission below 320 nm, was used to minimize light absorpion by $C_{10}H_8$,[29] while transmitting most of the 350-nm band of Ph_2CO.[30]

Results and Discussion

Neugebauer and Bamberger[4] detected the esr spectrum of $Ph_2N\cdot$ during the photolysis of a 0.2 M benzene solution of Ph_2NNPh_2 in a flow system. We have obtained a similar spectrum with improved resolution (line width = 80 mG vs. 350 mG) by photolyzing 10^{-2} M Ph_2NNPh_2 in benzene or toluene solution at room temperature. Direct interpretation of this spectrum yields hyperfine couplings (a_N = 8.82 ± 0.05 G (1 N), a_H = 3.67 ± 0.03 G (4 H), a_H = 1.52 ± 0.03
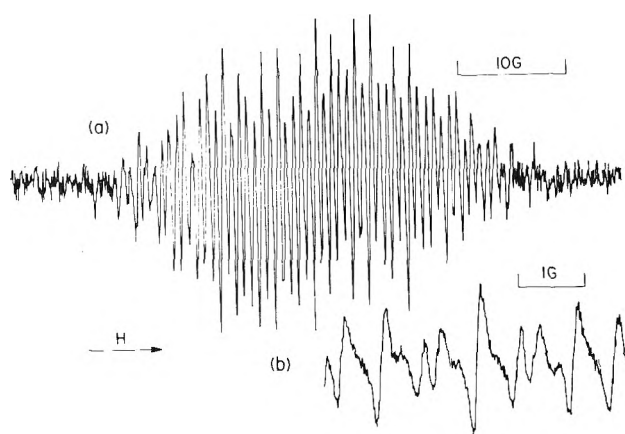
Figure 1. Esr spectra of $Ph_2N\cdot$ recorded during the photolysis of a benzene solution of Ph_2CO and Ph_2NH: (a) complete spectrum overmodulated; (b) center of spectrum at high resolution.

G (4 H), and α_H = 4.24 ± 0.03 G (2 H)) which agree with previous work.[4] The g value is 2.0032 ± 0.0001. The esr signal intensity was proportional to the square root of the light intensity (I) and under steady uv illumination decreased 50% in about 5 min. The transient decay was second order, and calibration with the nitroxide reference gave a second-order rate constant of $(1.2 ± 0.3)10^8$ M^{-1} sec^{-1}. For the same reaction, Shida and Kira[9] reported a rate constant based on optical measurements which was a factor of 5 smaller. The difference presumably lies in the method used to determine radical concentrations. While esr measurements are more reliable in this respect, our error in the above rate constant stems almost entirely from this very problem.

An equally well-resolved esr spectrum of $Ph_2N\cdot$ was found upon photolyzing mixtures of Ph_2CO and Ph_2NH in benzene, toluene, or n-hexane. Photolysis of Ph_2NH alone yields no signal. Under steady illumination $[Ph_2N\cdot]$ decreased 50% in about 30 min when both Ph_2CO and Ph_2NH were 10^{-2} M in benzene. $[Ph_2N\cdot]$, typically 10^{-6} M, was proportional to $I^{1/2}$ and $[Ph_2CO]^{1/2}$ and independent of $[Ph_2NH]$ for 10^{-3} M < $[Ph_2NH]$ < 8×10^{-2} M. For $[Ph_2NH]$ < 10^{-3} M, the steady-state condition was too brief for accurate measurements. The esr signal was quenched by $C_{10}H_8$. Rotating sector photolysis gave a second-order decay curve and a rate constant of $(5.0 ± 1.0)10^7$ M^{-1} sec^{-1}.

Careful line by line comparison of the high-resolution esr spectra of $Ph_2N\cdot$ obtained by the two methods afforded no evidence of radicals other than $Ph_2N\cdot$. However, at high magnetic field modulations, stable radicals (not diphenyl nitroxide) were occasionally detected in the Ph_2CO–Ph_2NH mixtures when the light was turned off after a brief photolysis. In addition the overmodulated $Ph_2N\cdot$ spectrum from the photolysis of Ph_2NNPh_2 and the overmodulated spectrum from the Ph_2CO–Ph_2NH mixtures were different. The latter spectrum can be interpreted as a spectrum superimposed on the former at about the same g value.

For our purposes the initial reactions may be formulated as

$$Ph_2CO + I(h\nu) \xrightarrow{k_*} Ph_2CO(T_1) \qquad (1)$$

$$Ph_2CO(T_1) + Ph_2NH \xrightarrow{k_r} Ph_2\overset{\cdot}{C}OH + Ph_2N\cdot \qquad (2)$$

and

$$Ph_2CO(T_1) \xrightarrow{k_d} Ph_2CO \qquad (3)$$
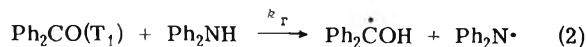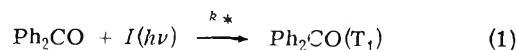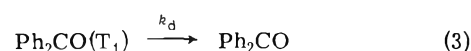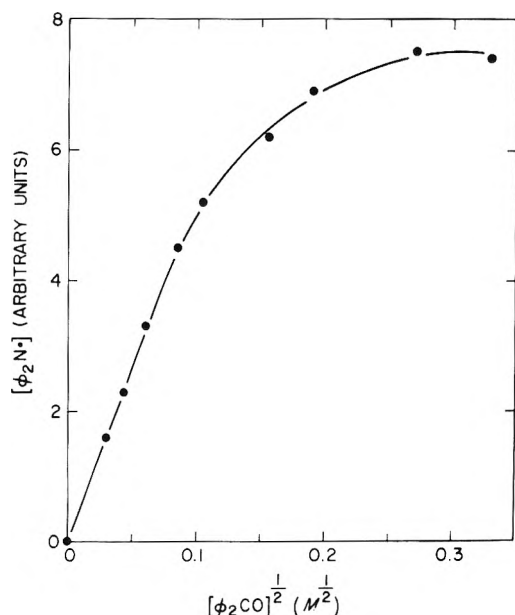
Figure 2. $[Ph_2N \cdot]$ vs. $[Ph_2CO]^{1/2}$ for $[Ph_2NH] = 3.34 \times 10^{-2}$ M.
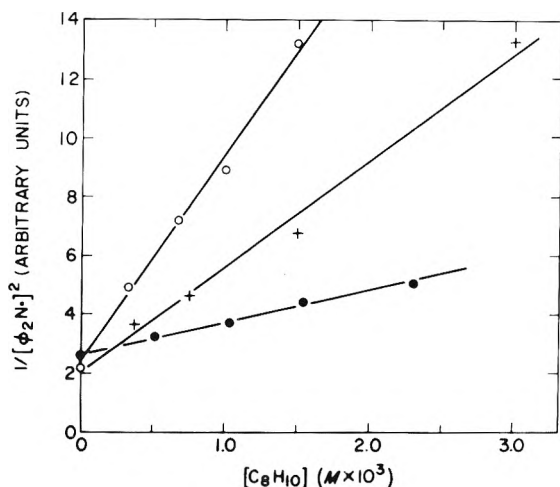
Figure 3. $1/[Ph_2N \cdot]^2$ vs. $[C_{10}H_8]$ for $[Ph_2CO] = 1.20 \times 10^{-2}$ M and the following $[Ph_2NH]$: 5.00×10^{-3} M (O), 1.00×10^{-2} M (+), and 3.00×10^{-2} M (●).

While $Ph_2\dot{C}OH$ has been photolytically generated from Ph_2CO and aliphatic amines to give excellent high-resolution esr spectra in toluene solutions,[31] one could explain its absence in our case by noting that the rate of dimerization of $Ph_2\dot{C}OH$ (2×10^9 M^{-1} sec^{-1})[32] is an order of magnitude greater than that of $Ph_2N \cdot$ (1.2×10^8 M^{-1} sec^{-1}).

In a simple dimerization scheme, one might propose in addition to (1), (2), and (3)

$$2Ph_2N \cdot \xrightarrow{k_4} Ph_2NNPh_2 \qquad (4)$$

$$2Ph_2\dot{C}OH \longrightarrow Ph_2C(OH)C(OH)Ph_2 \qquad (5)$$

and perhaps

$$Ph_2NNPh_2 + I(h\nu) \longrightarrow 2Ph_2N \cdot \qquad (6)$$
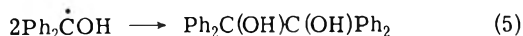
One may reject (6) as important because $[Ph_2N \cdot]$ is proportional to $[Ph_2CO]^{1/2}$.

For the above scheme, the rate of disappearance of Ph_2CO may be estimated from k_4 and the steady-state

concentration of $Ph_2N \cdot$, $d[Ph_2N \cdot]/dt = k_4[Ph_2N \cdot]^2 \approx 1.2 \times 10^{-4}$ M sec^{-1}. For 30 min of steady photolysis, a 0.2 M solution of Ph_2NH (or Ph_2CO) would be consumed, and this contradicts our experimental results.

The long sample life strongly suggests a reaction in which Ph_2CO is regenerated, i.e., (4) and (5) cannot represent the major reaction termination sequence. An alternative scheme is suggested by the results of others,[23-25] and in accord with the proposals of Davidson, et al.,[25] we favor the reaction sequence

$$Ph_2\dot{C}OH - Ph_2NH \xrightarrow{k_7} X \cdot \qquad (7)$$

$$X \cdot + Ph_2N \cdot \xrightarrow{k_8} Ph_2CO + 2Ph_2NH \qquad (8)$$
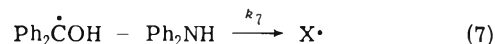
where $X \cdot$ is an unidentified radical.

Steady-state analysis of (1), (2), (3), (7), (8), and

$$Ph_2CO(T_1) + C_{10}H_8 \xrightarrow{k_q} Ph_2CO + C_{10}H_8(T_1) \qquad (9)$$
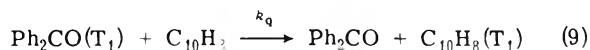
yields

$$[Ph_2N \cdot]^2 = \frac{k_* k_r I [Ph_2CO][Ph_2NH]}{K_8(k_r[Ph_2NH] + k_q[C_{10}H_8] + k_d)} \times \left(1 + \frac{[Ph_2\dot{C}OH]}{[Ph_2N \cdot]}\right) \qquad (10)$$

and

$$[Ph_2\dot{C}OH]/[Ph_2N \cdot] = k_8[Ph_2N \cdot]/k_7[Ph_2NH] \qquad (11)$$

If k_7 and k_8 are of similar magnitude, the absence of $Ph_2\dot{C}OH$ is explained. On the other hand, one then requires that $[X \cdot] \approx [Ph_2N \cdot]$ suggesting that $X \cdot$ is present although its esr spectrum is not observed. Reaction 8 would also account for the two different second-order rate constants with the slower 5.0×10^7 M^{-1} sec^{-1} rate assignable to k_8.

Figures 2–4 indicate that (1), (2), (3), and (7)–(10) are consistent with experiment. High concentration deviations are attributable to internal filtering and nonuniform sample illumination. From (10), the slopes of Figure 3, and the known values for k_q (3.6×10^9 M^{-1} sec^{-1})[19] and k_d (10^5 sec^{-1}),[32,33] k_r is calculated as $(2.3 \pm 0.2)10^9$ M^{-1} sec^{-1}. $k_r < k_q$ by only 35%. The molecular volume of Ph_2NH being larger than that of $C_{10}H_8$ suggests that the diffusion of Ph_2NH in benzene should be the slower of the two. If this is true and assuming that (9) is diffusion controlled,[19] one may infer that (2) is almost diffusion controlled.

Figure 4. $1/[Ph_2N \cdot]^2$ vs. $1/[Ph_2NH]$ for $[Ph_2CO] = 1.20 \times 10^{-2}$ M and $[C_{10}H_8] = 1.50 \times 10^{-2}$ M.

Examining (10) further, one notes that when the condition $k_d < k_r$ [Ph$_2$NH] is fulfilled, the steady-state [Ph$_2$N·] should be independent of [Ph$_2$NH] in the absence of $C_{10}H_8$. Since $k_r = 2.3 \times 10^9 \ M^{-1}$ sec^{-1}, the critical value of [Ph$_2$NH] is about $5 \times 10^{-5} \ M$. However, as [Ph$_2$NH] is decreased below approximately $10^{-3} \ M$, sample decomposition affects [Ph$_2$N·] before Ph$_2$CO(T$_1$) decay, and the critical [Ph$_2$NH] cannot be confirmed. Ph$_2$N· was barely detectable for [Ph$_2$NH] $\approx 5 \times 10^{-5} \ M$ and [Ph$_2$CO] $= 1.2 \times 10^{-2} \ M$.

High-resolution (line width $= 40$ mG) esr spectra of Ph$_2$ĊOH have been observed in toluene and other solvents and in the presence of various aliphatic amines.[31,34] The g values were approximately 2.0030. Assisted by these results we should have detected Ph$_2$ĊOH in a comparison of high-resolution spectra if (4) and (5) were correct. Furthermore, since a high-resolution spectrum is expected for Ph$_2$ĊOH, the broad resonance cannot be ascribed to it.

Because our results give little information concerning the identity of X·, we can only speculate that the 4-(N-phenylamino)phenyldiphenylmethanol isolated by Pac, et al.,[24] may be a clue. This reaction product might result from a precursor such as

PhNH—⟨ ⟩·—C(OH)Ph$_2$ / H

by the reactions

$$ \text{Ph·ĊOH} + \text{Ph}_2\text{NH} \longrightarrow \text{PhNH—⟨ ⟩—C(OH)Ph}_2 \text{ / H} \qquad (12) $$

and

$$ \text{PhNH—⟨ ⟩—C(OH)Ph}_2 \text{ / H} + \text{Ph}_2\text{N·} \longrightarrow $$

$$ \text{PhNH—⟨ ⟩—C(OH)Ph}_2 + \text{Ph}_2\text{NH} \qquad (13) $$
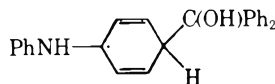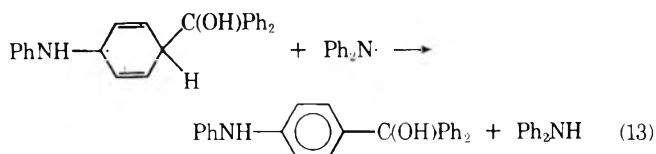
with (13) then competing with regeneration reaction (8)

$$ \text{PhNH—⟨ ⟩—C(OH)Ph}_2 \text{ / H} + \text{Ph}_2\text{N·} \xrightarrow{k_*} \text{Ph}_2\text{CO} + 2\text{Ph}_2\text{NH} $$
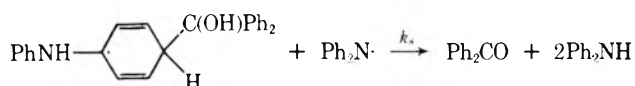
Summary

Well-resolved esr spectra of the Ph$_2$N· radical are detected upon the uv irradiation of benzene solutions of Ph$_2$CO and Ph$_2$NH. The Ph$_2$N· radicals are presumed to arise from hydrogen atom abstraction by Ph$_2$CO(T$_1$). Using naphthalene as a triplet quencher, the rate of this initial reaction is found to be $2.3 \times 10^9 \ M^{-1}$ sec^{-1} or nearly diffusion controlled.

For subsequent reactions, the undetectable Ph$_2$ĊOH radical and the relatively long sample lifetime under steady illumination imply a significant recycling, as opposed to consumption of the starting materials in a simple dimerization scheme. From the observed second-order decay of

Ph$_2$N· under transient illumination and the absence of Ph$_2$ĊOH, the formation of a radical adduct between Ph$_2$ĊOH and Ph$_2$NH is inferred. The adduct's identity is uncertain, although it may be responsible for a broad background esr spectrum superimposed upon that of the Ph$_2$N· radical. The adduct's reaction with Ph$_2$N· regenerates the starting materials and accounts for the second-order decay of Ph$_2$N·.

References and Notes

(1) A. T. Balaban, P. T. Frangopol, M. Frangopol, and N. Negoita, *Tetrahedron*, **23**, 4661 (1967).
(2) F. A. Neugebauer and P. H. H. Fischer, *Chem. Ber.*, **98**, 844 (1965).
(3) F. A. Neugebauer and H. Fischer, *Angew. Chem.. Int. Ed. Engl.*, **10**, 732 (1971).
(4) F. A. Neugebauer and S. Bamberger, *Angew. Chem., Int. Ed. Engl.*, **10**, 71 (1971).
(5) R. Hoskins, *J. Chem. Phys.*, **25**, 788 (1956).
(6) M. R. Das, A. V. Patankar, and B. Venkataramen, *Proc. Indian Acad. Sci., Sect. A*, **53**, 273 (1961).
(7) (a) J. Pannell, *Mol. Phys.*, **5**, 291 (1962); (b) J. Pannell, *ibid.*, **7**, 317 (1964).
(8) For a review of the chemistry of tetraarylhydrazines and of diarylamino and related radicals see the book by A. R. Forrester, J. M. Hay, and R. H. Thomson, "Organic Chemistry of Stable Free Radicals," Academic Press, New York, N.Y., 1968, pp 111–136.
(9) T. Shida and A. Kira, *J. Phys. Chem.*, **73**, 4315 (1969).
(10) D. A. Wiersma and J. Kommandeur, *Mol. Phys.*, **13**, 241 (1967).
(11) D. A. Wiersma, J. H. Lichtenbelt, and J. Kommandeur, *J. Chem. Phys.*, **50**, 2794 (1969).
(12) V. Franzen, *Justus Liebigs Ann. Chem.*, **604**, 251 (1957).
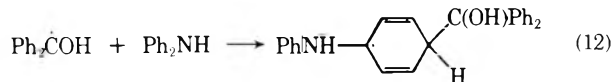(13) H. L. J. Backstrom and K. Sandros, *Acta Chem. Scand.*, **14**, 48 (1960).
(14) (a) G. Porter and F. Wilkinson, *Trans. Faraday Soc.*, **57**, 1686 (1961); (b) G. Porter and F. Wilkinson, *Proc. Roy. Soc., Ser. A*, **264**, 1 (1961).
(15) Pertinent literature on the photochemistry of benzophenone prior to 1968 has been reviewed in three books on the general topic of photochemistry. See ref 16, 17, and 18.
(16) N. J. Turro, "Molecular Photochemistry," W. A. Benjamin, New York, N.Y., 1965.
(17) J. G. Calvert and J. N. Pitts, Jr., "Photochemistry," Wiley, New York, N.Y., 1966.
(18) A. A. Lamola and N. J. Turro, "Energy Transfer and Organic Photochemistry," Interscience, New York, N.Y., 1969.
(19) W. M. Moore and M. Ketchum, *J. Amer. Chem. Soc.*, **84**, 1368 (1962).
(20) S. G. Cohen, A. Parola, and G. H. Parsons, Jr., *Chem. Rev.*, **73**, 141 (1973).
(21) (a) R. S. Davidson and P. F. Lambeth, *Chem. Commun.*, 1265 (1967); (b) R. S. Davidson and P. F. Lambeth, *ibid.*, 511 (1968).
(22) R. S. Davidson, P. F. Lambeth, J. F. McKellar, and P. H. Turner, *Chem. Commun.*, 732 (1969).
(23) M. Santhanam and V. Ramakrishnan, *Chem. Commun.*, 344 (1970).
(24) C. Pac, H. Sakurai, and T. Tosa, *Chem. Commun.*, 1311 (1970).
(25) R. S. Davidson, P. F. Lambeth, and M. Santhanam, *J. Chem. Soc., Perkin Trans. 2*, 2351 (1972).
(26) J. B. Guttenplan and S. G. Cohen, *J. Amer. Chem. Soc.*, **94**, 4040 (1972).
(27) E. G. Rozantsev, *Izv. Akad. Nauk SSSR, Ser. Khim.*, 2187 (1964).
(28) The tetraphenylhydrazine, supplied by E. A. Chandross of this laboratory, was prepared by the procedure described in the book by C. Weygand, "Organic Preparations," Interscience, New York, N.Y., 1945, p 244.
(29) I. B. Berlman, "Handbook of Fluorescence Spectra of Aromatic Molecules," Academic Press, New York, N.Y., 1965, p 104.
(30) Reference 17, p 378.
(31) R. S. Davidson and R. Wilson, *J. Chem. Soc. B*, 71 (1970).
(32) J. A. Bell and H. Linshitz, *J. Amer. Chem. Soc.*, **85**, 528 (1963).
(33) W. M. Moore, G. S. Hammond, and R. P. Foss, *J. Amer. Chem. Soc.*, **83**, 2789 (1961).
(34) R. Wilson, *J. Chem. Soc. B*, 84 (1968).

A Technique for the Determination of Absolute Emission Quantum Yields of Powdered Samples

Mark S. Wrighton,* **David S. Ginley, and David L. Morse**

Department of Chemistry, Massachusetts Institute of Technology, Cambridge, Massachusetts 02139

(Received January 10, 1974; Revised Manuscript Received August 1, 1974)

A technique is described for the determination of absolute emission quantum yields of powdered samples using a conventional scanning emission spectrophotometer. The technique is applied to the determination of the luminescence yields of National Bureau of Standards phosphors, sodium salicylate, tetrahalomanganese(II) complexes, $ClRe(CO)_3$(1,10-phenanthroline), $Ru(2,2'-bipyridine)_3^{2+}$, and bis(diphosphine) complexes of Rh(I) and Ir(I). Measurement of absolute emission yields involves (1) determining the diffuse reflectance of the sample relative to a nonabsorbing standard at the excitation wavelength, and then (2) measuring the emission of the sample under the same conditions. The quantum yield for emission is then the ratio of the emitted photons to the difference in the number of diffuse reflected photons from the sample and the nonabsorbing standard. The only calibration necessary is to determine the relative detector response at the excitation and emission wavelengths. The technique gives yields estimated to be ±25%, and the validity of the technique has been established by comparison of yields previously obtained for phosphors; by obtaining point-by-point reflectance spectra of powdered samples; and by demonstration that the luminescence quantum yields are independent of the fraction of incident light absorbed by the sample.

Introduction

Experimental study of the excited state decay of metal complexes has included largely measurement of the quantum efficiency for chemical change[1] and emission lifetime determination for luminescent complexes.[2] The measurement of absolute emission quantum yields[3] is, by comparison, a difficult and tedious procedure. Despite the fact that many metal complexes only emit in the solid state, luminescence quantum efficiencies of most molecules have been reported for solutions and are measured relative to a standard under conditions where the sample and standard have the same absorbance. Determination of the luminescence efficiency of powdered samples[4] has been restricted mainly to phosphors.[5-7]

Determination of absolute rates for radiative decay and nonradiative decay requires *both* a lifetime and an emission quantum yield determination.[1] Increasing interest in solid state chemistry, metal complex photochemistry, and investigation of the properties of surfaces has prompted us to seek a routine method for the determination of absolute luminescence yields of powdered samples. We now describe a technique for this measurement, which requires only a conventional scanning emission spectrophotometer. The technique is a reasonable extension of a previously reported method where the intensity of reflected plus emitted light of a powder is compared to the intensity of reflected light from a reflectance standard employing a constant response thermopile detector and a filtered mercury lamp excitation source.[5,6]

The Technique

Luminescence quantum yields of powdered samples can be obtained using a conventional scanning emission spectrophotometer equipped with a front surface emission attachment. The apparatus is schematically shown in Figure

1. The excitation light is incident normal to the sample; some of the light is reflected, some absorbed, and some emitted. For the infinitely thick powdered sample the angular distribution of diffuse reflected light and emitted light is assumed to be the same, i.e., obeys Lambert's law. Theoretical[8] and experimental[9] support for this assumption is available.[10] The same fraction of emitted and reflected light is thus collected by the mirror set at a constant, but arbitrary, angle. In practice the angle of the mirror is adjusted to maximize the emission signal. The light collected by the mirror is analyzed both with respect to relative intensity and spectral distribution. Without changing any parameters, and depending on a constant exciting source intensity, a powdered sample known not to absorb any light is placed in the sample position and the diffuse reflected light analyzed for the sample. A presentation of the required information is shown in Figure 2 for $[Et_4N]_2MnBr_4$. The luminescence quantum yield is just the ratio of the area under the corrected emission curve to the difference in corrected area under the diffuse reflectance curves for the sample and the nonabsorbing powder. The only prior instrumental calibration necessary is determination of the detector response as a function of energy.

Calibration of the relative excitation source intensity as a function of energy enables one to measure the luminescence quantum yield of a powder without requiring a reflectance standard. This is achieved by the following procedure: (1) measure the diffuse reflectance of the sample at an energy where it is known to be nonabsorbing (generally lower than the emission energy); (2) measure the diffuse reflected and emitted light at a second energy where some absorption occurs. The expected diffuse reflected light intensity at the second energy (if no absorption had occurred) is calculated from the measured value at the first energy and the relative output of the excitation source. The necessary experimental data for a luminescence yield de-
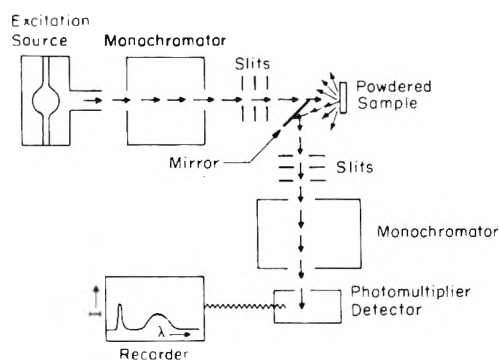
Figure 1. Idealized drawing of apparatus for determination of luminescence quantum yields.
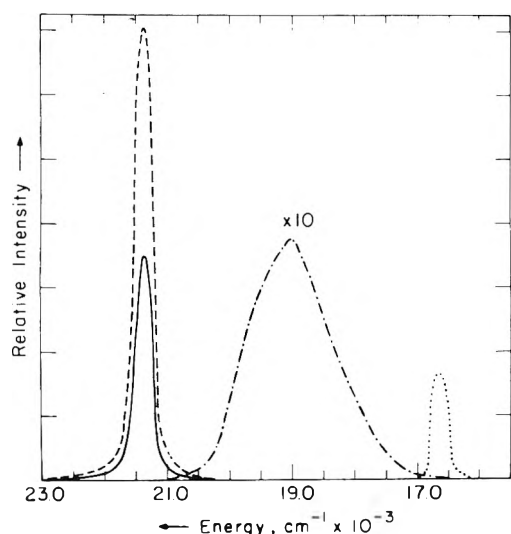
Figure 2. Raw data necessary for determination of emission quantum yield for [Et$_4$N]$_2$MrBr$_4$: (- - - -) diffuse reflectance of Na$_2$SO$_4$; (—) diffuse reflectance of [Et$_4$N]$_2$MnBr$_4$; (- $\cdot$ - $\cdot$) emission of [Et$_4$N]$_2$MnBr$_4$ recorded at ten times the sensitivity of the reflectance measurements; ($\cdot$ $\cdot$ $\cdot$ $\cdot$) diffuse reflectance of [Et$_4$N]$_2$MnBr$_4$ and Na$_2$SO$_4$.

termination are included in Figure 2 and the luminescence yield is found as above.

In equation form, the luminescence quantum yield, ϕ, is given by expression 1 where E is the area under the cor-

$$\phi = \frac{\text{no. of photons emitted}}{\text{no. of photons absorbed}} = \frac{E}{(R_{std} - R_{smpl})} \tag{1}$$

rected emission curve of the sample and R_{std} and R_{smpl} are the corrected areas under the diffuse reflectance curves of the nonabsorbing standard and the sample, respectively, at the excitation wavelength. For samples which do not absorb in the region of the emission no correction factor is appropriate. If the sample absorbs in the luminescent region then dilution with a nonabsorbing powder can be employed to minimize self-absorption. Otherwise, the luminescence quantum yield is to be multiplied by a correction factor to take into account self-absorption. The correction factor, C, is approximately given by expression 2[11] where R' is the re-

$$C = 2/(1 + R') \tag{2}$$

flectivity of the sample in the region of luminescence.

The only limitation of the technique, in principle, is that
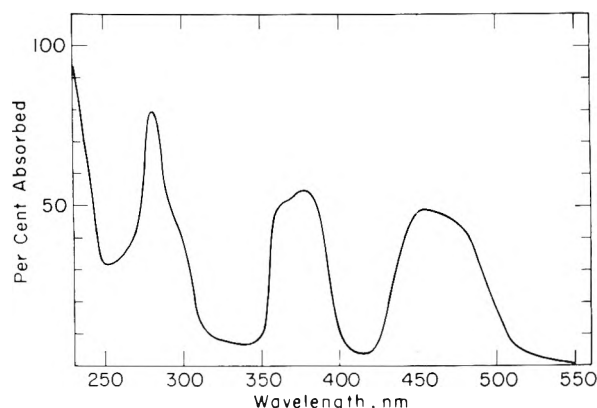
Figure 3. Point-by-point reflectance spectrum of pure powdered [Et$_4$N]$_2$MnBr$_4$; Na$_2$SO$_4$ is the reflectance standard. Measurement was made every 10 nm except at 270–290 nm where data were taken every 5 nm.

TABLE I: Reflectance Properties of Powders

| Wavelength, nm | Relative diffuse reflectance intensity[a] | | | |
	Fresh MgO[b] mirror	MgO powder	KBr	Na$_2$SO$_4$
300	0.5	0.6	0.6	0.6
325	2.8	3.0	2.7	2.8
350	13.7	12.4	14.0	13.7
375	35.0	36.0	36.0	35.0
400	66.0	67.0	72.0	64.0
425	91.0	90.0	86.0	87.0
450	116	118	102	109
475	124	126	134	118
500	108	110	109	101
525	106	109	107	98.0
550	85.0	87.0	86.0	80.0
575	65.0	67.0	67.0	61.0
600	45.0	45.0	47.0	42.0
625	28.0	29.0	30.0	27.0
650	18.0	17.0	19.0	17.0
675	8.0	8.0	9.0	8.0

[a] Relative maximum output from Aminco detector from diffusely reflected excitation by placing the powders in a cuvet in the solid sample accessory. Readings are uncorrected for variation in lamp output and detector sensitivity as a function of wavelength. [b] Prepared by burning Mg in air.

the luminescent material must absorb a measureable fraction of the excitation light. The validity of the technique can be established by (1) comparison of known quantum yields with our determinations; (2) obtaining point-by-point reflectance spectra to make certain that relative absorbances can be accurately determined; (3) demonstrating that the luminescence yields are independent of the fraction of light absorbed. The results of an investigation of these criteria are detailed below.

Results

a. Reflectance Spectra. A point-by-point (every 5 or 10 nm) diffuse reflectance spectrum for the pure solid [Et$_4$N]$_2$MnBr$_4$ is shown in Figure 3 using Na$_2$SO$_4$ as the reflectance standard. This spectrum typifies similar determinations for [bis(cis-1,2-bis(diphenylphosphino)ethylene)-rhodium(I)]$^+$ and -[iridium(I)]$^+$, Ru(2,2'-bipyridine)$_3^{2+}$, and ClRe(CO)$_3$(1,10-phenanthroline) in that spectral band maxima and relative absorption intensities parallel previous transmission and reflectance measurements for these

TABLE II: Luminescence Data for Powdered Samples

Sample	% light absorbed	Excitation λ, nm	Emission max, kcm^{-1}	Emission half-width, cm^{-1}	$\phi \pm 25\%$ [a]
[Et$_4$N]$_2$MnBr$_4$	31.0	450	19.20	1800	0.57
	22.7	450	19.20	1800	0.61
	14.6	450	19.20	1800	0.68
	47.6	460	19.20	1800	0.57, 0.50, 0.66
	45.7	470	19.20	1800	0.60
	33.1	450	19.20	1800	0.57
	23.4	440	19.20	1800	0.55
	3.3	430	19.20	1800	0.58
	62.5	290	19.20	1800	0.23
	36.5	254	19.20	1800	0.07
[n-Pr$_4$N]$_2$MnBr$_4$	38.4	460	19.34	1500	0.56
[Et$_4$N]$_2$MnCl$_4$	25.8	460	19.15	1600	0.32
[n-Bu$_4$N]$_2$MnI$_4$	46.0	460	19.30	1660	0.29
[Me$_4$N]$_2$MnI$_4$	64.5	460	18.96	1850	0.27
Ir(2=phos)$_2$Cl[b]	31.3	445	17.98	1170	0.24
	18.9	465	17.98	1170	0.23
	6.8	475	17.98	1170	0.26
Rh(2=phos)$_2$Cl[b]	39.9	445	17.00	2000	0.02
	13.8	505	17.00	2000	0.03
Ru(bipy)$_3$Cl$_2$[c]	38.6	450	16.95	1500	0.003
ClRe(CO)$_3$(phen)[d]	69.7	420	18.38	2300	0.006$_5$
	62.7	420	18.38	2300	0.005$_9$
	56.0	420	18.38	2300	0.005$_1$
Sodium salicylate	56.7	370	24.35	3800	0.62
	90.1	340	24.35	3800	0.53
NBS 1021 phosphor	71.2	254	19.46	1500	0.60
	23.3	290	19.46	1500	0.15
NBS 1028 phosphor	92.5	254	19.34	1640	0.41
	58.3	290	19.34	1640	0.27

[a] For samples which luminesce partially below the region of corrected spectra (lower energy than 16.7 kcm^{-1}) we have estimated the yield by assuming gaussian emission peaks. [b] 2=phos is cis-1,2-bis(diphenylphosphino)ethylene. [c] bipy is 2,2'-bipyridine. [d] Phen is 1,10-phenanthroline.
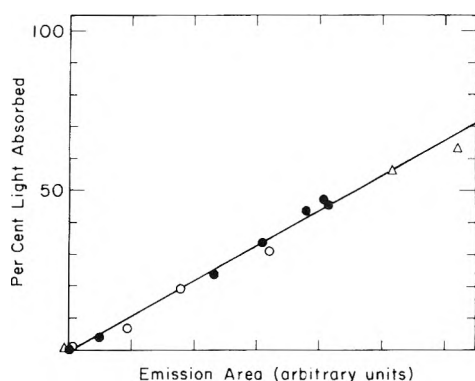
Figure 4. Plot of per cent light absorbed against the relative area under the resulting luminescence curve for [Et$_4$N]$_2$MnBr$_4$ (●) bis(cis-1,2-bis(diphenylphosphino)ethylene)iridium(I) (O), and ClRe(CO)$_3$(1,10-phenanthroline (△). Variable per cent light absorbed was achieved either by dilution of the sample with KBr or by varying the excitation wavelength within one absorption band.

complexes.[12] All of the complexes investigated except the [Et$_4$N]$_2$MnBr$_4$ required dilution with KBr to diminish the absorptivity to a level where absorption bands could be discerned. Reflectance standards used were common inorganic salts such as KCl, Na$_2$SO$_4$, or KBr which are essentially nonabsorbing in the region of interest. Table I gives evidence in the 300–675-nm region supporting the notion that the reflectivity of KBr and Na$_2$SO$_4$ are essentially the same as that of fresh MgO which has extremely high absolute reflectivity. Empirically, we find that particle size has little

bearing on the results. The matching of the reflectance of the standard and the sample at several wavelengths of lower energy than the emission has been our practical criterion of matching reflectance properties. In general, grinding the samples with mortar and pestle to similar consistency yielded satisfactory results.

b. Luminescence Quantum Yields. Emission quantum yields for several powdered samples are given in Table II. As shown for several cases the emission quantum yield is independent of the per cent light absorbed at a given excitation wavelength. An equivalent presentation of the data is given in Figure 4 where the per cent light absorbed is plotted against the relative luminescence area, and, as required, the plots are linear and extrapolation to zero light absorbed gives zero luminescence area.

The luminescence yields of two National Bureau of Standards phosphors which have been previously measured are included in Table II. We find 254-nm excitation yields of 0.60 and 0.41 for NBS no. 1021 and no. 1028 phosphors, respectively. Literature values for NBS no. 1021 are 0.45,[5] and 0.70,[6] and for NBS no. 1028 are 0.68[5] and 0.68.[6] Also, sodium salicylate as a pure compound has been measured and has a wavelength-independent emission yield. Previously measured values are 0.50,[13] 0.64,[14] and 0.99[9c] and we find 0.53 and 0.62 upon 340- and 370-nm excitation, respectively. We have also shown that the relative emission quantum yield is constant for several other data points between 340 and 375 nm.

Discussion

The results reveal that the proposed technique meets the

criteria outlined above to test its validity. Agreement of the values for the phosphor quantum yields is fair, given the large variation in the literature values, and the fact that for the phosphors measured the luminescence yield is extremely wavelength dependent[6] which may account for some discrepancy. The agreement of the absolute yields for sodium salicylate is extremely good. The 0.99 value[9c] for this compound is incorrect as it is known that the luminescence efficiency of sodium salicylate increases by at least 30%[14] upon cooling to 77°K. An independent determination[15] of the emission quantum yield for $[Et_4N]_2MnBr_4$ upon 460-nm excitation yields a value of 0.50 in excellent agreement with the values obtained here evidencing the ability of other workers to obtain consistent results. We find that the reproducibility of a given measurement is likely to be well within 10%. The error in the absolute yields, however, is likely to be much larger for the following reasons: (1) the measurement depends on knowing the relative response of the detector as a function of wavelength and we estimate at least ±5% and even worse at the extremes of the calibration range; (2) the absolute reflectivity of the salts used as standards is not unity as we have assumed and the reflectivity of samples in the luminescence region is also not unity; (3) the front surface of the cuvet holding the powder also gives a small amount of scattered light (<5% of the total diffuse reflected intensity); and (4) the real importance of particle size effects are beyond the scope of our study and have been poorly assessed in the past.[4] Thus, we estimate the absolute quantum yields to be ±25%.

In practice, the technique gives best results for highly luminescent powders where an excitation wavelength close to the emission can be used. Weakly luminescent samples are difficult due to intense scattered light from the solid, second-order grating effects, and poor monochromaticity of the excitation light. When an excitation line far removed from the emission is required relatively large differences in detector response may obtain, requiring careful calibration. This difficulty can be minimized by careful selection of photomultiplier tube and emission grating. In our experiments differences in detector response were less than a factor of 3 over the range 250–600 nm using an R136 photomultiplier.

Though the technique requires no luminescence standards, we point out that $[Et_4N]_2MnBr_4$ is easily synthesized, is stable, has high luminescence efficiency, and can be used without dilution. Thus, to gain familiarity with the technique determination of its emission yield upon 460-nm excitation is suggested. The emission yield of the $[Et_4N]_2MnBr_4$ is 0.55 ± 25%. Note that high-energy excitation of this sample gives smaller yields which is due to direct population of high-energy charge-transfer states which apparently neither emit nor fully decay via the ligand field excited states.[16] When uv absorbing samples are to be measured sodium salicylate should serve as a reasonable test standard.

Experimental Section

Emission Apparatus. An Aminco-Bowman SPF-2 emission spectrophotometer equipped with the front surface emission accessory from Aminco and an R136 or a 1P21 photomultiplier tube was used for all studies. The powdered sample was placed in a quartz square fluorescence cell. The relative excitation source (150-W xenon lamp) intensity as a function of wavelength was determined by monitoring the front surface emission at 630 nm of an etha-

nol solution of Rhodamine B. Using this information relative detector response as a function of wavelength could then be determined for each photomultiplier after reflecting the exciting light into the emission detection system and measuring the relative detector output. This calibration procedure is as reported in the literature.[17] The diffuse reflected exciting light and the luminescence from powdered samples are measured by simply scanning the emission monochromator through both the excitation and emission energy region.

Materials. Phosphors 1021 and 1028 were obtained from the National Bureau of Standards; tetrahalomanganese(II) salts were prepared by literature routes;[18] $ClRe(CO)_3(1,10-$ phenanthroline) was prepared by heating benzene solutions of $Re(CO)_5Cl$ (from Pressure Chemical Co.) and 1,10-phenanthroline to 60° followed by concentration by rotary evaporation and addition of n-pentane to precipitate the product, and purification by recrystallization from CH_2Cl_2 by addition of n-pentane; $Ru(bipy)_3Cl_2$ was a gift from G. S. Patterson; $Ir(2=phos)_2Cl$ and $Rh(2=phos)_2Cl$ were those used in a previous study;[12a] and the sodium salicylate was obtained from Mallinckrodt Chemicals.

Typical Procedure for Emission Quantum Yield Determination. Emission quantum yields for powdered samples were determined using the following procedure given in detail for $Ir(2=phos)_2Cl$. Spectroquality KBr was ground with a mortar and pestle for 2–3 min and placed in one of two square fluorescence cells (1 cm × 1 cm). The cell was filled with KBr to a mark such that the excitation beam was fully below the top of the KBr when placed in the sample position in the Aminco. The front surface was also examined to ensure the absence of gross cracks and crevices in the powder. Such cracks and crevices were removed by gently tapping the cell or by gently pressing on the KBr with a spatula. The $Ir(2=phos)_2Cl$ was diluted with KBr and ground with a mortar and pestle for 2–3 min and the resulting powder was placed in the remaining cell. The excitation wavelength of the Aminco was set to 600 nm and a 0.5-mm slit was placed at the exit of the monochromator. A 0.5-mm slit was also placed in each of the two slots for excitation slits in the front surface emission accessory of the Aminco. A 2.0-mm slit was placed in each of the two slots for emission slits in the front surface emission accessory; a 2.0-mm slit was placed at the entrance to the emission monochromator; and a 1.0-mm slit width was used at the entrance to the PMT housing. With the pure KBr sample in position the emission monochromator was scanned from 550 to 650 nm to observe the diffusely reflected 600-nm excitation light. The angle of the collecting mirror of the front surface emission accessory was varied to maximize the 600-nm signal. The pure KBr sample was then replaced with the $Ir(2=phos)_2Cl$ sample and the 550–650-nm emission region scanned to observe the 600-nm light. The signal at 600 nm from the KBr and the $Ir(2=phos)_2Cl$ was the same within 5%. The excitation monochromator was then set at 465 nm and the emission spectrum of $Ir(2=phos)_2Cl$ scanned as a function of the angle of the collecting mirror to check that the maximum emission intensity was achieved when diffusely reflected light intensity was maximized. The final data necessary for the quantum yield determinations were then collected: (1) with the pure KBr sample in place the emission monochromator was scanned slowly from 400 to 650 nm to observe the diffusely reflected 465-nm excitation light; (2) with the $Ir(2=phos)_2Cl$ sample in place the emission monochromator was scanned again

from 400 to 650 nm recording both the diminished (compared to pure KBr) diffusely reflected light at 465 nm and the Ir(2=phos)$_2$Cl emission; and (3) 1 and 2 were repeated. The spectra were then plotted (relative intensity $vs.$ cm^{-1}) using appropriate emission dection system correction factors. The quantum yield is the corrected emission area divided by the corrected area between the 465-nm reflectance peaks of pure KBr and the sample. The relative areas were determined by cutting and weighing the peaks. The quantum yield of the sample was redetermined at excitation wavelengths of 445 and 475 nm using the same powder.

References and Notes

(1) Photochemical reactions of coordination compounds are reviewed in V. Balzani and V. Carassiti, "Photochemistry of Coordination Compounds," Academic Press, New York, N.Y., 1970.

(2) Emission characteristics of inorganic complexes are reviewed in P. D. Fleischauer and Pl. Fleischauer, *Chem. Rev.*, **70**, 199 (1970).

(3) Procedures for measuring emission quantum yields are reviewed in J. N. Demas and G. A. Crosby, *J. Phys. Chem.*, **75**, 991 (1971).

(4) Luminescence efficiency measurements for powders are reviewed in F.

R. Lipsett, *Progr. Dielectrics*, **7**, 217 (1967).

(5) A. Bril in "Luminescence of Organic and Inorganic Materials," H. P. Kallman and G. M. Spruck, Ed., Wiley, New York, N.Y., 1962, pp 479–493.

(6) G. W. Ludwig and J. D. Kingsley, *J. Electrochem. Soc.*, **117**, 348, 353 (1970).

(7) Y. Uehara, I. Masuda, and Y. Kobuke, *J. Electrochem. Soc.*, **107**, 1 (1960).

(8) (a) E. J. Bowen, "The Chemical Aspects of Light," Clarendon Press, Oxford, 2nd ed, 1946, p 173; (b) N. Wotherspoon and G. Oster, "Physical Methods of Organic Chemistry," Vol. I, Part III of "Techniques of Organic Chemistry" 3rd ed, A. Weissberger, Ed., Interscience, New York, N.Y., 1960, p 2084; (c) J. W. T. Walsh, "Photometry," 3rd ed, Constable, London, 1958, pp 131–138; (d) B. I. Stepanov and A. M. Samson, *Bull. Acad. Sci. USSR, Phys. Ser.*, **24**, 502 (1960); (e) P. Pringsheim, "Fluorescence and Phosphorescence," Interscience, New York, N.Y., 1949, pp 6, 306, 389; (e) *cf.* also ref 4.

(9) (a) F. R. Lipsett and L. Tardif. *Can. J. Phys.*, **36**, 1438 (1958); (b) E. Waibel and R. Seiwert, *Z. Phys. Chem.*, **25**, 266 (1956); (c) R. Allison, J. Burns, and A. J. Tuzzolino, *J. Opt. Soc. Amer.*, **54**, 747 (1964).

(10) This assumption is implicit in the work reported in ref 5 and 6.

(11) G. Blasse and A. Bril, *J. Chem. Phys.*, **47**, 5139 (1967).

(12) (a) G. L. Geoffroy, M. S. Wrighton, G. S. Hammond, and H. B. Gray, *J. Amer. Chem. Soc.*, **96**, 3105 (1974); (b) F. A. Cotton, D. M. L. Goodgame, and M. Goodgame, *ibid.*, **84**, 168 (1962); (c) M. Wrighton and D. L. Morse, *ibid.*, **96**, 998 (1974); (d) F. E. Lytle and D. M. Hercules, *ibid.*, **91**, 253 (1969), and references therein.

(13) K. J. Mygaard, *Brit. J. Appl. Phys.*, **15**, 597 (1964).

(14) N. Kristianpoller, *J. Opt. Soc. Amer.*, **54**, 1285 (1964).

(15) The independent determination was by G. L. Geoffroy of the California Institute of Technology using an Hitachi MPF-3A emission spectrometer equipped with an R136 PMT. The from surface emission cell was one of custom design.

(16) M. Wrighton and D. S. Ginley, *Chem. Phys.*, **4**, 295 (1974).

(17) C. A. Parker, "Photoluminescence of Solutions," Elsevier, Amsterdam, 1968.

(18) N. S. Gill and F. B. Taylor, *Inorg. Syn.*, **9**, 136 (1967).

Radical Pairs, Electron Spin Resonance Relaxation Times, and Limiting Radical Concentrations in γ-Irradiated 3-Methylpentane Glass[1]

D. P. Lin and J. E. Willard*

Department of Chemistry, University of Wisconsin, Madison, Wisconsin 53706 (Received February 20, 1974)

This paper presents new evidence related to the spatial distribution and limiting concentration of 3-methylpentyl radicals in γ-irradiated 3-methylpentane glass at 77°K. An esr signal at g = 4 attributable to the ΔM_s = 2 transition of radical pairs has been observed. The steady-state concentration of isolated radicals at a dose rate of 3×10^{18} eV g^{-1} min^{-1} is $ca.$ 0.4 mol % at 77°K, and is reached after a dose of $ca.$ 2×10^{21} eV g^{-1}. The apparent value of the esr relaxation time, $(T_1 T_2)^{1/2}$, is nearly constant with dose to 1×10^{21} eV g^{-1} or higher, implying small intrinsic spur sizes. Previous evidence on radical pairs in polycrystalline hexadecane has been confirmed and extended.

Introduction

Knowledge of the spatial distribution of the trapped reaction intermediates (radicals, electrons, cations, anions) produced by γ-irradiation of organic solids[2] is of value in deducing the events by which the energy of the radiation is deposited and produces chemical change. In the present work we have sought to answer three questions, stated below, about the distribution of radicals produced in glassy 3-methylpentane (3MP) at 77°K.

(1) Are some radicals produced in pairs? It has been suggested[3] that excited matrix molecules may eject hot hydro-

gen atoms which abstract H from adjacent molecules thus forming such pairs, and other mechanisms of pair formation may also be postulated. Radical pairs have been observed in polymers,[4] crystalline hydrocarbons,[5] and glassy squalane (C$_{30}$H$_{62}$)[5] by their ΔM_s = 2 esr spectra at G = 4, but have not been reported in short-chain hydrocarbon glasses.

(2) Does the electron spin resonance relaxation time $(T_1 T_2)^{1/2}$ of the radicals decrease with increasing γ dose in a manner indicating progressive overlapping of radical spurs, and allowing an estimate of spur size? Such mea-

surements have been used to determine upper limits of the electron spur dimensions in several glasses[6] and of the radical spur dimensions in 2-methyltetrahydrofuran (MTHF).[7] The latter suggest that the radical spur is smaller than the electron spur.

(3) What steady-state concentration of radicals is achieved at high doses during continued irradiation at 77°K at a typical dose rate? This concentration can be considered as a lower limit on the limiting population density which might be achieved under optimum conditions of lower temperature and higher dose rate.

Earlier work has shown that the radicals produced by γ-irradiation of 3MP glass at 77°K are predominately secondary 3-methylpentyl radicals.[8] The G value is 3.0 ± 0.3.[9,10] A population of these radicals produced with a γ dose of 1 × 10^{19} eV g^{-1} decays 50% in the first 5 hr and <5% in the next 15 hr,[9] the relatively rapid decay being attributable to intraspur reaction and the slower decay to random second-order radical–radical reaction. The stable radiolysis products found on analysis include those expected from radical combination and disproportionation.[11]

Experimental Section

Phillips pure grade 3-methylpentane was further purified by passage through freshly activated silica gel, storage on the vacuum line over a sodium mirror, and degassing by pumping on the liquid. Esr measurements were made in the X-band with a Varian 4501 spectrometer using a V-4531 cavity, 10^5-Hz modulation, and a microwave power of 0.4 mW, except as otherwise indicated. For relaxation time measurements, 400-Hz modulation frequency was used to obtain saturation curves. γ-Irradiations were made with a ^{60}Co source giving a dose rate of about 3 × 10^{18} eV g^{-1} min^{-1}.

Results

Radical Pairs. Figure 1 shows the $\Delta M_s = 2$ radical pair spectrum at $g = 4$ from γ-irradiated 3MP glass. Measurements were made on a Varian E-15 spectrometer at high gain, modulation amplitude, and power and using a Varian computer of average transients (CAT) to provide signal averaging. The spectrum has at least five lines, with a splitting of ca. 9.6 G and line width of 4.5 G. After corrections for the spectrometer settings and the 100 CAT scans used for the $g = 4$ region, the ratio of the area under the integrated first derivative $\Delta M_s = 1$ spectrum of the isolated radicals to that of the spectrum of Figure 1 is ca. 2 × 10^5. To the extent that decay of the radical pairs may have occurred during the 50 min required for the 100 scans, the ratio is high. An estimate of the relative concentrations of the isolated radicals and radical pairs depends on the transition probabilities (see Discussion).

Preparatory to looking for radical pair spectra in γ-irradiated 3MP glass, we have observed the $\Delta M_s = 2$ and $\Delta M_s = 1$ spectra of radical pairs in γ-irradiated polycrystalline n-hexadecane at 77°K and the $\Delta M_s = 2$ signal from glassy squalane at 77°K, which have been reported by Iwasaki and coworkers.[4] The n-hexadecane signal in the $\Delta M_s = 2$ region for a sample which had received a γ dose of 4.6 × 10^{20} eV g^{-1} was unsaturated up to 20 mW, slightly saturated at 60 mW, and about 20% saturated at 190 mW. The signal of the isolated radicals was somewhat saturated at all powers above 0.4 mW and remained nearly constant with increasing power above 40 mW, under fast passage conditions. The $\Delta M_s = 2$ signal from squalane was a well-defined line with $\Delta H_{ms} = 42$ G centered at 1620 G with some indication of much weaker lines on the wings of the 400-G scan used.

Radical Concentration vs. γ Dose. Figure 2 shows the change with γ dose of the height of the second line of the first derivative esr signal of the isolated radicals produced in 3MP at 77°K. During the first 4 × 10^{20} eV g^{-1} the growth is approximately linear, as previously observed[6,12] for 3MP, 3-methyldecane, methylcyclohexane, and 2-methyltetrahydrofuran. After ca. 2 × 10^{21} eV g^{-1} of continuous irradiation, the peak height reaches a steady state. During a 9-hr interruption after a dose of 1.9 × 10^{21} eV g^{-1}, the peak height dropped by 52%, but grew to the former maximum with a further dose of 1 × 10^{21} eV g^{-1}.

Since the ratio of the height of peak 2 of the first derivative spectrum of isolated 3-methylpentyl to the area obtained by double integration of this spectrum increases by 30–40%[9] during the first few hours of decay (in samples having received doses of 10^{19} eV g^{-1}), it is expected that a plot of true radical concentration would fall somewhat below the curve of Figure 2.

Relaxation Times as a Function of γ Dose. Esr relaxation time data, $(T_1 T_2)^{1/2}$, for isolated 3-methylpentyl radicals in γ-irradiated 3MP at 77°K are plotted as a function

Figure 1. Esr spectra in 1620-G region: (A) radical pair signal from γ-irradiated 3-methylpentane; (B) signal from irradiated empty Suprasil esr tube; (C) signal from unirradiated Suprasil esr tube. All scans 200 G; $T = 77°K$; dose = 2.7 × 10^{20} eV g^{-1}; microwave power = 20 mW; modulation amplitude = 4 G; measurements made on E-15 spectrometer. Each spectrum is the sum of 100 scans with the computer of average transients.

Figure 2. Radical concentration as a function of dose during γ-irradiation of 3-methylpentane glass at 77°K as indicated by height of second peak from low-field end of esr spectrum. The sample was held at 77°K during the 9.5- and 11-hr interruptions of the irradiation.

Figure 3. Esr relaxation times of trapped species in γ-irradiated 3-methylpentane as a function of radiation dose: (▲) radicals at 77°K (this work); (●) electrons at 71°K (Lin and Kevan[6]). The dose rate for the electron experiments[6] was 4×10^{17} eV g^{-1} min^{-1} and that for the radical experiments was 3×10^{18} eV g^{-1} min^{-1}.

of radiation dose in Figure 3, together with analogous data of Lin and Kevan[6] for trapped electrons in the same matrix. The values of $(T_1 T_2)^{1/2} = 3^{1/2}/\gamma H_{1/2}$, where T_1 is the spin–lattice relaxation time, T_2 the spin–spin relaxation time, γ the magnetogyric ratio of the electron $(1.76 \times 10^7 G^{-1}$ sec$^{-1})$, and $H_{1/2}$ the microwave power at which the intensity of the second line of the free radical esr signal is one-half of that which would be observed in the absence of saturation.

In the absence of complicating effects, the horizontal line of Figure 2 for $(T_1 T_2)^{1/2}$ of the isolated radicals would indicate that they are produced in spurs of such small diameter that they do not overlap significantly up to a dose of 10^{21} eV g^{-1} or more. However, this interpretation is subject to considerable uncertainty due to unknown contributions to the measured $(T_1 T_2)^{1/2}$ which may accompany the change in the average age of the radical population during the 6.7-hr irradiation. These include the decrease in ratio of peak height to integrated area of the esr signal during initial radical decay and the decrease in ratio of relatively closely spaced radicals in spurs to randomly dispersed radicals as the average age increases. In addition changes in spin–spin relaxation between the radicals and the changing population of trapped electrons and cations may occur. The apparent values of $(T_1 T_2)^{1/2}$ for the radicals produced in 2-methyltetrahydrofuran by γ-irradiation have also been observed to be independent of dose, up to a dose of 5×10^{20} eV g^{-1} at a dose rate of 2.4×10^{19} eV g^{-1} hr^{-1}.[7]

Discussion

Radical Pairs. Determination of the concentration of the paired radicals relative to the isolated radicals requires a knowledge of the ratios of the transition probabilities of the $\Delta M_s = 2$ and $\Delta M_s = 1$ transitions, which depend on the distance between radicals within the pairs. In a polycrystalline sample this intrapair distance may be estimated from the hyperfine splitting of the $\Delta M_s = 1$ paired radical spectrum, but glassy samples do not give such a spectrum.[4] The separation distance can also be estimated from data on

saturation as a function of microwave power, but the difficulty of observing the $\Delta M_s = 2$ spectrum in 3MP has thus far precluded such measurements. For *assumed* intrapair separations of 5, 8, and 10 Å, the estimated transition probability ratios are 2.5×10^{-3}, 1.5×10^{-4}, and 4×10^{-5}, which give values for the percentage of radicals paired of 0.4, 6.2, and 19%, respectively. The estimates are made using the relation $P(\Delta M_s = 2)/P(\Delta M_s = 1) = (4.5\beta^2/r^6 H^2)$ $(\sin^2 \theta)$ derived for single crystals, where β = the Bohr magneton, r = the average radical separa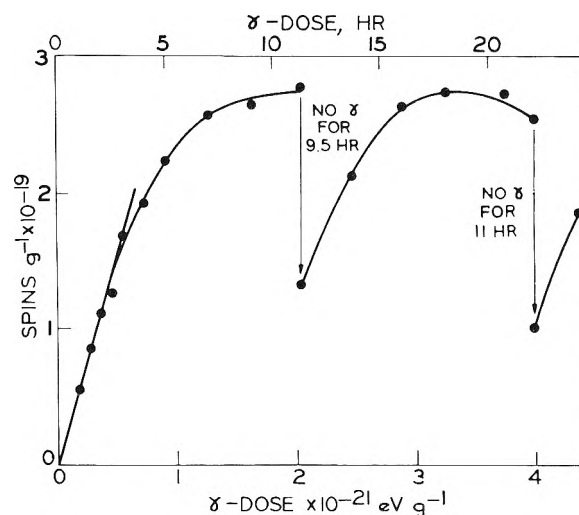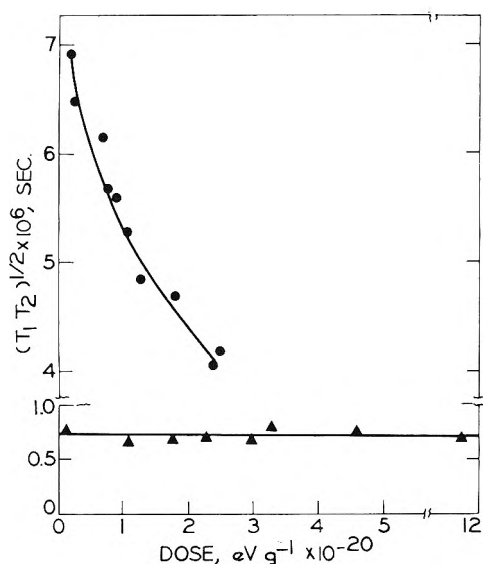tion distance in the pairs, H = the magnetic field at $g = 2$, and θ is the conventional angle in polar coordinates.

In polycrystalline n-hexadecane, saturation studies on the radical pair spectrum were possible. Assuming the maximum of the saturation curve, H_{1max}, to be at 190 mW, the average relaxation time $(T_1 T_2)^{1/2}$ may be estimated to be 1.7×10^{-8} sec by the relation $(T_1 T_2)^{1/2} = 1/2^{1/2} \cdot \gamma H_{1max}$.[13] The magnetogyric factor γ here is $2(1.76 \times 10^7) G^{-1}$ sec^{-1} rather than $1.76 \times 10^7 G^{-1}$ sec^{-1}, since the spectra were observed at $g = 4$ rather than $g = 2$. If the spin–lattice relaxation time is ca. 10^{-6} sec, as indicated by our experiments, the spin–spin relaxation time is ca. 10^{-10}. This is about two orders of magnitude less than that of isolated radicals. From this estimate of T_2 the average distance between radicals in the radical pairs is estimated to be 5.1 Å $(T_2 = r^3/\gamma^2 h/2\pi)$,[14] which gives a ratio of the esr transition probability for the radical pairs to that of the isolated radicals of 2.53×10^{-3}. The ratio 1/11,000, for the areas under the esr absorption curves of the paired radicals at $g = 4$ and the isolated radicals at $g = 2$, together with the transition probability indicates that 7% of all the radicals are produced in pairs identifiable by the $g = 4$ spectrum. In the earlier work[5] a separation of 5.75 Å between the radicals in the pairs in hexadecane was calculated from the spectral splitting due to zero field coupling, estimated from the hyperfine structure of the $\Delta M_s = 1$ radical pair spectrum. The ratio of integrated intensities of the pair spectrum at $g = 4$ to the isolated radical spectrum at $g = 2$ was 1/16,000 and the estimated percentage of paired radicals was 12.

Limiting Radical Concentration. Taking the initial slope of the growth curve of Figure 2 to be proportional to the G value of 3.09,[10] for production of isolated radicals, and assuming the peak height measurements to be proportional to the concentration of these radicals (which introduces some uncertainty), the plateau represents a concentration of ca. 0.4 mol %. At this concentration the distance between centers of the radicals, if evenly spaced, would be 6–8 molecular diameters and the average distance of a new radical produced in the system from one previously there would be about 2 molecular diameters. If the $(T_1 T_2)^{1/2}$ data of Figure 3 can be correctly interpreted to mean that there is little overlapping of radical spurs up to a dose of at least 1×10^{21} eV g^{-1}, it can be reasoned from the concentrations achieved that intraspur radical distances are ≤15 Å. For the reasons cited, this value may be low. However, it is not highly implausible. The upper limits of the "spur radii" for electrons in 3MP, triethylamine, and 2-methyltetrahydrofuran have been estimated[6] from $(T_1 T_2)^{1/2}$ vs. dose measurements to be 130, 101, and 63 Å, respectively. These are not the intrinsic spur radii but are expanded spur radii reflecting how far the electrons travel before being trapped.[6] A much lower limit on the average interradical than interelectron distance is to be expected because the radicals may be presumed to be trapped at their

site of formation and to diffuse only slowly. 100-eV electrons, presumed to be typical of the δ electrons which produced spurs, have linear energy transfer of 3.3 eV Å^{-1},[15] which would result in deposition of the energy along a path of <30 Å.

Conclusion

Radical pairs are produced by γ-irradiation of 3MP glass at 77°K. The mechanism of their formation is not yet known. Possibilities include: (1) abstraction by hot hydrogen atoms, as noted in the Introduction; (2) carbon–carbon bond rupture giving radicals of carbon number less than 6 whose spectra at $g = 2$ are obscured by the 3-methylpentyl radical spectrum; (3) encounter of isolated radicals by diffusion (a process which must occur for radicals to decay by combination and disproportionation). Experiments comparing the rate of decay of the pairs with that of the isolated radicals and experiments at 4°K should help to determine the source of the pairs.

The evidence from the measurements of $(T_1 T_2)^{1/2}$ as a function of dose, and of the concentration of radicals at the steady state, is consistent with the conclusion that radicals are separated in the spurs by only a few molecular diameters. A determination of the steady-state concentration of

radicals during irradiation at 4°K would presumably set a higher limit than the 77°K experiments on the maximum radical population density which the matrix can sustain.

References and Notes

(1) This work has been supported in part by the U. S. Atomic Energy Commission under Contract No. AT(11-1)-1715 and by the W. F. Vilas Trust of the University of Wisconsin.
(2) For a review and references see B. G. Ershov, "Spatial Distribution of Free Radicals in Irradiated Solids," in "Actions Chimiques et Biologique des Radiations, Quatorzième Série," M. Haissinsky, Ed., Masson et Cie, Paris, 1970.
(3) D. Timm and J. E. Willard, J. Phys. Chem., 73, 2403 (1969).
(4) M. Iwasaki, T. Ichikawa, and T. Ohmori, J. Chem. Phys., 50, 1984 (1969).
(5) M. Iwasaki, T. Ichikawa, and T. Ohmori, J. Chem. Phys., 50, 1991 (1969).
(6) D. P. Lin and L. Kevan, J. Chem. Phys., 55, 2629 (1971), and references given there.
(7) D. P. Lin, P. Hamlet, and L. Kevan, J. Phys. Chem., 76, 1226 (1972).
(8) D. J. Henderson and J. E. Willard, J. Amer. Chem. Soc., 91, 3014 (1969).
(9) M. A. Neiss and J. E. Willard, unpublished results.
(10) L. Perkey and J. E. Willard, J. Chem. Phys., 60, 2732 (1974).
(11) D. D. Mainwaring and J. E. Willard, J. Phys. Chem., 77, 2864 (1973).
(12) M. Shirom and J. E. Willard, J. Amer. Chem. Soc., 90, 2184 (1968).
(13) C. P. Poole, "Electron Spin Resonance," Interscience, New York, N.Y., 1967, Chapter 18.
(14) C. P. Slichter, "Principles of Magnetic Resonance," Harper and Row, New York, N.Y., 1963, p 29.
(15) D. E. Lea, "Actions of Radiations on Living Cells," Cambridge University Press, New York, N.Y., 1955, p 24.

Effects of Intramolecular Hydrogen Bonds on Intermolecular Hydrogen Bonding

J. N. Spencer,* K. S. Robertson, and E. E. Quick

Department of Chemistry, Lebanon Valley College, Annville, Pennsylvania 17003 (Received May 22, 1974)

The hydrogen bonding of phenol, guaiacol, and catechol to the electron pair donors, dimethyl sulfoxide, tetrahydrofuran, and di-n-butyl sulfide, was studied in CCl_4 solution at various temperatures by monitoring the hydroxyl stretching frequency at 3 μ. Only dimethyl sulfoxide was found to disrupt the intramolecular hydrogen bond of guaiacol. The intramolecular bond strength for guaiacol was found to be -3.3 kcal mol^{-1}. All donors disrupt the intramolecular bond in catechol with consequent formation of hydrogen bonded complexes containing one and two donor molecules. The frequency shifts and enthalpy changes for the formation of the monodonor complex with catechol are larger than the corresponding properties for the phenol complex and reflect the influence of the intramolecular hydrogen bond on intermolecular hydrogen bonding.

Introduction

A previous study[1] has shown that hydroxybenzenes capable of intramolecular hydrogen bonding form intermolecular complexes with diethyl ether having larger frequency shifts and enthalpies than those hydroxybenzenes that do not have intramolecular bonds. For compounds such as catechol (o-hydroxyphenol) the intramolecular hydrogen bond presumably changes the basicity of the oxygen of the free hydroxy group with a consequent increase in acidity of the proton of this group. This work continues the investigation of the influence of intramolecular bonding on intermo-

lecular bond properties. Phenol, catechol, and guaiacol (o-methoxyphenol) complexes with tetrahydrofuran (THF), dimethyl sulfoxide (DMSO), and di-n-butyl sulfide (n-Bu$_2$S) were investigated.

Several studies of the thermodynamic properties of the hydrogen bonded complexes of phenol with DMSO, THF, and n-Bu$_2$S have been reported. Gramstad[2] used ir measurements to find the enthalpy change for the DMSO–phenol complex to be -8.00 kcal mol^{-1}; the equilibrium constant was reported to be 230.2 at 20°. Drago, Wayland, and Carlson[3] investigating this same complex by uv techniques report ΔH as -6.5 kcal mol^{-1}; the equilibrium constant at

TABLE I: Thermodynamic Functions

	T, °C	K_1	K_2	$\Delta H°,$[a] kcal mol^{-1}	$\Delta S°,$ cal deg^{-1} mol^{-1}
Phenol–THF	20	13.5		$\Delta H = -4.9 \pm 0.2$	$\Delta S = -12$
	30	10.0			
	40	7.6			
	50	6.1			
Phenol–DMSO	25	186		$\Delta H = -6.33 \pm 0.07$	$\Delta S = -10.8$
	30	157			
	40	112			
	50	81			
Guaiacol–DMSO	25	3.75		$\Delta H = -3.04 \pm 0.14$	$\Delta S = -7.57$
	30	3.43			
	40	2.87			
	50	2.53			
Phenol–n-Bu$_2$S	20	1.9		$\Delta H = -3.3 \pm 0.5$	$\Delta S = -9.9$
	30	1.5			
	40	1.4			
	50	1.1			
Catechol–THF	10	27.7	78	$\Delta H_1 = -8.6 \pm 0.2$	$\Delta S_1 = -24$
	20	16.6	91	$\Delta H_2 = +3.6 \pm 0.3$	$\Delta S_2 = +22$
	30	9.9	120		
	40	6.4	140		
Catechol–DMSO	20	3.26×10^2	7.7×10^2	$\Delta H_1 = -9.4 \pm 0.9$	$\Delta S_1 = -21$
	25	2.60×10^2	1.22×10^3	$\Delta H_2 = +5.3 \pm 1.3$	$\Delta S_2 = +31$
	30	1.69×10^2	1.47×10^3		
	40	1.00×10^2	1.64×10^3		
	50	7.7×10^1	2.05×10^3		
Catechol–n-Bu$_2$S	20	1.22	8	$\Delta H_1 = -4.0 \pm 0.1$	$\Delta S_1 = -13$
	30	0.97	9	$\Delta H_2 = +1.1 \pm 0.6$	$\Delta S_2 = +8$
	40	0.78	9		

[a] The precision reported was obtained from the error in the least-squares slope of a plot of log K vs. T^{-1}.

TABLE II: Frequency Shifts[a] **for Hydroxybenzenes with Various Electron Donors**

	n-Bu$_2$S	THF	DMSO
Phenol	266	287	354
Hydroquinone	251	265	339
Resorcinol	254	289	356
Guaiacol			360
Catechol	321	363	445

[a] The frequency shift in cm^{-1} is the difference between the free hydroxyl stretching frequency and that of the complex in CCl$_4$ solution. For guaiacol the complex frequency is compared to 3611 cm^{-1}.

25° was found to be 182. The phenol–THF complex has been studied by Gramstad[4] who gives ΔH as -5.68 kcal mol^{-1} and K at 20° to be 12.90; Singh and Rao[5] report ΔH to be -4.0 kcal mol^{-1} and K at 25° as 13.6; Dunken and Fritzsche[6] give ΔH as -5.50 kcal mol^{-1} and K as 12.2 at 20°; Bellamy, Eglington, and Morman[7] report K to be 10.4 at 29°; West, et al.,[8] used measurements on the free OH first overtone band and found ΔH to be -5.29 kcal mol^{-1} and K to be 19.0 at 20°. All the investigations on THF were conducted by ir methods and the reported frequency shifts range from 283 to 301 cm^{-1}. West, et al.,[8] found the enthalpy change for the phenol–n-Bu$_2$S complex to be -4.19 kcal mol^{-1} and K calculated from their data at 20° is 1.49.

Experimental Section

Mallinkrodt analytical reagent grade dimethyl sulfoxide was refluxed over CaO and fractionally distilled under dry nitrogen. Baker analyzed reagent grade tetrahydrofuran was fractionally distilled from dri-Na under dry nitrogen. Aldrich analyzed di-n-butyl sulfide was fractionally distilled under dry nitrogen atmosphere. The purification of

the other reagents for this work and details of the experimental procedure have been previously described.[1]

The methods of calculation for the phenol and catechol complexes are the same as reported previously.[1] The calculations for the guaiacol complex with DMSO are identical with the calculations for the phenol complexes. Molar absorptivities for guaiacol, phenol, and catechol were determined as a function of temperature and were in agreement with those previously reported.[9] Concentrations of the hydroxybenzenes were about 0.002 M and the THF and n-Bu$_2$S concentrations ranged from 0.1 to 0.2 M. The DMSO concentration was about 0.003 M.

Results and Discussion

The thermodynamic properties and frequency shifts for the various complexes are given in Tables I and II, respectively. The standard enthalpy change was found from the slope of a plot of log K vs. T^{-1} and the entropy change was calculated from the intercept.

Spectra of solutions of guaiacol in CCl$_4$ solution show a single absorbance band at 3556 cm^{-1} corresponding to absorption by the intramolecular hydrogen bond. No cis-trans equilibrium is observed. No change in the molar absorptivity of this band other than that due to the normal temperature dependence was detected and no additional absorbance bands were found in solutions containing THF or n-Bu$_2$S indicating that the intramolecular bond in guaiacol persists at the electron donor concentrations used in this work. For solutions containing DMSO the molar absorptivity was found to decrease in proportion to the DMSO concentration and a second absorbance band at 3251 cm^{-1} was observed indicating that DMSO is a sufficiently strong electron donor to disrupt the intramolecular

hydrogen bond in guaiacol with consequent formation of an intermolecular hydrogen bonded complex.

The equilibrium constants for the guaiacol–DMSO complex (Table I) are less than those for the phenol–DMSO complex by a factor of nearly 50 and reflected the difficulty of disruption of the intramolecular bond. The frequency shift for the phenol–DMSO complex is 354 cm^{-1} as compared to 360 cm^{-1} for the guaiacol–DMSO complex. The enthalpy change is -6.3 kcal mol^{-1} for the phenol complex while that for the guaiacol complex is -3.0 kcal mol^{-1}. Such a large difference between the enthalpy changes would not be expected on the basis of the Badger–Bauer rule[10] but this rule cannot be expected to apply to the guaiacol–DMSO complex. The reason the rule fails in this instance is that the frequency shift is an approximate measure of the strength of the interaction between donor and acceptor but the enthalpy change is a measure of the sum of all the interactions leading to hydrogen bond formation. The Badger–Bauer rule does not take into account the disruption of the intramolecular hydrogen bond in guaiacol which precedes the intermolecular association but this is reflected in the enthalpy change. The frequency shifts for the phenol–DMSO and guaiacol–DMSO complexes are nearly identical. This would be expected if the strength of the donor–acceptor interaction is not altered by the methoxy group ortho to the hydroxyl group. It seems reasonable then to conclude that the strength of the intermolecular bond between guaiacol and DMSO is about the same as that between phenol and DMSO.

The enthalpy change for the formation of the guaiacol–DMSO complex may be considered to be given by the sum of the enthalpy change for the disruption of the intramolecular bond, ΔH_{intra}, and the enthalpy change resulting from formation of the intermolecular bond, ΔH_{inter}. If the enthalpy change for the formation of the intermolecular bond is about the same as that for the formation of the phenol–DMSO hydrogen bond, ΔH for the overall reaction is given by

$$\Delta H = \Delta H_{intra} + \Delta H_{inter} \qquad (1)$$
$$-3.0 = \Delta H_{intra} - 6.3$$

which gives the enthalpy for disruption of the intramolecular bond as $+3.3$ kcal mol^{-1}. All of the species participating in equilibria of this work are solvated to some extent. The above procedure should give a value for ΔH_{intra} which approximates a vapor-phase reaction because the solvation energies would be expected to nearly cancel by taking the difference $\Delta H - \Delta H_{inter}$.

The persistence of the intramolecular bond of guaiacol in solutions containing THF and n-Bu$_2$S, for which the enthalpy change for the formation of intermolecular bonds with phenol is -4.9 and -3.3 kcal mol^{-1}, respectively, must be due to an unfavorable entropy change.[11] If the equilibrium constant for the formation of the complexes of this work is much less than one, spectroscopic observation of the complex species becomes difficult. It is reasonable to suppose that THF and n-Bu$_2$S form complexes with guaiacol with overall enthalpy changes equal to the enthalpy required to disrupt the intramolecular bond plus the enthalpy released as a result of the formation of the interbond. If the interbond enthalpy is approximately that of the corresponding donor complex with phenol and if the intramolecular bond energy is about 3.3 kcal, ΔH for the formation of THF and n-Bu$_2$S complexes with guaiacol would be ex-

pected to be about -1.6 and 0 kcal mol^{-1}, respectively. For entropy changes on the order of those of this work ΔG^0 is not sufficiently negative to allow spectroscopic observation of the equilibrium. The larger donor–acceptor interaction for the intermolecular DMSO–guaiacol hydrogen bond is sufficient to over shadow the unfavorable entropy change so that spectroscopic observation of this complex species is possible.

The spectra of solutions of catechol in CCl$_4$ show two absorbance bands corresponding to absorption by the free hydroxyl at 3611 cm^{-1} and the intramolecularly hydrogen bonded hydroxyl at 3558 cm^{-1}. In the presence of DMSO, THF, and n-Bu$_2$S the molar absorptivity of both bands decreases and a third absorption band at lower frequency is found. Complex formation between catechol and these electron donors was considered to occur in stepwise fashion.[1]

$$(2)$$

$$(3)$$
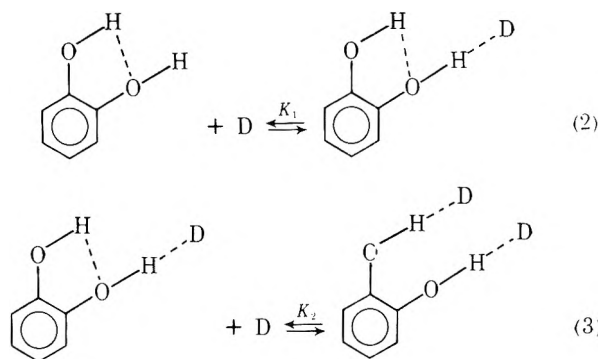
Table II lists the frequency shifts obtained for the various complexes with catechol. These shifts are seen to be considerably larger than those for the corresponding phenol complex. Also included in Table II are frequency shifts for the complex formation of the dihydroxybenzenes, resorcinol and hydroquinone, with the various proton acceptors. These shifts indicate that the presence of two hydroxyl groups is not in itself sufficient to account for the difference in frequency shift observed between the phenol and catechol complexes. If the two hydroxyls are ortho so that intramolecular bonding may occur, the frequency shift and ΔH_1, given in Table I, are seen to be significantly larger than those for the phenol complexes. Thus the intramolecular bond acts to increase the availability of the free hydroxyl proton for intermolecular hydrogen bonding.

Just as the intramolecular bond in guaiacol persists in solutions containing THF and n-Bu$_2$S because of unfavorable entropy changes, the intramolecular bond in catechol is disrupted by all the electron donors of this work due to a favorable entropy change. On the basis of the guaiacol–DMSO data, ΔH_2 for catechol complexes would be expected to be exothermic but less so than ΔH_1. However, ΔH_2 for all electron donors with catechol is positive.

The positive enthalpy change could conceivably result from a strengthening of the intramolecular bond in catechol due to the increased basicity of the oxygen of the hydroxyl group which has its proton intermolecularly hydrogen bonded. Nishimura, Ke, and Li[12] have accounted for the difference in K_1 and K_2 for TBP–H$_2$O complexes by considering that when one of the water hydrogens is bonded to TBP, the water oxygen becomes more basic. If this occurs for the catechol complexes, the increased basicity of the oxygen of the intermolecularly bonded hydroxyl could produce a stronger intramolecular bond. If ΔH_2 is viewed as a sum of the interactions necessary to break the intra-

molecular bond and form the intermolecular bond, the increase in the intramolecular bond strength due to increased oxygen basicity must be on the order of several kcal. Previous studies of the geometric relations between OH $\cdots$ O intramolecular bond lengths and energies[13] indicate that a change in energy of this magnitude must be accompanied by considerable changes in bond lengths and angles for the intrabond. Further, any changes sufficient to produce large energy differences in this bond would lead to a large frequency shift for the intramolecularly bonded band at 3558 cm^{-1}. No such shift is observed. It is possible to maintain the frequency difference between the 3611- and 3558-cm^{-1} bands constant by allowing the O $\cdots$ O and OH distances and angles of the intramolecular bond to vary, but at most only a few tenths of a kcal increase in bond strength can be realized in this fashion. Thus it appears that even if the basicity of the oxygen of the interbonded hydroxyl is increased only a small change in intramolecular bond strength can be achieved. Therefore other factors such as solvation must be held accountable for the endothermicity of the second step.

The influence of solvation effects on ΔH_2 may be seen by consideration of the cyclic process
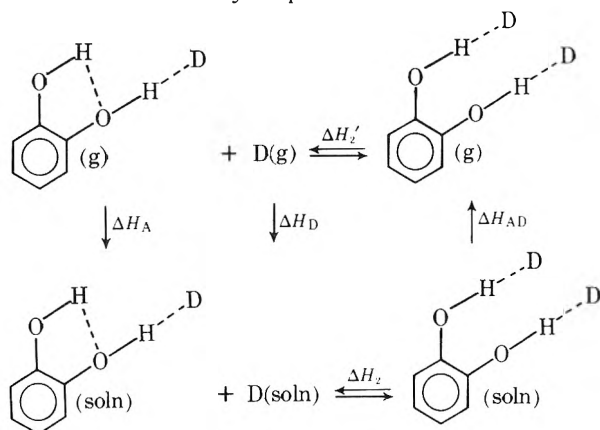
where

$$\Delta H_2' = \Delta H_A + \Delta H_D + \Delta H_2 + \Delta H_{AD} \qquad (4)$$

ΔH_2 is the enthalpy change determined in this work, $\Delta H_2'$ is the enthalpy change for the reaction in the vapor phase, and the remaining terms are enthalpies of solvation or desolvation. ΔH_A and ΔH_D would be expected to be negative terms corresponding to an exothermic solvation process. ΔH_{AD} should be a positive term corresponding to the vaporization of the dicomplex from solution. Thus $\Delta H_2'$ differs from ΔH_2 by

$$\Delta H_2' - \Delta H_2 = |\Delta H_{AD}| - |\Delta H_A| - |\Delta H_D| \qquad (5)$$

$\Delta H_2'$ would be expected to be negative because the enthalpy of the intermolecular bond formed following disruption of the intramolecular bond is greater than the enthalpy required to break the intramolecular bond. Because $\Delta H_2 > 0$, the difference in solvation enthalpies must be negative which means that the solvation enthalpies of the monocomplex, ΔH_A, and donor, ΔH_D, are greater than that of the dicomplex. In terms of the entropy changes, ΔS_2, this seems reasonable. A tighter more highly structured solvent orientation about the monocomplex and donor is indicated by the positive entropy change and this implies greater solvation enthalpies. This can be contrasted with the process corresponding to ΔH_1. Equation 2 shows
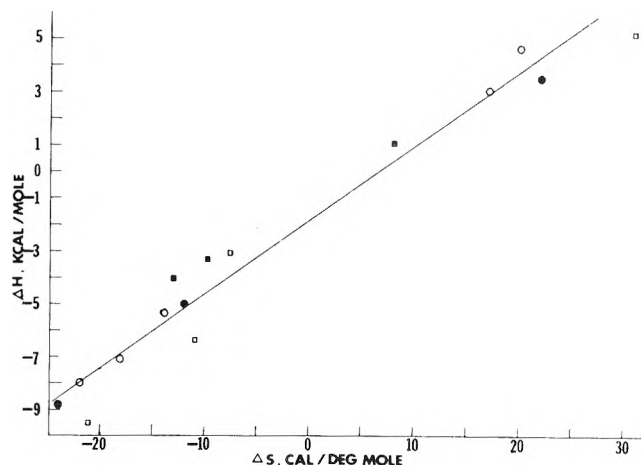
Figure 1. ΔH vs. ΔS for the hydrogen bonding of various donors to the hydroxybenzenes. The data for diethyl ether was taken from ref 1: O, Et$_2$O; ●, THF; □, DMSO; ■, n-Bu$_2$S. The solid line is the least-squares equation $\Delta H(\text{kcal}) = 0.27 \Delta S(\text{cal deg}^{-1} \text{ mol}^{-1}) - 1.82$. The coefficient of correlation is 0.98 and the standard deviation is 0.98.

that the donor and monocomplex appear on different sides of the reaction equation thus the solvation enthalpies would partially cancel for ΔH_1.

The difference $|\Delta H_{AD}| - |\Delta H_A|$ is expected to be nearly constant for each donor. However ΔH_D, the solvation enthalpy of the donor, will vary from donor to donor. The solvation enthalpy of DMSO would be expected to be more negative than that of THF which in turn should have a more negative solvation enthalpy than n-Bu$_2$S.

If $|\Delta H_{AD}| - |\Delta H_A|$ is taken to be roughly the same for the three donors, $\Delta H_2' - \Delta H_2$ will vary from system to system depending on the enthalpy of solvation of the donor, ΔH_D. A more negative ΔH_D translates to a more positive ΔH_2. For the systems studied here, the solvation effects, principally those of the donor, are evidently larger than the bonding interaction so that ΔH_2 is positive and becomes more positive as the solvation enthalpy of the donor increases. It also follows from this analysis that deviations from the Badger–Bauer rule for a given electron pair acceptor with different donors may be observed due to differences in solvation enthalpies of the donor.

Pimentel and McClellan[10] have shown that a linear relation exists between ΔH and ΔS for hydrogen bond formation. They explained this relationship by reasoning that a more negative ΔH implies stronger bonding with a more restricted configuration in the complex, hence a greater order and a larger negative value of ΔS. The results of this study and a prior study on the bonding of the hydroxybenzenes with diethyl ether[1] have been used to plot ΔH vs. ΔS as shown in Figure 1. It is seen that a linear relation is implied. The rationale of Pimentel and McClellan is reasonable if ΔH represents only the interactions directly responsible for formation of the hydrogen bond, however, for guaiacol this is not the case. As shown previously, there are interactions included in ΔH for the guaiacol–DMSO complex which are not representative of the strength of the donor–acceptor interaction. Likewise, it seems that ΔH_2 does not represent the strength of the donor–acceptor interaction but rather may be largely influenced by solvation effects. The $\Delta H - \Delta S$ relation like the Badger–Bauer rule does not permit a simple interpretation in terms of hydrogen bond strength. In particular, the fact that a given sys-

tem follows the $\Delta H - \Delta S$ relation does not necessarily mean that inferences regarding the tightness of bonds in the complexes can be made.

References and Notes

(1) J. N. Spencer, R. A. Heckman, R. S. Harner, S. L. Shoop, and K. S. Robertson, *J. Phys. Chem.*, **77**, 3103 (1973).

(2) T. Gramstad, *Spectrochim. Acta,* **19**, 829 (1963).

(3) R. S. Drago, B. Wayland, and R. L. Carlson, *J. Amer. Chem. Soc.,* **85**, 3125 (1963).

(4) T. Gramstad, *Spectrochim. Acta,* **19**, 497 (1963).

(5) S. Singh and C. N. R. Rao, *J. Amer. Chem. Soc.,* **88**, 2142 (1966).

(6) H. Dunken and H. Fritszche, *Z. Chem.,* **1**, 249 (1961).

(7) L. J. Bellamy, G. Eglinton, and J. F. Morman, *J. Chem. Soc.,* 4762 (1961).

(8) R. West, D. L. Powell, M. K. T. Lee, and L. S. Whatley, *J. Amer. Chem. Soc.,* **86**, 3227 (1964).

(9) E. A. Robinson, H. D. Schreiber, and J. N. Spencer, *J. Phys. Chem.,* **75**, 2219 (1971).

(10) G. C. Pimentel and A. L. McClellan, *Annu. Rev. Phys. Chem.,* **22**, 347 (1971).

(11) H. H. Jaffe, *J. Amer. Chem. Soc.,* **79**, 2373 (1957).

(12) S. Nishimura, C. H. Ke, and N. C. Li, *J. Amer. Chem. Soc.,* **90**, 234 (1968).

(13) W. R. Snyder, H. D. Schreiber, and J. N. Spencer, *Spectrochim. Acta, Sect. A,* **29**, 1225 (1973).

Effects of Anions on the Potentials of Zero Charge of Metals

Ashok K. Vijh

Hydro-Quebec Institute of Research, Varennes, Quebec, Canada   (Received December 21, 1973;

Revised Manuscript Received July 10, 1974)

By assuming that the specifically adsorbed anions form a surface compound on the electrode surface, considerations are developed for calculating the magnitude of the parameter, *b*, characteristic of the interactions involved between the metal electrode and the anions. This interaction parameter takes into account both the heats of hydration of the anions and the covalent bond energy involved in the binding between the electrode and the anions. It is shown that the specific adsorbability of a large number of anions on mercury is related *directly* to the calculated values of the parameter *b*; i.e., higher specific adsorbability is associated with higher magnitudes of the interaction parameter. The analysis presented also permits the evaluation of the interactions involved in the specific adsorption of a given anion on a series of metals and the correlation of these interactions with the specific adsorbability of the anion on these metals; the data available in the literature, however, are too scarce to allow a verification of the latter considerations.

Introduction

Barclay[1] has recently collected data on the potentials of zero charge of mercury in 0.1 *M* aqueous solutions of numerous salts covering a wide range of anions. His purpose was to examine the extent of specific adsorption of these anions, as shown by the departures of the potential of zero charge (pzc) in various solutions from the "reference value" of 437 mV (sce) in fluoride solutions, in relation to the properties of these anions. Qualitatively good results were obtained in correlating the specific adsorption with the "softness" or the "hardness" of the ions as expounded in the theories of Pearson.[2] It was further shown by Barclay[1] that his interpretations in terms of Pearson's ideas[2] qualitatively supported the concept of specific adsorption put forward by Grahame[3] in which contact adsorption is assumed to lead to a covalent bond between the electrode and the ion.

According to the criteria of Bockris, *et al.*,[3] supported by Devanathan and Tilak,[4] the degree and the type of ionic solvation determine predominantly the tendency of an ion to undergo contact adsorption. This viewpoint[3,4] was criti-

cized by Barclay[1] by maintaining that sulfide ions, which undergo strong contact adsorption,[5] are strongly hydrated and hence should not adsorb specifically on the basis of criterion of Bockris, *et al.*[3]

The only attempt to estimate quantitatively the magnitude of the interaction involved between the electrode and the specifically adsorbed ions is due to Bockris, *et al.*[3] They assumed a covalent bond (*cf.* Grahame[6]) between the mercury electrode and the specifically adsorbed halide ions and estimated the magnitude of the "bond energy" by means of the well-known Pauling equation.[7a] They found, however, that in the halide series, the order of specific adsorption was opposite to that of the magnitude of the M–X bond energy (where X is the halide) as estimated by the Pauling equation. As pointed out elsewhere,[7] the Pauling equation gives an estimate of the bond dissociation energy of an isolated *gas-phase* molecule and hence is really not too relevant in the estimation of the interactions involved in the specific adsorption of anions.

It is clear from the foregoing that a clear-cut quantitative correlation between the specific adsorption tendencies of

several anions and their various parameters has not yet been established. The object of the present paper is to explore this further by taking into account the previous suggestions[3,4,6] that hydration of the ions and the energy of the covalent bond between the adsorbed anion and the electrode are the important factors involved.

Correlation between Specific Adsorption of Anions and Their Energies of Interaction with the Electrode

It has been noted[1] that in fluoride solutions, in which the specific adsorption is absent (see, however, the evidence for slight contact adsorption of F^- ions in ref 7b), the $-E_{pzc}$ is 437 mV (vs. sce) and the specific adsorption of various anions pushes this potential to more cathodic values. As a semiquantitative measure of the extent of specific adsorption tendency of an anion, one may take the parameter ΔE_{pzc}, which is the difference between the pzc of mercury in the solution of a given anion and in the fluoride solution. Higher $-\Delta E_{pzc}$ (minus sign denotes the more cathodic direction of pzc resulting from the specific adsorption) values would thus indicate higher extent of specific adsorption.

In order to calculate the interaction energy, b, involved between the adsorbed anion, X^-, and the metal electrode, M, we assume that the specifically adsorbed anion is closely bound to the metal surface, thus leading to its demetallization[8] by forming a surface compound, MX. In some previous work 8b, such bond formation in specific adsorption has been suggested by Andersen and Bockris whose approach to the present problem involved a detailed consideration of dispersion energy. Our viewpoint involves the application of a Born–Haber cycle to the demetallized surface and the appropriate reaction involved in this picture of specific adsorption is

$$X_{aq}^{n-} + M(S/L) \longrightarrow MX(S) + ne \quad (1)$$

Here S denotes that the surface compound MX is a solid; M(S/L) denotes that the metal is in its standard state, being solid S for most metals and liquid L for mercury; n^- is the valency of the anion forming MX.

During the desorption (or removal) of the surface compound MX from the electrode, the reaction involved is opposite to that in eq 1, i.e.

$$MX(S) + ne \longrightarrow M(S/L) + X_{aq}^{n-} \quad (2)$$
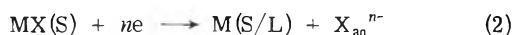
The enthalpy change in reaction 1 is equal to that in reaction 2 but opposite in sign; also this enthalpy change is the measure of the interaction energy, b, involved in the adsorption/desorption process taking place in the foregoing description of contact adsorption. The enthalpy change in reaction 2, i.e., the b can be shown, on the basis of an appropriate Born–Haber cycle,[7a] to be given by

$$b = -\Delta H_f + (1/2)\Delta H_{diss} + A_{x-} + (\Delta H_h)_{x-} + \phi \quad (3)$$

Where ΔH_f is the heat of formation (standard state) per anion of the surface compound MX formed (e.g., a metal halide); $(1/2)\Delta H_{diss}$ is half the heat of dissociation of a halide molecule (in the gas phase) to create the halide atom, X; A_{x-} is the electron affinity of the X atom; $(\Delta H_h)_{x-}$ is the heat of hydration of the halide ion, X^-; ϕ is the work function of the metal and refers to the energetic quantity involved in pulling out an electron from the conduction band of the metal and bringing it to the gas phase where it can react with X to give X^-. For a given metal, e.g., Hg (as in this section), ϕ is constant and hence may be ignored in the evaluation of the relative changes in the values of interac-

tion energy of various anions on a given metal, viz., Hg. It is clear that if the MX involves an anion other than a halide, $(1/2)\Delta H_{diss}$ will be replaced by an appropriate heat term needed to create that anion in its uncharged (i.e., atomic or molecular) state, e.g., S for the S^{2-} anion. The following discussion on Hg is facilitated by adopting an example here in which X represents a halide atom and the term in ϕ ignored for reasons stated above.

Now we define a quantity here, namely, the heat of formation of X^- in the aqueous solution, $(\Delta H_{fX-})_{aq}$. This quantity is given by

$$(\Delta H_{f_{X-}})_{aq} = (1/2)\Delta H_{diss} + A_{x-} + (\Delta H_h)_{x-} \quad (4)$$

By combining eq 3 and 4, we get

$$b = -\Delta H_f + (\Delta H_{f_{X-}})_{aq} \quad (5)$$

The interaction parameter b as calculated by eq 5 and the values of $(\Delta H_{fX-})_{aq}$ for various anions discussed by Barclay[1] are given in Table I together with their source references. A plot of this interaction parameter, b, against the $-\Delta E_{pzc}$ values (plotted on a log scale) for various anions on Hg shows (Figure 1) clearly that more cathodic ΔE_{pzc} values tend to be associated with higher b values, i.e., higher specific adsorption tendency heralds stronger interaction energy between the anion and the electrode, for the anions for which data are available. In order to explore the possibility of this correlation (Figure 1) for additional anions for which ΔH_f values could not be found, we note that an approximate linear correlation exists (Figure 2) between the parameters b and $(\Delta H_{fX-})_{aq}$ of eq 5; hence, a plot between $(\Delta H_{fX-})_{aq}$ and log $(-\Delta E_{pzc})$ would have the same rough significance as the plot between b and log $(-\Delta E_{pzc})$. The plot of log $(-\Delta E_{pzc})$ vs. $(\Delta H_{fX-})_{aq}$ values for 11 anions is examined in Figure 3 which supports the trend observed in Figure 1, which included eight anions only because of the unavailability of data for all anions.

It should be noted that the interaction parameter b of eq 5 (i.e., the enthalpy change in reaction 1 or 2) incorporates both of the conceptual factors thought to be important in the specific adsorption of anions, i.e., the covalent bond formation and the hydration of the anions. In eq 3, the heat of hydration comes in explicitly; as regards the covalent bond energy, we note that the covalent bond involved in specific adsorption refers to the enthalpy of the reaction

$$MX(S) \longrightarrow M(S/L) + X \quad (6)$$
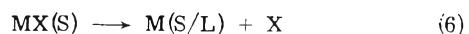
Reaction 6 is, of course, same as reaction 2 but involving only the rupture of the covalent bond of MX, without subsequent hydrated anion formation from the X. The bond energy E, of the bond breaking involved in eq 6, is given by

$$E = -\Delta H_f + 1/2\Delta H_{diss} \quad (7)$$

In other words, the first two terms on the right-hand side of eq 3 give the covalent bond energy involved in the bond breaking (desorption) or making (adsorption) involved in the specific anion adsorption; the term $(\Delta H_h)_{X-}$ on the right-hand side of eq 3 refers to the appropriate hydration (or dehydration, as the case may be) involved; however, an additional term, A_{X-} (and work function, ϕ, if different metal electrodes are being compared), also enters in the complete evaluation of this interaction parameter, b, assuming that specific anion adsorption and desorption proceeds by reactions 1 and 2, respectively.

In addition to the representation adopted here for the specific adsorption tendency of an anion, namely, ΔE_{pzc},

TABLE I[a]

Anion	$(\Delta H_{f_{X^-}})_{aq}$, kcal	$-\Delta H_f$, kcal	b, kcal	$-\Delta E_{pzc}$, mV
S^{2-}	7.8	13.5	21.3	443
I^-	-13.37	12.4	-0.97	256
CN^-	36.1	-31.2	4.9	208
CNS^-		-24.0		152
Br^-	-28.9	20.2	-8.9	98
N_3^-		-66.5		72
NO_3^-	-49.37	29.5	-19.87	41
ClO_4^-	-31.41			33
Cl^-	-40.2	27.5	-12.7	24
CH_3COO^-	-116.84	99.7	-17.14	19
NO_2^-				13
HCO_3^-	-165.18			3
CO_3^{2-}	-161.63			3
SO_4^{2-}	-216.9	168.3	-48.6	1
F^-	-78.66	47.5	-31.15	0

[a] The $(\Delta H_{f_{X^-}})_{aq}$ values are per mole of the anions (i.e., per anion) and are taken from Harvey and Porter.[8a] The ΔH_f values are also per *anion* of the MX compound formed and refer to the divalent mercury (i.e., MX in its highest oxidation state) compound in the crystalline form. These values are from ref 9 except for crystalline HgF_2 for which the value could be found only in Sanderson.[10] For the NO_3^-, the value of $-\Delta H_f$ available for $Hg(NO_3)_2 \cdot 0.5H_2O$ has been corrected by subtracting the heat of formation (in the liquid state) of $0.5H_2O$. The ΔH_f values for divalent Hg compounds have been used because (i) they refer to the stablest state of the demetallized Hg; (ii) ΔH_f values when taken as per *equivalent* (as here) are nearly identical for monovalent and divalent Hg compounds; e.g., $-(\Delta H_f)_c$ for HgO (a divalent compound) is 10.8 kcal whereas for Hg_2O (a univalent compound), it is 10.9 kcal.[9] The work function, ϕ, value for Hg is not included in the interaction parameter b (cf. Eq. (3)) for reasons stated in the text.
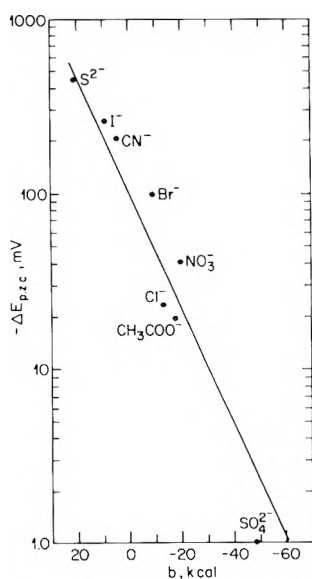
Figure 1. A plot of log $(-\Delta E_{pzc})$ vs. b; $-\Delta E_{pzc}$ refers to the difference in the pzc of Hg in the 0.1 N solution of the shown anions and in 0.1 N F^- ion solutions and is a measure (see text) of the specific adsorbability of the anion. b is the magnitude of the interaction energy between the anion and the mercury electrode, as computed by eq 5. See Table I for data and their source references, and the text for the significance of this correlation.

the specific adsorbability can also be represented by the superequivalent charge values determined on a metal in solutions of various anions. These data have been given by Bockris, et al.,[3] for the contact adsorption of halides on Hg.
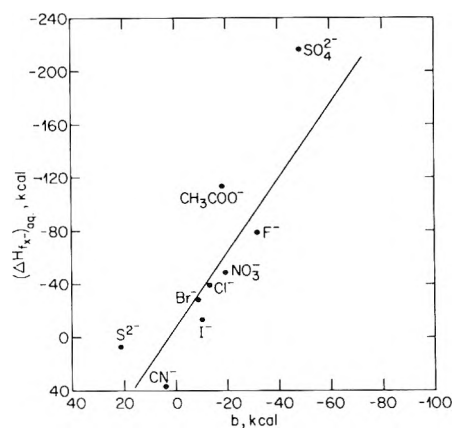
Figure 2. A plot of b vs. $(\Delta H_{X^-})_{aq}$, the latter being the heat of formation of the shown ions in their aqueous solutions. See Table I and the text.
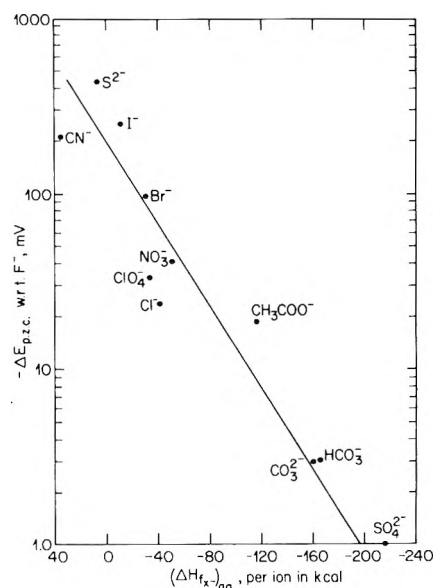
Figure 3. A plot of log $(-\Delta E_{pzc})$ vs. $(\Delta H_{X^-})_{aq}$ for the shown ions; these quantities are defined in the captions to Figures 1 and 2, and the text. The data are given in Table I.
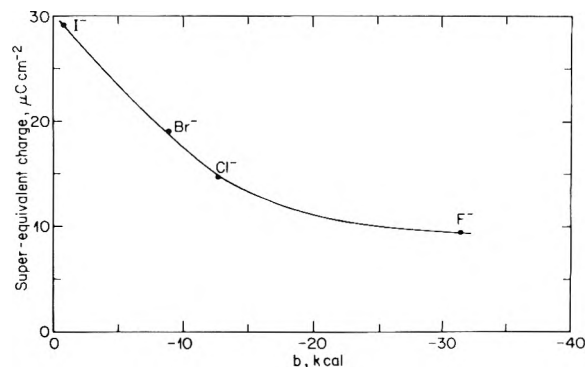
Figure 4. A plot of superequivalent charge[3] (which is a measure of the specific adsorbability) vs. the interaction parameter, b (Table I), for the halides on mercury in aqueous solutions.

When these superequivalent charge values are plotted against their interaction parameter, b, values (i.e., eq 5 and Table I), a rather smooth correlation is obtained (Figure 4). Higher superequivalent charge values (i.e., higher specific

adsorption tendencies) are associated with stronger interaction energy between the anion and the electrode.

Specific Adsorption of a Given Anion on Various Metals

The foregoing considerations can also provide a way to explore the specific adsorption tendency (as represented by $-\Delta E_{pzc}$) of a given anion on a series of metals. For a given anion, eq 3 becomes

$$b = -\Delta H_f + K + \phi \tag{8}$$

Here K is a constant for a given anion since it is the value of $(\Delta H_{fX^-})_{aq}$ as in eq 3 and 4. It follows that in the adsorption of a given anion, X^-, on a series of metals, the differences in the magnitudes of the interaction parameter b are accounted for by the corresponding differences in the ϕ values of metals and the $-\Delta H_f$ values of the MX, M'X, and M''X, etc. formed. To examine this suggestion, we need to know the $-\Delta E_{pzc}$ values on several metals under comparable conditions; these data, however, for a given anion on a *series* of metals are believed to be unavailable.

Some Limitations of the Foregoing Approach and Related Comments

It should be stated that ΔE_{pzc} as an indication of the relative degree of specific adsorption, as taken here, applies only to adsorption at the pzc, a case dealt with in this paper. At positively charged surfaces further removed from the pzc, some reversals in the trends of contact adsorption can occur. The later case is not treated here although the considerations developed here can probably provide an analysis of positively charged surfaces also.

A major assumption in the theory is the covalent bond formation between the metal and the specifically adsorbed anion. Lorenz and coworkers[11,12] have presented some di-

rect evidence for the partial transfer of charge of the adsorbed anion to the electrode, thus confirming our assumption of the formation of some sort of covalent bond. This work[11,12] has been recently critically reviewed by Parsons.[13] Also, from an intuitive point of view, when a dehydrated anion is within an interatomic distance of the electrode, formation of a chemical bond is to be expected.

Finally, the application of our arguments (*i.e.*, eq 8) to several metals can not be satisfactorily tested at the present time owing to the lack of extensive reliable data.

References and Notes

(1) D. J. Barclay, *J. Electroanal. Chem.*, **19**, 318 (1968).
(2) R. G. Pearson, *J. Amer. Chem. Soc.*, **85**, 3533 (1963).
(3) J. O'M. Bockris, M. A. V. Devanathan, and K. Muller, *Proc. Roy Soc., Ser. A*, **274**, 55 (1963).
(4) M. A. V. Devanathan and B. Tilak, *Chem. Rev.*, **65**, 635 (1965).
(5) R. D. Armstrong, D. F. Porter, and H. R. Thirk, *J. Electroanal. Chem.*, **16**, 219 (1968).
(6) D. C. Grahame, *Chem. Rev.*, **41**, 441 (1947).
(7) (a) A. K. Vijh, "Electrochemistry of Metals and Semiconductors," Marcel Dekker, New York, N.Y., 1973; (b) R. W. Reeves in "Modern Aspects of Electrochemistry," Vol. 9, B. E. Conway and J. O'M. Bockris, Ed, Plenum Press, New York, N.Y., in press.
(8) (a) K. B Harvey and G. B Porter, "Physical Inorganic Chemistry," Addison-Wesley, Reading, Mass., 1963, p 323; (b) T. N. Andersen and J. O'M. Bockris, *Electrochim. Acta*, **9**, 347 (1963).
(9) R. C. Weast, Ed., "Handbook of Chemistry and Physics," The Chemical Rubber Publishing Co., Cleveland, Ohio, 1968, p D-44.
(10) R. T. Sanderson, "Inorganic Chemistry," Reinhold, New York, N.Y., 1967.
(11) W. Lorenz and G. Kruger, *Z. Phys. Chem.*, **221**, 231 (1962).
(12) W. Lorenz, *Z. Phys. Chem.*, **224**, 145 (1963).
(13) R. Parsons, *Advan. Electrochem. Electrochem. Eng.*, **7**, 177 (1970).

Complex Solubility of Silver Iodide in Ethanol–Water, Methanol–Water, Acetone–Water, and Dioxane–Water Mixtures

Keith P. Anderson,* Eliot A. Butler, and Earl M. Woolley

Department of Chemistry, Brigham Young University, Provo, Utah 84602 (Received February 28, 1974)

Publication costs assisted by the Department of Chemistry, Brigham Young University

Results of a study of the solubility of silver iodide at 25° as a function of iodide ion concentration in water, in 10, 20, 30, 40, and 50% by weight methanol–water, ethanol–water, acetone–water, and dioxane–water mixtures, and in a 60% by weight dioxane–water mixture are presented. These results were obtained with previously established radiotracer techniques that are modified to include specific ion electrode measurements. All observed solubilities are interpreted in terms of the presence of iododisilver(I) ions, silver ions, undissociated silver iodide molecules, diiodoargentate ions, and triiodoargentate ions. Values of the thermodynamic equilibrium constants relating the activities of these species to the iodide ion activity are obtained by a least-squares treatment of the solubility data for each solvent mixture. The observed changes in these equilibrium constants are discussed in terms of electrostatics theory, solvation theory, and other specific solvent effects. It is notable that the formal solubility of silver iodide in "pure" solvent cannot be determined directly from its solubility product. The formation of stable iododisilver(I) ion increases the formal solubility of silver iodide to near that of silver chloride. The measured value of the solubility product constant of silver iodide in water compares well with values determined previously.

Introduction

The work reported in this paper is a continuation[1-3] of our study of the solubilities of slightly soluble silver salts as functions of anion concentration in aqueous–nonaqueous mixtures. The solubility of silver iodide and the various equilibria involved have been investigated in 0, 10, 20, 30, 40, and 50% by weight ethanol–water, methanol–water, acetone–water, and dioxane–water mixtures and in a 60% dioxane–water mixture at iodide ion concentrations between 10^{-6} and 10^{-1} M. A radiotracer technique described previously[3] was used to determine total silver concentrations. Silver ion activities were measured with an Orion Model 94-16 silver sulfide specific ion electrode. Our purposes were to determine what silver-containing species were present and to determine quantitatively the effects of the solvent compositions on the concentrations and equilibrium constants for formation of these species in solution and to interpret these effects.

Experimental Section

All chemicals used were reagent grade. Solutions were prepared from doubly distilled water which had a specific conductance $<1.3 \times 10^{-6}$ ohm^{-1} cm^{-1} at 25°. Gas chromatographic analysis of the four organic solvents used in solution preparations indicated the absence of water ($<0.1\%$) and volatile organic impurities.

The method of solution preparation, equilibration, and analysis has been described.[3] Solubility determinations (25), each at a different iodide ion concentration, were made in each aqueous–organic mixture. The solubility product constant, K_s, was determined from measurements of silver ion activities in solutions containing excess iodide ion by means of a specific ion electrode. The associated silver iodide formation constant, K_1, and the stepwise iododisilver(I), diiodoargentate(I), and triiodoargentate(I) ion formation constants, K_{12}, K_2, and K_3, were calculated using the modified least-squares method of data treatment

previously outlined[3,4] with the inclusion of an iterative procedure to avoid unequal weighting of data. The notation for the various equilibria is the generally accepted notation for consecutive or stepwise constants. The mass balance equation (eq 1a, 1b, and 1c) for these systems includes previous-

$$[Ag_{total}] = 2[Ag_2I^+] + [Ag^+] + [AgI] + [AgI_2^-] + [AgI_3^{2-}] \quad (1a)$$

$$[Ag_{total}] = \frac{2K_{12}K_1K_s^2 + K_s}{[I^-](\gamma_1^*)^2} + \frac{K_1K_s}{\gamma_0^*} + K_1K_2K_s[I^-] + \frac{K_1K_2K_3K_s[I^-]^2}{(\gamma_1^*)^2} \quad (1b)$$

$$[Ag_{total}] = \frac{A}{[I^-](\gamma_1^*)^2} + B + C[I^-] + \frac{D[I^-]^2}{(\gamma_1^*)^2} \quad (1c)$$

ly defined activity coefficients.[2] As can be seen in eq 1b and 1c, γ_0^*, the activity coefficient of the uncharged species in any solvent mixture, is constrained to be unity. This constraint forces the effect of the solvent to appear as variations in B values.[1] Values for the densities and dielectric constants of the solutions were obtained by interpolation of data as reported previously.[2,3] The potential difference between an Orion Model 94-16 silver sulfide electrode (which senses free silver ion in solution and free sulfide ion when silver ions are absent) and a double-junction calomel reference electrode was measured in the equilibrated solutions. An Orion Model 801 digital pH meter was used to measure the potential differences. The silver sulfide electrode was calibrated to read silver ion concentrations by measurements in standard AgNO$_3$ solutions of the same organic solvent content as the equilibrated sample solutions. Corrections for ionic strength effects were made.

The iodide ion concentrations were calculated from total iodide mass-balance equations. A value for the solubility product constant for AgI was calculated from the selective-ion-determined silver ion activity and the iodide ion activi-

TABLE I: Equilibrium Constants and Solubility Curve Equation Constants in Solvent Mixtures[a]

Wt % nonaqueous component	Dielectric constant	Mole fraction organic component	Log K_{12}	$-$Log K_s	Log K_2	Log K_3	$-$Log A	$-$Log B	%SD[b]
A. Ethanol–Water Mixtures									
0.00	78.54	0	13.45	16.21	2.35	1.81	9.34	6.88	16.3
9.67	72.99	0.0402	13.75	16.50	2.69	1.52	9.34	6.48	19.6
19.86	67.08	0.0885	14.14	17.23	2.20	2.10	9.67	6.34	12.1
34.47	58.37	0.1708	14.17	17.28	3.31	1.08	9.70	6.65	9.6
42.15	53.66	0.2220	13.33	16.76	3.65	0.74	10.01	6.41	18.7
54.23	46.66	0.3170	13.83	17.35	4.12	-1.33	10.11	7.12	12.5
B. Methanol–Water Mixtures									
9.47	74.36	0.0556	13.87	16.74	1.91	2.24	9.45	6.95	17.4
19.84	69.28	0.1223	14.34	17.35	1.33	2.94	9.60	6.51	9.2
34.48	62.19	0.2286	14.20	17.31	2.79	1.55	9.69	6.52	8.5
42.10	58.61	0.2905	13.60	17.00	2.72	1.75	9.98	5.79	10.6
54.20	52.88	0.3999	14.35	17.71	3.10	1.50	9.94	5.63	11.4
C. Acetone–Water Mixtures									
9.64	73.28	0.0321	13.16	16.19	1.87	2.46	9.62	6.32	18.4
19.80	67.73	0.0712	13.04	16.50	3.07	1.45	10.04	6.84	18.9
34.43	59.17	0.1402	12.83	16.66	3.89	1.24	10.41	6.43	4.1
42.08	54.41	0.1841	12.05	16.38	4.47	0.27	10.91	6.48	10.8
54.15	46.87	0.2684	11.81	16.62	5.86	2.18	11.39	4.59	6.4
D. Dioxane–Water Mixtures									
8.24	71.28	0.0181	12.80	15.84	1.66	2.63	9.62	6.58	18.3
20.47	60.37	0.0501	13.04	16.18	2.75	1.75	9.72	6.54	17.7
28.49	53.24	0.0754	12.43	15.97	3.44	1.06	10.13	7.50	11.5
40.75	42.33	0.1234	11.49	16.15	4.09	0.57	11.25	6.97	8.8
48.75	35.25	0.1630	11.69	16.28	4.58	-0.68	11.17	6.99	2.3
60.73	25.24	0.2405	11.20	16.32	5.10	1.98	11.70	6.31	5.1

[a] The assignment of meaningful values of uncertainties to be associated with our reported values of equilibrium constants is a difficult problem. The values we report here are given to what we consider to be a "reasonable" number of significant figures. [b] Relative (%) standard deviation of the experimental solubility data from the least-squares calculated solubility curve of eq 1.

ty in each of the equilibrated solutions. Values of K_s determined in this manner agreed with each other with an average deviation of only a few hundredths of a log unit until the mass-balance determination of free iodide ion became unreliably small. At low free iodide ion concentrations the concentrations of other iodide-containing species were no longer negligible in the determination of free iodide ion. Free iodide ion concentrations were calculated in this low concentration region using values of the mean solubility product constant and silver ion activities calculated from selective-ion electrode readings. Free iodide ion concentrations and total silver concentrations[5] were used to determine equilibrium constants by a least-squares fit of the data to eq 1c as discussed previously.[2,3] In the calculations it has been assumed that $\gamma_2^* = (\gamma_1^*)^4$.

Results and Discussion

A, B, C, and D of eq 1c were calculated by least-squares fitting of data to the solubility curves. The various stepwise formation constants were calculated from these constants and the solubility product constant determined through the use of the selective-ion electrode. The log values of A, B, K_{12}, K_s, K_2, and K_3 are listed in Table I. The deviation of B (the concentration of undissociated silver iodide species) from its value in pure water appears to be too large to be attributed to experimental error. In studies of solvent mixtures, variations in B caused by changes in the solvent mixture can be interpreted in terms either of variations in activity coefficient or variations in equilibrium constants. The former approach is used here. If it is supposed that

K_1K_s is constant in all solvent mixtures then variations in B can be interpreted in terms of differences between γ_0^* and γ_0, where γ_0 is the activity coefficient of the uncharged species in water solvent. An assumed constancy of K_1K_s implies the choice of a solvent-independent standard state for undissociated silver iodide so that variations in the value of K_1 with solvent composition reflect changes in the sum of the standard chemical potentials of Ag$^+$ and I$^-$, while variations in the value of K_2 reflect changes in the difference between the standard chemical potentials of I$^-$ and AgI$_2^-$.[1] The effect of holding K_1K_s constant is to subtract out nonlinear solvent effects that are apparently associated with the uncharged species.[6] Plots of log K_2 vs. $1/D$ show greatly improved linearity when K_1K_s is taken to be constant. Log K_1 values are not tabulated inasmuch as they are readily calculable from log B and log K_s values when K_1K_s constancy is assumed. Tabulated values of log K_2 are those arrived at using the K_1K_s constancy assumption. The values of $-$log K_s (log K_1), log K_{12}, log K_2, and log K_3 vs. the reciprocal of the dielectric constant of the solvent mixtures are plotted in Figures 1–3.

It should be noted that the values tabulated for 20% methanol and for 50% ethanol, acetone, and dioxane mixtures (excluding log K_s values) are less certain than those for the other mixtures. The experimental data for these four mixtures were uncertain at low free iodide concentrations.

The log K values given in Table I for pure water solvent are in good agreement with values from the literature. Typical values of $-$log K_s are 16.07,[7] 16.0,[8] 16.41,[9] and 16.09[10]
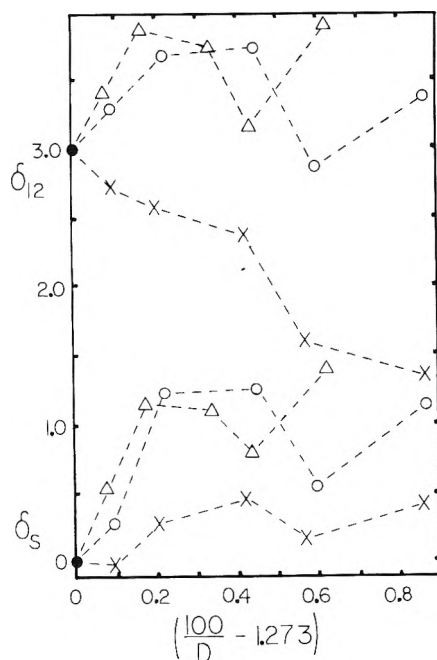
Figure 1. Plots of δ_{12} = log K_{12}(solvent) $-$ log K_{12}(water) + 3.00 and δ_s = log K_s (water) $-$ log K_s(solvent) according to Born electrostatic model:[2] ●, solvent = water; O, solvent = ethanol-water mixtures; △, solvent = methanol-water mixtures; ×, solvent = acetone-water mixtures.

Figure 3. Plots of δ_{12} = log K_{12}(water) $-$ log K_{12}(solvent) + 1.00, δ_3 = log K_3(water) $-$ log K_3(solvent) + 1.00, δ_s = log K_s(water) $-$ log K_s(solvent), and δ_2 = log K_2(solvent) $-$ log K_2(water) according to Born electrostatic model:[2] ●, solvent = water; □ and ■, solvent = dioxane-water mixtures.
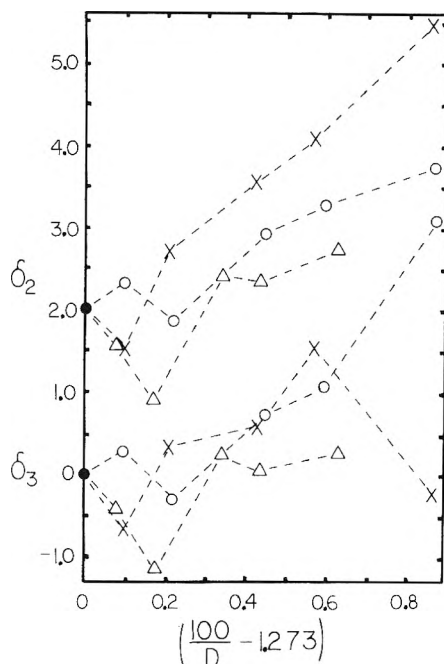
Figure 2. Plots of δ_2 = log K_2(solvent) $-$ log K_2(water) + 2.00 and δ_3 = log K_3(water) $-$ log K_3(solvent) according to Born electrostatic model:[2] ●, solvent = water; O, solvent = ethanol-water mixtures; △, solvent = methanol-water mixtures; ×, solvent = acetone-water mixtures.

compared to our value of 16.21. Previous workers have reported log K_1K_2 values of 10.7[7] and 11.2[11] compared to our value of 11.68. Our value of 13.49 for log $K_1K_2K_3$ compares with previously reported values of 13.4,[7] 14.00,[9] and 13.95.[12]

Kratohvil and Težak[9] report values of K_s (estimated), K_1K_2, and $K_1K_2K_3$ in 50% ethanol-water and in 48.5% ac-

etone-water that are in reasonable agreement with our values. They also give an estimated K_s value in 62% methanol-water.

The literature values of 13.20[13] and 10.3[14] for log K_1K_{12} in pure water solvent are significantly different from each other and from our value of 22.78. Our data are in reasonable agreement with those plotted by Kratohvil, Težak, and Vouk[15] through the concentration range that both of us studied. Our data, however, extend to much lower total silver concentrations, for we worked in excess I[-] while they worked in excess Ag^{+}. Moreover, there was a large difference in ionic strengths used by us and by Leden and Parck.[14] Those authors used 4 F NaClO$_4$ while we used ionic strengths below 0.1. The ionic strengths in our solutions where Ag$_2$I[+] is predominant are less than 0.001. Kratohvil, Težak, and Vouk[15] have already noted the large effect of ionic strength upon the solubility minimum, which is the region that leads to differences in K_1K_{12} values. The log of the formal concentration of dissolved silver is plotted $vs.$ the log of the free iodide concentration for pure water solvent in Figure 4. This plot is representative of data collected in all solvent mixtures and dramatically illustrates the increased solubility of silver iodide because of the formation of the stable Ag$_2$I[+] species.

Log K_{12}, log K_1 ($-$log K_s), log K_2, and log K_3 $vs.$ 1/D data fit straight lines constrained to pass through the water point fairly well. However the deviation from a straight-line fit is much more pronounced for log K_{12} and log K_1 data than for log K_2 and log K_3 data. The drastic effects of the initial disruption of the ordered pure water are notable in all instances.[1] The slopes of these plots (Table II) indicate that there are pronounced solvent effects which differ for each solvent system. It appears that both the molar volume of the organic component and its dipole moment may affect the rate of change of stability of a species, $i.e.$, the

TABLE II: Slopes of Plots of log K vs. $1/D$ (Figures 1-3)

	Methanol	Ethanol	Acetone	Dioxane
Log K_{12}	147	55	−201	−139[a]
Log K_1 and −log K_s	262	151	55	1
Log K_2	107[b]	201	386	149[a,c]
Log K_3	−42	−178[b,d]	−221[c,d]	−138

[a] The 60% point is omitted. [b] The 20% point is omitted. [c] The 10% point is omitted. [d] The 50% point is omitted.
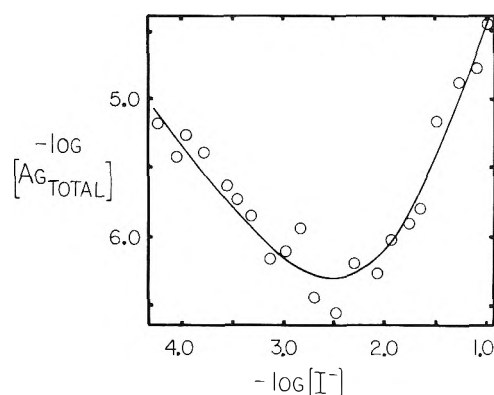
Figure 4. Plot of AgI solubility as a function of [I⁻] in aqueous solution illustrating the effect of Ag_2I^+ formation at low [I⁻]. (Compare eq 1.)

stability in a solvent mixture with a given dielectric constant. It is interesting to note that plots of log K_{12} and log K_1 vs. the product of the organic component mole fraction and the reciprocal of the dielectric constant of the solvent mixture (Figure 5) for the two alcohols are almost superimposable.

Plots of the logs of the constants A, B, C, and D appearing in eq 1 vs. the mole fraction of the organic component illustrate the similarities and dissimilarities in data obtained for OH and non OH containing organic solvents. Plots of log A, C, and D vs. organic component mole fraction can be approximated by straight lines.

One might expect the slopes of plots of log K vs. $1/D$ to be positive for equilibria involving electrostatic attraction between the reactants and negative for electrostatic repulsion. It is interesting that log K_{12} vs. $1/D$ has a positive slope for the two alcohols and a negative slope for mixtures containing organic components with no OH groups.

The magnitude of the slope of a plot of log K vs. solvent composition is a measure of the relative stabilities of the species at a given solvent-mixture dielectric strength. If the species involved were solvated to some extent by the organic component their effective radii would increase and the species formed by combination of these species should be less stable. This effect appears to be evident in equilibria described by K_{12}, K_1, and K_3, but is is reversed for the equilibrium described by K_2. The micro effect of electrostatic fields due to a large dipole moment for the organic component should diminish the electrostatic effects and make the complex species less stable. The dipole moments of methanol and ethanol are very nearly the same but that of acetone is much larger. This may in part explain the large changes in slope (stability at a given dielectric strength) when one compares mixtures containing methanol or ethanol with those containing acetone. Dioxane is a
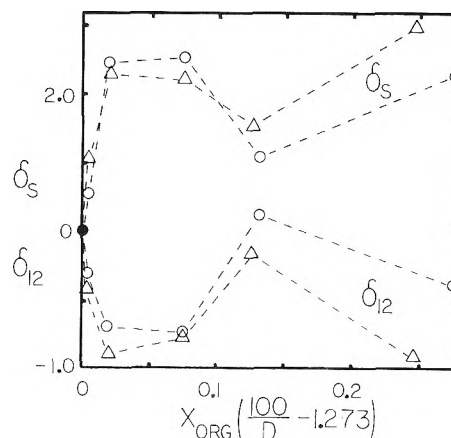
Figure 5. Plots of δ_{12} = log K_{12}(water) − log K_{12}(solvent) and δ_s = log K_s(water) − log K_s(solvent) illustrating similarities in effects of ethanol and methanol: ●, solvent = water; ○, solvent = ethanol–water mixtures; △, solvent = methanol–water mixtures.

large molecule with two polar oxygens but with a very small molecular dipole moment. It would be possible for the micro effects of dioxane to be that of a single polar oxygen, of a nonpolar molecule, or of some intermediate.

Acknowledgment. We are grateful to the Brigham Young University Research Division and to the NDEA Title IV Fellowship program for support of part of this work.

Supplementary Material Available. Solubility data consisting of [I⁻], [Ag$_{total}$], and ionic strengths of equilibrated solutions will appear following these pages in the microfilm edition of this volume of the journal. Photocopies of the supplementary material from this paper only or microfiche (105 × 148 mm, 24× reduction, negatives) containing all of the supplementary material for the papers in this issue may be obtained from the Journals Department, American Chemical Society, 1155 16th St., N.W., Washington, D.C. 20036. Remit check or money order for $3.00 for photocopy or $2.00 for microfiche, referring to code number JPC-74-2244.

References and Notes

(1) K. P. Anderson, E. A. Butler, and E. M. Woolley, *J. Phys. Chem.*, **77**, 2564 (1973).
(2) K. P. Anderson, E. A. Butler, and E. M. Woolley, *J. Phys. Chem.*, **75**, 93 (1971).
(3) K. P. Anderson, E. A. Butler, D. R. Anderson, and E. M. Woolley, *J. Phys. Chem.*, **71**, 3566 (1967).
(4) (a) K. P. Anderson and R. L. Snow, *J. Chem. Educ.*, **44**, 756 (1967); (b) T. P. Kohman, *ibid.*, **47**, 657 (1970).
(5) See paragraph at end of paper regarding supplementary material.
(6) K. P. Anderson, E. A. Butler. and E. M. Woolley, *J. Phys. Chem.*, **71**, 4584 (1967).
(7) D. D. Wagman, W. H. Evans, V. B. Parker, I. Halow, S. M. Bailey, and R. H. Schumm, *Nat. Bur. Stand. Tech. Note*, **No. 270-3** (1968); **No. 270-4** (1969).
(8) L. G. Sillen and A. E. Martell, "Stability Constants of Metal–Ion Complexes," The Chemical Society, London, 1964.
(9) J. Kratohvil and B. Težak, *Ark. Kemi*, **26**, 243 (1954).
(10) D. D. Wagman and M. V. Kildey, *J. Res. Nat. Bur. Stand., Sect. A*, **77**, 569 (1973).
(11) R. Alexander, E. C. F. Ko, Y. C. Mac, and A. J. Parker, *J. Amer. Chem. Soc.*, **89**, 3703 (1967).
(12) K. B. Yatsimirskii and V. P. Vasel'ev, "Instability Constants of Complex Compounds," Russian Translation, Consultants Bureau, New York, N.Y., 1960.
(13) D. C. Luehrs and K. Abate, *J. Inorg. Nucl. Chem.*, **30**, 549 (1968).
(14) I. Leden and C. Parck, *Acta Chem. Scand.*, **10**, 535 (1956).
(15) J. Kratohvil, B. Težak, and V. B. Vouk, *Ark. Kemi*, **26**, 191 (1954).

Laser Photoionization in Micellar Solutions. The Fate of Photoelectrons

M. Grätzel and J. K. Thomas*

Department of Chemistry and the Radiation Laboratory,[1] University of Notre Dame, Notre Dame, Indiana 46556 (Received June 20, 1974)

Publication costs assisted by the U. S. Atomic Energy Commission

Pyrene in aqueous micellar solution, either sodium lauryl sulfate (NaLS) or dodecyl trimethylammonium chloride (DTAC) may be photoionized by a 10^{-8}-nsec pulse of 347.1-nm light from a Q-switched ruby laser. The cation of pyrene is observed in the micelle phase and the electron in the aqueous phase as a hydrated electron. The reactions of the electron with solutes prior to thermalization and subsequent hydration are studied. The reactions of the hydrated electron with solutes on the micelle surface and the interior of the micelle are also studied. The reaction rates are subject to unusual salt effects. The data are discussed in terms of the double-layer theory of micelles, which also predicts a separation of 20–40 Å between the electron and the micelle. Ions such as Cu^{2+} and Cd^{2+} adsorbed in the micellar Stern layer of NaLS micelles are much less reactive with e_{aq}^{-} than in the free state. Hence the adsorption equilibria of these cations with NaLS may be measured. The binding constants are $K = 820$ and 1400 M^{-1} at 296°K for Cd^{2+} and Cu^{2+}, respectively. The adsorption equilibria are well described by a Langmuir isotherm.

Introduction

Photoionization of aromatic hydrocarbons has been observed in various polar and nonpolar liquids[2] and constitutes an important primary step in photochemical reactions. Recent laser photolysis studies have shown that the formation of ions often occurs *via* a biphotonic mechanism involving a direct two-quantum absorption of the ground state to give an excited state which ionizes.[3] Particular interest in photoionization and subsequent electron-transfer reactions arises from their importance in biological systems, for example it is suggested that these events play a major role in photosynthesis and vision processes.[4] Surfactant micelles serve as both structural and functional models for complex bioaggregates including proteins and biomembranes.[5] Of particular use is the knowledge of their static and dynamic properties such as microviscosity, aggregation number, and surface potential. In an effort to elucidate the nature of photoionization and electron-transfer processes in a biological environment we have initiated laser photolysis experiments with micellar model systems. Physical features of the photoionization of probes which reside in the hydrocarbon interior of micelles were reported in a previous communication.[6] Information was obtained about the range and energy loss of photoelectrons inside the micelles. In the present study the kinetic behavior and fate of parent cations and electrons is investigated. Photoelectrons which escape from the micelle become hydrated in the surrounding aqueous phase. The influence of the surface potential on the reactivity of hydrated electrons is analyzed and the electrical properties of the micellar double layer are used to determine the thermalization distance of photoelectrons. Photoelectrons can be scavenged by suitable solutes residing in the periphery region of the micelle. In such a system intramicellar electron transfer from the reduced form of the scavenger to the parent cation is observed.

Experimental Section

Materials. Sodium dodecyl sulfate (Matheson Coleman and Bell, USP grade) and dodecyl trimethylammonium chloride (Eastman) were recrystallized from methanol. Py-

rene (Kodak) was passed through silica gel in cyclohexane solution and then recovered. Benzoic acid, copper sulfate, and cadmium sulfate were Baker reagent grade and used without further purification. Laboratory-distilled water was redistilled from potassium permanganate.

Sample Preparation. Pyrene was solubilized in freshly prepared aqueous NaLS (0.1 M) solution by stirring the mixtures at 70°. The concentration of solubilizate was checked by optical density measurements. All samples were deoxygenated by bubbling with nitrogen for 30 min.

Apparatus. Laser photolysis experiments were carried out with a frequency-doubled, Q-switched ruby laser with an output of 250 mJ in the 347.1-nm line. The uv pulse had a duration of 20 nsec. Pulse radiolysis experiments were carried out using 1.5- or 15-nsec pulses of 2-MeV electrons from a Van de Graaff accelerator. Transients were detected by fast kinetic spectroscopy. Details of these techniques have been published elsewhere.[7]

Results and Discussion

A. Formation of Hydrated Electrons. Photoionization experiments were carried out in aqueous micellar solutions of sodium lauryl sulfate (NaLS) and dodecyl trimethylammonium chloride (DTAC). Pyrene which is quantitatively incorporated into these micelles was selected as the photoactive probe. In these solutions the photoionization event always occurs in the hydrocarbon-like environment of the micellar core. The prominent feature of the ionization process is that the photoejected electron has only to cross a short region of hydrocarbon phase, 10–20 Å depending on the chain length of the surfactant molecule, in order to reach the micelle water boundary where it becomes thermalized and hydrated

$$(e^-)_M \xrightarrow{\text{exit}} (e^-)_{H_2O} \xrightarrow{\text{thermalization}} (e_{th}^-)_{H_2O} \xrightarrow{\text{hydration}} e_{aq}^- \quad (1)$$
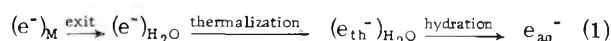
The events outlined in eq 1 occur on a very fast time scale. An upper limit for exit and thermalization time is estimated as 10^{-11} sec and a value of 2×10^{-12} sec has recently been reported for the hydration time of the electron.[8]

The subsequent fate of the hydrated electron depends on the charge of the micelles. In the case of an anionic micellar

solution such as NaLS, the reentry of e_{aq}^- is prevented by the repulsive electrostatic surface potential. Here the only feasible reaction of the hydrated electron is

$$e_{aq}^- + e_{aq}^- \longrightarrow H_2 + 2OH^- \qquad (2)$$

which has a rate constant of 5×10^9 M^{-1} sec^{-1}.[9] It was pointed out earlier[6] that the formation of hydrated electrons occurs via a biphotonic process with a surprisingly large quantum yield. Typical concentrations of hydrated electrons achieved from the photolysis of a 10^{-4} M solution of pyrene in 0.1 M NaLS are between 2 and 4×10^{-5} M. The calculated first half-lifetime of the e_{aq}^- decay is 5–10 μsec in agreement with the experimental observations. The lifetime of the positive parent ion which is left behind inside the micelle is very much longer ($\sim$25 msec) due to its slow exit rate from the micellar interior into the aqueous phase.

The course of photoionization events changes if solutes capable of scavenging "dry" photoelectrons or hydrated electrons are added to the micellar solution. A prerequisite to understanding these scavenging reactions is the knowledge of the electrical properties of the micellar double layer. Let us therefore briefly focus our attention on the potential distribution around a NaLS micelle.

B. Reactivity of Hydrated Electrons in NaLS Micellar Solution. 1. Potential Distance Function in the Diffuse Double Layer. The electrical potential ψ in a solution surrounding a spherical charged micelle is governed by the nonlinear Poisson–Boltzmann equation.

$$(r^{-2} \, d/dr)(r^2 \, d\Psi/dr) = (8\pi e n_{\pm} z_{\pm}/\epsilon) \sinh (z_{\pm} e\Psi/kT) \qquad (3)$$

where r is the distance from the center of the micelle, e is the elementary charge, n_+ is the number of ions per cubic centimeter in the solution bulk, $z_+ = z_-$ is their charge, and ϵ the dielectric constant. Solutions to this equation are required to satisfy the boundary conditions. $\psi(r_0) = \psi^0$, where r_0 is the radius of the micelle and ψ^0 the surface potential, and $\lim_{r\to\infty}\psi(r) = 0$.

While eq 3 has no direct analytical solution, approximate[10] and numerical[11,12] solutions have been given. In Figure 1 potential distance functions for two different values of ionic strength μ are shown which were obtained from a comprehensive collection of calculated data.[11] Parameters used are $r_0 = 17$ Å, for $\mu = 0.008$ M, $\psi^0 = -150$ mV[13] and reciprocal Debye length $1/\kappa = 30$ Å, and for $\mu = 0.1$ M, $\psi^0 = -75$ mV and $1/\kappa = 10$ Å. As is apparent from the figure the range of the Gouy–Chapman layer and the surface potential are greatly reduced upon addition of excess electrolyte.

The fact that the electrostatic potential in the Gouy–Chapman layer deviates from the potential in the bulk of the solution causes a gradient of ion concentration in the vicinity of the micelle described by Boltzmann's law

$$c(r) = c_b \exp[(\mp)z_{\pm}e\Psi/kT] \qquad (4)$$

where $c(r)$ is the concentration at a particular distance $r - r_0$ from the micellar surface and c_b is the ion concentration in the bulk. Distribution functions constructed from the potential distance curves by means of eq 4 are also shown in Figure 1. They provide a rationale for the behavior of hydrated electrons in NaLS micellar solution. Here $c(r)/c_b$ represents the probability of finding a hydrated electron at a distance $r - r_0$ from the micellar surface relative to the
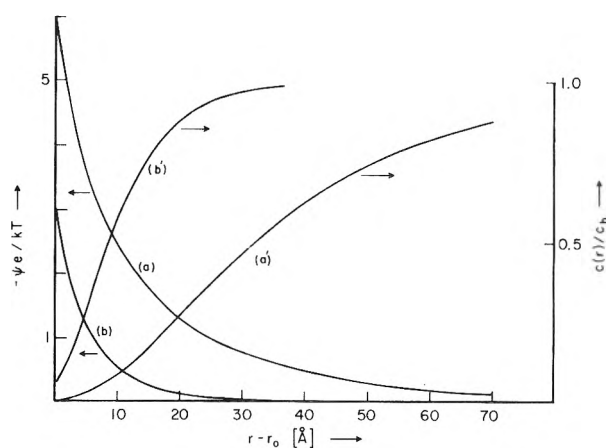
Figure 1. Left ordinate, potential distance function in the diffuse double layer of NaLS micelles: (a) $\mu = 0.008$ M; (b) $\mu = 0.1$ M. Right ordinate, distribution function for monovalent negative ions: (a') $\mu = 0.008$ M; (b') $\mu = 0.1$ M.

probability in the bulk phase, since the concentration of micelles usually outnumbers the concentration of hydrated electrons.

Kinetics of the reactions of e_{aq}^- with various solutes in NaLS micellar solution have been extensively studied by pulse radiolysis techniques.[14,15] In agreement with the probability function Figure 1a' it was found that scavengers solubilized exclusively in the micellar interior do not react with hydrated electrons. In cases where the scavenger is partitioning between the micellar and aqueous phase only the fraction present in water is reactive. This effect has been used as an analytical tool to determine distribution constants.[16] Similarly it may be applied to explore adsorption equilibria of various solutes which react with e_{aq}^-. Hydrated electrons are not expected to react with the adsorbed fraction of solute as the probability of contact between e_{aq}^- and NaLS micelles is practically zero in the absence of excess electrolyte (cf. Figure 1a'). Parameters for the adsorption of Cu^{2+} and Cd^{2+} ions are needed in order to interpret the photoelectron-transfer measurements described below.

2. Adsorption of Cu^{2+} and Cd^{2+} Ions at the Surface of NaLS Micelles. The pulse radiolysis technique was used to study the kinetics of reaction of hydrated electrons with Cu^{2+} or Cd^{2+} in aqueous micellar solutions of NaLS. Hydrated electrons are formed in homogeneous distribution by a 15-nsec pulse of high-energy radiation and their decay kinetics followed by fast kinetic spectroscopy (e_{aq}^- has a strong and characteristic absorption maximum at λ 720 nm). In these investigations the NaLS micelles usually did not contain solubilized pyrene; solutions with incorporated pyrene gave identical results. The half-lifetime of the decay τ is related to the scavenger concentration in the aqueous phase $[A]_w$ by[16]

$$[A]_w = (\ln 2/k)(1/\tau - 1/\tau_0) \qquad (5)$$

where τ_0 is the half-lifetime in the absence of scavenger and k is the rate constant for the reaction of e_{aq}^- with Cd^{2+} or Cu^{2+}. Literature values for $k_{Cu^{2+}}$ and $k_{Cd^{2+}}$ are 4.4×10^{10} and 6.4×10^{10} M^{-1} sec^{-1}, respectively.[17] After correcting for a small salt effect from the monomeric surfactant ions ($[NaLS]_{mon} = 8 \times 10^{-3}$ M) by means of eq 1 in ref 17 one obtains $k_{Cu^{2+}} = 3.1 \times 10^{10}$ M^{-1} sec^{-1} and $k_{Cd^{2+}} = 4.5 \times 10^{10}$ M^{-1} sec^{-1}. These values were used in eq 5 to calcu-

Figure 2. Adsorption of Cu^{2+} and Cd^{2+} ions on the surface of NaLS micelles, shown by a Langmuir isotherm plot of pulse radiolysis data; [NaLS] = 0.1 M.

Figure 3. Effect of ionic strength on the observed rate constant for the reaction of Cd^{2+} and e_{aq}^- in NaLS micellar solution; [NaLS] = 0.05 M, $[Cd^{2+}]$ = 10^{-3} M, added electrolyte NaCl.

late the amount of scavenger in the aqueous phase from the half-lifetime of the hydrated electron decay at different Cu^{2+} and Cd^{2+} concentrations. Subtraction of $[A]_W$ from the total analytical concen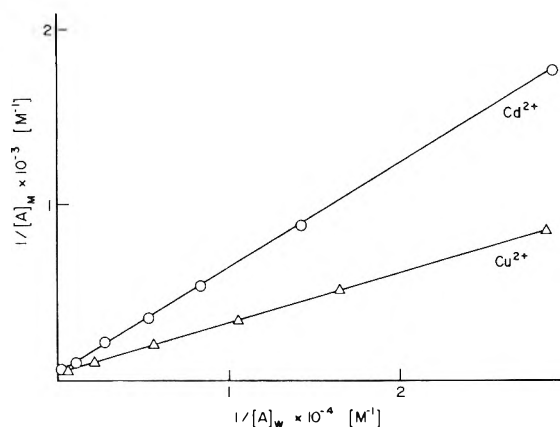tration yields the amount of adsorbed scavengers $[A]_M$. Plots of the functions $1/[A]_M$ vs. $1/[A]_W$ obtained from the above experiments are shown in Figure 2. The excellent linearity of the curves suggests that a Langmuir isotherm with the form

$$1/[A]_M = (1/KS)(1/[A]_W) + 1/S \qquad (6)$$

controls the adsorption process. This equation is derived from the more customary form of the Langmuir isotherm θ = $[A]_W/(1/K + [A]_W)$ by expressing θ, the fraction of free micellar surface covered with adsorbed molecules, as $[A]_M/S$ and rearranging. The common ordinate intercept of the curves in Figure 2 gives the amount of NaLS bound Cu^{2+} or Cd^{2+} ions at infinite concentration in the aqueous phase: $S_{Cu^{2+}} = S_{Cd^{2+}} = 2.1 \times 10^{-2}$ M. The concentration of micelles may be calculated from the total surfactant concentration, with cmc = 0.008 M and the aggregation number 62.[18] Hence on dividing the parameter $S_{Cu^{2+}}$ or $S_{Cd^{2+}}$ by the number of micelles it is possible to calculate the number of metal ions adsorbed on each micelle surface at monolayer saturation. The number found is 12 ions/micelle which corresponds to half the number of dissociated head groups of the micelle. Since this result is obtained by linear extrapolation of data from dilute Cu^{2+} or Cd^{2+} solutions, it does not imply that at high concentrations all free charges are neutralized on the micellar surface and no Na^+ is displaced. A suitable interpretation is that in dilute solutions of Cu^{2+} or Cd^{2+} an NaLS micelle offers place for maximal 12 bivalent ions in addition to its own atmosphere of Na^+ ions.

From the slope of the straight lines in Figure 2 we obtain for the binding constants $K_{Cd^{2+}} = 820$ M^{-1} and $K_{Cu^{2+}} = 1400$ M^{-1}. In Langmuir's[19] derivation of eq 6 it is assumed that the adsorption process involves the formation of a monolayer of adsorbed molecules on the surface of the adsorbent and that the adsorption enthalpy is independent of the degree of covering θ. Our finding and previous observations[20] indicate that both assumptions are good approximations for adsorption processes on micellar surfaces and underline the importance of the Langmuir isotherm in solubilization processes.

It should be noted that the half-lifetime of the hydrated
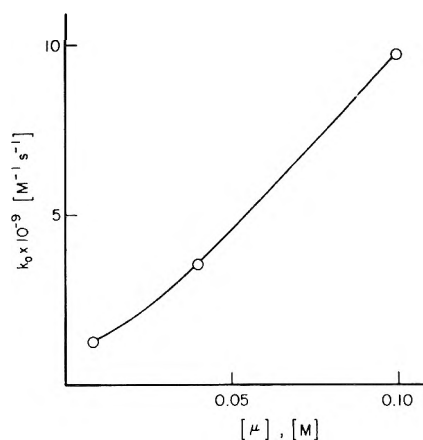
electrons reflects both its reaction with scavenger ion in the bulk solution and in the Gouy-Chapman layers. The latter contribution to the overall kinetics is neglected in determining the amount of adsorbed Cu^{2+} and Cd^{2+} ions by eq 5. However the error introduced by this approximation which may give rise to larger values of the binding constant is expected to be small, since the potential function is at its steepest close to the micellar surface.

It is concluded that both Cu^{2+} and Cd^{2+} are strongly adsorbed on the surface of NaLS micelles in a similar fashion to other bivalent transition metal ions.[21-23] The reason for this behavior may be found in electrostatic attraction and hydrophobic interaction of the ion and micelle. The latter phenomenon plays an important role in the kinetics of ester hydrolysis in NaLS micellar solution.[5] Inhibitory effects exerted by adsorbed cations in these reactions increase with the hydrophobicity of the ion indicating an increase of adsorption affinity with increased hydrophobic nature of the cation. Alternatively pK values of bulk ion pairing have been used as a measure of the "strength of binding" of cations in the Stern layer of NaLS.[21]

3. Effects of Ionic Strength. The pathway and kinetics of reactions in micellar solution and generally in multiphase systems containing charged interfaces are often extremely sensitive to salt effects. A suitable illustration of these interactions is the reaction of e_{aq}^- with Cd^{2+} in an aqueous micellar solution of NaLS. In Figure 3 observed rate constants (k_o = ln $2/(\tau[Cd^{2+}]_0)$) obtained from pulse radiolysis studies are plotted as a function of ionic strength. A tenfold increase of k_o is observed upon addition of 0.1 M NaCl to the solution. It is important to note that this rate augmentation is a drastic inversion of a normal salt effect (in pure water the same amount of electrolyte would decrease k_o by a factor of 2.6). These observations may be understood with the information from the previous section that Cd^{2+} ions are almost quantitatively adsorbed in the Stern layer of NaLS micelles. In the absence of NaCl hydrated electrons can react only with nonadsorbed Cd^{2+}; addition of electrolyte, on the other hand, makes it possible for e_{aq}^- to approach the micellar surface and react with adsorbed Cd^{2+} by decreasing the negative electrostatic surface potential. While the encounter probability between e_{aq}^- and NaLS micellar is practically zero in the absence of electrolyte, it is 30% at μ = 0.1 for a reaction radius of 6 Å as shown in Figure 1a' and 1b'. The observed rate constant in micellar solution at μ = 0.1 should then be about 3 times

smaller than the value in micelle-free solutions as indeed it is.

It is unlikely that the salt effect is due to a replacement of adsorbed Cd^{2+} by Na^+ ions. Double-layer theory predicts that monovalent ions are only effective in displacing divalent ones when they are present at 10^4 times higher concentration[24] even if no specific binding of the divalent cation in the Stern layer occurs.

A further feature which has to be considered here is the effect of electrolyte on the concentration and structure of NaLS micelles in our solutions. Addition of 0.1 M NaCl increases the aggregation number of NaLS micelles from 62 to 95[25-27] and decreases the cmc from 8×10^{-3} to 1.5×10^{-3} M.[28] From these values one calculates a decrease in micelle concentration from 6.7×10^{-4} to 5.1×10^{-4} M if 0.1 M NaCl is added to 0.05 M NaLS. It is unlikely that such a relatively small decrease in micellar shape can contribute significantly to the observed drastic rate augmentation.

An increased encounter probability of e_{aq}^- and NaLS micelles in the presence of added electrolyte is also illustrated by the reaction rate of e_{aq}^- with solutes dissolved exclusively in the interior of NaLS. For example the rate constant for $e_{aq}^- + $ pyrene which is smaller than 10^5 M^{-1} sec^{-1} in electrolyte free NaLS solution increases to 8×10^7 M^{-1} sec^{-1} in the presence of 0.2 M Na_2SO_4.

The above examples may suffice to demonstrate that the surface potential of a micelle has a decisive influence on the reactivity of hydrated electrons toward solubilized material. Double layers with potential gradients are frequently found in physiological solutions for example in the vicinity of polynucleotides (due to dissociated phosphate groups) and nerve membranes. Misleading results are then obtained if investigations of the reactions of e_{aq}^- with nucleotides or constituents of nerve membranes are conducted in pure aqueous phase as the effect of local electrostatic potentials and ionic strength on these reactions is neglected.

C. Reactions of "Dry" Photoelectrons in NaLS Micelles. Intramicellar Electron Transfer. While reactions of hydrated electrons in aqueous solutions have been extensively studied, there is little information available on the chemical behavior of its precursor the "dry" or nonsolvated electron. Dry photoelectrons are produced during the photoionization of hydrophobic probes in the micellar interior and become hydrated only after exiting into the aqueous phase. Hence photoionization experiments with micellar systems offer an excellent opportunity to investigate reactions of dry electrons with other solubilized species. The efficiency of photoelectron scavenging by added solutes is reflected by the yield of hydrated electrons since the scavenging process is competing with exit and hydration of the electron outlined in eq 1. The detailed course of photoionization events will depend on both the location of the scavenger within the micelle and the product of the scavenging reaction.

First a situation is considered where the scavenger is solubilized in the periphery region of the micelle and is there reduced by the dry electron according to

$$S + e^- \longrightarrow S^-$$ (7)

Subsequently intramicellar electron transfer from the reduced form of the scavenger to the parent cation may occur

$$S^- + P^+ \longrightarrow P + S$$ (8)
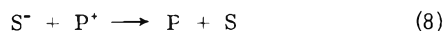
A schematic representation of these processes is given in Figure 4. Benzoic acid, Cd^{2+}, and Cu^{2+} were found to be
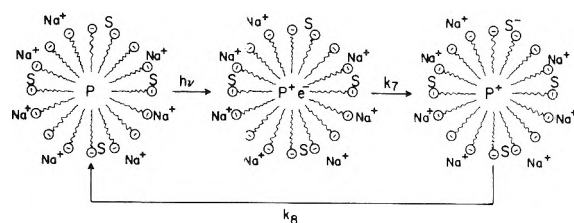
Figure 4. Schematic representation of photoelectron scavenging and subsequent electron transfer by solute S located in the periphery region of an NaLS micelle.
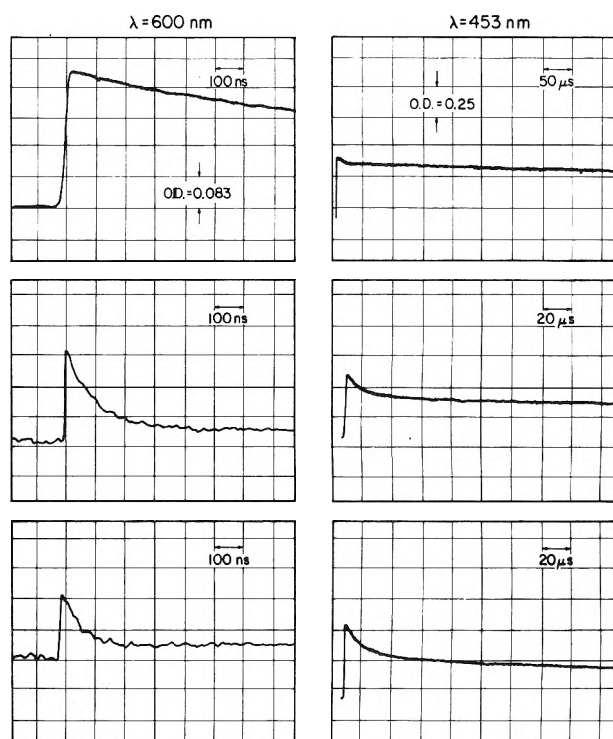
Figure 5. Effect of benzoic acid on the hydrated electron yield and decay kinetics of pyrene positive ions, from laser photoionization of 10^{-4} M pyrene in 0.1 M Na$_2$S; concentration of added benzoic acid from the top is 0, 2×10^{-3} M, and 4×10^{-3} M.

scavengers for dry electrons which illustrate the behavior suggested in the mechanism. Typical data obtained from the laser photoionization of 10^{-4} M pyrene in 0.1 M NaLS and added benzoic acid are shown in Figure 5. Transient absorptions at 600 nm (left-hand side) and 453 nm (right-hand side) reflect the behavior of hydrated electrons and pyrene cation radicals, respectively. The optical density at 600 nm immediately after the laser pulse decreases upon addition of 4×10^{-3} M benzoic acid by a factor of 2 indicating that half of the photoelectrons are scavenged with an average of two or three benzoic acid molecules solubilized in one micelle. In addition the rate of e_{aq}^- decay increases due to reaction with benzoic acid, benzoate, and H^+ in the aqueous phase.

In the absence of a photoelectron scavenger, the absorption at 453 nm decays very slowly during the first 500 μsec. The initial sharp decay at the beginning of the curve is due to a residual absorption of e_{aq}^- at this wavelength. In the presence of benzoic acid the decay at 453 nm occurs in two steps, a fast part followed by a slow component similar to that observed in the absence of benzoic acid. The fraction of pyrene cations corresponding to the initial fast decay

may be correlated with the decrease in hydrated electron yield. This initial decay increases with increasing benzoic acid concentration while the decay kinetics remain first order. This suggests that the fraction of photoelectrons scavenged by benzoic acid within the micelle is returned to the parent cations via the intramicellar electron-transfer process described by eq 8.

Cu^{2+} and Cd^{2+} ions adsorbed at the surface of NaLS micelles are also capable of scavenging "dry" photoelectrons. The amount of ions needed to reduce the yield of e_{aq}^- by 30% is $\sim 2 \times 10^{-2}$ M in 0.1 M NaLS which corresponds to about 12 adsorbed ions/micelle. This indicates that Cu^{2+} or Cd^{2+} ions interact much less efficiently with photoelectrons than benzoic acid. The surprisingly large scavenging cross section found for benzoic acid may be explained by its amphipatic character. While Cu^{2+} and Cd^{2+} are adsorbed in the Stern layer, benzoic acid is solubilized in such a way that the carboxylic group resides close to the NaLS head groups, the aromatic ring protruding into the palisade layer.[20] The movement of photoelectrons exiting from the micelle is random in the inner-core and also in the outer-core region where the phenyl ring is located. However, once the Stern layer is reached (the site of Cu^{2+} or Cd^{2+} ions), the electron diffusion is no longer random since it travels in the surface potential gradient directed away from the micelle. Hence the probability of reaction with ions located within the micellar Stern layer is expected to be small. Another contribution to the large difference in scavenging efficiency between benzoic acid and Cu^{2+} (Cd^{2+}) ions may come from the fact that the former molecule, being partially solubilized, occupies a greater solid angle than a molecule or ion of similar size in the Stern layer.

The reaction of photoelectrons with adsorbed Cu^{2+} or Cd^{2+} ions leads to the formation of Cu^+ or Cd^+ which have strong reducing properties and hence transfer the electron back to the pyrene parent ion. As in the case of the benzoic acid system the kinetics of this transfer reaction can be studied by measuring the transient absorption of pyrene positive ions at λ 453 nm. From oscillograms similar to those shown in Figure 5 one obtains a half-lifetime of 17 μsec for the intramicellar reaction

$$Cu^{2+}\ (Cd^{2+}) + P^+ \longrightarrow Cu^+\ (Cd^+) + P \qquad (8a)$$

from which a rate constant $k_{8a} = 4 \times 10^{-4}$ sec^{-1} is evaluated. This value is slightly lower than $k_8 = 6 \times 10^4$ sec^{-1} found for the benzoic acid system.

In order that electron transfer may occur, pyrene cations have to diffuse to the periphery of the micelle where the donor (S^-) is located. Although this diffusion time may be as short as 80 nsec,[29] a considerably longer time may elapse before a suitable encounter with the donor takes place, since the latter occupies only a small fraction of the surface. This explains the relatively low values of electron-transfer rate constants which are observed.

Up to this point, we have limited the discussion of the reactions of photoelectrons to scavengers located in the periphery region of NaLS micelles and obeying the mechanism outlined in eq 7 and 8. These investigations were extended to a variety of other scavenger systems. It was found that solutes which react rapidly with solvated electrons are generally capable of scavenging photoelectrons unless solubilization occurs in the inner-core region of the micelle. Thus biphenyl which is an excellent scavenger for solvated electrons does not react with photoelectrons even if an average of 10 biphenyl molecules is present in one mi-
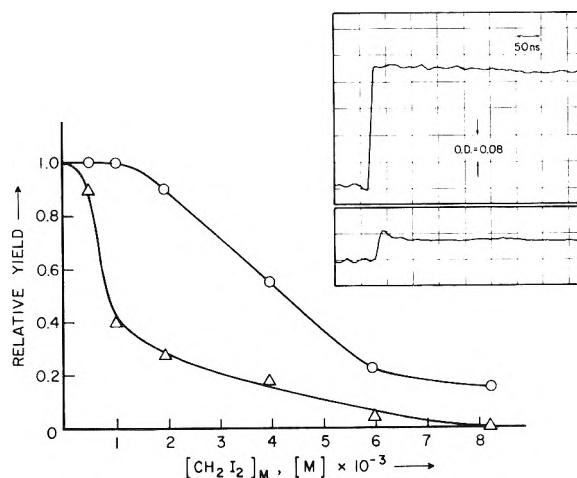
Figure 6. Effect of methylene iodide on the relative yield of hydrated electrons ($\triangle$, measured at 600 nm) and pyrene cations (O, measured at 453 nm) from the laser photoionization of 10^{-4} M pyrene in 0.1 M NaLS. Insert shows oscillograms of pyrene cation formation and decay at 453 nm: upper trace, $[CH_2I_2] = 2 \times 10^{-3}$ M; lower trace, $[CH_2I_2] = 6 \times 10^{-3}$ M.

celle as is evident from the finding that solubilized biphenyl fails to decrease the hydrated electron yield. This interesting effect may be due to a decrease of reaction probability with increasing excess energy of the photoelectron. Photoelectrons have their maximum excess energy in the inner core of the micelle where they are initially formed. As biphenyl is solubilized in the same region, it encounters mainly nonthermalized electrons with which it does not react. If the electron scavenger is located further away from pyrene at distances where thermalization occurs, then electron capture takes place.

Benzene molecules situated within NaLS micelles fail to scavenge photoelectrons. Benzene has been suggested to react with dry electrons in alcohols.[30]

A solubilizate which shows unusual effectiveness in interacting with photoelectrons is methylene iodide. Partitioning of this solute between NaLS micelles and water has already been investigated, the distribution constant being $K = 2.5 \times 10^3$ M^{-1} sec^{-1}.[16] Data obtained from the photoionization of 10^{-4} M pyrene in 0.1 M NaLS and added methylene iodide are shown in Figure 6. The yield of hydrated electrons drops sharply at an average concentration of only one CH_2I_2 molecule per micelle indicating efficient dry electron capture of solubilized CH_2I_2 according to

$$CH_2I_2 + e^- \longrightarrow CH_2I + I^- \qquad (9)$$
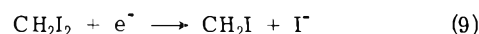
Also in Figure 6 the yield of pyrene cations measured from the OD change at 453 nm immediately after the laser pulse is plotted as a function of CH_2I_2 concentration. This yield also decreases, but only at high concentrations of methylene iodide. It is suggested that the decrease is due to a fast neutralization of parent cations by iodide formed in the micellar interior via reaction 9. It can be seen from the lower of the inserted oscillograms that most of the neutralization events occur during the laser pulse, and only the last portion of the reaction is observed as a spike at the beginning of the trace. Neutralization of ions in nonpolar environment is expected to occur rapidly as the rate constant in hydrocarbon solution is about 10^{12} M^{-1} sec^{-1}.[31]

Rapid neutralization does not take place at lower CH_2I_2 concentration. Iodide ions formed according to eq 9 seem to escape from the micelle rather than react with the parent

cation. This effect may be explained by a change in dynamic sites of solubilization of CH_2I_2 in NaLS micelles. The first few molecules solubilize preferentially in the outer-core region, while a shift toward the micellar interior occurs at higher CH_2I_2 concentration. Such a change in location is common in solubilization processes[32] but usually occurs at higher solute concentration.

D. Thermalization Distance of Photoelectrons. An estimate of the mean thermalization distance, $\langle \delta \rangle$, of photoelectrons in water can be made by comparing hydrated electron lifetimes from pulse radiolysis and laser photolysis experiments with NaLS micellar solutions containing pyrene in the micelles and NO_3^- as a scavenger in the aqueous phase. The former technique produces a homogeneous distribution of e_{aq}^- and reaction with NO_3^- occurs mainly in the solution bulk. This is reflected by the observed half-lifetime of 3 nsec in 2×10^{-2} M nitrate solution which is also calculated from the scavenging rate constant 1.2×10^{10} M^{-1} sec^{-1}. Addition of 0.1 M NaCl did not change the half-lifetime significantly. In the laser photolysis experiments hydrated electrons are initially formed within the micellar Gouy–Chapman layer where they encounter a lower nitrate concentration (*cf.* Figure 1) than in the solution bulk. This results in a longer half-lifetime which depends on the thermalization distance. Hydrated electrons formed by laser photolysis in NaLS micellar solution containing 2×10^{-2} M NO_3^- have a half-lifetime of 5 nsec which compares to 3 nsec in the pulse radiolysis experiments. This would indicate that thermalization mainly occurs in the outer Gouy–Chapman layer at 20–40 Å from the micellar surface. Since the hydrated electron diffuses a considerable distance during its reaction time, the $\langle \delta \rangle$ value cannot be determined more accurately. In the laser experiments addition of 0.1 M NaCl to the solution reduces the electron lifetime to 3 nsec, *i.e.*, to the same half-lifetime found in pulse radiolysis experiments. The absence of a double-layer effect on the electron rate at an ionic strength $\mu = 0.12$ indicates that the extension of the micellar Gouy–Chapman layer (*cf.* Figure 1b') is smaller than the thermalization range of the photoelectron.

The comparison of photoionization yields from solutions of aromatic molecules in anionic and cationic micelles also provides useful information on the thermalization distance of the photoejected electrons, through the micelle and into the aqueous phase. The potential in the vicinity of the cationic micelles is positive with respect to the solution bulk, and the potential distance function for a DTAC micelle calculated from the Poisson–Boltzmann equation (eq 3) with parameters given in the figure caption is shown in Figure 7. The probability curve for the location of a negatively charged species such as the hydrated electron at a given distance $r - r_0$ from the micellar surface is also included in Figure 7. Contrary to the NaLS system the hydrated electron is strongly attracted toward DTAC micelles, the Onsager distance of interaction being 18 Å. Photoelectrons which are thermalized and hydrated within the Onsager radius are retrapped by their parent micelles and recombine with the parent cations. Since this process is too fast to be followed on our time scale, these electrons are not expected to contribute to the observed yield of photoionization. It was found that yields of hydrated electrons formed by the laser photoionization of 10^{-4} M pyrene in 0.1 M DTAC solution and 10^{-4} M pyrene in 0.1 M NaLS were the same. It is concluded that the average thermalization distance of these photoelectrons in water is $\langle \delta \rangle \geq 18$ Å.
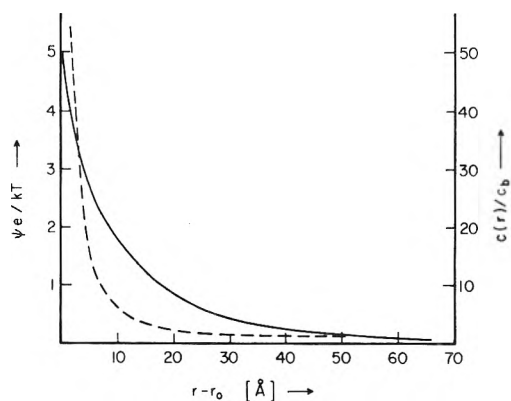
Figure 7. Left ordinate (solid line): potential distance function in the diffuse double layer of DTAC micelles, with $r_0 = 17$ Å, $\psi^0 e/kT = 5$, and $\mu = 0.015$.[13] Right ordinate (dashed line): statistical distribution of a monovalent negative ion in the double layer.

The above data indicate that photoelectrons with an excess energy of only 1 eV can cross a considerable span of hydrocarbon and aqueous phase before becoming thermalized and hydrated. This is in basic agreement with an estimate of the range of photoelectrons ejected from mercury[33] (10–100 Å). To narrow the range of uncertainty in the $\langle \delta \rangle$ values further, refinement of the micellar double-layer model is required. In particular, changes in the microscopic dielectric constant[34] have to be accounted for in the calculation of potential distance functions. Efforts in this direction are under way and will be reported later.

Conclusion

Photoionization of aromatic hydrocarbons such as pyrene in micellar solution occurs with a large cross section, the yields of ions obtained being much higher than in alcoholic solution.[3] Photoejected electrons may react with scavengers in the micellar interior or exit into the aqueous phase to become hydrated electrons. The subsequent behavior of hydrated electrons is controlled by the micellar surface potential leading to unusual ionic strength effects. Laser photolysis experiments with these micellar model systems yield significant information on the nature of photoionization events in physiological solutions of organized bioaggregates. These studies are now extended to micellar solutions of biologically important compounds such as retinal and β-carotene. Preliminary work on the retinal–NaLS system shows significant yields of ions formed during 347.1-nm laser photolysis.

References and Notes

(1) The Radiation Laboratory of the University of Notre Dame is operated under contract with the U. S. Atomic Energy Commission. This is AEC Document No. COO-38-942.
(2) L. P. Gary, K. de Groot, and R. C. Jarnagin, *J. Chem. Phys.*, **49**, 1577 (1968); S. D. Babenko and V. A. Bendarsky, *Opt. Spektrosk.*, **28**, 616 (1970); K. H. Grellmann and A. R. Watkins, *J. Amer. Chem. Soc.*, **95**, 983 (1973); G. Beck and J. K. Thomas, *J. Chem. Phys.*, **57**, 3643 (1972).
(3) Y. Taniguchi, Y. Nishiun, and N. Mataga, *Bull. Chem. Soc. Jap.*, **45**, 764, 2323 (1972); J. T. Richards, G. West, and J. K. Thomas, *J. Phys. Chem.*, **74**, 4137 (1970).
(4) T. Rosenfeld, A. Alchalal, and M. Ottolenghi, *Chem. Phys. Lett.*, **20**, 291

(1973); J. R. Harbour and G. Tollin, *Photochem. Photobiol.*, **19**, 69 (1974).

(5) E. H. Cordes, "Reaction Kinetics in Micelles," Plenum Press, New York and London, 1973, p ·27; E. H. Cordes and C. Gitler, *Progr. Bioorg. Chem.*, **2**, 1 (1973).

(6) S. C. Wallace, M. Grätzel, and J. K. Thomas, *Chem. Phys. Lett.*, **23**, 359 (1973).

(7) R. McNeil, J. T. Richards, and J. K. Thomas, *J. Phys. Chem.*, **76**, 1700 (1972).

(8) P. M. Rentzepis, R. P. Jones, and J. Jortner, *J. Chem. Phys.*, **59**, 766 (1973).

(9) S. Gordon, E. J. Hart, M. S. Matheson, J. Rabani, and J. K. Thomas, *Discuss. Faraday Soc.*, **36**, 214 (1963).

(10) S. L. Brenner and R. E. Roberts, *J. Phys. Chem.*, **77**, 2367 (1973).

(11) A. L. Loeb, J. Th. Overbeeck, and P. H. Wiersema, "The Electrical Double Layer around a Spherical Colloid Particle," MIT Press, Cambridge, Mass., 1961.

(12) N. E. Hoskin and S. Levine, *Proc. Roy. Soc., Ser. A*, **248**, 433 (1956).

(13) D. Stigter, *J. Colloid Interface Sci.*, **23**, 379 (1967).

(14) K. M. Bansal, L. K. Patterson, E. J. Fendler, and J. H. Fendler, *Int. J. Radiat. Phys. Chem.*, **3**, 321 (1971).

(15) S. C. Wallace and J. K. Thomas, *Radiat. Res.*, **54**, 49 (1973).

(16) P. P. Infelta, M. Grätzel, and J. K. Thomas, *J. Phys. Chem.*, **78**, 190 (1974).

(17) E. Peled and G. Czapski, *J. Phys. Chem.*, **74**, 2903 (1970).

(18) K. Mysels and L. H. Princen, *J. Phys. Chem.*, **63**, 1696 (1959).

(19) I. Langmuir, *J. Amer. Chem. Soc.*, **38**, 221 (1916); **40**, 1316 (1918).

(20) C. T. Donbrow and M. Rhodes, *J. Pharm. Sci.*, **54**, 1069 (1965).

(21) I. D. Robb, *J. Colloid Interface Sci.*, **37**, 521 (1971).

(22) J. Oakes, *J. Chem. Soc., Faraday Trans. 2*, 1321 (1973).

(23) K. K. Fox, *Trans. Faraday Soc.*, **67**, 2809 (1971).

(24) S. C. M. McLaughlin, G. Szabo, and G. Eisenmann, *J. Gen Physiol.*, **58**, 667 (1971).

(25) J. N. Phillips and K. J. Mysels, *J. Phys. Chem.*, **59**, 325 (1955).

(26) H. F. Huisman, *Proc. Kon. Ned. Akad. Wetensch., Ser. B*, **67**, 388 (1964).

(27) M. F. Emerson and A. Holtzer, *J. Phys. Chem.*, **69**, 3718 (1965).

(28) E. Matijeric and B. A. Petkica, *Trans. Faraday Soc.*, **54**, 587 (1968).

(29) M. Grätzel and J. K. Thomas, *J. Amer. Chem. Soc.*, **95**, 6885 (1973).

(30) H. Ogura and W. H. Hamill, *J. Phys. Chem.*, **78**, 504 (1974).

(31) L. Capellos and A. O. Allen, *J. Phys. Chem.*, **73**, 3264 (1969).

(32) J. C. Erikson and G. Gillberg, *Acta Chem. Scand.*, **20**, 2019 (1966).

(33) P. Delahay and V. S. Srinivasan, *J. Phys. Chem.*, **70**, 420 (1966).

(34) P. Mukerjee, *Advan. Colloid Interface Sci.*, **1**, 241 (1967).

An Optical Microscopic Study on the Catalytic Hydrogenation of Graphite

Akira Tomita* and Yasukatsu Tamai

Chemical Research Institute of Non-Aqueous Solutions, Tohoku University, Katahira-cho, Sendai, Japan

The catalytic activities of some transition metals in the hydrogenation of graphite crystals were investigated. The topography of the graphite basal plane was determined by using an optical microscope. The hydrogenation was accompanied by the formation of channels lead by catalyst particles. Some of these channels were of irregular shape, and others were straight with a preferred orientation. Straight channels were observed mainly in the $\langle 11\bar{2}0 \rangle$ direction. The ratio of channel length in the $\langle 11\bar{2}0 \rangle$ direction to that in the $\langle 10\bar{1}0 \rangle$ direction ranged from 4.7 for the iron catalyst to 25.3 for the nickel catalyst. The ratio determined by the channel number which appeared in each direction ranged from 4.1 for iron to 14.8 for nickel. Straight channels often bend at an angle of 60 or 120°. The larger the catalyst particle, the greater the probability of curving channels. A mechanism which can account for the above observations was proposed from an atomistic point of view. The actual hydrogenation reactions were considered to consist of a few reactions at the $\{10\bar{1}l\}$ faces of graphite and the subsequent zipper-like reactions at the $\{11\bar{2}l\}$ faces. The ordering force producing a long straight channel was attributed to the presence of the specific active sites in the metal catalyst.

Introduction

The present paper reports a continuation of our study on the catalytic hydrogenation of carbons.[1,2] In an earlier paper it was shown that the reaction pattern greatly depended on the structure of carbon. In a thermogravimetric study, active carbon was gasified to methane in two or three stages as the temperature was raised to 1200° at a constant rate. On the other hand, the catalytic hydrogenation of graphite took place only in one stage at high temperature.

In order to understand the mechanism of these interesting but complicated reactions, it was thought advisable to investigate the relatively simple reaction between graphite and hydrogen in detail. In the absence of catalyst, a simplified mechanism for this reaction was already presented by Hedden[3] and Breisacher and Marx.[4] The mechanism for the catalytic reaction is not as simple as proposed by them.

There are many problems to be solved: (1) the detailed mechanism of the catalytic function of a metal, (2) the anisotropy of the reaction rate with respect to c and a axes, or $\langle 10\bar{1}0 \rangle$ and $\langle 11\bar{2}0 \rangle$ directions on a basal plane, (3) the existence of a particular configuration with great reactivity on the carbon surface, as reported in the chemisorption of hydrogen on Graphon.[5] For these purposes, the microscopic technique is thought to be most useful. This technique was successfully used in studies of the oxidation of graphite single crystals.[6-10] A reaction between graphite and atomic hydrogen was also investigated by this method.[11] A topographic change was determined in this study for a natural graphite flake which was allowed to react with hydrogen molecules in the presence of several kinds of metal catalysts.

The catalytic reactions of carbon with gases are also of interest, since these reactions provide unique examples of

the solid-catalyzed solid–gas reactions. The metal-catalyzed hydrogenation seems to be one of the most simple model reaction to elucidate this undeveloped field. On the other hand, oxidation reactions of carbon are somewhat more complicated, because the active species cannot be exclusively decided. Both metal and metal oxide have catalytic activities.

Experimental Section

Materials. Natural crystals of flake graphite were purchased from Kanto Chemical Co., and were purified by boiling in a concentrated solution of hydrogen chloride. Metal catalysts were added to these crystals by the impregnation method. Aqueous solutions of metal chlorides were used as impregnating solutions. The final metal content after the reduction of salt to the metallic state was 4.8 wt %. In the experiment to determine the anisotropy, a drop of 0.2 mM solution of metal chloride was added to a few flakes of graphite which were cleaved by use of adhesive tape to expose fresh internal surfaces.

Procedure. Experimental conditions for TGA were almost identical with those reported elsewhere:[1] heating rate, 100°/hr; hydrogen flow rate, 60 ml/min; gas analysis, a gas chromatograph with a 2-m molecular sieve column.

Surface topographical change with time was determined as follows. A few flakes of graphite containing an iron catalyst were mounted on a silica plate and set horizontally in a reactor. After the evacuation to 10^{-6} Torr, the temperature was raised to 870°, and hydrogen was admitted at a flow rate of 60 ml/min. After the required time for hydrogenation, the system was evacuated again and cooled to a room temperature. A photograph of the particular area of the surface was taken, and the graphite was put into the reactor again. The hydrogenation reactions were repeated in this manner for the same sample.

In the experiments to determine the reaction anisotropy, the temperature was maintained at 1050° for 3 hr. The temperature was raised in flowing helium instead of *in vacuo*.

Topographical features of the graphite surface were mainly examined by an optical microscope, an Olympus MF. Some crystals were also examined in a scanning microscope (SEM), a JEOL-LSM-U3.

Results

TGA Experiments. The TGA curve of the rhodium-catalyzed hydrogenation of graphite was reported in an earlier paper.[1] In this study, we examined the catalytic effects of nickel and iron under the same experimental conditions. Only methane was detected as a product in all cases. The formation of methane became observable at 660, 770, and 810° for rhodium, nickel, and iron, respectively. For the noncatalytic reaction, methane could not be detected below 1000°. The methane content in the exit gas began to decrease at higher temperatures due mainly to an equilibrium restriction. The temperature of maximum methane formation was 925, 985, and 1050° for rhodium, nickel, and iron.

Figures 1 and 2 show a typical topograph of a graphite basal plane in the presence of iron catalysts. The hydrogenation was accompanied by the formation of channels lead by catalyst particles. An X-ray microanalysis shows that the particle found at the tip of channel is the iron catalyst. The channeling pattern sometimes shows a preferred orientation with respect to the twin bands, or more usually a random behavior. The channels in Figure 1 and the chan-
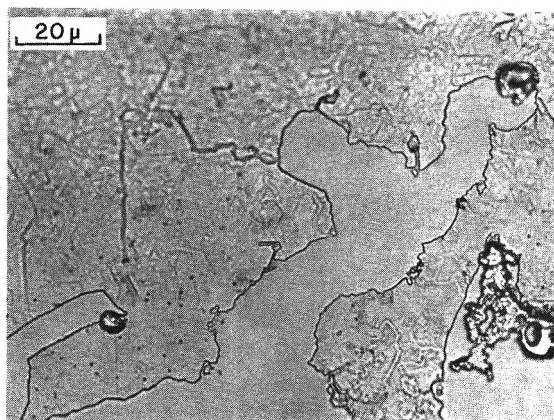
Figure 1. Broad and irregular channels formed by iron particles in the hydrogenation with rising temperature to 1100°.
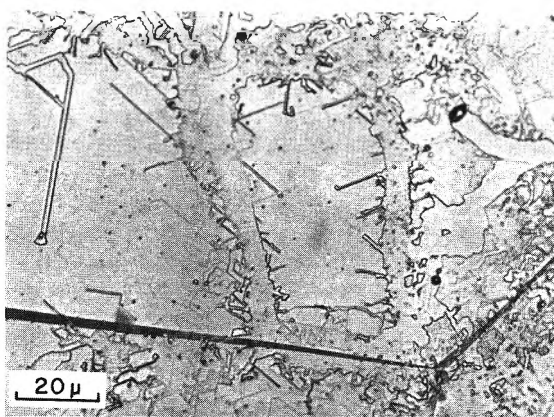
Figure 2. Straight channels formed by iron particles in the hydrogenation with rising temperature to 1100°.

nel on the right side of Figure 2 are examples of the latter, and the left-side channel of 1.2 μ width in Figure 2 is an example of the former. This width is the upper limit for the straight channel observed in this study. This channel and a large majority of straight channels are perpendicular to one of the twin bands which appeared, for example, on the bottom of Figure 2. As twin bands are in the $\langle 10\bar{1}0 \rangle$ direction,[7] the channels perpendicular to them must be in the $\langle 11\bar{2}0 \rangle$ direction. In the case of Figure 2, the total length of the channel in this direction was 168 μ, and that in the $\langle 10\bar{1}0 \rangle$ direction was 9 μ. Therefore, 95% of the straight channels were perpendicular to the twin band.

Movement of Catalyst Particles. In order to clarify the curious movement of catalyst particles, it was thought of interest to take photographs from the same view from time to time during the hydrogenation. Figure 3 illustrates the result of the iron-catalyzed reaction at 870°. The following qualitative observations were obtained. (1) Particles agglomerate or split frequently. (2) Small particles produced by such a splitting make straight channels. Thus, the straight channels begin to appear after a few hours under these conditions. (3) An irregular-shaped particle moves so as to maintain the largest contact area with the peripheral face of graphite. (4) There is no trouble for a catalyst to cross another channel. (5) The depth of the channel is different from particle to particle. (6) Generally speaking, the larger the catalyst the larger the forward rate. (7) The rate is not constant for catalysts larger than 2 μ in diameter.
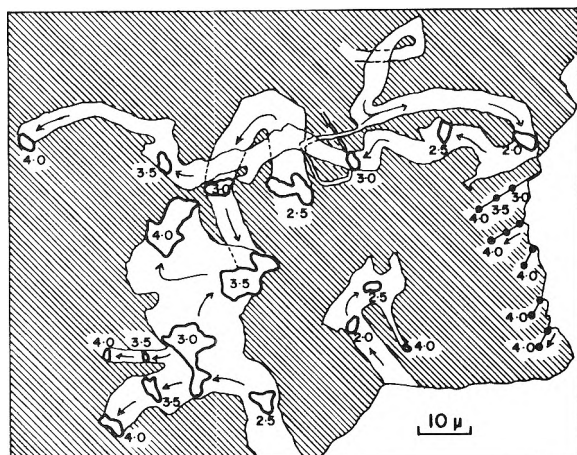
Figure 3. Catalytic channeling by iron particles at 870°. Numbers indicate the reaction time.

The rate varies irregularly with time. (8) The particle travelling from upper right to upper left in Figure 3 has an extraordinary large rate of 70 μ/hr on the average. (9) Smaller particles which produce straight channels move at relatively constant rates. (10) There is, however, a rate distribution for the smaller particles ranging from 5 to 8 μ/hr. (11) One catalyst particle (not shown in Figure 3) is found to change its direction from $\langle 10\bar{1}0 \rangle$ to $\langle 11\bar{2}0 \rangle$ after 3.2 hr. It may be noteworthy that the rate before and after bending is nearly equal. (12) There are many particles which stop moving after losing contact with graphite steps. Near the center of Figure 3, there is a particle which stopped moving after 2.5 hr. Baker and Harris[15] explained such a deactivation as a result of making a loop in their oxidation reaction study.

Reaction Anisotropy. Several isothermal reactions at 1050° were carried out to investigate the reaction anisotropy more quantitatively. First, we will comment briefly on the anisotropy with respect to c and a axes. As no etch pits are observed, the hydrogenation along the c direction seems to be extremely slow. When the graphite crystal after the experiment was cleaved by adhesive tape, the exposed internal surface was found to be almost fresh. A limited amount of channels were found at the edge of the crystal and along grain boundaries. The ratio of the rate constants along and perpendicular to the basal plane might be much larger than unity.

The examples of the anisotropy within a basal plane are shown in Figures 4 and 5. Narrow channels with preferred orientations are dominant channels in the case of cobalt (Figure 4) and iron catalysts. Their widths are around 0.5 μ. Most of these channels are perpendicular to the twin band. Figure 5 shows the channel produced by nickel catalysts. It can be seen that all channels started at steps. The angle at the bending points are frequently 60 or 120°. Thus, the channel direction is maintained to be $\langle 11\bar{2}0 \rangle$ even after bending. An SEM photograph is inserted in order to show the shape of catalyst and the straightness of the channel. The width of this channel is nearly equal to those indicated in the optical micrograph. For the nickel catalyst, most channels in other places are narrower than in this photograph. In cases of rhodium, iridium, and platinum catalysts, only short and narrow channels are observed at the vicinity of steps.

The degree of anisotropy may be estimated by comparing the channel lengths in each direction. For this purpose, 24 photographs were selected so as to include both straight
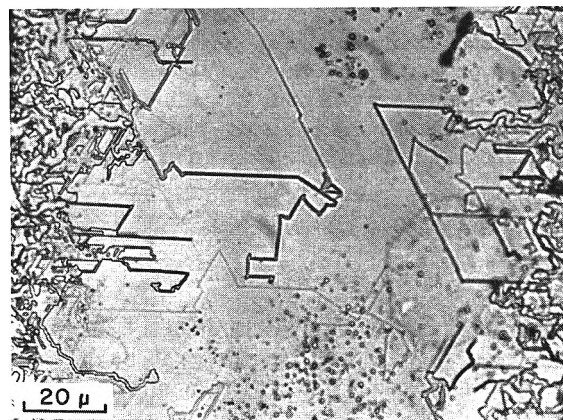

Figure 4. Straight channels formed by cobalt particles in the hydrogenation at 1050° for 3 hr.
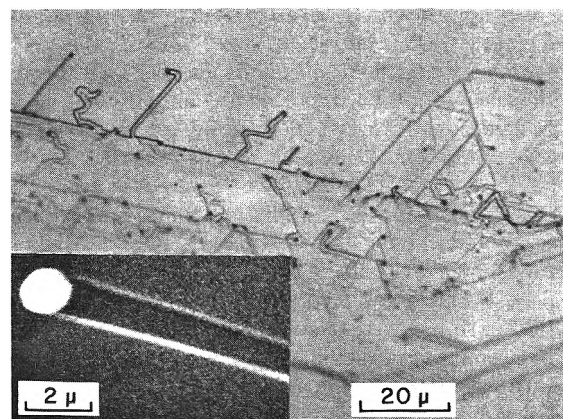
Figure 5. Channels formed by nickel particles in the hydrogenation at 1050° for 3 hr. An SEM photograph is inserted to show the tip of channel at a large magnification.

channels and twin bands. The total length of channels in each direction and their ratios are listed in Table I. The data in the last column give the ratios of channel numbers appearing in the $\langle 11\bar{2}0 \rangle$ direction to those in the $\langle 10\bar{1}0 \rangle$ direction. In case of iron catalyst, the ratios determined by two methods are nearly identical. This means that the average channel length in the $\langle 11\bar{2}0 \rangle$ direction is nearly equal to that in the $\langle 10\bar{1}0 \rangle$ direction. The difference of the total lengths is ascribed to the difference of the probability of initiating two anisotropic channel formations. Once the particle starts moving in any preferential direction, its velocity is independent of the crystal direction. This is in good agreement with the result (11) mentioned in the preceding section. Although the result for the rhodium catalyst is very similar to this case, the ratio of total lengths is almost two times of the ratio of channel numbers for the cobalt or nickel catalyst. In these cases, the average length in the $\langle 11\bar{2}0 \rangle$ direction is also two times of that in the $\langle 10\bar{1}0 \rangle$ direction. In summary, the large difference of total length is not due to the difference of the reaction rates in two directions, but due mainly to the difference of the probability of initiating straight channeling. The anisotropy depends on the kind of catalyst, but the number of photographs might be too small to discuss this dependence.

Discussion

Catalyst Mobility. In catalytic hydrogenation as well as oxidation,[7,8,10] all channels started at graphite steps. Parti-

Cat-alyst	No. of photo-graphs	Total length of channels, μ		$l_{\langle 11\bar{2}0 \rangle}/$ $l_{\langle 10\bar{1}0 \rangle}$	$n_{\langle 11\bar{2}0 \rangle}/$ $n_{\langle 10\bar{1}0 \rangle}$
		$l_{\langle 11\bar{2}0 \rangle}$	$l_{\langle 10\bar{1}0 \rangle}$		
Fe	5	2106	449	4.7	4.1
Co	10	5710	442	13.5	5.9
Ni	4	2476	98	25.3	14.8
Rh	5	3892	390	10.0	7.8

cles located on the flat basal plane are catalytically inactive. The driving force for the catalyst particle mobility was discussed by Hennig,[6] who explained this mobility due to the attractive force between a particle and the peripheral carbon atoms along the edge of the channel tip. This force should be much stronger than van der Waals force between a particle and the carbon atoms on a basal plane. This explanation may be also applied to the hydrogenation reaction. This is supported by the present observation that the leading side of a catalyst particle is always the longer side of the irregular-shaped particle. This observation shows that the resistance for a particle to proceed in the graphite lattice is not so large.

Elementary Chemical Processes. Structural changes of the graphite lattice during the hydrogenation will be discussed here from an atomistic point of view. Figure 6 illustrates three possible reaction paths. A reaction occurring at the {11$\bar{2}l$} face is termed a reaction of type A, and a reaction site having such an armchair configuration is termed a site A. A reaction occurring at the {10$\bar{1}l$} face is termed a reaction of type B. A reaction of type C takes place at the cross point of two {10$\bar{1}l$} faces, and this might not occur as frequently as A or B. Zielke and Gorin[12] proposed a hydrogenation mechanism through reactions of type A, and it seems to be accepted generally.[3,13,14] It is quite reasonable that this reaction occurs most easily, because this reaction requires no arrangement of π-electron systems in the graphite lattice. On the other hand, a type B reaction requires a complicated rearrangement of π-electron systems, and furthermore there is a large steric strain during this process as shown in Figure 6B. However, it is also true that channel formation cannot continue only through reactions of type A. This will be discussed below by using Figure 7.

Figure 7 shows a channel in the $\langle 1\bar{1}20 \rangle$ direction with a catalyst of 60 Å diameter, together with a channel in the $\langle 10\bar{1}0 \rangle$ direction. The sides and the tip of the lower channel consist of {10$\bar{1}l$} faces. When the rate of reaction A is so fast that all possible sites A preferentially disappear, the shape of channel tip would have such a configuration. Channel formation would stop at this configuration, if some reactions of type B and/or C are not taking place. Only two reactions of type B at B_2 and B_3 or only one reaction of type C at the extreme tip of the channel are sufficient to cause the catalyst particle to proceed by one atomic layer of graphite lattice, since these reactions may be followed by a series of zipper-like reactions of type A in this row.

It should be noted that there are three simplifications in this model which are not true: (1) the diameter of an actual catalyst which produces a straight channel ranges from 10^3 to 10^4 Å, (2) the actual shape of catalyst should not be spherical, and (3) the shape of the tip is not part of a hexagon. Such a geometrical structure of a tip was never observed experimentally. This means that sites A far from the
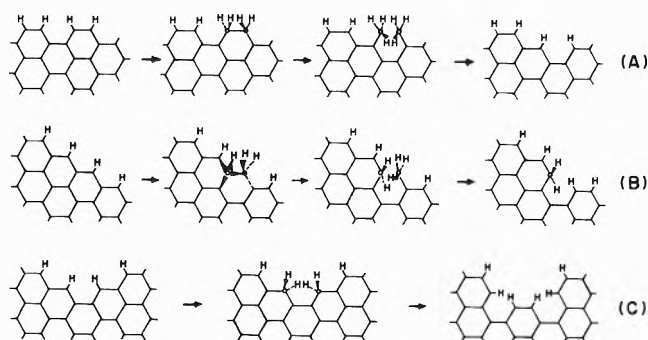
Figure 6. Three reaction types in the hydrogenation of graphite basal plane: (A) armchair face; (B) zigzag face; (C) cross point of two zigzag faces.
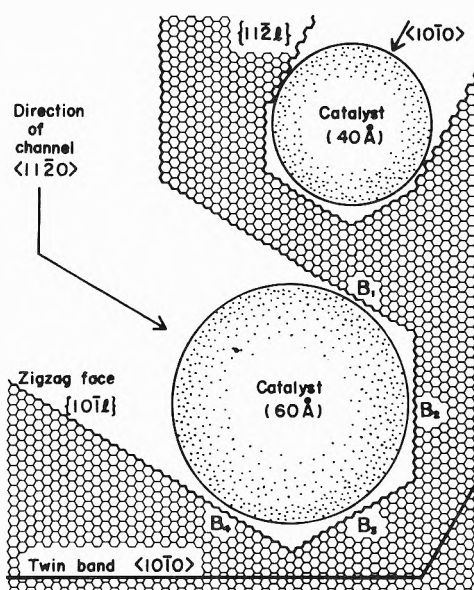
Figure 7. Schematic model for catalytic channeling. The lower channel is perpendicular to a twin band, and the upper right is parallel to a twin band.

catalyst are not as reactive. A certain fraction of an armchair configuration must be included in the actual structure of a tip, and the corners of the tip must be rounded off. In spite of these approximations, the fundamental mechanism seems to be understood with this model.

Channel with a Preferred Orientation. Many examples of anisotropic reactions have been reported for the oxidation of graphite single crystals. No detailed mechanism, however, has been proposed. Hennig[7] considered that the anisotropy was induced by the force maintaining a maximum contact area between catalyst and graphite. In his idea, the channel direction must be perpendicular to one of the directions with the largest reactivity. Thomas[8] reported a difference in the activation energy of 4 kcal/mol between the $\langle 11\bar{2}0 \rangle$ and $\langle 10\bar{1}0 \rangle$ directions, and stated that this difference was too small to account for the great difference in the electronic configuration between the {10$\bar{1}l$} and {11$\bar{2}l$} faces. McKee[9] suggested the possibility of the preferential adsorption of catalyst on certain sites in the carbon network. These discussions are limited to the comparison of overall rates in each direction. The atomistic point of view is lacking in them. We present the mechanism of the reaction anisotropy from this point of view. It would become clear that the actual atomistic reactions are nearly same for channel formation in two different directions.

In this study, many characteristic points were observed as follows in connection with the reaction anisotropy. (1) A number of straight channels are found in many cases. (2) Their directions are almost parallel to the $\langle 11\bar{2}0 \rangle$ direction, and about 10% of them are parallel to the $\langle 10\bar{1}0 \rangle$ direction. (3) A channel often bends at an angle of 60 or 120°. (4) A catalyst smaller than 0.5 μ in diameter generally produces a straight channel, and a channel produced by a large catalyst tends to curve irregularly. (5) The forward rate of a particle in the $\langle 10\bar{1}0 \rangle$ direction is same as that in the $\langle 11\bar{2}0 \rangle$ direction for some catalysts. The dependence of rate on the crystal direction is much smaller than that on the particle size. Any mechanism must explain, or accord with, the above results.

As was seen in our simplified model, Figure 7, the catalyst particle at the channel tip in the $\langle 11\bar{2}0 \rangle$ direction contacts with four sites of type B in a graphite lattice. In order to move the particle by one atomic distance (2.46 Å), at least two reactions of type B must take place. These elementary reactions are considered to determine both the overall rate and the geometrical pattern. Reactions at B_2 and B_3 followed by a number of zipper-like reactions of type A cause a straight movement of catalyst. On the other hand, reactions at B_1 and B_2 or at B_3 and B_4 would result in a bend at an angle of 120°. When such a bend occurs twice within the resolving power of the microscope, a bending at an angle of 60° can be observed. The direction of channel may be thus determined. The relative activity of the catalyst at these four B sites should be the most important factor in determining the direction. If the catalyst is much more active near B_2 and B_3 than the other sites, the catalyst particle would move straight for long time. The longest straight channel observed in this study was 72 μ, which corresponds to more than 10^5 atomic layers. Such a regularity is explained in this theory as due to the specific active sites of the catalyst. A catalyst having a complicated shape must contact with more than four sites of type B, and the catalyst must have many active sites in itself. Therefore, it might be difficult to maintain a constant channel direction in this case. This is the reason why the probability of channel bend increases with an increase of the particle size of catalyst, because the larger the size, the more complicated the shape of particle. A large and irregular-shaped particle usually moves randomly as shown in Figures 1-3.

It is interesting to discuss the difference of the reactivities in the $\langle 11\bar{2}0 \rangle$ and $\langle 10\bar{1}0 \rangle$ directions. In order to start channel formation, it is required for the particle to have suitable active sites at the contact points with graphite peripheral faces. Three sites are required for the channel formation in the $\langle 10\bar{1}0 \rangle$ direction, and only two sites for the $\langle 11\bar{2}0 \rangle$ direction as can be seen in Figure 7. This difference may be one reason why the probability of channel formation is smaller in the $\langle 10\bar{1}0 \rangle$ direction. Furthermore, hydrogen should tend to attack more labile sites A located on the channel sides. Only when there is no active sites on the catalyst near the $\{11\bar{2}l\}$ faces of graphite, the catalyst particle could move in the $\langle 10\bar{1}0 \rangle$ direction. Once the particle starts to move in any straight direction, the forward rate is almost independent of the direction. This observation can be clearly understood by considering the elementary chemical reactions for both cases. When the discussion is limited to the simplified model in Figure 7, two type B reactions are required for the advance of catalyst by one carbon atomic distance in both cases. In the $\langle 10\bar{1}0 \rangle$ direction, three type B reactions seem to be responsible at the first glance, but, in fact, only two reactions, on the average, are necessary to cause particle to proceed by one carbon atomic distance (2.13 Å). As these rate-determining reactions are followed by many type A reactions, elementary chemical reactions are nearly equal in both directions. This is one of the most important conclusions obtained from our hypothesis.

A part of this theory may be applied to the catalytic oxidation of graphite crystals to account for the reaction anisotropy.

References and Notes

(1) A. Tomita and Y. Tamai, *J. Catal.*, **27**, 293 (1972).
(2) A. Tomita, N. Sato, and Y. Tamai, *Carbon*, **12**, 143 (1974).
(3) K. Hedden, *Z. Elektrochem.*, **66**, 652 (1962).
(4) P. Breisacher and P. C. Marx, *J. Amer. Chem. Soc.*, **85**, 3518 (1963).
(5) R. C. Bansal, F. J. Vastola, and P. L. Walker Jr., *Carbon*, **9**, 185 (1971).
(6) G. R. Henning, *J. Chim. Phys.*, 12 (1961).
(7) G. R. Hennig, *J. Inorg. Nucl. Chem.*, **24**, 1129 (1962).
(8) J. M. Thomas, "Chemistry and Physics of Carbon," Vol. 1, P. L. Walker, Jr., Ed., Marcel Dekker, New York, N.Y., 1965, p 121.
(9) D. W. McKee, *Carbon*, **8**, 623 (1970).
(10) R. T. K. Baker and P. S. Harris, *Carbon*, **11**, 25 (1973).
(11) B. McCarroll and D. W. McKee, *Carbon*, **9**, 301 (1971).
(12) C. W. Zielke and E. Gorin, *Ind. Eng. Chem.*, **47**, 820 (1955).
(13) P. L. Walker, Jr., F. Rusinko, Jr., and L. G. Austin, *Advan. Catal. Relat. Subj.*, *11*, 133 (1959).
(14) F. S. Feates, *Carbon*, 6, 949 (1968).

Membrane–Water Partition Coefficients of Ions. Calculated Effects of Membrane Thickness

J. E. Anderson* and H. W. Jackson

*Scientific Research Staff, Ford Motor Company, Dearborn, Michigan 48121 (Received September 7, 1973;
Revised Manuscript Received May 23, 1974)*

The partition coefficients of ionized solutes between membranes and water have been calculated on the basis of electrostatics. The method of images was used. The calculated partition coefficients are insensitive to membrane thickness when this thickness exceeds 100×10^{-8} cm. Calculated partition coefficients for thinner membranes are strongly thickness dependent. This suggests a useful lower limit to the thickness of the solute rejecting layer in reverse osmosis studies.

Many uncharged membranes combine high permeability for water with low permeability for ions dissolved in water. These permselective membranes find application in such diverse fields as cell physiology and water purification. Small ionic concentrations in the membrane are largely responsible for low ionic permeability. This is reflected experimentally in small membrane–water partition coefficients of ionized solutes. The low ionic concentrations are best understood on the basis of electrostatic arguments.[1-6] Charged ions prefer to remain in a high dielectric constant medium, such as water, rather than pass into a low dielectric constant medium, such as a membrane.

Several experimental studies have shown that ionic permeabilities and membrane–water partition coefficients are *independent* of membrane thickness.[7,8] These studies were performed with desalination membranes whose effective thickness exceeded 1000×10^{-8} cm. Recent years have witnessed advances in desalination technology based on composite membranes with much thinner surface layers.[9,10] This makes it reasonable to question at what point ionic permeabilities become dependent on membrane thickness. The present communication deals with this issue.[11]

Our calculations involve only simple electrostatics—computation of the thermodynamic work required to bring a test charge up to an ion of radius b in a medium of dielectric constant ϵ. More elaborate electrostatic calculations might be made, e.g., using the Debye–Hückel theory and/or pore models for the membrane.[3-6] We only expect electrostatic calculations to be *qualitatively* correct. They take no account of ion pairing in media of low dielectric constant—a phenomenon that is both real and hard to calculate exactly. For this reason, we do not view differences between simple and refined electrostatic calculations as overly significant.

The present calculation considers the electrostatic energy of charged particles in media of different dielectric constant. We should point out that a similar problem, involving the electrostatic energy of dipolar (but uncharged) molecules in media of different dielectric constant, can be treated by similar methods. Bell has implicitly solved the latter problem for membranes of infinite thickness.[12]

The electrostatic calculations assume the membrane–solvent geometry shown in Figure 1. We compute the electrostatic energy of a spherical ion of radius b inside a membrane of dielectric constant ϵ_m. The ion is assumed to have

charge q; the membrane has total thickness L. The center of the ion is located a distance x_0 from the center of the membrane. The solvent, of dielectric constant ϵ_s, is presumed to extend to infinity on both sides of the membrane.

The method of image charges[13] can be used to compute the electrostatic potential at an arbitrary point P in the membrane; P has coordinates (ρ, x). The finite thickness of the membrane forces us to consider multiple image charges in regions 1 and 3, i.e., in the solvent. All of these images occur on the line $\rho = 0$. The x coordinates of successive images in region 1 are $x_n = nL + (-1)^n x_0$; those of successive images in region 3 are $\bar{x}_n = \{nL + (-1)^{n+1} x_0\}$. The electrostatic potentials can be expressed as

$$\Phi_1 = \frac{q_0}{\epsilon_s \sqrt{\rho^2 + (x - x_0)^2}} +$$
$$\sum_{n=1}^{\infty} \frac{q_n}{\epsilon_s \sqrt{\rho^2 + [x + nL + (-1)^{n+1} x_0]^2}}$$

$$\Phi_3 = \frac{\bar{q}_0}{\epsilon_s \sqrt{\rho^2 + (x - x_0)^2}} +$$
$$\sum_{n+1}^{\infty} \frac{\bar{q}_n}{\epsilon_s \sqrt{\rho^2 + [x - nL + (-1)^{n+1} x_0]^2}} \quad (1)$$

$$\Phi_2 = \frac{q}{\epsilon_m \sqrt{\rho^2 + (x - x_0)^2}} +$$
$$\sum_{n=1}^{\infty} \frac{Q_n}{\epsilon_m \sqrt{\rho^2 + [x + nL + (-1)^{n+1} x_0]^2}} +$$
$$\sum_{n=1}^{\infty} \frac{\bar{Q}_n}{\epsilon_m \sqrt{\rho^2 + [x - nL + (-1)^{n+1} x_0]^2}}$$

The constants q, q_0, $\bar{q}_0$, Q_i, $\bar{Q}_i$ are interrelated by the following boundary conditions: at $x = (L/2)$, $E_{1\rho} = E_{2\rho}$, $D_{1x} = D_{2x}$; at $x = -(L/2)$, $E_{2\rho} + E_{3\rho}$, $D_{2x} = D_{3x}$. The new parameters are defined as $E_{1\rho} = -(\partial\Phi_1/\partial\rho)$, $D_{1x} = \epsilon_s[-(\partial\Phi_1/\partial x)]$, etc. After some mathematical manipulation, the following results are obtained
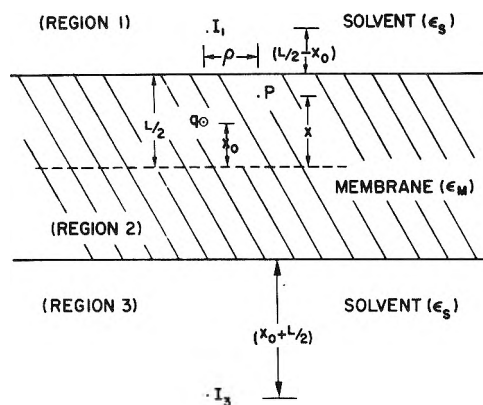
Figure 1. The membrane–solvent geometry assumed in the electrostatic calculations of ionic partition coefficients.

$$Q_n = \bar{Q}_n = q \left[\frac{\epsilon_m - \epsilon_s}{\epsilon_m + \epsilon_s} \right]^n$$

$$q_n = \bar{q}_n = \left[\frac{(\epsilon_m - \epsilon_s)}{(\epsilon_m + \epsilon_s)} \right]^n \left(\frac{2\epsilon_s}{\epsilon_m + \epsilon_s} \right) q$$

$$\Phi_2 = \frac{q}{\epsilon_m \sqrt{\rho^2 + (x - x_0)^2}} + \sum_{n=1}^{\infty} \frac{q}{\epsilon_m} \left(\frac{\epsilon_m - \epsilon_s}{\epsilon_m + \epsilon_s} \right)^n \times$$

$$\left\{ \frac{1}{\sqrt{\rho^2 + [x + nL + (-1)^{n+1} x_0]^2}} + \frac{1}{\sqrt{\rho^2 + [x - nL + (-1)^{n+1} x_0]^2}} \right\} \quad (2)$$

The potential of a charge spread uniformly over a spherical shell of radius b involves integrating $(x - x_0)$, ρ over a sphere. This task is simplified if we restrict ourselves to the situation where the sphere is completely within the membrane; i.e., when $|(L/2) - x| > b$. The potential *energy* is found by multiplying the potential by dq, and integrating from zero to the actual value of the charge. The end result amounts to writing $V(x,L) = (q/2)\Phi_2$, if we interpret q as the actual charge on the ion. The first term in eq 2 gives the self-energy, $q^2/2\epsilon_m b$. The contribution from the sum is equivalent to taking the limit of the sum as $\rho \to 0$, $x \to x_0$. This yields the expression

$$V(x, L) = \frac{q^2}{2\epsilon_m b} + \frac{q^2}{2\epsilon_m} \sum_{n=1}^{\infty} \left(\frac{\epsilon_m - \epsilon_s}{\epsilon_m + \epsilon_s} \right)^n \times$$

$$\left\{ \frac{1}{[x_0[1 + (-1)^{n+1}] - nL]} - \frac{1}{[x_0[1 + (-1)^{n+1}] - nL]} \right\}$$

$$= \frac{q^2}{2\epsilon_m b} + q^2 R \quad (3)$$

This can be approximated

$$V(x, L) \cong \frac{q^2}{2\epsilon_m b} + \frac{q^2}{\epsilon_m L} \left\{ \ln \left(\frac{\epsilon_m + \epsilon_s}{2\epsilon_s} \right) + \right.$$

$$\left[\left(\frac{\epsilon_m - \epsilon_s}{\epsilon_m + \epsilon_s} \right) \Big/ [(L/2x_0)^2 - 1] \right] +$$

$$\left. \frac{1}{3} \left(\frac{\epsilon_m - \epsilon_s}{\epsilon_m + \epsilon_s} \right)^3 \Big/ \left[\left(\frac{3L}{2x_0} \right)^2 - 1 \right] \right\} = \frac{q^2}{2\epsilon_m b} + q^2 R' \quad (4)$$

We now introduce an electrical neutrality constraint and calculate $E(x_0, L)$, the mean potential energy per mole.

Consider an $A_j B_i$ salt that dissociates completely into $j A^{i+}$ and $i B^{j-}$ ions (note that i and j are themselves both positive). $E(x_0, L)$ is computed as

$$E(x_0, L) = (i + j)^{-1}\{i[(je)^2/(2\epsilon_m b_+) + (je)^2 R] + j[(ie)^2/(2\epsilon_m b_-) + (ie)^2 R]\}$$

$$= [(ije^2)/(2\epsilon_m a)] + (ije^2)R$$

$$\cong [(ije^2)/(2\epsilon_m a)] + (ije^2)R'$$

where R and R' are defined by eq 3–4. Cationic and anionic radii are designated b_+ and b_-, respectively. They are related to a, the mean ionic radius, by the expression $a^{-1} = [(i/b_+) + (j/b_-)]/(i + j)$. The quantity e is the electronic charge. We note that $E(x_0, L)$ has the same functional form as $V(x_0, L)$ with (ije^2) replacing q^2 and a replacing b. Our entire calculation takes no account of interionic forces, and is strictly valid only at infinite dilution where individual charges remain at large distances from one another. Owing to the small ionic concentrations present in most membrane systems, we feel justified in omitting such interactions for the purpose of the present study. Our calculations might be modified, making use of the Debye–Hückel theory, to treat finite concentrations more precisely.

The potential energy of a mole of dissociated solute at infinite distance from the membrane is $E_\infty = (ije^2)/(2\epsilon_s a)$. We adopt this as a standard state. The relative ionic concentration at a distance x_0 from the interface is $C(x_0, L)$. This is proportional to $\exp[-(E(x_0, L) - E_\infty)/RT]$.

The solute permeability at position x_0, $P(x_0, L)$, is directly proportional to $C(x_0, L)$. The overall permeability, $P(L)$, is given by[14]

$$P(L)^{-1} = D_s^{-1} \int_{-T}^{T} \{2TC(x_0, L)\}^{-1} \, dx_0 = \{D_s K_s(L)\}^{-1} \quad (5)$$

where $T = \{(L/2) - a\}$. If one assumes that D_s, the solute diffusion coefficient in the membrane, is independent of membrane thickness, $P(L) = D_s K_s(L)$. The effective membrane–solvent partition coefficient, $K_s(L)$, is simply the reciprocal of the integral appearing in eq 5.

Optimum reverse osmosis rejection occurs when the solute permeability is minimal.[8] This corresponds to minimal $K_s(L)$ values. Figures 2–4 show calculated $K_s(L)$ values obtained by numerical integration of eq 5. In all of these calculations, we chose $\epsilon_s = 78$, the dielectric constant of water at 25°.

It comes as no surprise that the smallest $K_s(L)$ values are associated with membranes of lowest dielectric constant (large ϵ_s/ϵ_m ratios), and with solutes of high valence (large ij products). Compare Figures 2 and 3. Our calculations indicate that the greatest change in $K_s(L)$ with membrane thickness occur in the range below 100×10^{-8} cm. The calculated $K_s(L)$ values of thicker membranes are insensitive to thickness.

The small salt partition coefficients calculated for 100×10^{-8} cm thick membranes are consistent with the low salt permeabilities observed in studies of lipid bilayer membranes where $L \simeq 80 \times 10^{-8}$ cm. Our calculations suggest a steep dependence of permeability upon thickness in this range; it might prove interesting to speculate about the effects of stochastic fluctuations in membrane thickness upon membrane transport properties.
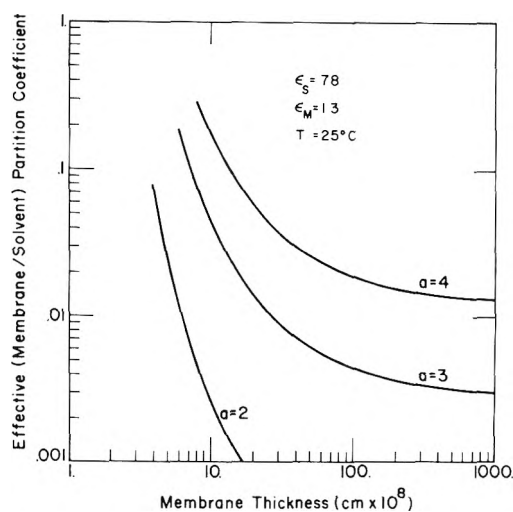
Figure 2. Effective (membrane–solvent) partition coefficients for 1:1 electrolytes as a function of membrane thickness. The a values give the mean ionic radii (in cm $\times$ 10^8) assumed in the calculation: $\epsilon_s = 78$, $\epsilon_m = 13$.
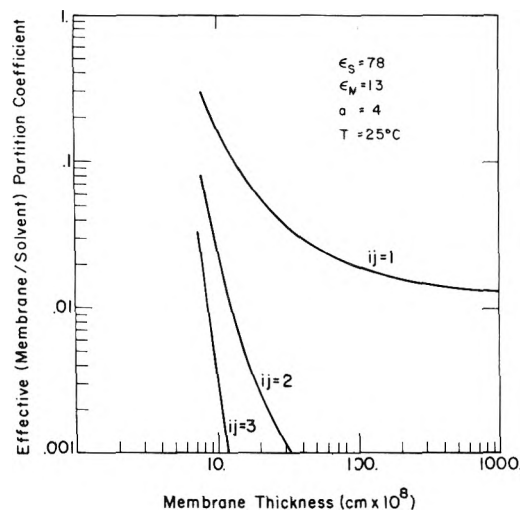
Figure 3. Effective (membrane–solvent) partition coefficients as a function of membrane thickness. The mean ionic radius is taken to be 4×10^{-8} cm. The ij values denote the product of cation and anion valence: $\epsilon_s = 78$, $\epsilon_m = 13$.

Figure 4. Effective (membrane–solvent) partition coefficients with $\epsilon_s = 78$ and $\epsilon_m = 26$. Calculated data are shown for $a = 2,4 \times 10^{-8}$ cm; $ij = 1,2$. Note that the curves for $a = 2 \times 10^{-8}$ cm, $ij = 1$ and for $a = 4 \times 10^{-8}$ cm, $ij = 2$, merge as L becomes large. This is a general result. For large L, one need only consider a reduced solute size $(a/\overline{ij})$.

Our calculations indicate that membrane–water partition coefficients should increase with increasing ionic size: note the size dependence of K_s for very thick membranes in Figures 2–4. Scatchard's analysis[1] also predicts such a trend. Various pore model calculations[3-6] of ionic partition coefficients result in a functional form similar to Eq 3–4 with a pore radius replacing a. As long as a is less than the pore radius, partition coefficients calculated from pore models are insensitive to solute size. The difference between these calculations can be traced to the self-energy terms appearing in eq 3–5. In a pore model, the liquid in the pore is presumed to have the same physical properties as the bulk solvent. This causes the self-energy of an ion in the pore liquid and in the bulk solvent to be identical. The self-energy term disappears, by subtraction, when the partition coefficient is calculated. Our use of a dielectric continuum assumes implicitly that the intimate mixing of solvent and polymer causes both constituents to lose their

bulk properties. Thus, we consider a spatially homogeneous continuum with its own dielectric characteristics. This leads to a membrane self-energy, $[ije^2/(2\epsilon_m a)]$, different from that of the bulk solvent, and to a size-dependent partition coefficient.

It is by no means clear where the dividing line between homogeneous and heterogeneous dielectrics should be drawn—which spatial arrangements of solvent and polymer (*i.e.*, membranes) should be viewed as a continuum, and which must be treated as a two-phase system. It is our belief that a dielectric continuum approximation is the more reasonable when spatial heterogeneities in the membrane ("pore dimensions") only extend over distances comparable to the range of surface forces, *e.g.*, 10^{-7} cm or less.

In a parallel report,[15] we present experimental data showing that the *mean* partition coefficients of NaCl, NaBr, NaI, and $NaClO_4$ between "fully dense" cellulose acetate membranes and water are 0.013, 0.036, 0.077, and 0.35 [(grams of salt/milliliter of CA membrane)/(grams of salt/milliliter of water solution)]; the partition coefficients increase with the size of the anion. This supports the size-dependence prediction of the present calculations.[16] The membranes used in these experiments were typically 5–12 $\times$ 10^{-3} cm thick; thickness dependence was not examined. Corresponding studies of size effects for salts with a common anion are difficult. Not only do cations hydrate to varying degrees (thereby changing their effective dimensions), but the extent of their hydration depends on the medium in which they are immersed. For this reason, one is safer comparing salts with a common anion, as described above; anions do not hydrate appreciably.

We know of no corresponding pore model calculations concerning the effects of membrane thickness on solute permeability.

In summary, electrostatic calculations indicate that membranes with effective thickness greater than 50×10^{-8} cm should have useful desalination properties. This minimum thickness is a factor of 4–8 smaller than the *surface* layers of current composite membranes,[9,10] and should serve as a useful goal for experimental work. The reader is

referred to other calculations[17] which suggest that membranes with effective thicknesses in this range cannot be prepared from asymmetric films.

Acknowledgment. We are grateful to our colleague, Robert Ullman, for constructive criticism in the course of this work.

References and Notes

(1) G. Scatchard, *J. Phys. Chem.*, **68**, 1056 (1964).
(2) S. Sourirajan, *Ind. Eng. Chem., Fundam.*, **3**, 206 (1964).
(3) A. Parsegian, *Nature (London)*, **221**, 844 (1969).
(4) E. Glueckauf, *Proc. Int. Symp. Water Desalination, 1st, 1965*, 143 (1967).
(5) T. O. Hodgson, *Desalination*, **8**, 99 (1970).
(6) C. P. Bean in "Membranes, A Series of Advances," G. Eisenman, Ed. Marcel Dekker, New York, N.Y., 1972, p 1.
(7) C. E. Reid and E. J. Breton, *J. Appl. Polym. Sci.*, **1**, 133 (1959).
(8) H. K. Lonsdale, U. Merten, and R. L. Riley, *J. Appl. Polym. Sci.*, **9**, 1341 (1965).
(9) R. L. Riley, H. K. Lonsdale, and C. R. Lyons, *J. Appl. Polym. Sci.*, **15**, 1267 (1971).
(10) R. L. Riley, H. K. Lonsdale, C. R. Lyons, and U. Merten, *J. Appl. Polym. Sci.*, **11**, 2143 (1967).
(11) Scatchard (ref 1) and Parsegian (ref 3) have calculated the partition coefficient of ions between water and the middle of a membrane. They do not treat the integrated membrane–water partition coefficient, which governs ionic permeability.
(12) R. P. Bell, *Trans. Faraday Soc.*, **27**, 797 (1931).
(13) The method of image charges is widely used in classical electrostatic calculations. It provides a handy way of satisfying Laplace's equation under a variety of conditions. See, for example, J. D. Jackson, "Classical Electrodynamics," Wiley, New York, N.Y., 1962, Chapter 2.
(14) See, for example, R. M. Barrer in "Diffusion in Polymers," J. Crank and G. S. Park, Ed., Academic Press, New York, 1968.
(15) M. E. Heyde, C. R. Peters, and J. E. Anderson, to be submitted for publication. Apart from the work of C. R. Thomas and R. E. Barker, Jr. (*J. Appl. Polym. Sci.*, **7**, 1933 (1963)), these comprise the first independent measurements of cation and anion partition coefficients for specific salts. Separate determinations prove important because of the small concentration of fixed negative charge on cellulose acetate.
(16) H. K. Lonsdale (in "Desalination by Reverse Osmosis," U. Merten, Ed., MIT Press, Cambridge, Mass., 1966, pp 113–115) has pointed out the possibility that the thick cellulose acetate membranes used by Thomas and Barker (ref 14, above) were not fully equilibrated with the external aqueous solutions.
(17) J. E. Anderson and R. Ullman, *J. Appl. Phys.*, **44**, 4303 (1973).

Effect of Pressure on the Surface Tension of Water. Adsorption of Low Molecular Weight Gases on Water at 25°[1]

R. Massoudi and A. D. King, Jr.

Department of Chemistry, University of Georgia, Athens, Georgia 30602 (*Received March 14, 1974*)

Publication costs assisted by the National Science Foundation

The variation of interfacial tension with hydrostatic pressure has been determined for a number of gas–water systems at 25° using the capillary-rise method. Measurements are reported for water with He, H_2, O_2, N_2, Ar, CO, CO_2, N_2O, CH_4, C_2H_4, C_2H_6, C_3H_8, and $n\text{-}C_4H_{10}$. Adsorption isotherms are derived from polynomial fits to the data through the Gibbs equation. Depending upon the gas, adsorption isotherms of types I and III are found[2] with low molecular weight gases exhibiting type I behavior and the more polarizable gases yielding type III isotherms. In general, the degree of adsorption increases monatonically with polarizability of the gas. At low surface coverages however, it is found that adsorption coefficients for CO_2, N_2O, and C_2H_4 are abnormally large. This is interpreted as indicating that in addition to van der Waals forces, weak interactions, either electrostatic or chemical in nature, exist between molecules of these gases and the aqueous surface. It is also found that in the zero-coverage limit, the free energy of adsorption for the *n*-alkanes is a linear function of the number of methylene groups indicating correspondence with Traube's rule. Values extrapolated to higher members of this series agree well with those determined experimentally using gas chromatographic methods.[3]

Introduction

In recent years there has been a resurgence in interest concerning bulk and surface properties of water.[4] One area of research that has received comparatively little attention concerns the effect of pressure on the surface tension of water. This is somewhat surprising since such experiments are capable of providing a great deal of information concerning adsorption of low molecular weight species at aqueous surfaces. To these authors' knowledge, ref 5–11 constitute a complete bibliography on this subject.

This paper reports results obtained in measuring interfa-

cial tension as a function of pressure for a wide variety of gas–water systems at 25°. The data for the hydrocarbon gases represent an extension to lower carbon numbers of earlier work by Cutting and Jones.[12] The isotherms derived from these data also complement recent studies by Karger, *et al.*,[3] in which net retention volumes of various hydrocarbons chromatographed on columns having water as the stationary liquid phase are used to determine isotherms directly at low surface coverages.

The systems involving water with carbon dioxide and nitrous oxide were of particular interest since it is known that on one hand these gases are more soluble than expected in

bulk water[13] while on the other hand water is abnormally soluble in compressed CO_2 and N_2O[14] leading to the question of whether a corresponding anomaly is to be found with respect to adsorption at the interface of water with these two gases.

Experimental Section

The changes in surface tension of water under dense gas atmospheres were determined using the capillary-rise technique. The experiments were carried out in a thermostated cylindrical brass bomb having an internal diameter of 1.75 in. and a length of 8 in. A single capillary (0.3-mm i.d.) was suspended from a polished 0.125-in. diameter stainless steel rod which passes through an "O" ring in the top closure. This rod was connected to a micrometer drive mounted on the outside of the closure thus allowing the suspended capillary to be raised or lowered while the system is under pressure. This permitted a series of capillary-rise determinations to be made using the same section of capillary bore at all pressures. A thin-walled glass liner was used to contain the liquid at the bottom of the bomb. The bomb was equipped with a 0.5 in. thick Plexiglas window providing a 0.75 × 3.5 in. viewing area along one side. Capillary rise was measured to 0.03 mm with a cathetometer, and pressures were measured with Bourdon gauges which were periodically calibrated against a dead-weight tester. The system was designed with a safety factor of 2 at the upper limit in pressure of 1000 psi. The temperature of the bomb was controlled to within ±0.2°, and all measurements reported here were made at 25° as determined by a thermocouple located in the central cavity of the bomb.

Surface tensions were calculated using the relation[15]

$$\gamma = \tfrac{1}{2}rg(h + r/3)(\rho_l - \rho_g) \qquad (1)$$

where γ is the surface tension, g the acceleration of gravity, and h the capillary rise, with ρ_l and ρ_g being the densities of the bulk liquid and gas phases, respectively. The radius r of the section of capillary used in a given series of measurements was determined from eq 1 using a value of h extrapolated to zero pressure and a value of $\gamma_0 = 71.98$ dyn/cm,[16] for the surface tension of water in equilibrium with its pure vapor at 25°.

Gas densities were calculated from PVT data found in ref 17–28 while that for water was assumed constant over the pressures of this work. All gases used in these experiments were CP grade or the equivalent having quoted purities of 99.0% or higher for the hydrocarbon gases and 99.5% or higher for the others. Laboratory-distilled water was used without further purification.

Results and Discussion

A representative sample of the experimental data is shown in Figure 1 where the relative surface tension, γ/γ_0, of water is shown plotted against total pressure. The experimental surface tension data for each H_2O–gas system were fit to a polynomial expansion in pressure and the results are shown in Table I. The curves generated by the polynomials in Table I are capable of reproducing the experimental results within an average deviation of ±0.2 dyn/cm for CO_2 and N_2O and ±0.06 dyn/cm for all other gases. The decreased precision of the CO_2 and N_2O data reflects the increased experimental error associated with systems for which gas solubility in the liquid phase is significant. Polynomial expansions of degree 2 or less provided a satisfactory fit to all data except those involving CO_2 and N_2O. The

TABLE I: Interfacial Tension as Function of Pressure for Pure Water with Various Gases at 25°[a]

Gas	$\gamma = \gamma_0 + BP + CP^2 + DP^3$		
	B, dyn/cm atm	C, dyn/cm atm^2	D, dyn/cm atm^3
He	0.0000		
H$_2$	−0.0250		
O$_2$	−0.0779	+0.000104	
N$_2$	−0.0835	+0.000194	
Ar	−0.0840	+0.000194	
CO	−0.1041	+0.000239	
CH$_4$	−0.1547	+0.000456	
C$_2$H$_4$	−0.6353	+0.00316	
C$_2$H$_6$	−0.4376	−0.00157	
C$_3$H$_8$	−0.9681	−0.0589	
N$_2$O	−0.6231	+0.00287	−0.000040
CO$_2$	−0.7789	+0.00543	−0.000042
n-C$_4$H$_{10}$	−2.335	−0.591	

[a] All coefficients are quoted to one extra significant figure in order to minimize effects of round-off error in generating values for γ.
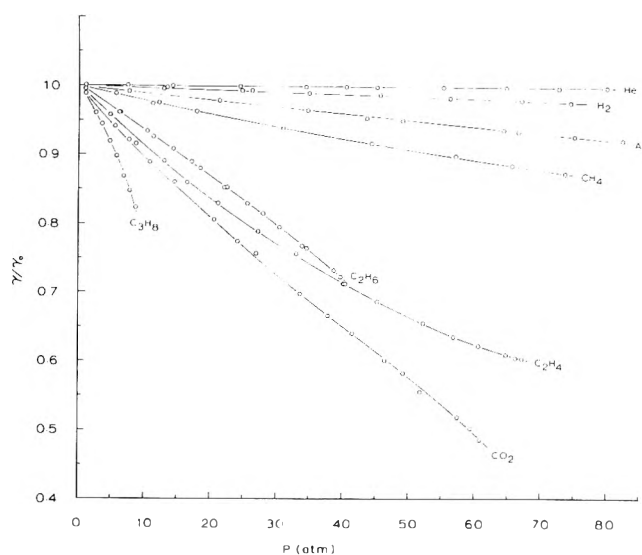
Figure 1. Relative surface tension as a function of pressure for various gas–water systems at 25°.

γ–P curves for the latter two gases exhibited a point of inflection at about 30 atm necessitating the cubic terms found in Table I. Similar measurements involving water with He, H_2, N_2, CH_4, CO_2, and C_2H_6 at room temperature, approximately 25°, have been reported in graphical form by Slowinski, et al.[7] More precise measurements were subsequently carried out for the systems water–N_2 and water–Ar, at 30°, by Masterton, Bianchi, and Slowinski.[8] Hough and coworkers[10] have used the pendent-drop method to determine the surface tension of water in the presence of compressed CO_2 at temperatures of 100°F and greater. The data obtained here for water with He, H_2, N_2, CH_4, CO_2, and C_2H_6 at 25° agree well with those shown in ref 7. A comparison of the N_2, Ar, and CO_2 data with those taken at higher temperature[8,10] indicates that the drop in surface tension with pressure is somewhat larger at the lower temperature of this work as would be expected where positive adsorption of gas occurs at the aqueous interface. No minimum is found in the surface tension data for water with CO_2 at 25° over the range of pressures encountered here.

TABLE II: Surface Excess ($\Gamma_2^{(1)}$) for Various Gases on Water at 25° (molecules/cm² × 10⁻¹⁴)

P, atm	H₂	O₂	N₂	Ar	CO
10	0.06	0.18	0.19	0.20	0.25
20	0.12	0.36	0.37	0.37	0.46
30	0.18	0.53	0.53	0.54	0.66
40	0.23	0.69	0.66	0.68	0.83
50	0.29	0.84	0.78	0.80	0.98
60	0.35	0.99	0.88	0.91	1.1
70	0.40	1.1	0.96	1.0	1.2
80			1.0	1.1	1.3
	$\Delta G_A = 0.5$ kcal/mol	$\Delta G_A = -0.2$ kcal/mol	$\Delta G_A = -0.2$ kcal/mol	$\Delta G_A = -0.2$ kcal/mol	$\Delta G_A = -0.3$ kcal/mol

P, atm	CH₄	C₂H₄	CO₂	N₂O	C₂H₆
10	0.36	1.5	1.8	1.5	1.2
20	0.69	2.8	3.4	3.1	3.0
30	0.98	4.0	5.0	5.0	5.5
40	1.2	5.2	7.1	7.8	10
50	1.4	6.3	10	12	
60	1.6	7.8	15		
70	1.7				
	$\Delta G_A = -0.6$ kcal/mol	$\Delta G_A = -1.4$ kcal/mol	$\Delta G_A = -1.5$ kcal/mol	$\Delta G_A = -1.4$ kcal/mol	$\Delta G_A = -1.2$ kcal/mol

P, atm	C₃H₆	P, atm	C₄H₁₀
2	0.60	0.5	0.36
4	1.5	1.0	0.88
6	2.7	1.5	1.6
8	4.4		
	$\Delta G_A = -1.7$ kcal/mol		$\Delta G_A = -2.2$ kcal/mol

Such minima have been reported in data taken at higher pressures and temperature.[10]

Surface excesses for the various gases, $\Gamma_2^{(1)}$, have been calculated according to the common convention which places the Gibbs plane such that the surface excess of water equals zero using the equation

$$\left(\frac{\partial \gamma}{\partial P}\right)_T = -\Gamma_2^{(1)}\left(\frac{ZkT}{P}\right) \qquad (2)$$

Here Z represents the compressibility factor of the pure gas at pressure P and temperature T while k designates the Boltzmann constant. The surface excesses listed in Table II were calculated using eq 2 with values of $(\partial\gamma/\partial P)_T$ derived from the appropriate polynomial expansion from Table I. Values of Z were taken from ref 17–28.

Figure 2 shows the surface excess $\Gamma_2^{(1)}$ as a function of gas concentration for a representative sample of gases. While not shown, the isotherm for nitrous oxide parallels that of the CO₂ while $\Gamma_2^{(1)}$ for CO, N₂, and O₂ nearly coincide with the data for argon. Since the molecular areas of the gases are typically of the order of 20 Å² per molecule, a coverage of 5 × 10⁺¹⁴ molecules/cm² approximates complete monolayer coverage for these gases. Thus it is seen that the adsorption behavior of the gases fall into two general categories. The gases having critical temperatures well below 25° all exhibit type I isotherms and appear to approach saturation coverages corresponding to 50% or less of monolayer coverage. On the other hand, the higher molecular weight hydrocarbon gases having critical temperatures above 25° exhibit type III behavior with isotherms that are concave upward and pass smoothly through the monolayer region. The isotherms do not, however, become asymptotic to their saturated vapor concentration in agreement with earlier investigations concerning the adsorption of higher molecular weight alkanes on water by Cutting and Jones.[12]

Ethylene appears to occupy a position intermediate to the other gases in that its isotherm is concave to the concentration axis and yet passes smoothly to values exceeding those expected for monolayer coverage.

Both CO₂ and N₂O are unique among the gases studied here in that their isotherms exhibit points of inflection which occur in the vicinity of $\Gamma_2^{(1)} = 5 \times 10^{14}$ cm⁻², that is, at conditions of approximately 100% monolayer coverage. This suggests that the overall mechanism for adsorption at low coverages differs from that responsible for multilayer adsorption for these two gases. At the right of this point of inflection in the multilayer adsorption region the surface excesses at a given gas concentration arrange themselves in an ascending order with increasing gas polarizability (α) as might be expected if London dispersion forces were the dominant mode of attraction while to the left at low coverages the order relative to ethane ($\alpha = 4.5$ Å²) is reversed in the case of CO₂ ($\alpha = 2.7$ Å²), N₂O ($\alpha = 3.0$ Å²), and even C₂H₄ ($\alpha = 4.3$ Å²). The anomalous behavior of these gases is revealed quite clearly in Figure 3 which shows the adsorption coefficient at zero coverage

$$K_A = \lim_{C_2^g \to 0} \left(\frac{\partial \Gamma_2^{(1)}}{\partial C_2^g}\right)$$

plotted against gas polarizability for each gas. It is apparent that in the zero-coverage limit the adsorption isotherms of these three gases differ significantly from the rest.

The absence of information regarding enthalpies and entropies of adsorption of these gases precludes any detailed discussion concerning likely causes for the anomalous adsorption of CO₂ and N₂O. Nevertheless, a qualitative picture emerges in which at monolayer coverages or less, CO₂ and N₂O are adsorbed at the aqueous interface to a greater extent than would be expected if van der Waals forces were the sole cause of attraction between water and these gases.
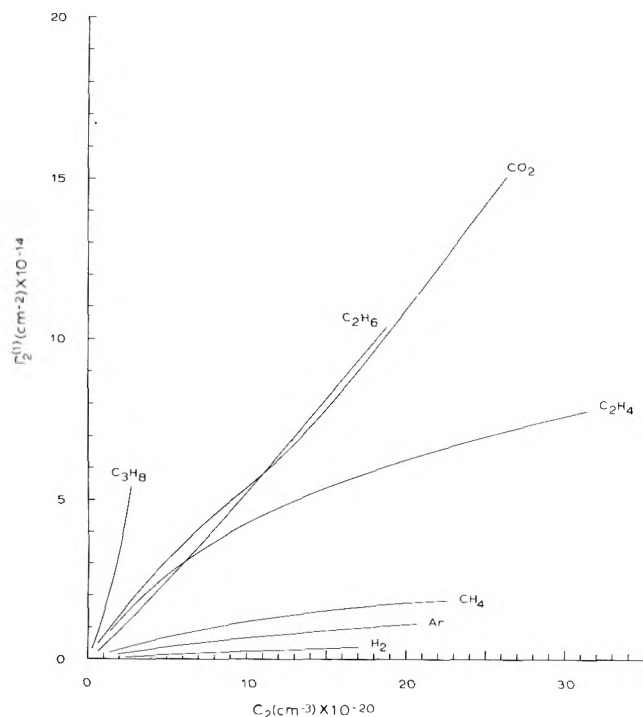
Figure 2. Surface excess as a function of gas concentration for various gas–water systems at 25°. Estimated error in $\Gamma_2^{(1)}$: ±3%.
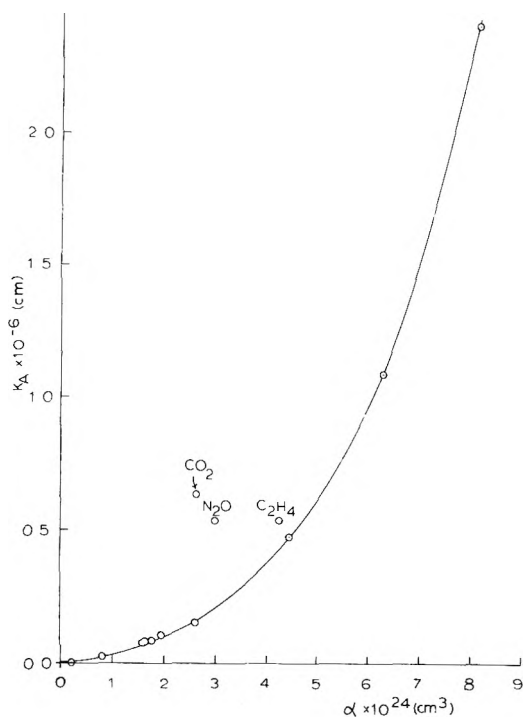

Figure 3. Adsorption coefficient at zero coverage vs. average polarizability of gaseous component.

In this sense the enhanced adsorption of these gases at low coverages parallels earlier observations that mutual solubilities of these gases with water are unusually large both in the liquid phase[13] and the gas phase.[14] On the other hand, multilayer adsorption of these three gases appears to involve a mechanism more in common with the other gases.

There is considerable evidence suggesting that a high degree of order exists at the surface of hydrogen-bonded liquids.[29] In the case of water it is thought that a preponderance of the molecules near the surface are oriented with their hydrogen atoms directed toward the gas phase.[30,31] This suggests that the anomalous adsorption of these gases at low coverages may be the result of hydrogen bonding with the highly oriented water molecules acting as proton donors to the carbonyl-like functions of CO_2 and N_2O. Such a mechanism also explains the enhanced adsorption of ethylene at low coverages since olefins are known to serve as proton acceptors in hydrogen bonds.[32] Karger and coworkers have invoked a similar argument to explain the enhanced adsorption of di-n-propyl ether on water at low coverages.[33] Such a model is consistent with the observed rearrangement in the order of $\Gamma_2^{(1)}$ for CO_2 and N_2O relative to the other gases shown in Figure 3 since beyond a monolayer coverage only physical interactions of a van der Waals type can be effective in determining the degree of adsorption for these gases. It should be pointed out that other factors such as dipole–quadrupole interactions or the known acidity of CO_2 may also play a significant role in determining the adsorption behavior of these gases.[34]

The idea that at low coverage specific interactions exist between water and certain gases in addition to dispersion forces is supported in the case of CO_2 by other data of Slowinski, et al.,[7] which show that, in contrast to the data of Figure 1, the surface tensions of n-hexane with CO_2 lie intermediate to those of n-hexane with methane and ethane at all pressures as would be expected if London dispersion forces alone were effective.

Standard free energies of adsorption at zero coverage, ΔG_A, have been calculated for the various gases using 1 atm and the Kemball–Rideal[35] convention as standard states. The results are listed in Table II. It is seen that beginning with ethane, ΔG_A increases by a constant increment of −0.5 kcal/mol per methylene group indicating a correspondence with Traube's rule. The free energy increment calculated here is in exact agreement with those obtained by Posner, et al.[36] In addition, extrapolation to the next higher member this series, n-pentane, yields ΔG_A = −2.7 kcal/mol, which when corrected to 12.5° using the Gibbs–Helmholtz equation and a value of ΔH_A = −5.7 kcal/mol[3] becomes ΔG_A = −2.8 kcal/mol, agreeing with the value obtained by Karger, et al., using gas chromatographic techniques.[3] The excellent correlation between the free energies obtained in this work and those derived from the direct determination of surface excesses at low coverages by Karger, et al., is very encouraging and supports the validity of the extrapolations to zero surface coverage used here.

References and Notes

(1) This work was supported in part by a grant from the National Science Foundation (GP-38386) and ir part by the NIH. Biomedical Sciences Support Grant (5 505 RR07025).
(2) S. Brunauer, "The Adsorption of Gases and Vapors," Vol. 1, Princeton University Press, Princeton, N. J., 1945.
(3) A. Hartkopf and B. L. Karger, *Accounts Chem. Res.*, 6, 209 (1973).
(4) Recent reviews covering these topics can be found in (a) F. Franks, Ed., "Water, A Comprehensive Treatise," Plenum Press, New York, N. Y., 1973; (b) W. Drost-Hansen, "Aqueous Interfaces, Methods of Study and

Structural Properties," *Ind. Eng. Chem.*, **57** (3), 38 (1965); **57** (4), 18 (1965).

(5) E. W. Hough, M. J. Rzasa, and B. B. Wood, Jr., *Trans. AIME*, **192**, 57 (1951).

(6) E. W. Hough, B. B. Wood, Jr., and M. J. Rzasa, *J. Phys. Chem.*, **56**, 996 (1952).

(7) E. J. Slowinski, Jr., E. E. Gates, and C. E. Waring, *J. Phys. Chem.*, **61**, 808 (1957).

(8) W. L. Masterton, J. Bianchi, and E. J. Slowinski, Jr., *J. Phys. Chem.*, **67**, 615 (1963).

(9) C. S. Herrick and G. L. Gaines, Jr., *J. Phys. Chem.*, **77**, 2703 (1973).

(10) E. W. Hough, G. J. Heuer, and J. W. Walker, *Trans. AIME*, **216**, 469 (1959).

(11) G. J. Heuer, Ph.D. Dissertation, University of Texas, 1957; *Diss. Abstr.*, **17**, 2559 (1958).

(12) C. L. Cutting and D. C. Jones, *J. Chem. Soc.*, 4067, 4076 (1955).

(13) J. H. Hildebrand and R. L. Scott, "The Solubility of Nonelectrolytes," Reinhold, New York, N. Y. 1950; reprinted by Dover Publications, New York, N. Y., 1964, p 248.

(14) C. R. Coan and A. D. King, Jr., *J. Amer. Chem. Soc.*, **93**, 1857 (1971).

(15) A. Weissberger, "Physical Methods of Organic Chemistry," 3rd ed., Interscience, New York, N. Y., 1959, Part 1, pp 767–769.

(16) H. A. Landolt and R. Bornstein, "Zahlenwerte und Funktionen," Vol. II, 6th ed, Springer-Verlag, Berlin, 1956, Part 3, p 420. Data for nitrogen from ref 8 were used to correct surface tensions measured against air to equilibrium-vapor values cited in text.

(17) He: R. Wiebe, V. L. Gaddy, and C. Heins, Jr., *J. Amer. Chem. Soc.*, **53**, 1721 (1931).

(18) H$_2$: A. Michels and M. Goudeket, *Physica*, **8**, 347 (1941).

(19) O$_2$: A. Michels, H. W. Schamp, and W. De Graaff, *Physica*, **20**, 1209 (1954).

(20) N$_2$: R. J. Lunbeck, A. Michels, and G. L. Wolkers, *Appl. Sci. Res.*, Sect. A, 3, 197 (1952).

(21) CO: A. Michels, J. M. Lupton, T. Wassenaar, and W. De Graaff, *Physica*, **18**, 121 (1952).

(22) Ar: A. Michels, H. Wijker, and H. K. Wijker, *Physica*, **15**, 627 (1949).

(23) CH$_4$: A. Michels and G. W. Nederbragt, *Physica*, **3**, 569 (1936).

(24) C$_2$H$_4$: A. Michels, S. R. De Groot, and M. Geldermans, *Appl. Sci. Res.*, Sect. A, **1**, 55 (1947).

(25) C$_2$H$_6$: A. Michels, W. Van Straaten, and J. Dawson, *Physica*, **20**, 17 (1954).

(26) C$_3$H$_8$: G. W. Thomson, *Ind. Eng. Chem.*, **35**, 895 (1943).

(27) CO$_2$: A. Michels and C. Michels, *Proc. Roy. Soc.*, Ser. A, **153**, 201 (1936).

(28) N$_2$O: E. J. Couch and K. A. Kobe, *J. Chem. Eng. Data*, **6**, 229 (1961).

(29) R. J. Good, *J. Phys. Chem.*, **61**, 810 (1957).

(30) M. Blank and R. H. Ottewill, *J. Phys. Chem.*, **68**, 2206 (1964).

(31) N. H. Fletcher, *Phil. Mag.*, **18**, 1287 (1968).

(32) R. West, *J. Amer. Chem. Soc.*, **81**, 1614 (1959).

(33) B. L. Karger, R. C. Castells, P. A. Sewell, and A. Hartkopf, *J. Phys. Chem.*, **75**, 3870 (1971).

(34) A recent investigation by A. W. Adamson and B. R. Jones, *J. Colloid Interface Sci.*, **37**, 831 (1971), suggests that chemisorption involving the formation of carbonic acid occurs at the ice–CO$_2$ interface at low temperatures.

(35) C. Kemball and E. K. Rideal, *Proc. Roy. Soc.*, Ser. A, **187**, 73 (1946).

(36) A. M. Posner, J. R. Anderson, and A. E. Alexander, *J. Colloid Sci.*, **7**, 623 (1952).

Surface Drag Viscosity of Bovine Serum Albumin Monolayers

Henri L. Rosano,* Shu Hsien Chen, and James H. Whittam

The City College of the City University of New York, New York, New York 10031 (Received January 11, 1974; Revised Manuscript Received May 28, 1974)

It has been observed that compression or decompression of bovine serum albumin monolayers spread on an aqueous substrate near the isoelectric point will produce surface pressures that are dependent on the distance between the measuring device and the compression barrier. As the pH of the substrate is varied, either above or below the isoelectric point, the effect diminishes. Similar results have been observed with β casein. This phenomena fails to appear for small molecules (myristic acid, eicosyl sodium sulfate) even when the substrate contains substituted alkanol amines. A theory is provided which suggests that the major effect is due to a surface drag viscosity.

Introduction

Proteins are often used in emulsion and foam formulations because of their stabilizing properties. A useful method to correlate the effects of proteins on the above systems is to study the properties of protein monolayers on liquid substrates. As can be expected, the surface behavior of these macromolecules are quite different from ordinary low molecular weight compounds.

This paper is concerned with an interesting series of effects observed with bovine serum albumin (BSA) when spread on a clean liquid surface.

Experimental Section

The experimental apparatus for measuring surface pressures has previously been described by Christodoulou and Rosano.[1] The compression and expansion rates were varied between 0.009 and 0.03 cm/sec. Isotherms were determined by compressing (and expanding) for short durations of time and then allowing the system to reach equilibrium.

The surface pressures were determined from surface tension measurements which were made by suspending a wettable sand-blasted platinum blade from a microforce transducer–amplifier system (Model 311 A, The Sanborn Co., Waltham, Mass.). The transducer output was recorded continuously on an x–y recorder (Model 370, Keithley Instruments, Inc., Cleveland, Ohio). The surface tensions were reproducible within ±0.1 dyn.

An aqueous protein solution containing 0.5% of 1-pentanol was deposited onto the aqueous substrate with an Agla micrometer syringe (Burroughs Wellcome Co., Tuckahoe, N.Y.). The substrate and film were retained in an edge paraffin coated silica trough (65 × 14 × 2 cm).

The surface was cleaned by dusting calcinated talcum powder on the substrate and removing it with the aid of a hollow glass tip connected to an aspirator.

The bovine serum albumin crystals were purchased from the Nutritional Biochemicals Corporation, Cleveland, Ohio. A solution was prepared by dissolving about 50 mg of protein in a 10 ml solution of 0.5% 1-pentanol (Fisher Scientific Co., Fairlawn, N.J.).

The water for the substrate was distilled from a Stokes still and foamed in a 600-ml medium-porosity sintered glass funnel. The foam was removed several times by sweeping the surface to remove surface active impurities.[1]

Results

Bovine serum albumin was spread on an isoelectric substrate (pH 5.3) and initially compressed to a pressure (π) of 5 dyn/cm. The molecular weight of the protein was determined to be 66,590 g/mol (pH 5.35 at 26°) with a cosurface of 12,000 Å^2/molecule. This was determined by using a surface micromanometer.[2] The moving barrier compressed the monolayer at a constant rate of 1.96×10^{-2} cm/sec for an interval of 70 sec while the surface pressure was continuously recorded at various positions in the trough. Figure 1 describes the results of π vs. time at various distances from the moving barrier. It is obvious that the surface pressure recorded is dependent on the distance between the wettable plate and the moving barrier. In addition, the further away from the barrier the pressure is recorded the smaller is the slope ($\partial\pi/\partial T$).

The horizontal lines (in Figure 1) indicate that the pressure at each distance X remained constant after the barrier had compressed the monolayer (surface) for a period of 70 sec and was then stopped.

A hysteresis phenomenon is observed when one expands the monolayer after it has been compressed for 70 sec. Increasing the rate of compression yields a set of π vs. T curves similar to Figure 1 only with slopes of $\partial\pi/\partial T$ which are larger. The rate of compression had little or no effect on the pressure when measured at a fixed distance providing the monolayer was compressed to the same area.

Figure 2 describes the effect of pH on the surface pressure (π) of bovine serum albumen monolayers when determined at various distances from the moving barrier. Each reading was taken after the barrier was compressed at a rate of 1.96×10^{-2} cm/sec for 60 sec. The initial pressure of the system was 5 dyn/cm. The pH was altered by mixing an appropriate amount of 0.1 N HCl and 0.1 N NaOH. Although the pH was varied the ionic strength was kept constant. When the ionic strength of the aqueous substrate was varied from 0.001 to 0.1 N by adding NaCl, the effect was obvious in all cases but the greatest effect appeared at the lowest ionic strength.

Recent experiments in this laboratory indicate similar effects for β casein when spread on distilled water (pH 5.5, 23.5°)–6 N urea (pH 6.5, 24.5°), at various ionic strengths and over different pH ranges.

When a monolayer of myristic acid spread on 0.01 N HCl was used over the same pressure range (5 dyn/cm), the change in pressure on compression and expansion was independent of the position of the wettable blade from the moving barrier.

Additional experiments were conducted on eicosyl sodium sulfate monolayers spread over (1) 0.1 N 2-amino-2-methyl-1-propanol (pH 9.65, 24.5°) and (2) 0.1 N 2-amino-1-butanol solution (pH 8.5, 24.5°). In all cases of compres-
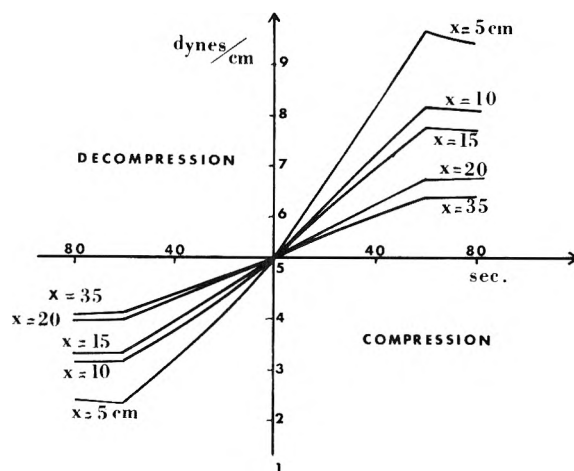
Figure 1. Bovine serum albumin monolayer on water (pH 5.2, 24°) compressed first at 5.0 dyn/cm; rate of compression (or decompression) 1.5 cm/min.
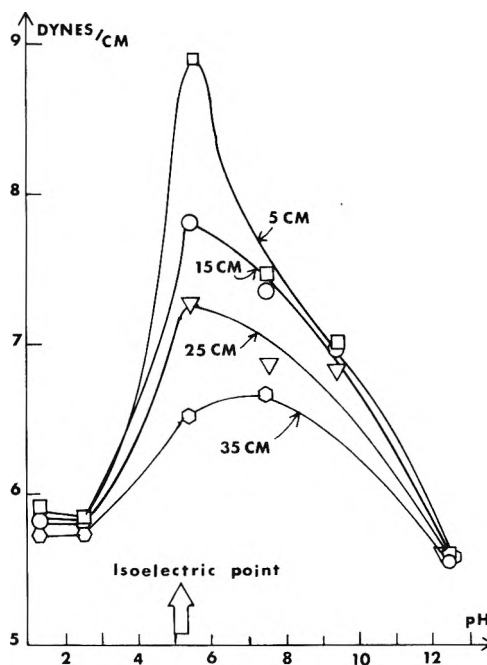
Figure 2. Effect of pH on surface pressure measured at various distances from the compression barrier. Measurements taken after compressing at a rate of 1.96×10^{-2} cm/sec for 60 sec. Initial pressure 5 dyn/cm: □, −5 cm; ○, −15 cm; ▽, −25 cm; ○, −35 cm.

sion or decompression, the measured surface pressures were independent of the distance between the measuring device and the compression barrier.

Interpretation

The surface properties of macromolecules is most likely due to the unfolding of the long chains in the surface region. Flory and Huggins[3] developed a theory in 1942 for polymer solutions and Singer[4] later applied it to surface films. Since then Frish and Simha[5] and Silberberg[6] have proposed additional models which take into account that the portions of the polymer chain will be pushed into the bulk phase or even lifted off the surface as compression takes place.

In the case of protein this phenomena of chain unfolding and coiling is known as denaturation.

This denaturation effect is most likely responsible for the results appearing in Figure 1. As the monolayer is compressed, the long chains of the protein reorient themselves in the monolayer and, therefore, the surface viscosity will be affected. The region of greatest reorientation will be near the barrier, thus one should expect the most dramatic change in the viscosity coefficient in this region.

This behavior is easiest to understand if each individual protein molecule is considered equivalent to an elastic spring and a dashpot in parallel (Kelvin model). As the barrier is compressed a force is developed on the mechanical model. The dashpot begins to compress and exerts a resisting force (this is analogous to the surface viscosity force between the protein and bulk phase). As the piston is compressed the spring will also begin to apply a force (this being analogous to the viscosity force developed within the protein molecule as it coils). Finally, as the entire "Kelvin solid" is moved, the force will be transferred to the models right behind it which is analogous to the viscosity within the monolayer produced by intensity models. With this type of model the pressure will be dependent on position.

From the above model, it may be assumed that the resistance to the moving barrier may be due to a viscosity effect which is developed in the following ways: (1) the viscosity within the monolayer itself which can be attributed to the coiling of the molecule and protein protein interaction; (2) the viscosity developed between the sheath of water molecules bound to the monolayer and the bulk phase (surface drag viscosity). Numerous authors have conducted experiments on this phenomena by determining the amount of substrate carried by a moving monolayer (Crisp,[7] Pak and Gershfeld[8]). For example, Schulman and Teorell[9] have estimated that the thickness of the aqueous bulk layer dragged with a moving monolayer of oleic acid is around 0.03 mm. Rosano[10] has determined for an 0.15 M Na_2SO_4–1-butanol–water cell that the diffusion layer at the interface is of the order of 300 μ. With this concept in mind the following mathematical model is proposed with the objective of explaining if the phenomena is due to the protein monolayer or the surface drag viscosity effect.

A small and local pressure change is produced in a monolayer by compressing at a constant rate. The propagation of the surface pressure is detected at various distances from the point of surface perturbation.

Consider a small element of the monolayer (length M, width ∂x) perpendicular to the x axis. At time $t = 0$ the perturbation is produced by the moving barrier. At time t the perturbation has reached the small element of the monolayer $M\partial x$ (where M is the width of the trough). Let us call $\partial \pi$ the difference in surface pressure on each side of the surface element $M\partial x$ and u the velocity of the perturbation. The forces acting on this small element of surface are the following: (1) the force due to the surface pressure

$$\partial f_1 = \partial \pi M \tag{1}$$

(2) the force due to the two-dimensional surface viscosity and the friction between the surface film and the subphase (∂f_2). These two forces equal the inertial force of the surface element of mass ∂m.

$$\partial f = \partial m (\partial U / \partial t) \tag{2}$$

t being the time. Therefore

$$\partial f_1 - \partial f_2 = \partial f \tag{3}$$

substituting and dividing by $M\partial x$

$$\frac{\partial \pi}{\partial x} - \partial f_2 = \frac{\partial m}{M \partial x} \frac{\partial U}{\partial t}$$

but $\partial m/M\partial x$ equals the surface density δ thus

$$\frac{\partial \pi}{\partial x} - \frac{\partial f_2}{M \partial x} = \delta \frac{\partial U}{\partial t} \tag{4}$$

Let us define

$$\partial f_2 / M \partial x \tag{5}$$

Our first objective must be to determine Y. Later we will try to analyze our results to define cases when one of the two viscosity factors is predominant. Equation 6 becomes

$$\frac{\partial \pi}{\partial x} - Y = \delta \frac{\partial U}{\partial t} \tag{6}$$

From the continuity equation it can be shown that

$$\frac{\partial \delta}{\partial t} + \frac{\partial (\delta U)}{\partial x} = 0$$

$$\frac{\partial \delta}{\partial t} + \frac{\partial \delta}{\partial x} U + \delta \frac{\partial U}{\partial x} = 0$$

For a small perturbation the surface film density remains practically constant and

$$\frac{\partial \delta}{\partial t} + \delta \frac{\partial U}{\partial x} = 0$$

$$\frac{\partial \ln \delta}{\partial t} = -\frac{\partial U}{\partial x}$$

Gibbs[11] pointed out that there is an elasticity associated with a liquid film if the surface tension varies with the area of the surface; for a thin liquid film of area s, the Gibbs elasticity is given by

$$E = \sigma (\partial \gamma / \partial \sigma)$$

where E is the film elasticity, σ the molecular area, γ the surface tension, and δ the surface density. Since

$$\sigma = 1/\delta$$

$$\partial \sigma = -\frac{1}{\delta^2} \partial \delta$$

$$E = -\frac{1}{\delta} \delta^2 \frac{\partial \gamma}{\partial \delta} = -\delta \frac{\partial \gamma}{\partial \delta}$$

but

$$\partial \gamma = -\partial \pi$$

Therefore

$$E = \partial \pi / \partial \ln \delta$$

introducing Gibb's elasticity coefficient E which equals $\partial \pi / \partial \ln \delta$ in the above equation one obtains

$$\frac{1}{E} \frac{\partial \pi}{\partial t} = -\frac{\partial U}{\partial x}$$

$$U = \int_x^{x_1} \frac{1}{E} \frac{\partial \pi}{\partial t} \partial x$$

TABLE I[a]

x, cm	$\partial\pi/\partial x$, dyn/cm²	$\delta(\partial U/\delta x)$, dyn/cm²	Y, dyn/cm²	$\eta_\epsilon = 50\text{Å}$, cP	$\eta_\epsilon = 5 \times 10^{-2}$cm, cP
6.4	-6.16×10^{-2}	10^{-11}	6.16×10^{-2}	5.41×10^{-4}	54.1
10.7	-3.81×10^{-2}	10^{-11}	3.81×10^{-2}	3.44×10^{-4}	34.4
18.5	-7.84×10^{-3}	10^{-11}	7.84×10^{-3}	8.83×10^{-4}	8.83
27.7	-4.45×10^{-3}	10^{-11}	4.45×10^{-3}	7.07×10^{-5}	7.07

[a] Initial pressure = 9.3 dyn/cm. Bovine serum albumin on water (pH = 5.2, 24.0°).

Experimental Determination of Y

(a) The elasticity coefficient E and the surface density δ is determined directly from the compression isotherm (π vs. σ).

(b) The monolayer is compressed from a given surface pressure with the position of the wettable blade at a distance X from the compression barrier, i.e., compressed from 5.0 to 5.5 dyn/cm. Graphs of π vs. time plotted for various positions of the blade (distance X) compressing over the same area. Figure 1 is the representation of a family of curves for bovine serum albumin

Once $\partial\pi/\partial T$ has been calculated from Figure 1 it is then possible to determine $U(t)$. This is accomplished by graphically intergrating $(1/E)(\partial\pi/\partial T)$ vs. X. From $U(t)$ it is possible to find $\partial U(t)/\partial T$. Next, cross plotting Figure 1 at constant time $\partial\pi/\partial X_T$ can be calculated. Substitution in eq 6 of $\partial\pi/\partial X$ and $\delta(\partial U/\partial T)$ yields Y.

According to Table I the term $\delta(\partial U/\partial T)$ is negligible as compared to $(\partial\pi/\partial x)$. This would indicate that the inertial force due to the monolayer is negligible and the shear Y (dyn/cm²) due to friction is equal to $\partial\pi/\partial x$. If it is assumed that the local velocity gradient decreases linearly perpendicular to the interface (Newtonian profile at each point X) it is then possible to compare what the average three-dimensional viscosity for a film thickness $\epsilon = 50$ Å and a situation where water is dragged along during the perturbation $\epsilon = 0.05$ cm.[10] In case 1 the calculated viscosity varies between 7.07×10^{-5} and 5.41×10^{-4} cP while in the second case it varies from 54 to 8 cP (with increasing distance from the barrier). Therefore, *it must be concluded that the contribution of the surface viscosity is negligible and the observed effect must be attributed to the water bound to the monolayer.*

Discussion

In previous experiments,[7-9] it has been observed that a *moving* monolayer can drag along a considerable amount of substrate. The experiments conducted in this paper deal only with the compression and expansion of the monolayer. From these observations, we conclude that not only is the coiling of the protein monolayer important in the observed effect but the structure of the sheath of bound water immediately below the monolayer (subphase) and the extent to which it is bound to the monolayer plays a role in the surface viscosity. This leads us to advance the following hypothesis of a nonstructured and a structured subphase.

For example, in the case of myristic acid and eicosyl sodium sulfate spread on aqueous substrates and substrates containing alkanol amines, the subphase is oriented due to dipole–dipole interactions but is still in the liquid state. This orientation has been accounted for in many monolayer studies concerned with surface potential.[12-14] Upon compression, the substrate molecules although oriented can slip or be squeezed into the bulk thus the transmission

of surface pressure will be instantaneous and independent of the position of the device for measuring the surface pressure. In the case of the protein monolayers the subphase is bound strongly to the protein[15] and produces a "pseudo gel" phase as described by Colacicco, et al.[16] This helps to explain our observed phenomenon since, on compression, the gel will deform and drag along the monolayer. This idea of a structured subphase explains why protein solutions, while not necessarily good foaming agents, are usually good foam stabilizers. Blank and Lee[17] have also reported the existence of surface tension gradients when studying films of lung extract.

Lastly, the observed decrease in the effect with bovine serum albumin above and below the isoelectric point indicates that, as the protein becomes ionized, the gel subphase breaks down to become similar to that of the myristic acid subphase.

In conclusion, a phenomenon has been observed which appears only noticeable on protein monolayers. We hypothesize that not only is the protein monolayer responsible for the effect but the subphase structure also plays an important role. It should also be noted that experiments concerned with the transfer of surface films (Abribat, Rosano, and Vaillet[18] and La Mer and Blank[19]) and surface viscosity experiments[7-9] involve the concomitant movement of an underlying layer of bound water. However, if the monolayer is in a two-dimensional rigid structure no transfer of the film of bound water is to be expected. This erroneously implies that there exists no subphase. Our technique demonstrates that the subphase does indeed exist and produces an effect when the monolayer is compressed. Nevertheless, no matter how one interprets the theory, the implications of this experiment are by far more important and should be understood and taken into account for future work on macromolecular monolayer systems. We stress the use of an additional variable, the distance the surface pressure measuring device is from the point of perturbation, which must be included in future work to assure accuracy and reproducibility of monolayer studies.

References and Notes

(1) A. P. Christodoulou and H. L. Rosano, *Advan. Chem., Ser.,* **No. 84** (1968).
(2) A. P. Christodoulou, Ph.D. Dissertation, City University of New York. New York, N. Y., 1968.
(3) P. J. Flory, "Principles of Polymer Chemistry," Cornell University Press, Ithaca, N. Y., 1953.

(4) S. J. Singer, *J. Chem. Phys.*, **16**, 872 (1948).
(5) H. L. Frish and R. Simha, *J. Chem. Phys.*, **27**, 702 (1957).
(6) A. Silberberg, *J. Phys. Chem.*, **66**, 1872 (1962).
(7) D. J. Crisp, *Trans. Faraday Soc.*, **42**, 619 (1946).
(8) C. Y. Pak and N. L. Gershfeld, *Nature (London)*, **214**, 888 (1967).
(9) J. H. Schulman and T. Teorell, *Trans. Faraday Soc.*, **34**, 1337 (1938).
(10) H. L. Rosano, *J. Colloid Interface Sci.*, **23**, 73 (1967).
(11) J. W. Gibbs, "Collected Works," Vol. I, Yale University Press, New Haven, Conn., 1936, p 301.
(12) G. L. Gaines, "Interscience Monographs on Physical Chemistry," Interscience, New York, N. Y., 1966, Chapter 4.
(13) J. T. Davies and E. K. Rideal, "Interfacial Phenomena," Academic Press, New York, N. Y., 1963, Chapter 5.
(14) A. W. Adamson, "Physical Chemistry of Surfaces," 2nd ed, Interscience, New York, N. Y., 1967, pp 123–136.
(15) M. Karel, *J. Food Sci.*, **38**, 756 (1973).
(16) G. Colacicco, A. R. Buckelew, Jr., and E. M. Scarpelli, *J. Colloid Interface Sci.*, **46**, 147 (1974).
(17) M. Blank and B. Lee, *J. Colloid Interface Sci.*, **36**, 1 (1971).
(18) M. Abribat, H. L. Rosano, and G. Vaillet, *C. R. Acad. Sci.*, **238**, 1219 (1954).
(19) V. K. La Mer and M. Blank, *J. Colloid Interface Sci.*, **11**, 608 (1956).

Singlet–Triplet Intersystem Coupling in Formaldehyde

J. C. D. Brand* and D. S. Liu

Department of Chemistry,[1] University of Western Ontario, London, Ontario, Canada N6A 3K7   (Received June 7, 1974)

A number of rotational transitions in the $2\nu_2' + \nu_4'$ ($2_0{}^2 4_0{}^1$) vibronic band of the $S_1 \leftarrow S_0$ electronic system of CH_2O show a Zeeman effect in external magnetic fields of 1–13 kG. An analysis of this magnetically sensitive perturbation, combined with measurements of the magnetic rotation spectrum in the same spectral region, leads to a determination of the coupling constants for spin–rotation and spin–spin coupling in the principal perturbing level, namely, the $1^1 2^2 4^1$ vibrational level of the $T_1(^3A_2)$ state. The magnetic spin–rotation interaction in the T_1 state depends strongly on the vibrational energy in that state, indicating that T_1 is itself coupled to the next-higher T_2 state of the triplet manifold. A tentative analysis of the vibrational dependence of spin–rotation coupling shows (i) that the T_2 state is uniquely identified as a $^3A_1$ state (*i.e.*, the state which correlates with the $^3\pi\pi^*$ configuration of planar CH_2O), and (ii) that the energy separation of the coupled triplet states is small, approximately 1.1 eV.

Introduction

The electronic states of polyatomic molecules are normally weakly coupled to one another through vibronic, spin–orbit, or other terms in the Hamiltonian. These couplings give rise to the photophysical and simple photochemical channels open to molecules in optically excited states and are therefore important to the interpretation of rate and lifetime measurements.[2,3] To the present relatively little use has been made of the optical spectra themselves in studying these couplings even though the effects of vibronic, rotational–electronic, and spin–orbit coupling are often observed and characterized in the ordinary course of spectral analysis. In vapor spectra, these couplings are observed when the rotational fine structure of the spectrum is resolved: the CH_2O molecule meets this prescription and has the further advantage that the rotational structure of several bands in the $S_1 \leftarrow S_0$ and $T_1 \leftarrow S_0$ systems has been analyzed in detail.[4–7] This paper examines certain aspects of the interactions between the triplet and singlet states of the first excited electronic configuration of CH_2O, $T_1(^3A_2) \leftrightarrow S_1(^1A_2)$, in regions where the potential surfaces of S_1 and T_1 intersect, causing perturbations to appear in bands of the $S_1 \leftarrow S_0$ system.

An analysis of the triplet–singlet perturbations observed in absence of external fields has been given in previous papers.[8,9] The effects of coupling are most visible in the $2\nu_2' + \nu_4'$ ($2^2 4^1$) vibrational level of the S_1 state which interacts weakly by spin–rotation coupling with the $1^1 2^2 4^1$ vibrational level, and by vibronic spin–orbit coupling with the $1^1 2^2$ vibrational level of T_1.[9] The present paper analyzes the effect on the interaction of an external magnetic (Zeeman) field which can be used to "tune" the coupling between individual rotational levels into resonance. In the course of analysis further couplings are detected within the triplet manifold which enables us to form a rough estimate of the location of the $T_2(^3A_1)$ state.

Experimental Section

The experiments record the $2_0{}^2 4_0{}^1$ band of the $S_1 \leftarrow S_0$ system of CH_2O, near 3260 Å, in absorption in an external magnetic field whose axis is parallel to the axis of the absorption cell. Perturbations of the $2^2 4^1$ upper state of the transitions by levels of the T_1 state are detected by the presence of magnetically sensitive lines which broaden or shift in frequency when the external field is applied. In these experiments the $S_1 \leftarrow S_0$ transition carries the oscillator strength, and the coupling with the T_1 state is sensed through the response of these mainly singlet–singlet transitions to the Zeeman field.

The apparatus was similar to that previously described,[9] modified to improve the field homogeneity. Magnetic fields were obtained by a capacitor discharge through a solenoid 90 cm in length by 6 cm in diameter, the pitch of the coil being adjusted so that the field strength was uniform to

±0.5% over 70 cm. The source was a capillary discharge timed to coincide with the peak of the field pulse. Spectra were photographed with 2.1 Torr of CH_2O vapor in a 70-cm cell mounted coaxially with the solenoid, using a 3.4-m spectrograph with reciprocal linear dispersion of about 3 Å/cm. Frequency measurements were referred to Fe hollow-cathode standards, and the field strength was monitored periodically by coils mounted on the absorption cell. A section of the $2_0^2 4_0^1$ band ($S_1 \leftarrow S_0$ system) recorded at four values of the field strength is shown in Figure 1. A total of some 70 magnetically sensitive lines were observed in this band, representing about 10% of the rotational transitions developed under the pressure-path conditions of the experiment. Using a single field strength, 13.0 kG, Brand and Stevens[9] recorded 29 sensitive lines all of which are confirmed in the present work.

Besides the Zeeman spectra, a magnetic rotation spectrum (MRS) of the same wavelength regions was made available to us by Dr. J. M. Brown and Dr. D. A. Ramsay.[10] This high-resolution spectrum, comprising about 40 sharp lines, was photographed at a field strength of 1.2 kG. The existence of an MRS in this region was first established by Kusch and Loomis in 1939.[11]

Even a casual inspection of the Zeeman and MRS data shows that the spectra are not duplicates of one another. MRS lines occur close to the Zeeman-sensitive absorption lines but coincidences are rare; typically the relative frequency shift ranges up to 0.5 cm^{-1}. Discrepancies of this size cannot possibly arise from measurement errors. The MRS and absorption (Zeeman) spectra must therefore represent different rovibronic transitions.

Zeeman Spectra

The system considered is that of a set of rotational levels of the S_1 state coupled by matrix elements of the singlet-triplet interaction to a similar set of levels of T_1. An external magnetic field acts upon the T_1 set in competition with the internal magnetic interactions of spin-spin and spin-rotation coupling in that state. Its effects are then transmitted by the coupling to levels of the S_1 set and are observed as a broadening or shift of lines in the $S_1 \leftarrow S_0$ absorption.

The Van Vleck effective Hamiltonian for a nondegenerate electronic state of an asymmetric rotor is, ignoring centrifugal terms[12]

$$\mathcal{H}_{rot} = \mathbf{N \cdot B \cdot N} + \mathbf{S \cdot \epsilon \cdot N} + \mathbf{S \cdot D \cdot S} \qquad (1)$$

Here, $\mathbf{N = J - S}$ is the total angular momentum excluding spin and $\mathbf{D}$, ϵ, and $\mathbf{B} = h/(8\pi^2 c \mathbf{I})$ are respectively the tensors of spin-spin coupling, spin-rotation coupling, and overall rotation of the molecule. In molecules of orthorhombic symmetry, including planar CH_2O, $\mathbf{D}$ and ϵ are diagonal in the principal axis system. The T_1 state of CH_2O is nonplanar,[6,7] therefore not orthorhombic, but the off-diagonal elements of $\mathbf{D}$ and ϵ are expected to average to zero because the inversion frequency is much higher than the spin splittings.

The Zeeman operator is[13]

$$\mathcal{H}_{Zm} = -g_s \beta H_Z S_Z \qquad (2)$$

where H_Z is the field strength along the axis Z of a space-fixed set XYZ, $\beta = e\hbar/2m_e c$ is the Bohr magneton, $g_s \simeq 2.0$, and S_Z is the component of the spin operator along the field axis. Since $\mathcal{H}_{Zm}$ operates in the space of the spin,
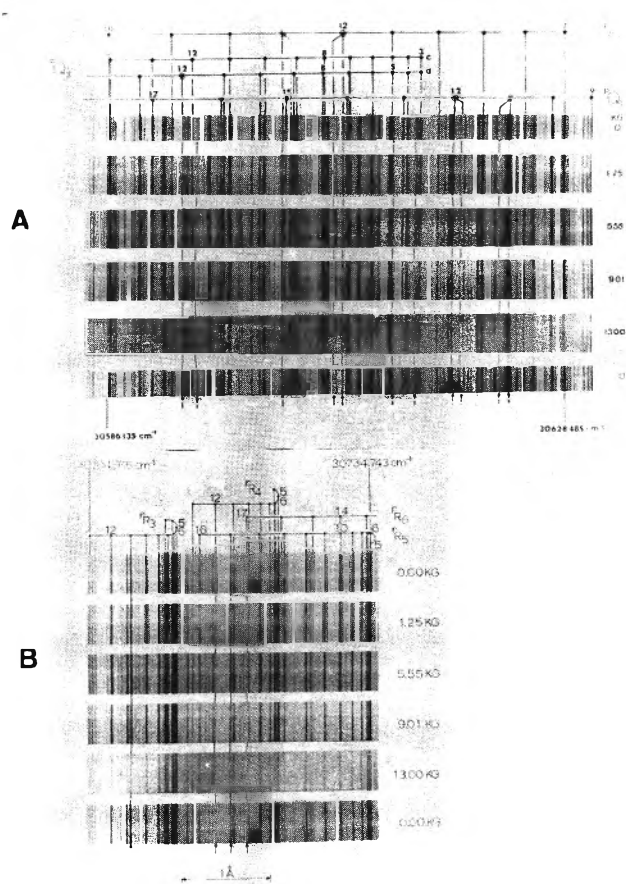
Figure 1. Zeeman effects near (A) 3267 and (B) 3254 Å. Strips 2-5 are recorded at field strength of 1.25, 5.55, 9.01, and 13.0 kG, respectively, as indicated on the right of the diagram. Zero-field reference spectra are shown in strips 1 and 6. Magnetically sensitive lines are indicated by arrows at the foot of the spectra.

which is only loosely coupled to the molecular rotation, the field is not expected to induce new singlet-triplet interactions over and above those already present at zero field.

To a good approximation the matrix of $\mathcal{H}_{rot} + \mathcal{H}_{Zm}$ for a near-case (b) triplet state is diagonal in N, K, and $\tau = K_{-1} - K_1$, except in those K submanifolds where asymmetry effects are large. The external field then acts on each rovibronic level $NK\tau$ in the manner shown schematically in Figure 2 for the case (b) limit. In this diagram the energy gradients are approximately $2\beta M_S$, where $M_S = 0, \pm 1$ is the projection quantum number for space-fixed spin functions, and the figure is effectively equivalent to that used to discuss esr transitions of a free-spin system with $S = 1$. In the rotating molecule however each M_S sublevel is $(2N + 1)$-fold degenerate, the components of the degeneracy being indexed by M_N. When the internal magnetic interactions due to spin-spin and spin-rotation coupling are different from zero this degeneracy is lifted to an extent dependent on the magnitude of the zero-field splitting.

Zeeman effects in a triplet state are communicated indirectly to a neighboring singlet state by elements of the singlet-triplet interaction, as described previously.[8] In Figure 2 the coupled singlet rovibronic level is energetically higher than the triplet level and the interaction matrix element is assumed small, on the order of 0.1 cm^{-1}. As illustrated, the Zeeman field tunes the M_S triplet sublevel into resonance with the singlet in a field of about 5.5 kG; in lower or higher fields, the singlet level is shifted up or down in energy.

TABLE I: Zeeman Effects Assigned to $2^2 4^1(S_1)$–$1^1 2^2 4^1(T_1)$ Interactions

ν_{obsd}, cm^{-1}	Assignment $\Delta K_{\Delta J_{K''}}(J'')$	J', K'	Zeeman effect^a 1.25 kG	5.55 kG	9.01 kG	13.0 kG	Remarks^b
30,603.70vw	$^pP_{1d}(12)$	11, 0	←————————Vanishes————————→				'Extra' line (D)
30,605.184s	$^pP_{1d}(12)$	11, 0			(+)	b	Figure 1A (A)
30,621.15w	$^pQ_{1c}(11)$	11, 0	←————Vanishes————→				'Extra' line (D)
30,622.661vs	$^pQ_{1c}(11)$	11, 0			(+)	+0.05	Figure 1A (D)
30,658.960vs	$^pR_{1d}(10)$	11, 0				b	Blended line (C)
30,598.888s	$^pP_{1d}(13)$	12, 0	b				Figure 1A (A)
30,616.787s	$^pQ_{1c}(12)$	12, 0	−0.05				Figure 1A (C)
30,657.30vw	$^pR_{1d}(11)$	12, 0	b				(C)
30,563.818vw	$^pP_{3d}(12)$	11, 2c	←—Vanishes—→		(−)		'Extra' line (B)
30,564.308m	$^pP_{3d}(12)$	11, 2c	b				(A)
30,620.262w	$^pR_{3d}(10)$	11, 2c		(−)	(−)		(B)
30,563.405vs	$^pP_{3c}(12)$	11, 2d				b	(B)
30,557.884vw	$^pP_{3d}(13)$	12, 2c	b	−0.10	−0.08	(−)	(B)
30,589.409s	$^pQ_{3c}(12)$	12, 2c			(−)	(−)	(A)
30,589.872m	$^pQ_{3c}(12)$	12, 2c	b	−0.13	−0.15	−0.15	'Extra' line (D)
30,678.584w	$^rR_{1d}(11)$	12, 2c	b				(B)
30,678.802w	$^rR_{1d}(11)$	12, 2c	b	b	b	b	'Extra' line (B)
30,690.021s	$^rR_{1d}(11)$	12, 2c	b		(−)	(−)	(B)
30,556.53vw	$^pP_{3c}(13)$	12, 2d		−0.05	b		(C)
30,588.325m	$^pQ_{3d}(12)$	12, 2d	b	+0.09	+0.05		Figure 1A (B)
30,616.509w	$^rP_{1c}(13)$	12, 2d	b	b	b	b	(C)
30,660.806vs	$^rQ_{1d}(12)$	12, 2d	b	b	b	b	Blended line (B)
30,661.350vw	$^rQ_{1d}(12)$	12, 2d	b	b	b	b	'Extra' line (D)
30,531.132w	$^pP_{1c}(14)$	13, 3c	(+)	(+)			(D)
30,660.590vw	$^rQ_{2c}(13)$	13, 3c	+0.05	+0.05	b		(C)
30,695.398s	$^rR_{2d}(12)$	13, 3c				b	Blended line (A)
30,663.75vw	$^rQ_{2d}(13)$	13, 3d			(−)		(D)
30,693.16m	$^rR_{2c}(12)$	13, 3d	b	+0.03	+0.06		(A)
30,517.774s	$^pP_5(13)$	12, 4			(−)	(−)	Blended line (A)
30,549.02	$^pQ_5(12)$	12, 4		Induced			'Extra' line
30,549.360s	$^pQ_5(12)$	12, 4			(+)	−0.09	(A)
30,578.537w	$^pR_5(11)$	12, 4	b	b	(−)		Blended line (B)
30,679.781s	$^rQ_{3d}(12)$	12, 4			(+)	b	(C)
30,708.970s	$^rR_3(11)$	12, 4			(+)	−0.07	Figure 1B (A)
30,510.898s	$^pP_5(14)$	13, 4			(+)	(+)	(A)

^{a} b = broadened line. Frequency shifts are specified (in cm^{-1}) for shifts >0.05 cm^{-1}; if the shift is <0.05 cm^{-1} its sense is indicated by ±. ^{b} The clarity of Zeeman effects is assessed A (good) to D (poor), depending upon line strength and freedom from interference by other lines.
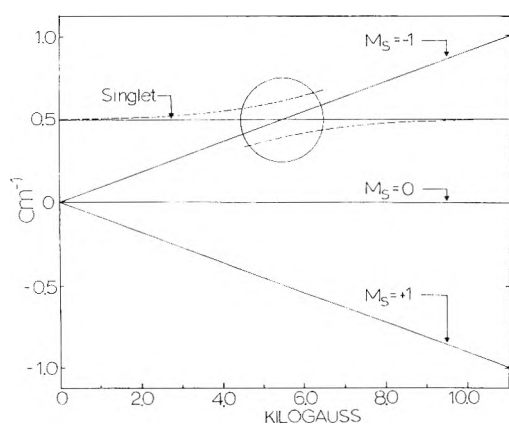

Figure 2. Resonance "tuning" of a singlet–triplet interaction. Although the intersystem coupling matrix element is independent of field strength, the gradient of the $M_S = +1$ sublevel induces a frequency shift in the singlet term as indicated by the broken line.

Near resonance, the singlet level also broadens if the M_N degeneracy of the triplet is lifted by the internal magnetic interactions. This figure explains schematically the behavior of the singlet transition $^rR_4(12)$ in Figure 1B; this transition shows a small high-frequency shift at 1.25 kG, broadens at 5.5 kG, and is again sharp but shifted toward lower frequency in the 9.0- and 13.0-kG spectra.[14] This discus-

sion is given in order to show that Zeeman tuning assists in locating the perturbing triplet system when the latter are too weak to observe directly in absorption.[15] A resonance near $H = 5.5$ kG signifies that the center of gravity of the perturbing triplet must lie $2\beta H \simeq 0.5$ cm^{-1} from the perturbed singlet level. This is considerably more precise than the information[9] available from the zero-field perturbation alone.

Figure 3 gives the computed profiles of the $^pQ_1(11)$, $^pP_1(12)$, $^pQ_1(12)$, and $^pP_1(13)$ transitions of the $2_0^2 4_0^1(S_1 \leftarrow S_0)$ vibronic band. The upper state of the first two transitions has J', $K' = 11$, 0 while that of the latter pair is 12, 0. In the recorded spectrum, Figure 1A, the $^pP_1(12)$ and $^pP_1(13)$ transitions are unblended and their Zeeman effects are correspondingly more distinct that for the Q-branch lines. The calculation satisfactorily reproduces the low-field (1.25 kG) broadening of $^pP_1(13)$ and the high-field (13.0 kG) broadening of $^pP_1(12)$, though the high-frequency shift calculated for the 11, 0 term at 9.0 kG is larger than observed. These profiles are computed without approximation following full-matrix diagonalization. Details will be given elsewhere.[16]

Table I summarizes the Zeeman effects observed in the $2_0^2 4_0^1(S_1 \leftarrow S_0)$ vibronic band, attributed to the spin–rotation coupling of $2_0^2 4_0^1(S_1)$ with $1^1 2^2 4^1(T_1)$. This table includes about 40% of the magnetically sensitive lines present. From the Zeeman effects listed one may deduce values
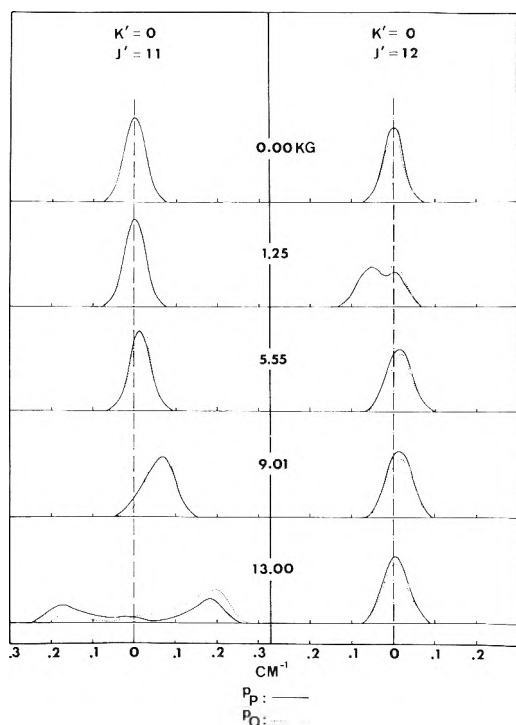
Figure 3. Computed line profiles for the perturbed singlet–singlet transitions $^PP_1(12)$, $^PQ_1(11)$, $^PP_1(13)$, and $^PQ_1(12)$. The separation of interacting levels is computed using Parkin's constants (see ref 4) for $S_1(2^24^1)$, the data of Table II for $T_1(1^12^24^1)$, and the intersystem coupling parameter $(a_{xx} + a_{yy}) = 0.023$ cm^{-1}.[9] Each curve is an envelope of overlapping M_J components assigned a gaussian profile with full-width at half-height of 0.05 cm^{-1}.

TABLE II: Constants of the $^3A_2$ State (in cm^{-1})

	0^{+a}	$1^12^24^1$
T_0	$25,194.3\bar{c}_5$	$30,649.7_2$
A	8.672_6	$8.5_8{}^b$
B	1.155_6	1.16_6
C	1.041_7	1.04_4
10^4D_N	0.04_0	0.08_7
10^4D_{NK}	0.5_8	0.3_5
10^4D_K	$7.5_5{}^c$	10.0_5
ϵ_{aa}	-0.07_5	-0.25_5
$\epsilon_{bb} + \epsilon_{cc}$	$-0.010_8{}^d$	-0.01_2
$D(= 3\alpha)$	0.14^e	0.8_7

[a] Reference 7. [b] Constants A–D_K transferred from ref 9. [c] δ_K and δ_J also determined. [d] ϵ_{bb} and ϵ_{cc} obtained individually. [e] $E = \frac{1}{2}(D_{bb} - D_{cc})$ also determined.

for the spin–spin coupling constant α and the spin–rotation coupling constants a and a_0 for the $1^12^24^1$ vibrational level of the T_1 state. The procedure involves matching the profile of the magnetically sensitive lines to the observed line shapes, as in Figure 3, varying the constants D, ϵ_{aa}, and $(\epsilon_{bb} + \epsilon_{cc})$ in order to optimize the fit. The results are given in Table II, where the constants, A, B, C, D_N, D_{NK}, and D_K, have been transferred without change from the zero-field analysis.[9] For comparison, the table includes also the constants of the 0^+ vibrational level of T_1 determined recently by Birss, Dong, and Ramsay.[7]

Magnetic Rotation Spectrum

MRS lines lie near magnetically sensitive absorption lines, but the two spectra do not coincide.[17] However, using the results in Table II one may calculate the frequency of
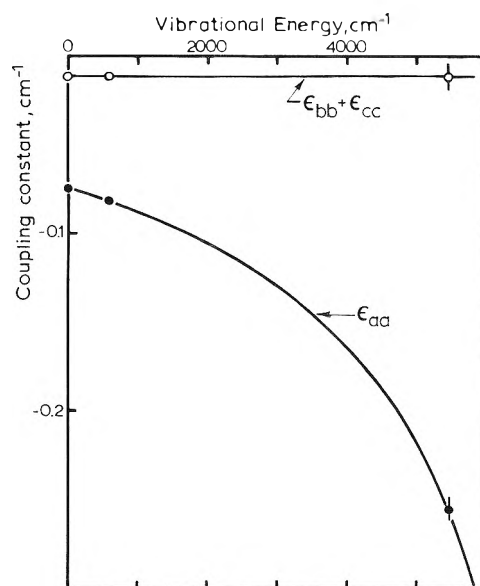

Figure 4. Vibrational dependence of the spin–rotation coupling constants ϵ_{aa} and $(\epsilon_{bb} + \epsilon_{cc})$.

rovibronic lines of the transition from the ground state to the triplet state of the coupled system; when this is done (see Table III) a majority of the MRS transitions are accounted for. The MRS therefore marks transitions to the triplet state of the perturbed system which in absorption appear only as weak "extra" lines of the perturbation.

It should be emphasized that Table III is not a calculation of MRS intensity. Instead we have calculated the frequency, for zero external field, of transitions to the $F_1(J = N + 1)$, $F_2(J = N)$, and $F_3(J = N - 1)$ components of the triplet state using the constants given in the third column of Table II. A magnetic field mixes F_1, F_2, and F_3, and splits them into bands of sublevels $M_J = M_N + M_S$ whose width in a field of $\sim$1.2 kG ranges up to ±0.06 cm^{-1}. Since the MRS line must lie within the spread of Zeeman sublevels, the zero-field calculation may be in error by this amount. The precise MRS line position and intensity, which depends in complex fashion on the magnetic circular dichroism and rotary dispersion,[19] was not calculated in this work.

Vibrational Dependence of Spin–Rotation Coupling

The data in Table II show a strong dependence of ϵ_{aa} and $D = D_{aa} - \frac{1}{2}(D_{bb} + D_{cc})$ on vibrational energy in the T_1 state. This is further illustrated in Figure 4 which includes also the data[7] available for the 4^2 vibrational level. The smooth curve connecting the points is schematic since the effects must depend to some extent on the vibrational quantum number, not just the gross vibrational energy. The strong dependence found for ϵ_{aa} is sharply differentiated from the almost-constant values obtained for $(\epsilon_{bb} + \epsilon_{cc})$. Behavior of this sort is expected if T_1 is spin–orbit coupled to a higher state T_2 of the triplet manifold, the energy gap $E_{T_2} - E_{T_1}$ being of the same order of magnitude as the vibrational energy range of Figure 4.

Spin–rotation coupling in multiplet states of an asymmetric rotor is a second-order coupling, in which rotation excites orbital angular momentum which then couples to the spin by spin–orbit coupling.[12] In this case we expect that ϵ_{aa} will encompass a vibrationally dependent contribution from $T_1(^3A_2)$–$T_2(^3A_1)$ coupling, because T_2 proba-

TABLE III: MRS Assignments

ν_{obsd}, cm^{-1}	Resonance with (S$_1$ ← S$_0$)		$2^2 4^1$(S$_1$) J', K'	$1^1 2^2 4^1$(T$_1$) N', K'(F$_i$)	ν_{calcd}, cm^{-1}	$\Delta\nu$, cm^{-1} (obsd − calcd)
30,531.639m	$^pP_4$ (14)		13, 3c	13, 3c (F$_1$)	30,531.584	+0.055
30,556.383w	$^pP_{3c}$(13)		12, 2d	12, 2d (F$_3$)	30,556.397	−0.014
30,556.729s	$^pP_{3c}$(13)		12, 2d	12, 2d (F$_2$)	30,556.734	−0.005
30,557.730m	$^pP_{3d}$(13)		12, 2c	12, 2c (F$_1$)	30,557.743	−0.013
30,557.966s	$^pP_{3d}$(13)		12, 2c	12, 2c (F$_3$)	30,557.987	−0.021
30,558.359s	$^pP_{3d}$(13)		12, 2c	12, 2c (F$_2$)	30,558.383	−0.024
30,588.015w	$^pQ_{3d}$(12)		12, 2d	12, 2d (F$_1$)	30,587.915	+0.100
30,616.067s	$^pR_{3c}$(13)		14, 2d	14, 2d (F$_2$)	30,615.988	+0.079
30,617.391w	$^pR_{3c}$(10)		11, 2d	11, 2d (F$_1$)	30,617.462	−0.071
	or	$^pR_{3c}$(11)	12, 2d	12, 2d (F$_3$)	30,617.341	+0.050
30,617.700w	$^pR_{3c}$(10)		11, 2d	11, 2d (F$_3$)	30,617.742	−0.042
	or	$^rP_{1c}$ (13)	12, 2d	12, 2d (F$_2$)	30,617.678	+0.022
30,618.600vw	$^pR_{3d}$(11)		12, 2c	12, 2c (F$_1$)	30,618.569	+0.031
30,618.788m	$^pR_{3d}$(11)		12, 2c	12, 2c (F$_3$)	30,618.823	−0.035
30,619.062m	$^pR_{3d}$(10)		11, 2c	11, 2c (F$_2$)	30,619.052	−0.010
30,625.892m	$^rP_{2d}$(15)		14, 3c	14, 3c (F$_2$)	30,625.988	−0.096
30,631.859vw	$^rP_{1d}$(13)		12, 2c	12, 2c (F$_3$)	30,631.791	+0.068
30,632.108w	$^rP_{1d}$(13)		12, 2c	12, 2c (F$_2$)	30,632.187	−0.079
30,667.490w	$^rQ_{2d}$(12)		12, 3d	12, 3d (F$_3$)	30,667.515	−0.025
30,678.486s	$^rR_{1c}$(11)		12, 2d	12, 2d (F$_2$)	30,678.500	−0.014
30,689.879m	$^rR_{1d}$(11)		12, 2c	12, 2c (F$_1$)	30,689.896	−0.017
30,693.641w	$^rR_{2c}$(12)(?)		13, 3d	13, 3d (F$_1$)	30,693.496	+0.145
30,695.284ww	$^rR_{2d}$(13)		14, 3c	14, 3c (F$_1$)	30,695.362	−0.078
30,695.892s	$^rR_{2d}$(12)		13, 3c	13, 3c (F$_1$)	30,695.833	+0.059

bly lies quite close to T$_1$, plus a smaller almost-constant contribution from remote states of the triplet manifold having the same orbital symmetry as T$_2$. The variable part is given by an expression similar to eq 11 of ref 8, namely

$$2\sum_{k_2}\langle\Gamma_1, k_1|H_{so}|\Gamma_2, k_2\rangle\langle\Gamma_2, k_2|H_{or}|\Gamma_1, k_1\rangle \times$$

$$\langle V_{k_1}|V_{k_2}\rangle\langle V_{k_2}|V_{k_1}\rangle/[E_1, k_1 - E_2, k_2] \quad (3)$$

where k_1 and k_2 denote the vibrational quantum numbers in the T$_1$(Γ_1) and T$_2$(Γ_2) states, respectively, and the notation otherwise is transferred from ref 8. If the spin-electronic integrals in the numerator of eq 3 are abbreviated as $L_{1,2}$ the complete expression for ϵ_{aa}, including an almost-constant contribution ϵ_{aa}' from remote states, becomes

$$\epsilon_{aa} = \epsilon_{aa}' + \sum_{k_2} L_{1,2}\langle V_{k_1}|V_{k_2}\rangle\langle V_{k_2}|V_{k_1}\rangle/$$

$$(E_2, k_2 - E_1, k_1) \quad (4)$$

Not knowing the Franck–Condon integrals we make the heuristic assumption that overlap is most important for low-lying vibrational levels of T$_2$. Granted this, the denominator in eq 4 is effectively constant and the expression simplifies to

$$\epsilon_{aa} = \epsilon_{aa}' + L_{1,2}/(E_{2,0} - E_1, k_1) \quad (5)$$

where $E_{2,0}$ is the electronic energy of the T$_2$ state. The curve connecting the ϵ_{aa} values in Figure 4 is calculated from the parameters $\epsilon_{aa}'/A = 0.0030$ cm^{-1}, $L_{1,2}/A = -100$ cm^{-1}, and $E_{2,0} - E_{1,0} = 8500$ cm^{-1} (1.05 eV). Given the limitations of the model the numerical values should not be taken too seriously.[20]

In order to contribute to ϵ_{aa}, T$_2$ must be a ^{3}A$_1$ state. Further, treating $\mathcal{H}_{so}$ as a one-electron operator, $\mathcal{H}_{so} = \Sigma_i a_i \mathbf{l}_i \cdot \mathbf{s}_i$, the sign[22,23] of the spin integrals is such that $L_{1,2}$ is negative (as found) if the excitation T$_1$ → T$_2$ occurs by promotion of one electron from a filled to half-filled orbital.

Consequently the T$_1$ → T$_2$ promotion must be $\pi \to$ n, and the state T$_2$ is uniquely identified with the electron configuration that correlates with $^3\pi\pi^*$ of planar CH$_2$O. Ab initio calculations identify ^{3}A$_1$ as a low-lying state of the triplet manifold[24] though the state has never been directly observed. The most recent calculation[24d] places the T$_2$ state 2.2 eV higher in energy than T$_1$ at the ground state geometry.

The spin–spin parameter D has a large first-order dipolar contribution besides second-order spin–orbit terms. The vibrational dependence of D (see Table II) is not less sharp than that of ϵ_{aa}, but the spin–orbit contribution to D arising from T$_1$–T$_2$ coupling is expected to be negative whereas a positive trend is observed. We have no solution to this paradox at present. The data are such that the value of D is determined largely by the $K' = 0$ resonance, while ϵ_{aa} is derived from resonances in the $K' = 2$, 3, and 4 manifolds. Possibly the $K = 0$ manifold is subject to some other perturbation which interferes with the determination of D.

Conclusion

This analysis attempts to account for details of the S$_1$–T$_1$ intersystem coupling in the lower manifold of states of CH$_2$O, using conventional spectroscopic methods to probe the interaction. It is shown that the triplet state of the coupling is the ^{3}A$_2$(T$_1$) state, since the rotational constants obtained for the coupled state serve as a fingerprint of that state. The example studied is one of weak coupling and is therefore unlikely to be of importance to the photophysical rate processes of excited CH$_2$O, though it is of possible significance as a prototype for interactions between states of different multiplicity. Strong interactions, whether they involve states of the same or different multiplicity, may be extremely difficult to analyze by ordinary spectroscopic methods because the organization of the spectrum is then concealed by the large, irregular perturbations. In fact this appears to be the main obstacle to analysis of, for example, the visible absorption bands of NO$_2$.[25]

The spin–rotation coupling constant ϵ_{aa} of the ^{3}A$_2$ state

has a strong vibrational dependence attributed to the coupling of $^3A_2$ with the next-higher $^3A_1$ state of the triplet manifold, leading to a rough estimate of the energy of the latter state, $E_{T_2} = E_{T_1} + 1.05$ eV $= 4.17$ eV.

Acknowledgment. Acknowledgment is made to the donors of the Petroleum Research Fund, administered by the American Chemical Society, for the support of this research.

References and Notes

(1) Contribution No. 102 from the Photochemistry Unit.
(2) A. E. Douglas, *J. Chem. Phys.*, **45**, 1007 (1966).
(3) J. Jortner, S. A. Rice, and R. M. Hochstrasser, *Advan. Photochem.*, **7**, 149 (1969).
(4) V. A. Job, V. Sethuraman, and K. K. Innes. *J. Mol. Spectrosc.*, **30**, 365 (1969).
(5) V. Sethuraman, V. A. Job, and K. K. Innes. *J. Mol. Spectrosc.*, **33**, 189 (1970).
(6) W. T. Raynes, *J. Chem. Phys.*, **44**, 2755 (1966).
(7) F. W. Birss, R. Y. Dong, and D. A. Ramsay, *Chem. Phys. Lett.*, **18**, 11 (1973).
(8) C. G. Stevens and J. C. D. Brand, *J. Chem. Phys.*, **58**, 3324 (1973).
(9) J. C. D. Brand and C. G. Stevens, *J. Chem. Phys.*, **58**, 3331 (1973).
(10) We thank Dr. J. M. Brown and Dr. D. A. Ramsay for providing this spectrum.
(11) P. Kusch and E. W. Loomis, *Phys. Rev.*, **55**, 850 (1939).
(12) J. H. Van Vleck, *Rev. Mod. Phys.*, **23**, 2·3 (1951); W. T. Raynes, *J. Chem. Phys.*, **41**, 3020 (1964).
(13) The complete Zeeman operator is

$$\mathcal{H}_{Zm} = -(L_Z + g_s S_Z)\beta H_Z$$

but the effects of the small term $-\beta L_Z H_Z$ are neglected in this application.
(14) The frequency shift at 9.0 and 13.0 kG is clearly visible against the unshifted line immediately to the left of $^rR_4(12)$ in Figure 1B.
(15) A few "extra" lines due to the perturbation appear weakly in absorption, especially when the deperturbed separation of singlet and triplet levels is small.
(16) D. S. Liu and J. C. D. Brand, to be submitted for publication.
(17) The MRS in this region of the $S_1 \leftarrow S_0$ system was first attributed to a singlet–triplet perturbation by Herzberg.[18]
(18) G. Herzberg, "Electronic Spectra of Polyatomic Molecules," Van Nostrand, Princeton, N. J., 1966, p 274.
(19) A. D. Buckingham and P. J. Stevens, *Ann. Rev. Phys. Chem.*, **17**, 399 (1966).
(20) A simple calculation using the MO's of Pople and Sidman,[21] retaining one-center integrals only, gives $L_{1,2}/A = -188$ cm^{-1}, in order of magnitude agreement with the value above. In this calculation the atomic spin–orbit coupling constant was assigned the value $\zeta_{2p}(0) = 147$ cm^{-1}.[22]
(21) J. A. Pople and J. W. Sidman, *J. Chem. Phys.*, **27**, 1270 (1957).
(22) R. N. Dixon, *Mol. Phys.*, **13**, 77 (1967).
(23) S. H. Glarum, *J. Chem. Phys.*, **39**, 3141 (1963).
(24) (a) R. J. Buenker and S. D. Peyerimhoff, *J. Chem. Phys.*, **53**, 1368 (1970); (b) I. Absar, C. S. Lin, and K. L. McEwen, *Can. J. Phys.*, **50**, 646 (1972); (c) R. Ditchfield, J. E. Del Bene, and J. A. Pople, *J. Amer. Chem. Soc.*, **94**, 4806 (1972); (d) S. R. Langhoff, S. T. Elbert, and E. R. Davidson, *Int. J. Quantum Chem.*, **7**, 999 (1973).
(25) J. C. D. Brand, J. L. Hardwick, R. J. Pirkle, Jr., and C. J. Seliskar, *Can. J. Phys.*, **51**, 2184 (1973).

Self-Diffusion of Solid and Liquid Sodium[1]

D. E. O'Reilly

Argonne National Laboratory, Argonne, Illinois 60439 (Received January 7, 1974)

The two processes of self-diffusion in solid sodium observed recently by Mundy are tentatively interpreted in terms of nearest-neighbor and next-nearest-neighbor vacancy diffusion. Preexponential factors are evaluated for both processes and compared with experiment. Experiments and computer calculations are suggested to corroborate the proposed mechanisms. Self-diffusion data for liquid sodium are interpreted by means of a primitive quasilattice model and also an extended quasilattice model which has recently been formulated. The agreement of the predictions of the model with experiments is good and volumes of activation for self-diffusion are calculated which may be compared with experimental results when they become available. Theoretical preexponential factors and activation energies for viscosity are calculated and compared with experiment. The hard-sphere model of self-diffusion in metals is compared with the present models and experiments are proposed to clarify the nature of self-diffusion in liquid sodium metal.

I. Introduction

Self-diffusion in solid[2] and liquid[3a,b] sodium has been studied extensively by the radioactive tracer method. For the solid, a non-Arrhenius behavior of the temperature dependence of the coefficient of self-diffusion was observed by Mundy.[2a] This result was interpreted[2a] as due to two (possibly three) diffusion processes and volumes of activation were determined for the two diffusion mechanisms. In the present work we will give a refined version of an earlier[3c] theory of self-diffusion in solids and calculate preexponential factors for two types of vacancy diffusion in sodium metal. Entropies of activation will be derived from experimental volumes of activation using an approximate expression given earlier[4] (section II).

Coefficients of self-diffusion in liquid sodium will be interpreted with a primitive quasilattice model[5] and also an extended quasilattice model[6] for self-diffusion in liquids. The work required to create a vacancy in the liquid is evaluated from (1) liquid density,[7] (2) isothermal compressibility,[7] and (3) the scaled particle theory[8] (section III). The

quasilattice model is compared with the hard-sphere model of self-diffusion proposed by Dymond and Alder[9] and applied to liquid sodium by Protopapas, *et al.*[10] (section V).

II. Diffusion in Solid Sodium

A. Theory. In the following we will explicitly consider vacancy diffusion although the results will apply to other types of diffusion as well. Our starting point is the relationship[11] between the coefficient of self-diffusion D and the velocity autocorrelation function $\psi(\tau)$

$$D = \frac{1}{3} \int_0^\infty \langle \mathbf{v}(0 \cdot \mathbf{v}(\tau) \rangle \, d\tau \tag{1}$$

where $\mathbf{v}$ is linear velocity and the brackets in the integrand of eq 1 signify either an average over all initial times ($\tau = 0$) or a thermal (ensemble) average for a specific molecule. We will restrict the discussion to face centered cubic (fcc) or body centered cubic (bcc) lattices with one type of diffusing unit. This assumption will ensure that $\psi(\tau)$ vanishes after a single jump to a vacancy (neglecting correlation which we will take into account later). First we will evaluate $\psi(\tau)$ by performing an average over all initial times and then consider the thermal average. Let the mean time duration of a jump be τ_c, the mean time between jumps is τ_0 and the average mean square velocity during a jump is $\langle v^2 \rangle$. Then $\psi(\tau)$ is given by (Appendix A)

$$\psi(\tau) = \langle v^2 \rangle (\tau_c/\tau_0)[1 - (\tau/\tau_c)] \tag{2}$$

for $0 \leq \tau \leq \tau_c$. Hence

$$D = \frac{1}{3} \int_0^\infty \psi(\tau) d\tau = \langle v^2 \rangle \tau_c^2/6\tau_0 = l^2/6\tau_0 \tag{3}$$

where l is the jump distance. Equation 3 is the familiar Einstein relationship[11,12] between D, l, and τ_0.

Now let us evaluate D by performing a thermal average in the evaluation of $\psi(\tau)$. We will assume that the Maxwell–Boltzmann distribution of molecular velocities is valid for the molecules of the solid. This assumption will be valid for most solids at moderately low temperatures and especially at high temperature. In the evaluation of the "sliding" part[3c] of $\psi(\tau)$ we consider the probability of those states of a molecule where (1) the molecule has a mean square velocity greater than $2\epsilon_0/m$ (ϵ_0 = translational energy barrier, m = molecular mass) and (2) there is a vacancy at a neighboring site subtended by the direction of $\mathbf{v}$. We denote the probability mean square velocity greater than $2\epsilon_0/m$ by $\langle v^2 \rangle_{\epsilon_0}$ and the probability of a molecular vacancy by p_v. With the aid of the cosine approximation[3c,5] to the velocity profile in traversing the potential energy barrier one obtains

$$\psi_s(\tau) = \langle v^2 \rangle_{\epsilon_0}[\alpha + \beta \cos (2\pi\tau/\tau_c)]p_v(1 - \tau/\tau_c) \tag{4}$$

where[5a] $\alpha \approx 1$ and $\beta \ll \alpha$ and, as above, $0 \leq \tau \leq \tau_c$. Equation 4 results from the assessment of the initial probability mean square velocity for diffusion and the time dependence evaluated in connection with eq 2. Placing the above expression for $\psi_s(\tau)$ in eq 1, integrating, and using the approximation that the potential barrier has a cosine dependence on distance[3c,5] one obtains the following expression for D

$$D = \frac{k_0}{3\pi^{1/2}} \left(\frac{\epsilon_0}{kT} \right)^{1/2} \left[\frac{2\epsilon_0}{m} + \frac{3kT}{m} \left(1 + \frac{kT}{2\epsilon_0} \right) \right]^{1/2} \times$$
$$\left(1 + \frac{kT}{2\epsilon_0} \right)^{1/2} l \exp[(s_0 + s_v)/k] \exp\left[-\left(\frac{\epsilon_0 + w}{kT} \right) \right] \tag{5}$$

where k_0 is the correlation factor. Equation 5 is essentially the same as eq 18 of ref 3c except D is a factor of one-half smaller here due to the more accurate evaluation of $\psi_s(\tau)$. In eq 5 s_0 and s_v are the entropy terms associated with ϵ_0 and w. w is the work of vacancy formation and $p_v = \exp(-w/kT)$.

Now we consider the temperature and pressure dependence of $\Delta E_D = \epsilon_0 + w$. In a first approximation, ΔE_D is a function of the lattice parameter d only[3c] which depends on pressure and temperature. By definition $s_D = s_0 + s_v = (\partial \Delta E_D/\partial T)_P = (\partial \Delta E_D/\partial d)_P(\partial d/\partial T)_P$ and the volume of activation ΔV_D is equal to $(\partial \Delta E_D/\partial P)_T = (\partial \Delta E_D/\partial d)_T(\partial d/\partial P)_T$. Hence in the approximation that ΔE_D is a function of d only, one obtains

$$\Delta V_D = s_D \beta/\kappa \tag{6}$$

where β is the isothermal compressibility and κ is the coefficient of volume expansion of the crystal. From experimental values of ΔV_D, values of s_D may be estimated from eq 6; theoretical values of w are available for solid sodium and hence theoretical preexponential factors may be calculated using eq 5.

B. Comparison with Experiment. In the following we shall interpret the two diffusion processes observed in solid sodium as due to vacancy diffusion to nearest-neighbor and next-nearest-neighbor vacancies. In the bcc lattice there are six nearest neighbors at the saddle point for diffusion to a nearest-neighbor vacancy and the distance to nearest neighbors at the saddle point is $(\sqrt{11}/4)d = 0.828d$ in the rigid lattice. For diffusion to a next-nearest-neighbor vacancy, there are four nearest neighbors at the saddle point and the distance to nearest neighbors at the saddle point is $(\sqrt{2}/2)d = 0.707d$ in the rigid lattice. It is very likely that the diffusion process to a next-nearest-neighbor vacancy has the larger value of ϵ_0 and we will tentatively assign this process to the component with the larger value of $\Delta E_D = \epsilon_0 + w$ observed by Mundy. Values of ϵ_0 and w were calculated for nearest neighbor vacancy diffusion by Worster, *et al.*,[13] using the pair potential of Paskin and Rahman.[14] For the potential LRO-2,[15] $\epsilon_0 = 1.27w$ and the sum $\epsilon_0 + w$ is very nearly equal to the smaller value of ΔE_D observed by Mundy. Assuming that the diffusion process observed to be dominant at low temperatures is due to vacancy diffusion to a nearest-neighbor vacancy, we calculate that $w = 3.8$ kcal mol^{-1}. Values of s_D for each of the processes considered here were calculated from the observed coefficient of cubical expansion[16] ($\kappa = 1.92 \times 10^{-4}$ K^{-1}) and isothermal compressibility[16] ($\beta = 1.6 \times 10^{-11}$ dyn^{-1} cm^2) and the observed[2a] volumes of activation using eq 6 and are listed in Table I. Also given in Table I are values of ϵ_0 (computed from the value of w given above and values of ΔE_D given in ref 2a) and preexponential factors calculated using eq 5. The calculated value of D_0 is in good agreement with experiment for process I but is an order of magnitude smaller than the observed value of D_0 for process II. Part of this latter difference may result from the inherent error in the experimental value of D_0 which is estimated to be about a factor of 3 larger or smaller than the value quoted in ref 2a.

TABLE I: Entropy of Activation (s_D), Barrier Height (ϵ_0), and Preexponential Factors (D_0) for Self-Diffusion in Solid Sodium

Process	s_D, cal K^{-1} mol^{-1}	ϵ_0, kcal mol^{-1}	calcd D_0, cm^2 sec^{-1}	obsd^a D_0, cm^2 sec^{-1}
I First-nearest-neighbor vacancy diffusion	2.0	4.7	5.8×10^{-3}	5.7×10^{-3}
II Second-nearest-neighbor vacancy diffusion	4.7	7.7	4.9×10^{-2}	7.2×10^{-1}

^{a} Reference 2a.

Another, perhaps more important, reason for the discrepancy may be due to a contribution to s_D in addition to that calculated from eq 6. This contribution to s_D could be evaluated by accurate measurements of D at constant volume and variable temperature and evaluation of D_0 from the data.

III. Diffusion in Liquid Sodium

A. Evaluation of Work Required to Create a Vacancy. The density of liquid sodium (ρ_l) may be expressed as follows[7] in the quasilattice approximation

$$\rho_l = \rho_s[1 - f_0 \exp(s_w/R) \exp(-w/kT)] \quad (7)$$

where ρ_s is the temperature-dependent density of the solid, f_0 is the fraction of the molecular volume (V_m) occupied by a vacancy, s_w is the entropy associated with w ($s_w = -(\partial w/\partial T)_P$), and w is the mean work required to create a vacancy. By plotting log $[(\rho_s - \rho_l)/\rho_s]$ vs. $1/T$, w and the product $f_0 \exp(s_w/R)$ may be determined. The densities of liquid and solid sodium are represented by[16]

$$\rho_s = 0.985 - 1.89 \times 10^{-4}(T - 273) \text{ g cm}^{-3} \quad (8a)$$

$$\rho_l = 0.928 - 2.58 \times 10^{-4}(T - 373) \text{ g cm}^{-3} \quad (8b)$$

where T is the absolute temperature. Log $[(\rho_s - \rho_l)/\rho_s]$ is plotted in Figure 1 vs. reciprocal temperature over the temperature range 373–623°K. One obtains $w = 0.78$ kcal mol^{-1} and $f_0 \exp(s_w/R) = 0.11$. As will be seen below this value of $f_0 \exp(s_w/R)$ leads to a value of $f_0 = 0.40$. This result seems unreasonable and the reason for the difficulty is that it appears that a better approximation to the structure of liquid sodium is attained with a fcc quasilattice rather than a bcc quasilattice as has been assumed above. This is indicated by integration of the radial distribution function $g(r)$ of liquid Na obtained by molecular dynamics[17] out to the first minimum of $g(r)$. One obtains a mean number of nearest neighbors equal to about 12 which is more suggestive of a fcc structure than a bcc structure. Thus in computing f_0 and w from eq 7, for ρ_s one should use a density and coefficient of expansion for fcc solid sodium. Such data do not appear to be available at various temperatures but we expect that such an analysis would yield a value of f_0 closer to unity as found for van der Waals liquids.[18]

The quantity w may also be estimated[7] from the temperature dependence of the isothermal compressibility[19] β.
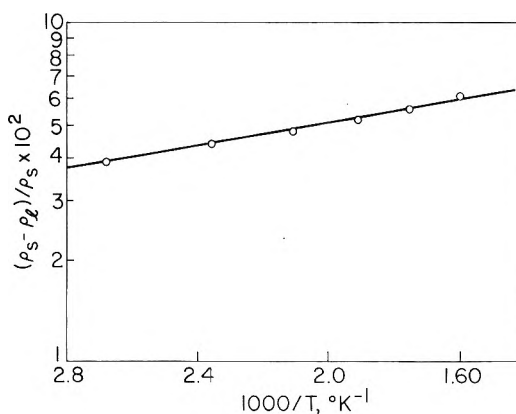

Figure 1. The quantity $(\rho_s - \rho_l)/\rho_s$ vs. reciprocal absolute temperature for liquid sodium.
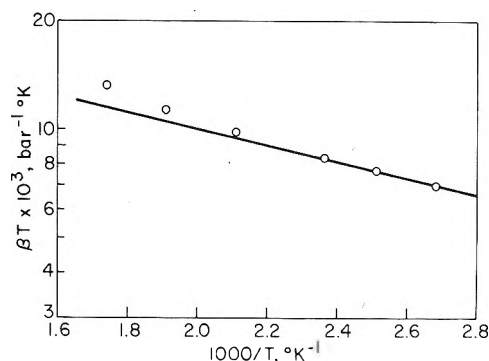

Figure 2. Product of the isothermal compressibility (β) and absolute temperature (T) vs. reciprocal temperature for liquid sodium.

Following the procedure given in ref 7 one obtains the following approximate expression for β in a fcc quasilattice

$$\beta \approx \frac{\exp(-w/RT) \exp(s_w/R) V_m}{3.25 R T} \quad (9)$$

Log β is plotted vs. reciprocal temperature in Figure 2 over the temperature range 373–523°K. At the higher temperatures the data deviate from a straight line as found with van der Waals liquids.[18] From the data of Figure 2 one obtains $w = 1.06$ kcal mol^{-1} and $\exp(s_w/R) \approx 0.33$.

A final source of w for liquid sodium may be obtained from the scaled particle theory of liquids.[20] The collision diameter[17] σ of sodium in the liquid is 3.30 Å and values of w were calculated at constant pressure at 400, 500, and 600°K for a cavity radius $\bar{r} = 2.1$ Å where $\bar{r} = (3V_m/4\pi)^{1/3}$. Over this temperature range the apparent value of w is 0.43 kcal mol^{-1} and $s_w/R = -1.29$, i.e., w increases with increase in temperature. At 400°K $w = 1.36$ kcal mol^{-1}. The apparent value of w was obtained by plotting w/kT vs. $1/T$ and calculating the slope of the resulting straight line. The value of s_w/R derived from this procedure is deemed to be more reliable than that obtained above from the compressibility. Using $s_w/R = -1.29$, one obtains $f_0 = 0.40$ from the density data. That is, the volume of a vacancy in liquid sodium is calculated to be 40% of the molecular volume as noted above, this value seems somewhat small and it must be pointed out that it depends in a sensitive way on the temperature dependence of the density of the liquid and solid. The arithmetic mean value of w is 0.75 ± 0.23 kcal mol^{-1}. The values of w and $(\partial w/\partial T)_P$ calculated from the scaled particle theory depend in a sensitive manner on the
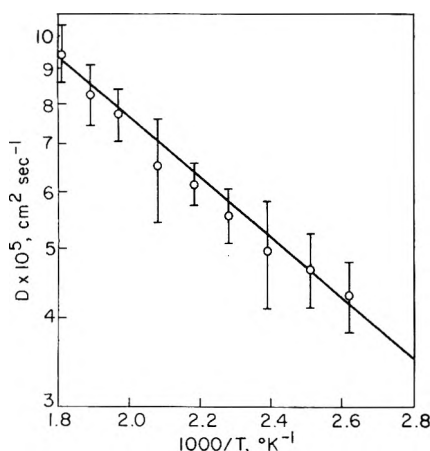
Figure 3. Self-diffusion coefficient (D) of liquid sodium at constant volume vs. reciprocal temperature (ref 3b).

values of $\bar{r}$ and σ that are chosen. σ appears to be rather accurately known[10,11] but may depend slightly on temperature.[10] Placing $\bar{r} = (3V_m/4\pi)^{1/3}$ yields good results for van der Waals and polar liquids but the precise value that one should use is uncertain by about 10%.

B. Preexponential Factors for Self-Diffusion. Let us first evaluate D_0 for liquid sodium using a primitive quasilattice model which has been formulated recently.[5] D_0 is given by the following expression

$$D_0 = \frac{4\sqrt{2}}{9\sqrt{\pi}}\left(1 + \frac{kT}{2\bar{\epsilon}_0}\right)^{1/2}\left(\frac{\bar{\epsilon}_0}{kT}\right)^{1/2}\left[\frac{\bar{\epsilon}_0}{m} + \frac{3kT}{2m}\left(1 + \frac{kT}{2\bar{\epsilon}_0}\right)\right]^{1/2} l \exp(\bar{s}_0/R) \quad (10)$$

where $\bar{\epsilon}_0$ is the mean barrier height in the liquid, l is the mean distance between lattice sites, and $\bar{s}_0$ is a mean entropy. $\bar{s}_0 = \bar{s}_w + \bar{s}_\epsilon$ where $\bar{s}_w$ is defined above and $\bar{s}_\epsilon$ is the entropy associated with $\bar{\epsilon}_0$ (*i.e.*, $\bar{s}_\epsilon = -(\partial\bar{\epsilon}_0/\partial T)_P$). As was noted in ref 5a, $\bar{\epsilon}_0$ is expected to depend on temperature as follows for a liquid quasilattice

$$\bar{\epsilon}_0 = \bar{\epsilon}_L[1 - f_0 \exp(s_w/R) \exp(-w/RT)] \quad (11)$$

where $\bar{\epsilon}_L$ is a mean barrier height for a hypothetical liquid without vacancies and w is constant, independent of temperature. From eq 11 it follows that[5b]

$$s_\epsilon = \bar{\epsilon}_0' w p_v' f_0 / RT_m^2 (1 - f_0 p_v') \quad (12)$$

where $p_v = \exp(s_w/R) \exp(-w/R)$, T_m is the absolute melting temperature and the prime on $\bar{\epsilon}_0$ and p_v signifies that these quantities are to be evaluated at T_m. Meyer and Nachtrieb[3a] reported that the coefficient of self-diffusion of liquid sodium is given by

$$D = 1.10 \times 10^{-3} \exp(-2.43/RT) \text{ cm}^2 \text{ sec}^{-1} \quad (13)$$

Hence D_0 may be calculated by calculation of $\bar{\epsilon}_0$; the calculated value of D_0 is 0.49×10^{-3} cm^2 sec^{-1} ($f_0 = 0.40$) which is somewhat smaller than the observed value. For $f_0 = 1$, one obtains $D_0 = 0.58 \times 10^{-3}$ cm^2 sec^{-1}.

The self-diffusion coefficients of liquid sodium were reported by Ozelton and Swalin[3b] at constant volume over the temperature range 381–552°K and are shown in Figure 3 with the errors in D given. The data are represented by

$$D = (5.5 \pm 2.4) \times 10^{-4} \exp[-(1.95 \pm 0.51)/RT] \text{ cm}^2 \text{ sec}^{-1} \quad (14)$$

The quasilattice model for self-diffusion predicts that the activation energy for D at constant volume $((\Delta E_D)_V)$ is related to the activation energy for D at constant pressure $((\Delta E_D)_P)$ by the following equation

$$(\Delta E_D)_P = (\Delta E_D)_V + w \quad (15)$$

since there is a constant density and variable temperature the quantity $\exp(-w/RT)$ will be constant as predicted by eq 7. The quantity w/RT was calculated using the scaled particle theory at temperatures ranging from 400 to 600°K and at constant density and found to be strictly independent of temperature. The quasilattice model yields $(\Delta E_D)_V = 1.68 \pm 0.23$ kcal mol^{-1} and D_0 at constant pressure equal to 2.5×10^{-4} cm^2 sec^{-1}. These values are in good agreement with experiment (eq 14).

Also of interest is the volume of activation (ΔV_D) for self-diffusion in the liquid. The method of derivation of an expression for ΔV_D follows that given earlier[5a] and here we give only the result as follows

$$\Delta V_D = \left[\bar{\epsilon}_L + \frac{RT}{f_0 p_v}\left(1 - \frac{f_0 p_v}{1 - f_0 p_v}\right)\right]\frac{\beta_l - \beta_s}{\rho_s}\rho_l \quad (16)$$

where $p_v = \exp(\bar{s}_w/R) \exp(-w/RT)$ and β_l and β_s are the isothermal compressibility of the liquid and solid, respectively. At 400°K one calculates $\Delta V_D = 2.6$ cm^3 mol^{-1} ($f_0 = 0.40$) which is 11% of the molar volume and 1.0 cm^3 mol^{-1} for $f_0 = 1$ which is only 4% of the molar volume. An experimental value for this quantity does not appear to have been reported in the literature, so that no comparison between theory and experiment can be made here. In the derivation of eq 16 we have neglected the pressure dependence of f_0, $\bar{\epsilon}_L$, and $\exp(\bar{s}_w/R)$.

The quasilattice model of self-diffusion in liquids has recently been reexamined under less restrictive conditions.[6] The result for D in this extended quasilattice model is as follows[6]

$$D = \frac{1}{2\pi\rho_1\sigma^2}\left(\frac{\bar{\epsilon}_0}{kT}\right)^{1/2}\left(\frac{1}{mkT}\right)^{1/2}\left[\bar{\epsilon}_0 + \frac{3}{2}kT\left(1 + \frac{kT}{2\bar{\epsilon}_0}\right)\right]\exp(\bar{s}/R)\exp(-(\bar{\epsilon}_0 - \bar{\epsilon}_0' + w)/RT) \quad (17)$$

where ρ_1 is the number density, $\bar{\epsilon}_0$ is the mean energy barrier height in the liquid, and $\bar{s} = \bar{s}_\epsilon - \bar{s}_0' + \bar{s}_w$ is the mean entropy of activation. $\bar{s}_\epsilon = -(\partial\bar{\epsilon}_0/\partial T)_P$ and $\bar{s}_0' = -(\partial\bar{\epsilon}_0'/\partial T)_P$ where $\bar{\epsilon}_0'$ is the mean potential energy of interaction of a pair of sodium atoms at closest approach during a hard collision. In the derivation of eq 17 the "rattling" contribution to D has been neglected.[6]

To evaluate the preexponential factor in eq 11 it is necessary to evaluate the quantity $\bar{\epsilon}_0'$. This is carried out approximately in the Appendix B. The result is as follows

$$\bar{\epsilon}_0' \cong \frac{3}{2}kT + \frac{\bar{\epsilon}_0}{2} - \epsilon \quad (18)$$

where ϵ is the depth of the minimum in the pair potential between atoms (ϵ is equal[20] to 0.84 kcal mol^{-1}). Hence $\bar{s}_0' \cong -(3/2)k + (\bar{s}/2)\epsilon$, $\Delta E_D \simeq (\bar{\epsilon}_0/2) + \epsilon + w$ and thus $\bar{\epsilon}_0 \cong$ 1.7 kcal mol^{-1}. Evaluating $\bar{s}_\epsilon$ from eq 12 and using the value of s_w obtained from the scaled particle theory above one obtains $D_0 = 1.6 \times 10^{-3}$ cm^2 sec^{-1} ($f_0 = 0.40$) and $D_0 = 1.7 \times 10^{-3}$ cm^2 sec^{-1} ($f_0 = 1.0$). These values of D_0 are somewhat higher than the experimental value (1.10×10^{-3} cm^2 sec^{-1}). Equation 15 is valid to good approximation for the extended quasilattice model also and the agreement of the

model with the results at constant volume is reasonably good.

The volume of activation for self-diffusion in the extended quasilattice model may be derived by noting that the dependence of D on p_v is essentially as follows

$$D = \frac{K\{\bar{\epsilon}_L(1 - f_0 p_v) + (3/2)RT\}}{\rho_s(1 - f_0 p_v)^{1/2}} p_v \exp(-\{\bar{\epsilon}_L(1 - f_0 p_v)\}/2RT\}) \quad (19)$$

From the definition of ΔV_D, i.e.

$$\Delta V_D = -RT(\partial \ln D/\partial P)_T \quad (20)$$

it follows that

$$\Delta V_D = RT\beta_s + \left\{\frac{\bar{\epsilon}_L}{2} + \frac{RT}{f_0 p_v}\left[1 - \frac{f_0 p_v}{2(1 - f_0 p_v)} \times \frac{-\epsilon_L f_0}{\{\epsilon_L(1 - f_0 p_v) + (3/2)RT\}}\right]\right\} \frac{\rho_l}{\rho_s}(\beta_l - \beta_s) \quad (21)$$

where as in the derivation of eq 16 we have neglected the pressure dependence of $\exp(\bar{s}_w/R)$, f_0, and $\bar{\epsilon}_L$ and have evaluated $(\partial p_v/\partial P)_T$ from eq 7. At 400°K, one obtains $\Delta V_D = 7.1$ cm^3 mol^{-1} ($f_0 = 0.40$) which is nearly a factor of 3 larger than the value of ΔV_D given by the primitive quasilattice model ($\Delta V_D = 2.6$ cm^3 mol^{-1}). For $f_0 = 1.0$, $\Delta V_D = 5.5$ cm^3 mol^{-1}.

IV. Viscosity of Liquid Sodium

The viscosity[21] of liquid sodium is well represented by an Arrhenius equation

$$\eta = (8.8 \pm 0.3) \times 10^{-4} \exp\{-[(1.56 \pm 0.04)/RT]\} \text{ P} \quad (22)$$

where the average of the preexponential factors (η_0) and activation energies (ΔE_V) from ref 21 are given. There are three approximate relationships between D and η which are useful in the estimation of η from theoretical models of self-diffusion such as the quasilattice models discussed in section III. These are as follows

$$\eta = kT/4\pi Da$$
(modified Stokes–Einstein relation[22]) (23)

$$\eta = kT\rho_l\lambda^2/24D \quad \text{(cubical cell model}[23]\text{)} \quad (24)$$

$$\eta = 2a^2\rho_l kT/5D \quad \text{(hard spheres}[24]\text{)} \quad (25)$$

where a is an effective hydrodynamic radius in eq 23 and is the hard-sphere radius in eq 25. ρ_l is the number density and λ is the effective dimension of the cubic unit cell in the liquid. All three of the above equations predict that η depends on temperature essentially as T/D. Over the temperature range of measurement[21b] of η(400–1100°K) T is well represented by $T \cong 1.7 \times 10^3 \exp(-1.25/RT)$ °K and hence we expect that $\Delta E_D \cong \Delta E_V + 1.25 = 2.81$ kcal mol^{-1}. This estimate is not much larger than the observed[3a] value of ΔE_D (2.43 kcal mol^{-1}). Values of the preexponential factor η_0 calculated from eq 23–25 using D_0 from eq 13 are given in Table II and compared with the experimental value (eq 22). The agreement is good, especially for the cubical cell model.

V. Discussion

The two processes of vacancy diffusion proposed for solid sodium require additional support from computer calculations of ϵ_0 and also w using more accurate potentials

TABLE II: Theoretical Values of η_0 for Three Approximate Relationships between η and D

Relationship	$\eta_0 \times 10^4$, P
Stokes–Einstein, eq 23, $a = \sigma/2$	10.3
Cubical cell model, eq 24, $\lambda = 2\sigma$	9.4
Hard spheres, eq 25, $a = \sigma/2$	5.6
Experiment, eq 22	8.8 ± 0.3

such as that proposed by Shyu, Singwi, and Tosi.[25] In addition, accurate measurements of D vs. T at constant volume would be very useful. It appears likely that the low-temperature process proceeds by a relaxed vacancy diffusion mechanism but the nature of the high-temperature process is in considerable doubt.

In the liquid state, the scaled particle theory yields a considerably smaller value of w than the values obtained from the analysis of density and compressibility data. However, this value of w is a very sensitive function of the effective collision diameter used and is regarded as being somewhat uncertain. Both quasilattice models are in fairly good agreement with the experimental values of D_0 at constant pressure and constant volume and $(E_D)_V$. Likewise the temperature dependence of the coefficient of shear viscosity is accurately given by the cubical cell model. It would be of considerable interest to experimentally determine the volume of activation in liquid Na at several temperatures.

The model for self-diffusion based on the theory for hard spheres[6,9,24] has been applied to sodium metal recently by Protopapas, Andersen, and Parlee.[10] These authors use a semiempirical expression for the temperature dependence of the effective hard-sphere diameter and have calculated values of D that agree remarkably well with the experimental data. However, volumes of activation and values of D at constant volume should be calculated for this model for further corroboration. An obvious criticism of the hard-sphere model is that the velocity autocorrelation function $\psi(\tau)$ for hard spheres decays exponentially,[6] yet molecular dynamics calculations[17] on liquid Na yield a highly nonexponential behavior for $\psi(\tau)$. The nonexponential behavior of $\psi(\tau)$ may be explained using the quasilattice model.[5a] By a careful comparison of the predictions of the hard sphere and quasilattice models with the experimental temperature and pressure dependence of D and the results of molecular dynamics calculations ($\psi(\tau)$, isotope effect[6]) it should be possible to conclude which model (if either) is most representative of the nature of self-diffusion in liquid metals. Of particular interest is the self-diffusion coefficient of light or heavy sodium atoms in ordinary sodium. The hard-sphere model predicts[6] that D will be strictly inversely proportional to the square root of reduced mass while experiments on van der Waals liquids[26,27] have shown that D is nearly independent of the mass of the foreign molecule.

Appendix A

Velocity Autocorrelation Function for Jump Diffusion. The mean time duration of a jump is τ_c, the mean time between jumps is τ_0, and the average mean square velocity during a jump is $\langle v^2 \rangle$. During the time intervals between jumps the average velocity is equal to zero. We wish to construct $\psi(\tau)$, i.e.

$$\psi(\tau) = \langle v(\tau) \cdot v(0) \rangle \quad (A1)$$

For $\tau > \tau_c$, $\psi(\tau) = 0$ since after the initial jump the average value of the dot product (in fcc or bcc symmetry) will be

equal to zero (neglecting correlation). Consider the brackets in eq A1 as an average over all initial times. The probability that $v(0)$ is not equal to zero is equal to τ_c/τ_0 since the jumps occur at random. We will reckon time from the beginning of a pulse ($t = 0$) and find the average value of $\psi(\tau)$ as follows. Let $\tau_c - t = \tau_i$ then

$$\psi_i(\tau, \tau_i) = \langle v^2 \rangle (\tau_c/\tau_0) \qquad 0 < \tau < \tau_i$$

and

$$\psi_i(\tau, \tau_i) = 0 \qquad \tau_i < \tau < \tau_c$$

hence $\psi(\tau)$ is given by an average of $\psi_i(\tau, \tau_i)$ over all initial times t.

$$\psi(\tau) = \frac{1}{\tau_c} \int_\tau^{\tau_c} \psi_i(\tau, \tau_i) \, d\tau_i \tag{A2}$$

since $\psi_i(\tau, \tau_i)$ is different from zero only for $\tau < \tau_i < \tau_c$. Performing the integral in eq A2 one obtains

$$\psi(\tau) = \langle v^2 \rangle \frac{\tau_c}{\tau_0} \left(1 - \frac{\tau}{\tau_c}\right) \tag{A3}$$

as given in eq 2.

Appendix B

Approximate Evaluation of the Potential Energy ($\bar{\epsilon}_0'$) *at Closest Approach during a Hard Collision.* In the following we will consider a hard-core collision between a "hot" molecule (1) with another molecule (2) with average velocity. At the point of closest approach between the two molecules the incident relative kinetic energy $(1/4)mV^2$ will be completely converted to potential energy, where $\mathbf{V} = \mathbf{v}_1 - \mathbf{v}_2$ and $\mathbf{v}$ is linear velocity. The hard collisions that are of interest are those which occur when molecule 1 has sufficient kinetic energy to surmount the mean potential energy barrier encounted in self-diffusion. The mean square velocity $\langle v^2 \rangle_{\bar{\epsilon}_0}^0$ of the hot molecule 1 is readily shown as follows

$$\langle v^2 \rangle_{\bar{\epsilon}_0}^0 \cong \frac{2\bar{\epsilon}_0}{m} + \frac{3kT}{m} \tag{B1}$$

using the Maxwell–Boltzmann distribution as in ref 5a. In deriving eq B1 we have simplified the result by assuming that $\bar{\epsilon}_0 \gg kT/2$. The mean value of the incident relative kinetic energy is given by

$$\frac{1}{4}m\langle V^2 \rangle \cong \frac{1}{4}m\left\{ \langle v_1^2 \rangle_{\bar{\epsilon}_0}^0 + \frac{3kT}{m} \right\} \tag{B2}$$

where we have dropped the cross term $-2\langle \mathbf{v}_1 \cdot \mathbf{v}_2 \rangle$ which is small compared to $\langle v_1^2 \rangle_{\bar{\epsilon}_0}^0$.

The mean molecular potential energy in the liquid is proportional to ϵ, the minimum value of the pair potential energy between molecules. The change in the mean potential energy for molecules 1 and 2 between the positions they

normally occupy in the quasilattice and at the point of closest approach during a hard collision is approximately equal to $\bar{\epsilon}_0' + \epsilon$, neglecting the change in potential energy between molecules 1 and 2 and all the remaining molecules in the liquid. Hence $\bar{\epsilon}_0'$ is, by conservation of energy, given as follows

$$\epsilon_0' \cong \frac{1}{4}m\langle V^2 \rangle - \epsilon \tag{B3}$$

$$\cong \frac{\bar{\epsilon}_0}{2} + \frac{3}{2}kT - \epsilon \tag{B4}$$

as given by eq 18.

References and Notes

(1) Based on work performed under the auspices of the U. S. Atomic Energy Commission.
(2) (a) J. N. Mundy, *Phys. Rev. B*, **3**, 2431 (1971); (b) J. N. Mundy, L. W. Barr, and F. A. Smith, *Phil. Mag.*, **14**, 785 (1966); (c) N. A. Nachtrieb, E. Catalano, and J. A. Weil, *J. Chem. Phys.*, **20**, 1185 (1952); (d) N. H. Nachtrieb, J. A. Weil, E. Catalano, and A. W. Lawson, *ibid.*, **20**, 1189 (1952).
(3) (a) R. E. Meyer and N. H. Nachtrieb, *J. Chem. Phys.*, **23**, 1851 (1955); (b) M. W. Ozeiton and R. A. Swalin, *Phil. Mag.*, **18**, 44 (1968); (c) D. E. O'Reilly and E. M. Peterson, *J. Chem. Phys.*, **56**, 5536 (1972).
(4) (a) A. W. Lawson, *J. Chem. Phys. Solids*, **3**, 250 (1957); (b) D. E. O'Reilly, E. M. Peterson, C. E. Scheie, and E. Seyfarth, *J. Chem. Phys.*, **59**, 3576 (1973).
(5) (a) D. E. O'Reilly, *J. Chem. Phys.*, **55**, 2876 (1971); erratum, **58**, 1272 (1973); (b) *ibid.*, **56**, 2490 (1972).
(6) D. E. O'Reilly, *J. Chem. Phys.*, to be submitted for publication.
(7) D. E. O'Reilly and E. M. Peterson, *J. Chem. Phys.*, **55**, 2155 (1971).
(8) H. Reiss, H. L. Frisch, E. Helfand, and J. L. Lebowitz, *J. Chem. Phys.*, **32**, 119 (1960).
(9) J. H. Dymond and B. J. Alder, *J. Chem. Phys.*, **45**, 206 (1966); **48**, 343 (1968); **52**, 923 (1970).
(10) P. Protopapas, H. C. Andersen, and N. A. D. Parlee, *J. Chem. Phys.*, **59**, 15 (1973).
(11) P. A. Egelstaff, "An Introduction to the Liquid State," Academic Press, New York, N.Y., 1967, Chapter 11.
(12) G. Joos, "Theoretical Physics," Hafner Publishing Co., New York, N.Y., 1934, p 562.
(13) J. Worster, R. C. Brown, N. H. March, R. C. Perrin, and R. Bullough in "Diffusion Processes," Vol. 1, J. N. Sherwood, Ed., Gordon and Breach, New York, N.Y., 1971, p 191.
(14) A. Paskin and A. Rahman, *Phys. Rev. Lett.*, **16**, 300 (1964).
(15) The potential LRO-2 gave a better fit to the radial distribution function and yielded a value of the coefficient of self-diffusion in the liquid in better agreement with experiment than the LRO-1 potential.
(16) E. W. Washburn, Ed., "International Critical Tables," McGraw-Hill, New York, N.Y., 1926: Vol. 3, p 147; Vol. 2, p 461.
(17) A. Rahman in "Interatomic Potentials and Simulation of Lattice Defects," P. C. Gehlene, J. R. Beeler, and R. I. Jaffee, Ed., Plenum Press, New York, N.Y., 1972, p 233.
(18) (a) D. E. O'Reilly and E. M. Peterson, *J. Chem. Phys.*, **56**, 2262 (1972); (b) D. E. O'Reilly, E. M. Peterson, and C. E. Scheie, *J. Chem. Phys.*, **60**, 1603 (1974).
(19) Yu S. Trelin, I. N. Vasil'ev, V. B. Proskurin, and T. A. Tsygovova, *Teplofiz. Vys. Temp.*, **4**, 364 (1966) [*High Temp. (USSR)*, **4**, 352 (1966)].
(20) H. Reiss, H. L. Frisch, E. Helfand, and J. L. Lebowitz, *J. Chem. Phys.*, **32**, 119 (1960).
(21) (a) W. Menz, F. Sauerwald, and K. Fischer, *Acta. Met.*, **14**, 1617 (1966); (b) E. E. Shpil'rain and V. A. Formin, *Teplofiz. Vys. Temp.*, **7**, 877 (1969).
(22) See, for example, E. McLaughlin, *Trans. Faraday Soc.*, **55**, 28 (1959).
(23) G. Houghton, *J. Chem. Phys.*, **40**, 1628 (1964).
(24) H. C. Louguet-Higgins and J. A. Pople, *J. Chem. Phys.*, **25**, 884 (1956).
(25) W. M. Shyu, K. S. Singwi, and M. P. Tosi, *Phys. Rev. B*, **3**, 237 (1971).
(26) G. G. Allen and P. J. Dunlop, *Phys. Rev. Lett.*, **30**, 316 (1973).
(27) A. Rahman, private communication.

On the Determination of Cross-Term Diffusion Coefficients in Ternary Systems by the Capillary Cell Method

Kazuo Toukubo and Koichiro Nakanishi*

Department of Industrial Chemistry, Kyoto University, Kyoto 606, Japan (Received April 22, 1974)

The extended Fick equation for the diffusion in ternary systems has been solved with the initial and boundary conditions pertinent to the open-ended capillary cell method. An analytical solution has been obtained which makes it possible to convert the experimentally measurable quantities to the four (main and cross) diffusion coefficients without introducing either mathematical or physical approximations. Application of this technique to the determination of the diffusion coefficients in dilute solutions is discussed.

Introduction

Coupled diffusion with interacting flow in ternary systems may be expressed by the extended Fick equation[1]

$$\nabla J_1 = \frac{\partial c_1}{\partial t} = D_{11}\frac{\partial^2 c_1}{\partial x^2} + D_{12}\frac{\partial^2 c_2}{\partial x^2}$$

$$\nabla J_2 = \frac{\partial c_2}{\partial t} = D_{21}\frac{\partial^2 c_1}{\partial x^2} + D_{22}\frac{\partial^2 c_2}{\partial x^2}$$

(1)

where J_i is the flux relative to the volume averaged velocity and c_i is the concentration, both of species i. The D_{ij}'s represent the ternary diffusion coefficients. The four D_{ij}'s appearing in eq 1 have been determined by the Gouy diffusiometer[1,2] or the diaphragm cell method.[3] In an earlier stage in the studies on ternary diffusion, effort had been devoted to the verification of the validity of the Onsager reciprocal relation (ORR) which insists the equality of the cross-term phenomenological coefficients, $L_{12} \equiv L_{21}$. The principle contribution comes from the studies of Gosting and coworkers who established elaborate experimental technique for Gouy's diffusiometer and the method of calculation of D_{ij}'s from the experimentally measurable quantities.[1]

Recently much attention has been paid to the systems where there is a strong interacting flow and accordingly the absolute values of the cross diffusion coefficients, D_{12} and/or D_{21}, are fairly large.[4] It seems therefore desirable to establish simple yet reasonably accurate method to obtain the cross coefficients. In this paper, we present an analytical solution of eq 1 with a boundary condition pertinent to the open-ended capillary cell experiment.[2,5] This solution has been obtained without any mathematical and physical approximations and allows the calculation of four diffusion coefficients from two independent measurements with different times of diffusion.

Solution of the Diffusion Equation

Equation 1 may be solved with the boundary conditions of the capillary cell method as follows. Let the components 1 and 2 be the diffusing species, the component 3 be a solvent, and the concentration of each component outside the capillary is assumed constant throughout the measurement. Then the initial and boundary conditions become: initial conditions, $t = 0$

$$0 \leq x \leq a;\ c_1 = c_1{}^0,\ c_2 = c_2{}^0$$

$$x > a;\ c_1 = c_1',\ c_2 = c_2'$$

(2)

boundary conditions, $t > 0$

$$x = 0;\ \partial c_1/\partial x = \partial c_2/\partial x = 0$$

$$x \geq a;\ c_1 = c_1',\ c_2 = c_2'$$

(3)

where a is the length of capillary.

In order to satisfy the boundary conditions, c_1 and c_2 may be expressed by the following equations

$$c_1 - c_1' = \sum_{n=0}^{\infty} \cos\frac{(2n+1)\pi}{2a}x\left[A_n e^{-\left\{\frac{(2n+1)\pi}{2a}\right\}^2 Rt} + a_n e^{-\left\{\frac{(2n+1)\pi}{2a}\right\}^2 St}\right]$$

(4)

$$c_2 - c_2' = \sum_{n=0}^{\infty} \cos\frac{(2n+1)\pi}{2a}x\left[B_n e^{-\left\{\frac{(2n+1)\pi}{2a}\right\}^2 Rt} + b_n e^{-\left\{\frac{(2n+1)\pi}{2a}\right\}^2 St}\right]$$

(5)

where A_n, B_n, a_n, and b_n are the coefficients to be determined from the initial conditions, and

$$R = [(D_{11} + D_{22}) + \sqrt{(D_{11} - D_{22})^2 + 4D_{12}D_{21}}]/2$$

(6)

$$S = [(D_{11} + D_{22}) - \sqrt{(D_{11} - D_{22})^2 + 4D_{12}D_{21}}]/2$$

(7)

Substituting the initial conditions, $c_1 = c_1{}^0$ and $c_2 = c_2{}^0$ at $t = 0$ into eq 4 and 5 and using the Fourier analysis, the following expressions are obtained

$$A_n + a_n = \frac{4(-1)^n}{(2n+1)\pi}(c_1{}^0 - c_1')$$

(8)

$$B_n + b_n = \frac{4(-1)^n}{(2n+1)\pi}(c_2{}^0 - c_2')$$

(9)

On the other hand, substitution of eq 4 and 5 into eq 1 must lead to equations valid for any values of x and t. From this condition

$$A_n R = D_{11}A_n + D_{12}B_n$$

(10)

$$a_n S = D_{11}a_n + D_{12}b_n$$

(11)

If we set the ratio A_n/B_n and a_n/b_n as P and Q, then the following equations are obtained by eliminating R and S from eq 6 and 7.

$$P = A_n/B_n = [(D_{11} - D_{22}) + \sqrt{(D_{11} - D_{22})^2 + 4D_{12}D_{21}}]/2D_{21} \quad (12)$$

$$Q = a_n/b_n = [(D_{11} - D_{22}) - \sqrt{(D_{11} - D_{22})^2 + 4D_{12}D_{21}}]/2D_{21} \quad (13)$$

Equations 8, 9, 12, and 13 can easily be solved to give A_n, B_n, a_n, and b_n. These are then substituted into eq 4 and 5 to obtain the following solution which satisfies the original equation (eq 1).

$$c_1 - c_1' = \frac{1}{P - Q} \sum_{n=0}^{\infty} l_n \cos k_n x \{P[(c_1^0 - c_1') - Q(c_2^0 - c_2')]e^{-k_n^2 Rt} - Q[(c_1^0 - c_1') - P(c_2^0 - c_2')]e^{-k_n^2 St}\} \quad (14)$$

$$c_2 - c_2' = \frac{1}{P - Q} \sum_{n=0}^{\infty} l_n \cos k_n x \{[(c_1^0 - c_1') - Q(c_2^0 - c_2')]e^{-k_n^2 Rt} - [(c_1^0 - c_1') - P(c_2^0 - c_2')]e^{-k_n^2 St}\} \quad (15)$$

where

$$l_n = 4(-1)^n/(2n + 1)\pi \quad (16)$$

$$k_n = (2n + 1)\pi/2a \quad (17)$$

In the capillary cell experiments, it is a common practice to determine the average concentration of solutes c_{av} in the capillary after the time of duration t. Since

$$c_{av}(t) = \frac{1}{a} \int_0^a c(t, x) \, dx \quad (18)$$

eq 14 and 15 are integrated to give the final equation

$$c_{1,av} - c_1' = \frac{1}{P - Q} \sum_{n=0}^{\infty} h_n \{P[(c_1^0 - c_1') - Q(c_2^0 - c_2')]e^{-k_n^2 Rt} - Q[(c_1^0 - c_1') - P(c_2^0 - c_2')]e^{-k_n^2 St}\} \quad (19)$$

$$c_{2,av} - c_2' = \frac{1}{P - Q} \sum_{n=0}^{\infty} h_n \{[(c_1^0 - c_1') - Q(C_2^0 - c_2')]e^{-k_n^2 Rt} - [(c_1^0 - c_1') - P(c_2^0 - c_2')]e^{-k_n^2 St}\} \quad (20)$$

where

$$h_n = 8/[(2n + 1)^2 \pi^2] \quad (21)$$

and P, Q, R, S, and k_n are given by eq 12, 13, 6, 7, and 17, respectively. The four diffusion coefficients to be calculated can be expressed by the combination of P, Q, R, and S as in the following equations.

TABLE II: Cross Coefficients and Corresponding Concentration Decrease in the Capillary Cell Experiment

	Input data		Output results[b]	
	D_{12}[a]	D_{12}[a]	$c_{1,av}$	$c_{2,av}$
$a = 7.00$ cm	0.01	0.10	0.1928	0.1516
$t = 1.728 \times 10^5$ sec	0.05	0.10	0.1919	0.1516
$c_1^0 = 0.25$	0.10	0.10	0.1908	0.1516
$c_2^0 = 0.20$	0.20	0.10	0.1886	0.1517
$c_1' = c_2' = 0$	0.50	0.10	0.1819	0.1518
$D_{11} = D_{22} = 1.00$[a]	0.50	0.50	0.1831	0.1412

[a] 10^5 cm² sec⁻¹. [b] Calculated from eq 19 and 20.

$$D_{11} = (PR - SQ)/(P - Q)$$
$$D_{12} = [(S - R)PQ]/(P - Q)$$
$$D_{21} = (R - S)/(P - Q)$$
$$D_{22} = (PS - QR)/(P - Q)$$
$$(22)$$

Equations 19 and 20 are valid irrespective of whether $c_i^0 > c_i'$ or $c_i^0 < c_i'$. For the measurements in dilute solutions, either c_i^0 or c_i' can be set to zero in all the equations given in this section.

Calculation of Diffusion Coefficients

In the capillary cell experiments, the initial and average concentrations of components 1 and 2, c_1^0 and c_2^0 (or c_1' and c_2') at $t = 0$, and $c_{1,av}$ and $c_{2,av}$ at $t = t$, are experimentally determined. Since one diffusion run yields two equations (eq 19 and 20), two runs with the same initial concentration and different t suffice to determine four unknown variables, i.e., P, Q, R, and S.

Equations 19 and 20 indicate that the c_{av} can be expressed as the sum of an infinite series. Preliminary calculation shows that this series converges rather rapidly under usual experimental conditions and only the first four terms are necessary for calculating the D_{ij}'s with an accuracy of 0.1%.

In order to obtain the four diffusion coefficients from the experimentally measurable quantities, the four-variable Newton–Raphson method may be used. A computer program in fortran language has been prepared as shown in Table I.[6] This program was proved to work well with reverse calculated data.

Discussion

The capillary cell method has been widely used for the determination of the intradiffusion coefficients with radioactive tracer.[2,5] It is also applied to the determination of the mutual diffusion coefficients of diluted solute in binary or ternary solutions.[7] The measurements with this method may be classified into two types according to the relative magnitude of c_0 to c'. If $c_0 > c'$, then it is conventional "diffuse out" type measurement. On the other hand, $c_0 < c'$ may be termed as "diffuse in" type, which has been adopted by Bockris and Hooper.[8] Relative merit of one of these two techniques over another would be judged by the ease with which the method chosen can be fitted more rigorously to the boundary conditions imposed.

In ternary nonideal solutions, it is ultimately desirable to obtain the values of the four diffusion coefficients over the whole composition range. However, most of the available data, especially those for aqueous solutions of electrolytes

or nonelectrolytes, have been obtained in a corner area of triangle coordinate for ternary systems where two solutes are diluted in a solvent. Since the mutual diffusion coefficient is essentially equal to the intradiffusion coefficient of solute in this corner area, the present method may best be applied to the measurements in such dilute solutions.

It is interesting to examine how far the small difference in concentration should be detected for the cases that the cross coefficients, D_{12} and D_{21}, are relatively smaller than the main coefficients, D_{11} and D_{22}. Table II shows several examples of test calculations, in which C_{av}'s are directly calculated by eq 19 and 20 with appropriate input data. It is seen that the errors in concentration determination should not exceed 0.1%, when D_{12} and D_{21} are less than one tenth of D_{11} and D_{22}. This is a very difficult assignment and special experimentation must be necessary. However, if the main and cross coefficients are of comparable magnitude, such demands for higher accuracy will be greatly reduced.

In conclusion, if the absolute values of the cross coefficients are fairly large, the capillary cell method should furnish a simple device to estimate the cross diffusion coefficients in ternary systems. Furthermore, a test of the ORR for ternary molten salt mixtures with a common ion[9] may be possible, provided that very high accuracy at higher temperature could be achieved. To this end, preliminary measurements are currently in progress.

Supplementary Materials Available. Table I will appear following these pages in the microfilm edition of this volume of the journal. Photocopies of the supplementary material from this paper only or microfiche (105 × 148 mm, 24× reduction, negatives) containing all of the supplementary material for the papers in this issue may be obtained from the Journals Department, American Chemical Society, 1155 16th St., N.W., Washington, D. C. 20036. Remit check or money order for $3.00 for photocopy or $2.00 for microfiche, referring to code number JPC-74-2281.

References and Notes

(1) D. D. Fitts, "Nonequilibrium Thermodynamics," McGraw-Hill, New York, N. Y., 1962, Chapter 8.
(2) For review of the method, see ref 1 and A. L. Geddes and R. B. Pontius, in "Physical Methods of Chemistry," A. Weissberger and B. W. Rossiter, Ed., revised edition, Vol. 1, part IV, Wiley-Interscience, New York, N. Y., 1971.
(3) For review of the method, see R. Mills and L. A. Woolf, "The Diaphragm Cell," Australian National University Press, Camberra, A.C.T., Australia, 1968.
(4) See, for example, (a) G. R. Reinfelds and L. F. Gosting, *J. Phys. Chem.,* **68,** 2464 (1964); (b) A. Revzin, *ibid.,* **76,** 3419 (1972).
(5) H. J. V. Tyrrell, "Diffusion and Heat Flow in Liquids," Butterworths, London, 1961, Chapter 5.
(6) See paragraph at end of text regarding supplementary material.
(7) See, for examples, (a) E. W. Haycock, B. J. Alder and J. H. Hildebrand, *J. Chem. Phys.,* **23,** 659 (1953); (b) K. Nakanishi and T. Ozasa, *J. Phys. Chem.,* **74,** 2956 (1970).
(8) J. O'M. Bockris and G. W. Hooper, *Discuss. Faraday Soc.,* **32,** 218 (1961).
(9) This is one of four kinds of ternary systems, for which the experimental verification of the ORR has not yet been available (see ref 1).

Diffusivities and Viscosities of Some Binary Liquid Nonelectrolytes at 25°

R. K. Ghai*[1] and F. A. L. Dullien

Department of Chemical Engineering, University of Waterloo, Waterloo, Ontario, Canada N2L 3G1 (*Received March 18, 1974*)

Publication costs assisted by the National Research Council of Canada

The intradiffusivities for three binary liquid systems n-hexane + toluene, carbon tetrachloride + n-hexane, and toluene + carbon tetrachloride and mutual diffusivities for two systems n-hexane + carbon tetrachloride and toluene + carbon tetrachloride have been measured at 25° and ambient pressure, covering the complete composition range. The diaphragm-cell technique was employed for these measurements. The density and viscosity values were also determined for each of these systems. The data have been used to test the validity of various diffusivity equations proposed in the literature. It has been concluded that these probably apply only in ideal solutions. The comparison of the limiting mutual and intradiffusion coefficients did not indicate an isotope effect on the rate of diffusion.

Introduction

As is well known, two types of diffusion coefficients are commonly used in diffusional theories of binary mixtures: one mutual diffusion coefficient, D_{AB}, and two intradiffusion coefficients, D_{A^*} and D_{B^*}. In a mutual diffusion process, components A and B interdiffuse into each other in such a way as to smooth out the inequalities in the concen-

trations. Intradiffusion is unlike mutual diffusion in that it takes place in a chemically homogeneous mixture; the transport due to random motion of molecules is determined with the aid of trace amounts of tagged molecules A or B.

Various relations have been proposed between mutual and intradiffusion coefficients.[2] Those originating from Darken[3] and Hartley and Crank[4] have been used most ex-

tensively. According to Darken

$$D_{AB} = (x_A D_{B^*} + x_B D_{A^*})\beta \qquad (1)$$

where x_A and x_B are mole fractions of components A and B, and β is a thermodynamic factor, given by

$$\beta = d \ln a_i / d \ln x_i \quad i = A, B \qquad (2)$$

a_i is the activity of component i. An assumption of equal molal volumes of components A and B (that is $V = \bar{V}_A = \bar{V}_B$) has been made in the derivation of eq 1.

The Hartley–Crank equation is

$$D_{AB} = (\psi_A D_{B^*} + \psi_B D_{A^*})\beta \qquad (3)$$

The only difference between eq 3 and 1 is that the former contains volume fractions ψ_A and ψ_B instead of mole fractions. Evidently, eq 3 becomes identical with eq 1 if $V = \bar{V}_A = \bar{V}_B$. Equation 3 was originally derived for the case when the partial molal volumes of the constituents are composition independent. However, this equation can be developed without making such an assumption.[5]

Another form of the Hartley–Crank equation was obtained by Carman and Stein.[6]

$$D_{AB} = \frac{kT}{\eta}\left\{\frac{x_A}{\sigma_B} + \frac{x_B}{\sigma_A}\right\}\beta \qquad (4)$$

where σ is usually called the "friction factor," η is the viscosity, and T is the absolute temperature.

The central idea, common to both the Darken and the Hartley–Crank theory, the postulate of independent intrinsic mobilities for the components and a compensating bulk flow, seems to lack physical reality in the case of liquids.[2] These equations, however, have been used very widely in the literature.[2] Any deviation of the experimental data from these diffusional models has been generally rationalized by assuming that the kinetic units are molecular aggregates rather than the individual molecules,[7,8] although this assumption is at variance with some experimental facts.[9,10]

The statistical–mechanical theory of Bearman and Kirkwood[11] and the irreversible thermodynamic formalism[12] also led to Darken's equation for a certain class of solutions where the radial distribution function is assumed to be independent of composition ("regular" solutions).

Three binary systems of simple, nonpolar, organic compounds were chosen to test these models accurately, namely, n-hexane + toluene, toluene + carbon tetrachloride, and n-hexane + carbon tetrachloride.[5] The components in these systems do not associate or form complexes. The molecules are geometrically simple and of similar size; carbon tetrachloride can be treated as a quasispherical molecule. Mutual diffusion coefficients were available for $CCl_4 + n$-hexane, and isothermal activity data for all three systems. Mutual diffusivities for the other two systems and intradiffusion coefficients, viscosities, and densities for all three systems were measured in this work.

Experimental Section

Diffusion Measurements. The diaphragm cell was used to measure mutual, self-, and intradiffusivities. For the determination of self- and intradiffusivities, a small fraction of tagged molecules, labeled with radioactive isotope, was used.

Two different types of Stokes diaphragm cells[13] were used in this study. One was developed by Dullien and coworkers,[14] and the other by Albright and Mills.[15]

Fine grade diaphragms of 2–5-μ pore size were used to reduce bulk flow to a negligible level.[16,17] Too small a pore size might cause hindrance to the diffusion process.[18] The diaphragm and the other components of the cell were made of Pyrex glass.

It is well known[13,16,17,19] that with this kind of cells the speed of stirring does not influence the measured diffusivity over a wide range of speeds. A rate of 60 rpm was employed in this study.

A prediffusion step has been generally employed to establish a "linear" concentration gradient at the start of the experiment. It has been verified experimentally,[16,20] however, that the solution filled technique, employed in this study both for calibrations and subsequent runs, does not introduce any significant error if the compartment volumes are nearly equal and the diaphragm volume is sufficiently small. The chief advantage of this method lies in saving costly chemicals.

The diffusion equation for the solution filled technique is

$$\bar{D}_{AB} = \frac{1}{\beta_c t} \ln\left\{\frac{\Delta C_A^i}{\Delta C_A^f}(1 - \lambda/6)\right\} \qquad (5)$$

where $\bar{D}_{AB}$ is the integral diffusivity, t is the time of a diffusion run, C_A the concentration of component A, and β_c is the cell constant given by

$$\beta_c = \frac{A}{l}\left\{\frac{1}{V_L} + \frac{1}{V_U}\right\}(1 - \lambda/6) \qquad (6)$$

λ appearing in eq 5 and 6 is

$$\lambda = 2V_D/(V_L + V_U) \qquad (7)$$

where V_D is the volume of the diaphragm; V_L and V_U are, respectively, the volumes of the lower and upper compartments; A is the effective cross-sectional area, and l is the effective diffusion path length in the diaphragm. The superscripts i and f represent initial and final conditions in the diaphragm.

The diaphragm cells were calibrated by following diffusion of an aqueous 0.5 M KCl solution diffusing into pure water. The KCl concentrations were measured gravimetrically by evaporating these solutions to dryness. The organic solutions were analyzed by density measurements for the mutual diffusion runs. The cell constants of the cells employed in this study ranged from 0.07 to 0.35 cm^{-2}. Their values did not change during the duration of this study.

As the overall chemical concentrations remain constant during self- and intradiffusion experiments, in this case eq 5 gives "differential" diffusivities, *i.e.*

$$D_{j^*} = \frac{1}{\beta_c t} \ln\left\{\frac{\Delta C_j^i}{\Delta C_j^f}(1 - \lambda/6)\right\} \qquad j = A, B \quad (8)$$

where D_{j^*} is the self- or intradiffusivity of component j and C_j is the tracer concentration. The lower compartment and the diaphragm were initially filled with a nonradioactive solution, and the upper compartment with a radioactive solution. Therefore, $C_{jL}^i = 0$. When a component mass balance equation is used in conjunction with eq 8, the following equation is obtained

$$D_{j^*} = \frac{1}{\beta_c t} \ln\left\{\frac{(C_{jU}^f/C_{jL}^f)(1 + \lambda'/2) + (V_L/V_U + \lambda'/2)}{C_{jU}^f/C_{jL}^f - 1}\right. \times$$
$$\left.(1 - \lambda/6)\right\} \qquad (9)$$

where $\lambda' = V_D/V_U$.

Equation 9 shows that a knowledge of the absolute values of the radioactivities is not required for the determination of self- and intradiffusivities. Only the concentration ratio $C_{jU}{}^f/C_{jL}{}^f$ needs to be evaluated.

The diffusion time for which analytical errors become minimum is given by Robinson's rule[21]

$$t_{opt} = 1.2/\beta_c \bar{D} \tag{10}$$

Since some cell constants were very low, diffusion runs were also conducted for shorter lengths of time. The maximum increase in expected error was 20% for $t/t_{opt} = 0.6$.

Gordon[22] pointed out that if the ratio t/t_{opt} for calibration and subsequent runs is kept the same, the error remains very close to the minimum value. Therefore, the same t/t_{opt} was used in the calibration and subsequent runs.

All diffusivity measurements were at $25 \pm 0.01°$.

Viscosity. Glass capillary viscometers of the Cannon-Ubbelohde type were used. The method of operation and the equations used for the determination of viscosities have been reported in an earlier publication.[23] The measurements were done at $25 \pm 0.01°$.

Density. A digital precision density meter (purchased from Anton Paar K.G., Model No. DMA 02C 113X) was employed for the determination of densities.[5,14] This electronic instrument utilizes the principle of variation of the natural frequency of a hollow oscillator when filled with different fluids. The following three-parameter equation was used for the determination of densities

$$\rho = \frac{At_s{}^2}{1 - Bt_s{}^2} - C \tag{11}$$

where ρ is the density and t_s is the period of oscillation. The values of parameters A, B, and C were determined at $25°$ from the known density values of five substances. The density values used for the calibration were either measured in this study using pycnometers or taken from the literature. The densities were determined at $25 \pm 0.01°$.

Liquid Scintillation Counter. A liquid scintillation counter was set up in order to analyze the radioactive solutions. The method of analysis was essentially the same as that suggested by Mills and Woolf.[16] The details of the equipment and the procedure have been described in ref 5. The background count rate in these experiments was smaller by 2 to 4 orders of magnitude than the sample count rate. Since the fractional error in the total count rate depends on the total number of counts, an attempt was made to count approximately 10^6 counts so that the errors due to statistical fluctuations were not more than 0.1%. The precision in the ratio of the counts of the upper and lower compartment solutions was estimated to be 0.2% for 10^6 counts. However, in the case of CCl_4 and CCl_4 mixtures, this precision was not obtained because CCl_4 is a severe quencher. A period of 2–3 hr was generally used, and 10^5 counts were obtained for these samples.

In order to determine the ratio of the counts for eq 9 accurately, the upper compartment solution (always more active in these experiments) was diluted with enough carrier solution to equalize the activities in the two solutions. A carrier solution is one which is of the same chemical composition, but is nonradioactive. All the dilutions were carried out gravimetrically.

Materials. All the organic chemicals used in this study were of ACS grade, and were purchased from Fisher Scien-tific Co. In addition, carbon tetrachloride and toluene of spectrophotometric quality were purchased from J. T. Baker Chemical Co. Chromatoquality n-hexane was bought from Matheson Coleman and Bell.

Radiochemicals benzene-1-^{14}C, carbon tetrachloride-^{14}C, and toluene-1-^{14}C were bought from Amersham/Searle Corp. n-Hexane-1-^{14}C was supplied by ICN Chemical & Radioisotope Division.

The stated purity of all these chemicals was minimum 99 mol %. They were used without any further purification.

The KCl supplied by Baker Chemical Co. was 99.9 wt %.

Results

The experimental density and viscosity values of the binary systems measured in this study and those reported earlier[23] were fitted to equations of the form

$$\rho = \sum_{i=0}^{n} A_i w_A{}^i \tag{12}$$

and

$$\eta = \sum_{i=0}^{n} A_i x_A{}^i \tag{13}$$

where w_A and x_A are, respectively, mass and mole fractions of component A. The values of parameters A_i, calculated by the method of least squares, are reported in Tables I and II. The average per cent deviation of the computed values from the experimental ones is also reported in these tables for each system.

The density values for the systems n-hexane + toluene and toluene + CCl_4 were measured by the density meter. All other density values were obtained using pycnometers.

The mutual diffusivities for the systems n-hexane + toluene and toluene + carbon tetrachloride were measured at $25°$ over the complete composition range. The differential diffusion coefficients D_{AB} were calculated from the integral values in the usual way.[5] The raw data may be found also in this reference. The mutual diffusivity data for the system carbon tetrachloride + n-hexane were available.[24,25] The least-squares constants of the equation

$$D_{AB} = \sum_{i=0}^{n} A_i x_A{}^i \tag{14}$$

best fitting the experimental data together with the per cent average deviations are shown in Table III.

The self-diffusion coefficient of benzene was measured eight times at $25°$. All the measured values and their averages are presented in Table IV. The self-diffusion coefficients of n-hexane, carbon tetrachloride, and toluene, determined in this work, are also presented in Table IV.

The intradiffusivities of components A and B in the three binary mixtures are shown in Figures 1–3, together with the mutual diffusivities. The values of the parameters A_i in equations of the form of eq 14, which best fit the experimental intradiffusivity data, are reported in Table V.

Discussion

Experimental Accuracy and Precision. The densities measured with the density meter were found to be reproducible within $\pm 5 \times 10^{-6}$ g/cm³ even for the systems consisting of volatile components. Since the density of the sample is measured in a closed quartz or glass tube, the evaporation problem experienced with the pycnometers

TABLE I: Least-Squares Constants for the Equation[a] $\rho = \Sigma_i A_i w_A{}^i$

System	A_0	A_1	A_2	A_3	A_4	% av deviation
m-Bromotoluene + toluene	0.86194	0.34323	0.08464	0.11246		0.038
n-Hexane + toluene	0.86147	−0.26837	0.07497	−0.01319		0.033
p-Xylene + toluene	0.86225	−0.00629	0.00073			0.003
Carbon disulfide + toluene	0.86239	0.25225	0.07629	0.06496		0.050
CCl₄ + n-hexane[b]	0.65162	0.48486	−0.18986	0.62958		0.410
Toluene + CCl₄	1.58431	−1.31619	1.01326	−0.58862	0.16916	0.008
Mesitylene + CCl₄	$\rho = 1/(0.631412 + 0.54439w_A - 0.013933w_A{}^2)$					0.008

 ^{a} The units of ρ are g cm^{-3}. ^{b} Reference 21.

TABLE II: Least-Squares Constants for the Equation[a] $\eta = \Sigma_i A_i x_A{}^i$

System	A_0	A_1	A_2	A_3	A_4	% av deviation
CBr₄ + benzene	0.6029	1.9026	3.9669	−2.4859		0.05
m-Bromotoluene + toluene	0.5534	0.4391	0.0776	0.1374	−0.0540	0.03
n-Hexane + toluene	0.5530	−0.5592	0.5395	−0.3425	0.1050	0.05
p-Xylene + toluene	0.5538	0.0577	−0.0111	0.0089	−0.0047	0.02
Carbon disulfide + toluene	0.5530	−0.2364	0.0064	0.0415	−0.0059	0.28
p-Xylene + CCl₄	0.9077	−0.3849	0.0691	0.0626	−0.0500	0.10
Mesitylene + CCl₄	0.9074	−0.5615	0.7299	−0.6558	0.2390	0.06
CCl₄ + n-hexane	0.2969	0.1643	0.4177	−0.5107	0.5376	0.31
Carbon disulfide + CCl₄	0.9089	−1.3840	2.4202	−2.8903	1.3069	0.67
Toluene + CCl₄	0.9098	−0.4668	0.1181	−0.0081		0.06
1-Propanol + toluene	0.5545	−0.1273	1.7989	−1.9609	1.6891	0.38
Benzene + toluene	0.5535	0.0059	0.0482	−0.0053		0.04

^{a} Units of η are cP.

TABLE III: Least-Squares Constants for the Equation $D_{AB} = \Sigma_i A_i x_A{}^i$

| System	A_0	A_1	A_2	A_3	% av deviation
n-Hexane(A) + toluene(B)	2.4786	−0.6466	2.3070	0.1963	0.11
Toluene(A) + CCl₄(B)	1.4794	0.2345	0.9421	−0.5129	0.22
CCl₄(A) + n-hexane(B)[b]	3.8663	−3.2599	1.1059	−0.2445	0.30

^{a} Units of D_{AB} are 10^{-5} cm²/sec. ^{b} Using the data of Bidlack and Anderson.[25]

TABLE IV: Self-Diffusivities of Benzene, n-Hexane, CCl₄, and Toluene (10^{-5} cm²/sec) at 25°

Cell no.	Benzene	n-Hexane	CCl₄	Toluene
1	2.208	4.223	1.283	2.293
2	2.200	4.205	1.291	2.261[b]
3	2.173[a]	4.193	1.300	2.287
4	2.214[a]			
5	2.202			
6	2.205			
7	2.210			
8	2.203			
Av value	2.204	4.208	1.291	2.290

^{a} This value was ignored because the cell with which this value was determined (cell No. 5 "old") was later found to be malfunctioning. ^{b} These values were ignored because they were obtained with the top plug left open. Evaporation was found to take place.

was not encountered here. The accuracy of the density meter is subject to the accuracy of the densities of the standard liquids used for calibration. Three highly accurate density values are required since there are three unknowns in the density meter equation, eq 11. Very accurate density values were not available except for water. In order to minimize errors due to uncertainty in the densities of the standard liquids, five substances, as mentioned earlier, were chosen for calibration.
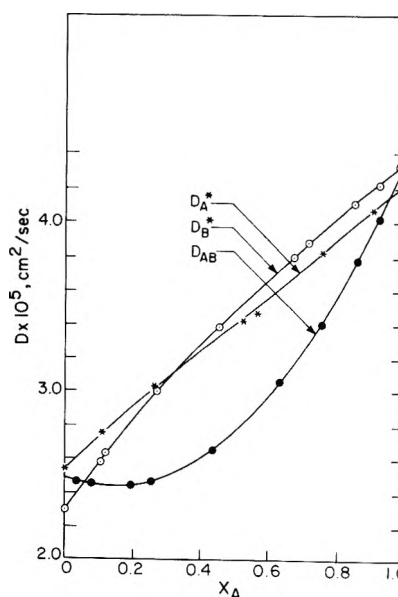
Figure 1. Mutual and intradiffusion coefficients *vs.* mole fraction ($t = 25°$) for n-hexane(A) + toluene(B).

The reproducibility of the viscosities both of pure components and mixtures was found to be better than 0.1% in most cases. Details of this work may be found in ref 23.

TABLE V: Least-Squares Constants for the Equation[a] $D_j^* = \Sigma_i A_i x_A{}^i$, $j = A, B$

| | n-Hexane(A) + toluene(B) | | Toluene(A) + CCl$_4$(B) | | CCl$_4$(A) + n-hexane(B) | |
	D_A*	D_B*	D_A*	D_B*	D_A*	D_B*
A_0	2.530$_7$	2.290$_2$	1.469$_7$	1.295$_5$	3.931$_0$	4.220$_5$
A_1	1.868$_6$	2.859$_3$	0.297$_7$	0.609$_2$	−2.626$_0$	−4.039$_8$
A_2	−0.491$_0$	−1.219$_4$	0.747$_7$	0.347$_9$	−0.392$_1$	2.677$_3$
A_3	0.309$_5$	0.4136	−0.223$_6$	0.100$_2$	0.371$_4$	−1.426$_9$
% av deviation	0.26	0.33	0.44	0.48	0.67	0.91

[a] Units of D_j* are 10^{-5} cm^2/sec.

TABLE VI: Limiting Diffusion Coefficients (10^{-5} cm^2/sec)

System	$D_{AB}{}^0$	$D_{AB}{}^\infty$	D_A*^0	D_A*^∞	D_B*^∞	D_B*^0
Toluene(A) + CCl$_4$(B)	1.479	2.143	1.470	2.290	1.291	2.152
CCl$_4$(A) + n-hexane(B)	3.866	1.468	3.931	1.291	4.208	1.431
n-Hexane(A) + toluene(B)	2.479	4.335	2.531	4.208	2.290	4.344
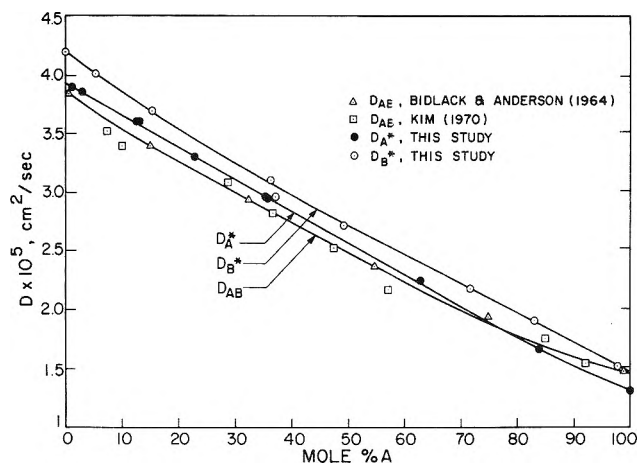
Figure 2. Mutual and Intradiffusion coefficients vs. mole fraction ($t = 25°$) for CCl$_4$(A) + n-hexane(B).

By repetitive measurements of the self-diffusion coefficient of benzene, the experimental precision was found to be ±0.3% (cf. Table IV). The mean value of 2.204 × 10^{-5} cm^2/sec of the self-diffusivity of benzene is in good agreement with Mills' value of 2.207 × 10^{-5},[26] Harris and Dunlop's 2.210 × 10^{-5},[20] and Eppstein and Albright's 2.19 ± 0.005,[27] all obtained by the diaphragm cell technique, and with Ertl and Dullien's value of 2.21 × 10^{-5},[28] determined by the nmr technique.

The self-diffusivity of n-hexane was found to be 4.208 × 10^{-5} cm^2/sec. Shieh and Lyons[29] reported 4.131 ± 0.047, Albright and Aoyagi,[30] 4.105, and Dunlop and coworkers[20] 4.263 × 10^{-5} for the self-diffusion of n-hexane. The value obtained in this study falls about 1% below that of Dunlop, but is higher than those of Shieh and Lyons and of Albright and Aoyagi by about 2%. Douglass and McCall,[31] using the spin-echo method, obtained 4.21 × 10^{-5} cm^2/sec.

The self-diffusivity value of carbon tetrachloride, 1.291 × 10^{-5} cm^2/sec, as obtained here, agrees very well with a value of 1.296 obtained by Collings and Mills.[32] The level of precision for carbon tetrachloride measurements is poorer than that for benzene and n-hexane because the strong quenching in carbon tetrachloride solutions reduces the counts drastically. It should be noted that Collings and Mills[32] also reported increased uncertainty (±0.4%) in their CCl$_4$ measurements.

The average value of the self-diffusivity of toluene has been found to be 2.290 × 10^{-5} cm^2/sec in this study. The
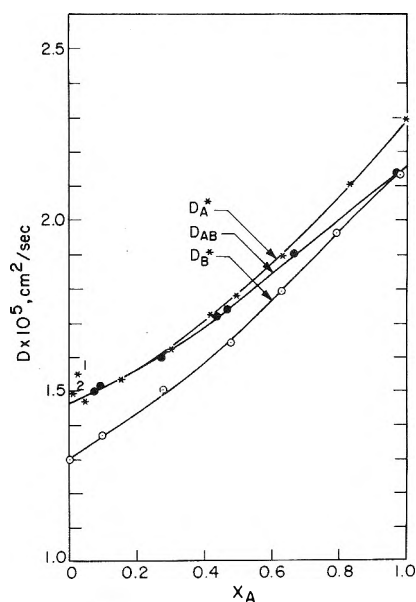

Figure 3. Mutual and intradiffusion coefficients vs. mole fraction ($t = 25°$) for toluene(A) + CCl$_4$(B).

only published value with which our value can be compared is due to Kamal and McLaughlin,[33] who obtained 2.23 × 10^{-5} cm^2/sec. Their value falls about 3% below our value. The reason for this discrepancy is unknown.

The reproducibility of the intradiffusivity measurements is about ±0.5% for those systems containing carbon tetrachloride as a component. Point 1 in Figure 3 for intradiffusivity of toluene in mixture with carbon tetrachloride at 2.853 mol % toluene is quite unreliable because of low counting due to high CCl$_4$ concentration. Point 2 in the same figure was obtained with a much higher specific activity of the sample. The reproducibility of the intradiffusivities of the system n-hexane + toluene was found to be better (see Figure 1 and Table V).

The mutual diffusivity data determined in this study lie on smooth curves (see also Table III). Hammond and Stokes[34] also measured the mutual diffusivities for the system toluene + CCl$_4$, but only in the dilute CCl$_4$ region. Their values are in good agreement with the values obtained in this study.

Limiting Diffusion Coefficients and the Isotope Effect. The values of D_A*^∞ and D_B*^∞ reported in Table VI are the self-diffusion coefficients of A and B, respectively. D_A*^0

and $D_{AB}{}^0$ are, respectively, the limiting intradiffusion and mutual diffusion coefficients when the concentration of A is infinitely small and $D_{B*}{}^0$ and $D_{AB}{}^\infty$ are the limiting diffusion values at the other end, that is, when the concentration of B is infinitely small. The limiting diffusion coefficients were calculated from the polynomial equations best fitting the experimental data, using the constants listed in Tables III and V.

It is important to note that the extrapolated values are usually not very accurate since there is a factor of uncertainty involved in the extrapolations. Different values may be extrapolated with different equations all of which fit the data equally well.[35] For instance, Bidlack and Anderson[25] reported for the system CCl_4 + n-hexane $D_{AB}{}^\infty$ = 1.49 × 10^{-5} cm^2/sec compared with the value of 1.47 × 10^{-5} obtained by eq 14, which represents their data with an average deviation of 0.3%. Recently Ratcliff and Lusis[36] have reported the value 1.41 ± 0.04 × 10^{-5} cm^2/sec for $D_{AB}{}^\infty$.

According to most theories of diffusion, the limiting mutual diffusion coefficient and the corresponding limiting intradiffusion coefficients should be identical. It has always been assumed in these theories that the isotopically labeled and the stable molecules are diffusionally identical. The validity of this assumption is still a controversial point.

Inspection of Table VI shows that for the system toluene + CCl_4, the limiting intradiffusion coefficients of toluene and CCl_4 are equal to the corresponding limiting mutual diffusion coefficients, within the experimental error. In the system n-hexane + toluene, however, while the limiting intradiffusion coefficient and mutual diffusion coefficient of toluene agree, the other limiting intradiffusion coefficient is about 2% larger than the corresponding mutual diffusion value. Similar differences were also found for both components in the system CCl_4 + n-hexane.

If the isotope effect were present, the limiting intradiffusivity should be lower than the corresponding mutual diffusivity.[30] The data in Table VI show that in two out of the three instances when significant differences were found the value of the intradiffusivity is the higher one of the two. Therefore, the observed discrepancies are not likely to be caused by isotope effects, but are probably due to the magnification of experimental errors in the extrapolation process.

More accurate data are required for both intra and mutual diffusivities in order to establish the existence of mass effect.

Activity Corrected Diffusivities. The activity coefficients γ_i were calculated from isothermal vapor–liquid equilibrium data in the literature. For the system n-hexane + toluene, Funk and Prausnitz[37] expressed the experimental data by the three-parameter Redlich–Kister equation

$$\frac{\bar{G}^E}{RT} = x_A x_B \{A + B(x_A - x_B) + C(x_A - x_B)^2\} \quad (15)$$

where $\bar{G}^E$ is the molal excess free energy.

The activity coefficients are related to the excess free energy by

$$\ln \gamma_A = \frac{1}{RT} \left[\frac{\partial G^E}{\partial N_A} \right]_{T, P, N_B} \quad (16)$$

where G^E is the total free energy, and N_A and N_B are the number of moles of A and B, respectively.

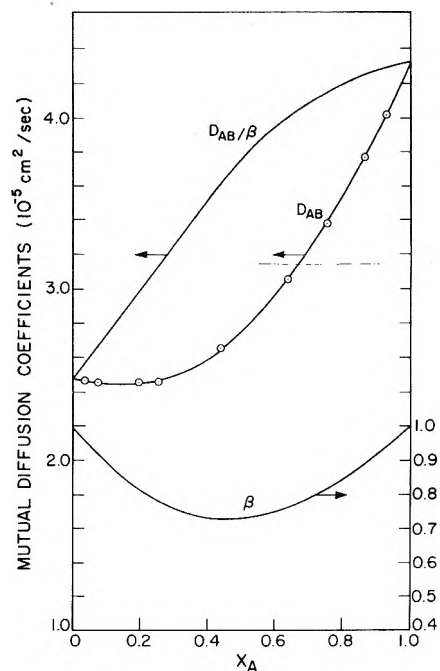Elementary calculation[5] gives the result

Figure 4. Experimental and activity corrected diffusivities for n-hexane(A) + toluene(B): ⊙, experimental D_{AB} values.

$$\beta = 1 - x_A x_B \{2A + 6B(x_A - x_B) + 10C(x_A{}^2 + x_B{}^2 - 2.8x_A x_B)\} \quad (17)$$

The activity coefficients of component A for the system toluene + carbon tetrachloride were represented by Wang[38] as follows

$$\ln \gamma_A = x_B{}^2 \{A + B(x_B - 3x_A) + C(x_B - x_A)(x_B - 5x_A)\} \quad (18)$$

Therefore

$$\beta = 1 - x_A x_B \{2A + 6B(x_B - x_A) + 10C(1 - 4.8x_A x_B)\} \quad (19)$$

For the system carbon tetrachloride + n-hexane, the equation used by Bidlack and Anderson[25] was employed

$$\beta = 1 - 2kx_A x_B \quad (20)$$

The activity corrected and the uncorrected diffusivities, together with the β values have been plotted *vs.* mole fractions for the three systems in Figures 4–6.

It is apparent from these diagrams that the deviation from linearity of the diffusivity *vs.* mole fraction curves increases with the increasing nonideality of the systems as measured by the deviation of β from unity. The nonideality increases in this order: toluene + CCl_4, CCl_4 + n-hexane, and n-hexane + toluene. For all three systems, the diffusivities show negative deviations with respect to straight line behavior, and the β values are less than unity. The activity corrected diffusivities, however, tend to have at least some positive deviations from linearity.

Test of the Darken and the Hartley-Crank Equation. The mutual diffusivities predicted by Darken's equation, eq 1, along with the experimental values for the three systems, are plotted in Figures 7–9. The maximum deviation of this equation is about 4% for the nearly ideal systems toluene + carbon tetrachloride and CCl + n-hexane, but it is 8% for n-hexane + toluene.
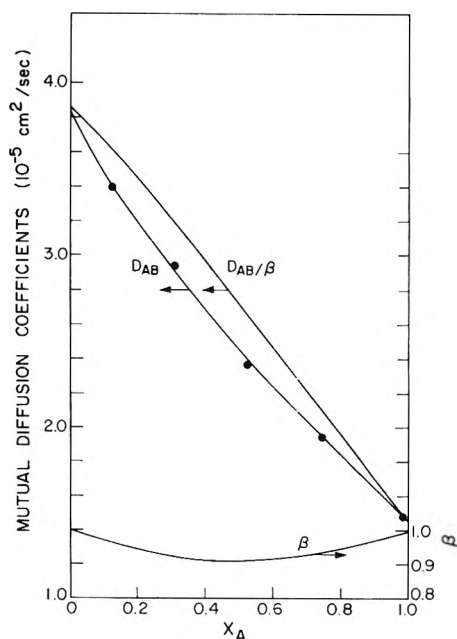
Figure 5. Experimental and activity corrected diffusivities for $CCl_4(A)$ + n-hexane(B): ●, D_{AB} values taken from Bidlack and Anderson.[25]
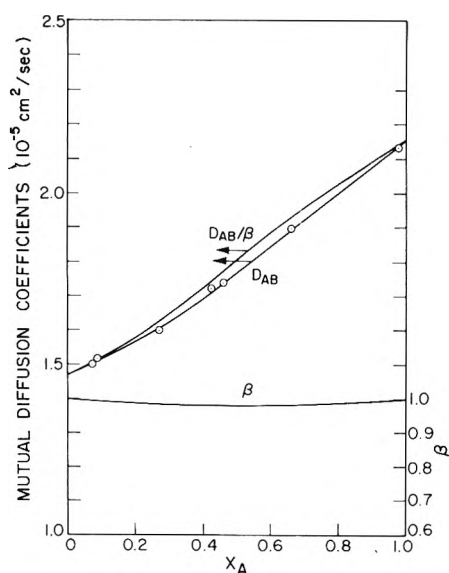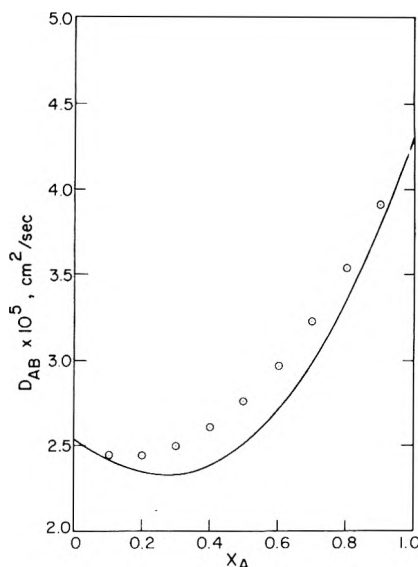

Figure 7. Test of Darken's equation for n-hexane(A) + toluene(B): (—) Darken's equation; ⊙, experimental values.
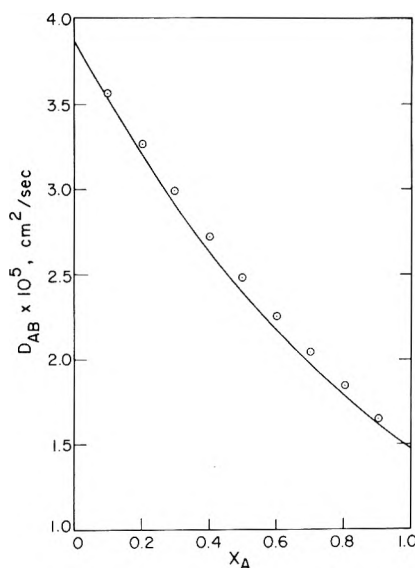

Figure 6. Experimental and activity corrected diffusivities for toluene(A) + $CCl_4(B)$: ⊙, experimental D_{AB} values.

Figure 8. Test of Darken's equation for $CCl_4(A)$ + n-hexane(B): (—) Darken's equation; ⊙, experimental values.

Shieh and Lyons[29] reported that the maximum deviation of the Darken equation from the experimental data is 2.3% for the system n-hexane + n-dodecane at 25°. Even less deviation was reported for the system n-octane + n-dodecane at this temperature.[39] Similarly, the diffusivities of the system benzene + diphenyl,[40] and those of heptane + cetane[41] follow Darken's equation satisfactorily. However, the diffusivities of the system benzene + carbon tetrachloride measured by Hardt, et al.,[42] are not in agreement with this equation.

Therefore it appears that Darken's equation is satisfactory only for mixtures of structurally closely similar species, as it breaks down for some simple nonpolar systems.

The Hartley–Crank equation, eq 3, has been found to be superior to Darken's equation for the systems benzene +

diphenyl studied by Mills[40] and for n-octane + n-dodecane studied by Van Geet and Adamson.[39] However. for the systems studied here this equation was found no better than Darken's equation. Partial molal volumes $\bar{V}_A$ and $\bar{V}_B$ were calculated by the method of Ellerton, et al.[43]

The Carman–Stein form of the Hartley–Crank equation, eq 4, may be tested by plotting the group $D_{A3}\eta/\beta$ against mole fractions. If the friction factors σ_A and σ_B remain constant with composition, then, according to this equation, the group $D_{AB}\eta/\beta$ should be a linear function of mole fraction for isothermal diffusion. The Bearman–Kirkwood theory and Eyring's theory of diffusion also lead to a linear dependence of this group for "regular solutions."

The groups $D_{AB}\eta$ and $D_{AB}\eta/\beta$ were plotted in Figure 10 for all three systems. It can be seen from these plots that neither of these groups is a linear function of the mole fraction for any of the three systems. The group $D_{AB}\eta/\beta$ always departs less from linearity than $D_{AB}\eta$ for the same system.

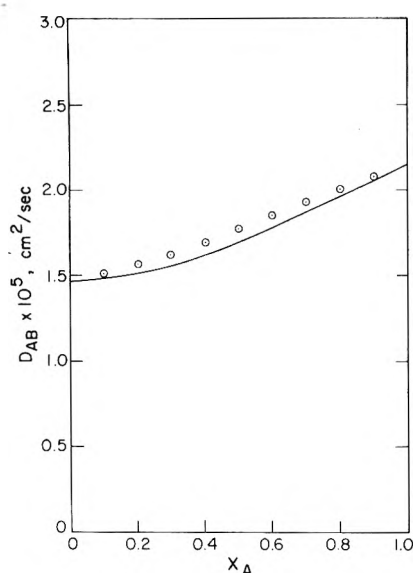Much more pronounced deviations from linearity of the

Figure 9. Test of Darken's equation for toluene(A) + CCl₄(B): (—) Darken's equation; ⊙, experimental values.
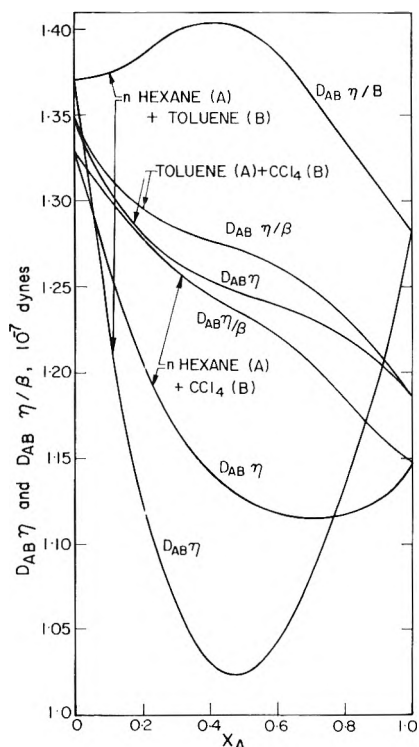

Figure 10. Test of linearity of the groups $D_{AB}\eta$ and $D_{AB}\eta/\beta$.

group $D_{AB}\eta/\beta$ were observed for the highly nonideal systems acetone + CCl₄, acetone + benzene, and acetone + chloroform.[8]

The present results suggest that the Hartley–Crank equation fails already for systems consisting of mixtures of nonpolar molecules of similar size. It certainly does not seem justified to draw any conclusion regarding the nature of the kinetic units on the basis of applicability of the Hartley–Crank or the Darken equation.

Test of Constancy of $D_{i*}\eta$. The Bearman–Kirkwood theory provides an expression for viscosity.[44] Bearman[11] showed that the product $D_{i*}\eta$ should be independent of composition for "regular solutions."
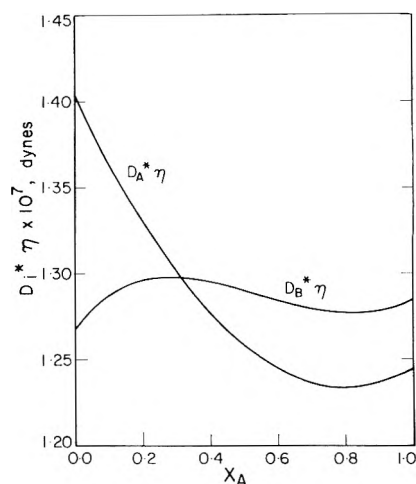
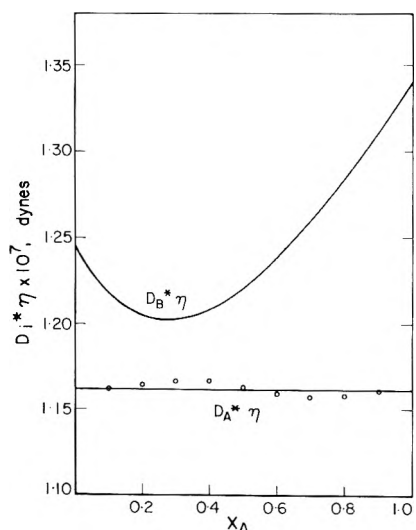Figure 11. Test of constancy of the group $D_i \cdot \eta$ for *n*-hexane(A) + toluene(B).

Figure 12. Test of constancy of the group $D_i \cdot \eta$ for CCl₄(A) + *n*-hexane(B).

The values of the products $D_{i*}\eta$ were calculated from the experimental data for each component in the three binary systems. The results are presented in Figures 11–13. These plots reveal that the product $D_{i*}\eta$ does depend on composition, however, for a given system, its change is much less for one component than the other in all three systems. Always the component with lower diffusivities shows less variation. This also happens to be the component that deviates less from the spherical molecular shape. In particular, $D_{i*}\eta$ for carbon tetrachloride in both systems departs only slightly from constancy (see Figures 12 and 13).

Significant variations of this product were also observed for the systems benzene + carbon tetrachloride and cyclohexane + carbon tetrachloride.[45] The CCl₄ products again showed less variation.

According to Bearman's definition of "regular solutions" the radial distribution functions are independent of composition. The three systems investigated here conform to this type of solution to varying degrees of approximation. It appears that complete conformance may require that the solution be perfectly ideal, rather than just "regular."

Test of Vignes' and Cullinan's Equations. According to these authors[46,47] the activity corrected diffusivities are, for
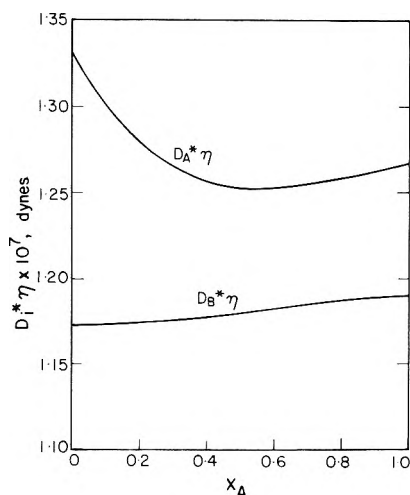
Figure 13. Test of constancy of the group $D_i \cdot \eta$ for toluene(A) + CCl$_4$(B).

"nonassociating" nonideal systems, exponential functions of mole fractions. That is

$$\frac{D_{AB}}{\beta} = (D_{AB}{}^0)^{x_B}(D_{AB}{}^\infty)^{x_A} \tag{21}$$

where $D_{AB}{}^0$ and $D_{AB}{}^\infty$ are the limiting mutual diffusion coefficients. It was found in the present work that this equation is obeyed only by the system toluene + carbon tetrachloride (maximum error $\simeq 1\%$). For the other two systems the calculated values were significantly lower than the experimental data (maximum error $\simeq 13\%$ for both systems).

Leffler and Cullinan[48] obtained the equation

$$\frac{D_{AB}\eta}{\beta} = (D_{AB}{}^0\eta_B)^{x_B}(D_{AB}{}^\infty\eta_A)^{x_A} \tag{22}$$

which was found to agree more closely with the experimental data than eq 21. Maximum error for both nearly ideal systems toluene + carbon tetrachloride and carbon tetrachloride + n-hexane was about 2%. For the much less ideal system n-hexane + toluene, it was about 6%.

Conclusions

The equations of Darken, Hartley and Crank, Carman and Stein, Bearman, Vignes, and Leffler and Cullinan have been tested with accurate data on the systems n-hexane + toluene, carbon tetrachloride + n-hexane, and toluene + carbon tetrachloride. Significant differences between the measured data and the predictions have been found in every system, but the deviations were usually small for the two systems containing carbon tetrachloride as a compo-

nent. On the basis of the present results it appears that these equations are valid only for ideal solutions.

References and Notes

(1) WNRE, Atomic Energy of Canada, Pinawa, Manitoba, Canada.
(2) R. K. Ghai, H. Ertl, and F. A. L. Dullien, *AIChE J.*, **19**, 881 (1973).
(3) L. S. Darken, *Trans. Amer. Inst. Mining, Met. Eng.*, **175**, 184 (1948).
(4) G. S. Hartley and J. Crank, *Trans. Faraday Soc.*, **45**, 801 (1949).
(5) R. K. Ghai, Ph.D. Thesis, University of Waterloo, 1973.
(6) P. C. Carman and L. H. Stein, *Trans. Faraday Soc.*, **52**, 619 (1956).
(7) P. C. Carman, *J. Phys. Chem.*, **71**, 2565 (1967).
(8) D. K. Anderson, J. R. Hall, and A. L. Babb, *J. Phys. Chem.*, **62**, 404 (1958).
(9) F. A. L. Dullien and G. H. Shroff, *J. Phys. Chem.*, **76**, 2463 (1972).
(10) F. A. L. Dullien, *Trans. Faraday Soc.*, **59**, 856 (1963).
(11) R. J. Bearman, *J. Phys. Chem.*, **65**, 1961 (1961).
(12) R. W. Laity, *J. Phys. Chem.*, **63**, 80 (1959).
(13) R. H. Stokes, *J. Amer. Chem. Soc.*, **72**, 763, 2243 (1950).
(14) G. D. Wedlake and F. A. L. Dullien, *J. Chem. Eng. Data*, in press.
(15) J. G. Albright and R. Mills, *J. Phys. Chem.*, **69**, 3120 (1965).
(16) R. Mills and L. A. Woolf, "The Diaphragm Cell," DRU Report RRI, Australian National University Press, Canberra, Australia, 1968.
(17) F. A. L. Dullien and L. W. She, *Can. J. Chem. Eng.*, **39**, 242 (1961).
(18) R. E. Beck and J. S. Schultz, *Science*, **170**, 1302 (1970).
(19) R. L. Robinson, Ph.D. Thesis, Oklahoma State University, 1964.
(20) K. R. Harris, C. K. N. Pua, and P. J. Dunlop, *J. Phys. Chem.*, **74**, 3518 (1970).
(21) R. L. Robinson, W. C. Edmister, and F. A. L. Dullien, *J. Phys. Chem.*, **69**, 258 (1965).
(22) A. R. Gordon, *Ann. N. Y. Acad. Sci.*, **46**, 285 (1945).
(23) R. K. Ghai and F. A. L. Dullien, *Can. J. Chem. Eng.*, **49**, 260 (1971).
(24) J. D. Kim, M.A.Sc. Thesis, University of Waterloo, 1970.
(25) D. L. Bidlack and D. K. Anderson, *J. Phys. Chem.*, **68**, 3790 (1964).
(26) R. Mills, *Trans. Faraday Soc.*, **67**, 1654 (1971).
(27) L. B. Eppstein and J. G. Albright, *J. Phys. Chem.*, **75**, 1315 (1971).
(28) H. Ertl and F. A. L. Dullien, *AIChE J.*, **19**, 1215 (1973).
(29) J. C. Shieh and P. A. Lyons, *J. Phys. Chem.*, **73**, 3258 (1969).
(30) K. Aoyagi and J. G. Albright, *J. Phys. Chem.*, **76**, 2572 (1972).
(31) D. C. Douglass and D. W. McCall, *J. Phys. Chem.*, **62**, 1102 (1958).
(32) A. F. Collings and R. Mills, *Trans. Faraday Soc.*, **66**, 2761 (1970).
(33) I. Kamal and E. McLaughlin, *Proc. Symp. Thermophys. Prop., 4th 1968*, 278 (1968).
(34) B. R. Hammond and R. L. Stokes, *Trans. Faraday Soc.*, **51**, 1641 (1955).
(35) F. A. L. Dullien, *Ind. Eng. Chem., Fundam.*, **10**, 41 (1971).
(36) G. A. Ratcliff and M. A. Lusis, *Ind. Eng. Chem., Fundam.*, **10**, 474 (1971).
(37) E. W. Funk and J. M. Prausnitz, *Ind. Eng. Chem.*, **62**, No. 9, 8 (1970).
(38) J. L. H. Wang, L. Boublikova, and B. C.-Y. Lu, *J. Appl. Chem.*, **20**, 172 (1970).
(39) A. L. Van Geet and A. W. Adamson, *J. Phys. Chem.*, **68**, 238 (1964).
(40) R. Mills, *J. Phys. Chem.*, **67**, 600 (1963).
(41) L. Miller and P. C. Carman, *Trans. Faraday Soc.*, **58**, 1529 (1962).
(42) A. P. Hardt, D. K. Anderson, R. Rathbun, B. W. Mar, and A. L. Babb, *J. Phys. Chem.*, **63**, 2059 (1959).
(43) H. D. Ellerton, G. Reinfelds, D. F. Mulcahy, and P. J. Dunlop, *J. Phys. Chem.*, **68**, 398 (1964).
(44) R. J. Bearman and P. F. Jones, *J. Chem. Phys.*, **33**, 1432 (1960).
(45) J. K. Horrocks and E. McLaughlin, *Trans. Faraday Soc.*, **58**, 1357 (1962).
(46) A. Vignes, *Ind. Eng. Chem., Fundam.*, **5**, 189 (1966).
(47) H. T. Cullinan, Jr., *Ind. Eng. Chem., Fundam.*, **5**, 281 (1966).
(48) J. Leffler and H. T. Cullinan, Jr., *Ind. Eng. Chem., Fundam.*, **9**, 84 (1970).

Cation Exchange Diffusion Experiments[1]

V. Vitagliano,* R. Sartorio, and L. Costantino

Istituto Chimico, Università di Napoli, Naples, Italy (*Received January 22, 1974; Revised Manuscript Received June 21, 1974*)

Some exchange diffusion experiments are presented in ternary electrolyte solutions. The following systems were studied: (1) NaCl–NH$_4$Cl 0.6 equiv/l. at 15, 25, and 35°; (2) sodium polyacrylate–ammonium polyacrylate 0.6 equiv/l. at 15 and 25°. In both cases the exchange diffusion coefficients were computed from the distribution of the concentration inside the boundary. The experimental results are briefly discussed.

It is well known that free diffusion boundaries between solutions of more than two components may develop gravitational instability, even if the upper solution has a lower density than the bottom one. Such instability is due to the growing of liquid layers with reverse density inside the boundary.[2-4] In general, gravitational instability favors the appearance of convective motions that may rapidly destroy the diffusion boundary.

In a recent paper[5] some of us have shown that when the gravitational instability grows at the upper and lower border of the diffusion boundary the appearance of convective motions along the diffusion cell walls promotes an apparent overstabilization of the boundary which spreads with a velocity corresponding to an apparent diffusion coefficient two to three orders of magnitude smaller than the true one.

We present here some further experiments on a ternary system in agreement with our previous finding. Furthermore the boundary behavior when the gravitational instability grows at its center is shown. The following system was studied: sodium chloride–ammonium chloride–water (average total salt concentration 0.6 equiv/l.) at 15, 25, and 35°.

The quite different slope of isodensity and isorefractive index curves of this system allowed us to make also some exchange diffusion experiments (Figure 1) visualizing two extremum points on the total salt concentration inside the boundary. Diffusion coefficients were computed from the Rayleigh fringe patterns obtained in the exchange diffusion experiments. The experimental results are briefly discussed.

Some data are also given for a similar system: sodium polyacrylate–ammonium polyacrylate–water (average total salt concentration 0.6 equiv/l.) at 15 and 25°.

Experimental Section

Material. NaCl was reagent grade. NH$_4$Cl solutions were prepared by neutralization of a titrated NH$_4$OH solution with HCl and dilution to the desired concentration. Redistilled water was used. Polyacrylic acid (HPA) was prepared by polymerization of acrylic acid as described elsewhere.[6] A fraction of viscosimetric molecular weight M_v = 100,000 was used. Sodium and ammonium polyacrylate solutions were prepared by 97.4% neutralization of the stock HPA solution with the proper hydroxide and dilution to the desired concentration.

Densities of NaCl and NH$_4$Cl aqueous solutions at 25° are given by the following expressions obtained as a best fitting of literature data

$$d_{NaCl} = 0.99707 + 0.040975c - 1.1294 \times 10^{-3}c^2 +$$
$$1.0222 \times 10^{-4}c^3 - 4.67 \times 10^{-6}c^4 \pm$$
$$0.00005 \quad (c < 5 \ M)^7 \quad (1)$$

$$d_{NH_4Cl} = 0.99707 + 0.01732c - 0.00250c^2 +$$
$$0.00080c^3 \pm 4 \times 10^{-6} \ (c < 0.8 \ M)^8 \quad (2)$$

By assuming volume additivity in the range of total salt concentration $C_{NaCl} + C_{NH_4Cl}$ = 0.6 equiv/l., isodensity lines as shown in Figure 1 are obtained.

Refractive Index Data at λ 546.1 nm (Hg green line). For water at 25°, n = 1.33405,[9] corresponding to a Rayleigh fringe number J_0 = 61070

$$J = (a/\lambda)\Delta n = 2.500 \Delta n/5.461 \times 10^{-5} =$$
$$4.578 \times 10^4 \Delta n \quad (3)$$

where a is the diffusion (2.500 cm) or interference cell thickness. The refractive index of NaCl aqueous solutions were computed by integration of the J_m data of some available diffusion measurements at various temperatures.[10,11] At 25°

$$J = J_0 + 470c - 21.2c^2 \quad (c < 0.7 \ \text{equiv/l.}) \quad (4a)$$

$$n = 1.33405 + 0.01858c - 0.00040c^2 \quad (4b)$$

The J data at 0.6 equiv/l. and different temperatures are collected in Table I.

For the NH$_4$Cl aqueous solutions, a critical analysis of the refractive index dispersion given in literature[12] suggests a linear relationship between refractive index and concentration, up to 3 equiv/l. On the basis of the total refractive index difference between 0.6 M NaCl and 0.6 M NH$_4$Cl, as measured in exchange diffusion experiments, the following expression was obtained at 25°

$$J = J_0 + 475.2c \quad (5a)$$

$$n = 1.33405 + 0.01038c \quad (5b)$$

Some refractive index measurements were also made at 25° with a Rayleigh interferometric refractometer in order to determine the refractive index dependence on the substitution of Na$^+$ with NH$_4^+$ in their 0.6 N chloride and polyacrylate solutions. A graph of the results is given in Figure 2; a good linear dependence was found for the system NaCl–NH$_4$Cl, no linearity was found for the polyacrylate system.

Figure 1 is a graph showing the isodensity lines and the

TABLE I: Exchange Diffusion Data for the System NaCl–NH₄Cl (0.6 equiv/l.)[a]

Temp, °C	J_1^{0} [b]	J_m	D_{11} [c]	D_{22} [c]	D_1^{0} [d]	D_2^{0} [e]
15	281.2	6.15	1.158 ± 0.007	1.411 ± 0.007	1.130	
25	274.4	10.71	1.487 ± 0.014	1.798 ± 0.016	1.475	1.872
35	268.8	14.46	1.912 ± 0.028	2.253 ± 0.034	1.860	

[a] Diffusion coefficients are in $cm^2 sec^{-1} \times 10^5$; index 1 is for NaCl and index 2 for NH₄Cl. [b] J_1^{0} values used in eq 8–10 (see eq 4) obtained by integration of the J_m data of some previous diffusion measurements on NaCl aqueous solutions at various temperatures;[10,11] the 15° value is from graphical interpolation. In any case the D_{ii} data are not very sensitive to changes on the J^0 values, depending mainly on the difference: $J_m = J_2^0 - J_1^0$. [c] Exchange diffusion coefficients for sodium and ammonium and mean square errors. [d] Free diffusion coefficients of NaCl in aqueous solution,[10,11] the value at 15° was interpolated. [e] Free diffusion coefficient of NH₄Cl in aqueous solution.[21]
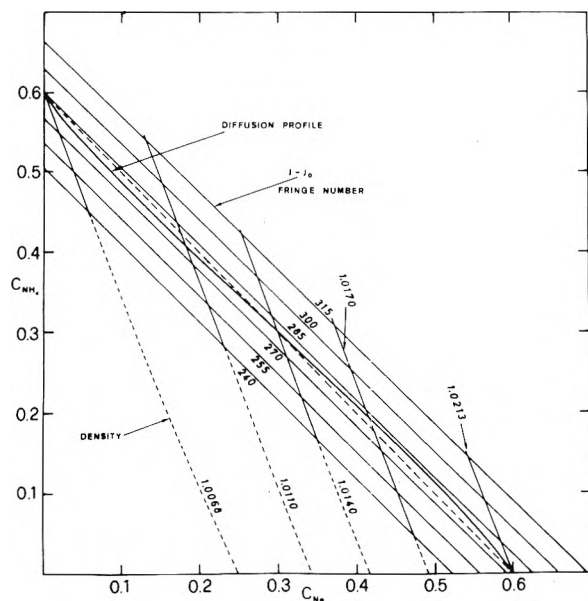
Figure 1. Graph of densities and refractive indexes for the system NaCl–NH₄Cl–H₂O at 25°. The refractive index curves are given in terms of Rayleigh fringe numbers for the diffusion cell (eq 3). The exchange diffusion concentration profile, as obtained from eq 8, is also shown.
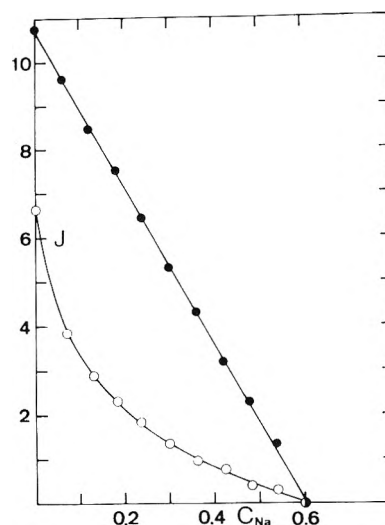

Figure 2. Refractive index difference on interchanging Na⁺ with NH₄⁺ ions in their salt solutions at 25°: ●, (Na, NH₄)Cl 0.6 equiv/l.; O, (Na, NH₄)PA 0.6 equiv/l. The refractive index is given for the Hg green light (λ 5461 Å) in terms of Rayleigh fringe number for the diffusion cell (eq 3).

isorefractive index lines (in term of Rayleigh fringes) for the system NaCl–NH₄Cl–water at 25° in the concentration range of diffusion experiments.

Diffusion. The technique employed was that of free diffusion from an initially sharp boundary between two solutions of different composition, the spreading of the boundary with time was followed with the aid of the astigmatic lens technique,[13,14] and with the aid of Rayleigh interference fringes[15,16] a 2.500-cm cell with a comparison channel was used.[16]

Exchange diffusion runs were started by stratifying, with the syphoning technique, an ammonium salt solution over a sodium salt solution at the same equivalent concentration (0.6 equiv/l.). Figure 3B shows a picture of a Rayleigh pattern obtained for the system NaCl–NH₄Cl at 25°.

Two runs were also taken with the upper and lower solution compositions being along the 1.0140 density line (NaCl and NH₄Cl 0.3 equiv/l., see Figure 1C and 1D), with solutions having the compositions shown in Table II. Solutions of run C have refractive index values reversed with respect to density, as in the exchange diffusion experiments. In free diffusion experiments gravitational instabilities grow at the upper and lower borders of the boundary; according to our previous finding,[5] convective motions appearing along the cell walls favor a washing of the upper and lower

borders of the boundary and promote an apparent overstabilization of the boundary which spreads at a much lower velocity than expected from simple brownian diffusion. A peculiar shape of the refractive index gradient curves[5] with two maxima can be observed (Figure 4C). Solutions of the run D have refractive index and density differences of the same sign; in free diffusion experiment a gravitational instability with reverse density layers grows at the center of the boundary. This fact promotes a circular convective motion within the boundary which spreads at a higher velocity than expected from simple brownian diffusion. This can be seen in Figure 4D where the blurring of the refractive index gradient curve at the center of the boundary indicates the existence of some turbulence.

It is interesting to note that in both cases the boundaries are stable in time and the gravitational instability is not sufficient to destroy them.

Treatment of Experimental Data

Diffusion in a ternary system is described by the generalized Fick equations which include four coefficients

$$\frac{\partial c_i}{\partial t} = \sum_k D_{ik} \frac{\partial^2 c_k}{\partial x^2} \qquad (i = 1, 2) \qquad (6)$$

By assuming that the D_{ik}'s are constant through the boundary, eq 6 can be integrated in the case of free diffusion. A general solution of eq 6 was given by Fujita and
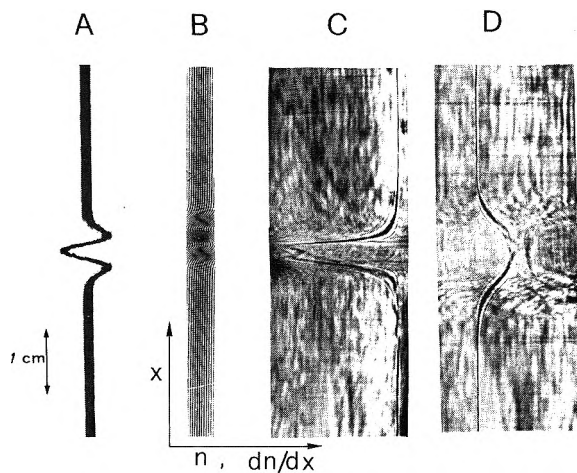
Figure 3. (A) Example of schlieren pattern (Philpot technique using an inclined slit) for NaCl–NH$_4$Cl exchange diffusion at 25°. (B) NaCl–NH$_4$Cl exchange diffusion, Rayleigh fringe pattern, 6 min after stopping syphoning. (C) Ternary diffusion boundary (solutions composition in the text) with gravitational instabilities at the upper and lower borders of the boundary, boundary overstabilized by convective washing (time 72 min). (D) Ternary diffusion boundary (solutions composition in the text) with gravitational instability and convective motions at its center (time 30 min). (C and D, Philpot technique using a phase plate.)

Figure 4. NaCl–NH$_4$Cl at 25°, t = 10 min. Experimental and computed J values (through eq 8): D_{11} = 1.474 × 10^{-5} and D_{22} = 1.782 × 10^{-5} cm^2 sec^{-1}; ϵ_J = 0.076; A = 0.097.

Gosting.[17] Furthermore, by assuming a linear dependence of the refractive index on concentration through the boundary, the Fujita and Gosting equation (ref 17, eq 38 and 39) can be written in terms of Rayleigh fringe number J

$$J = (J_m/2) + (K_2^+ - K_1^+)\Phi(y\sqrt{\sigma_+}) + (K_2^- - K_1^-)\Phi(y\sqrt{\sigma_-}) + A \quad (7)$$

where $J = a(n - n_0)/\lambda$ is proportional to $(c_{total} - c_0)$,[18,19] n_0 being the refractive index of sodium salt solution at concentration c_0 to which the fringe number $J = 0$ was given. J_m is the total number of fringes going from the sodium to ammonium solution. The following boundary conditions have been used

$$l = 0, \quad x > 0, \quad c_1 = 0 \text{ and } c_2 = c_2^0$$
$$x < 0, \quad c_1 = c_1^0 \text{ and } c_2 =$$
$$t > 0, \quad \lim_{x^- \to +\infty} c_1 = 0, \quad \lim_{x^- \to -\infty} c_1 = c_1^0$$
$$\lim_{x^- \to +\infty} c_2 = c_2^0, \quad \lim_{x^- \to -\infty} c_2 = 0$$

in all cases $c_1^0 = c_2^0 = 0.6$ equiv/l. Index 1 refers to sodium and index 2 to ammonium.

If we assume that the cross coefficients D_{12} and D_{21} are zero, eq 7 reduces to

$$J = \frac{J_m}{2} + \frac{J_2^0}{\sqrt{4\pi D_{22}l}} \int_0^x \exp\left[-\frac{x^2}{4D_{22}l}\right] dx - \frac{J_1^0}{\sqrt{4\pi D_{11}l}} \int_0^x \exp\left[-\frac{x^2}{4D_{11}l}\right] dx + A^{18} \quad (8)$$

The experimental behavior of $J = f(x)$ is obtained from the Rayleigh fringe patterns (see Figure 3B), an example of this function is given in Figure 4.

Differentiating eq 8 the following expressions are obtained: (a) for the slope at $x = 0$

$$\left[\frac{dJ}{dx}\right]_0 = \frac{1}{\sqrt{4\pi t}}\left[\frac{J_2^0}{\sqrt{D_{22}}} - \frac{J_1^0}{\sqrt{D_{11}}}\right] \quad (9)$$
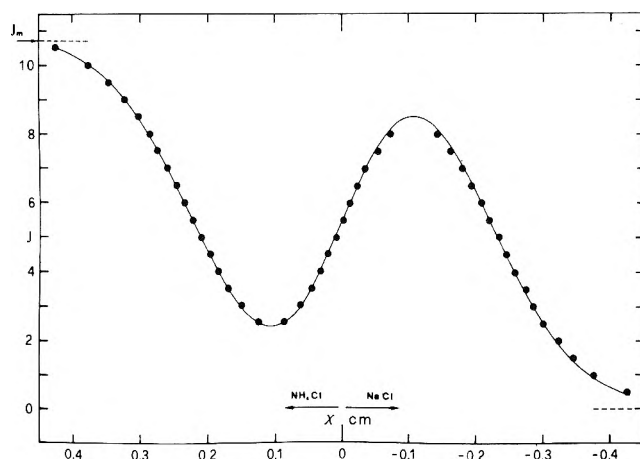
and (b) for the distance Δx between the maximum and the minimum of the J function

$$(\Delta x)^2 = \frac{16D_{11}D_{22}}{D_{22} - D_{11}}t \ \ln\left(\frac{J_1^0\sqrt{D_{22}}}{J_2^0\sqrt{D_{11}}}\right) \quad (10)$$

Equation 10 also gives the condition for the existence of a maximum and a minimum in the function $J = f(x)$.

Equations 9 and 10 can be easily solved by numerical methods to give the diffusion coefficients D_{11} and D_{22}. If D_{12} and D_{21} are different from zero it is still possible, at least in principle, to obtain them by a least-squares method. A steepest descent technique could be used, starting from the D_{ik} values given by solving eq 9 and 10, to change their values in order to find the best agreement between the experimental J's and those computed through eq 7.

Discussion

The NaCl–NH$_4$Cl System. Three runs were performed at 15, 25, and 35°; the use of eq 9 and 10 allowed obtaining a set of self-consistent diffusion data at each temperature. Figure 5 is a graph of the D_{ii} obtained at 25° plotted vs. 1/t, the extrapolated value at 1/t = 0 gives the diffusion coefficient.[20]

The experimental results are collected in Table I. Figure 4 shows the agreement between the experimental J's and those computed through eq 8 by using the D_{ii} values obtained by solving eq 9 and 10. The mean square error on ΔJ is in general less than 0.1 fringe, the value of the A constant has also been found very small.

From these results we may argue that the interchange diffusion between NaCl and NH$_4$Cl can be well described as the independent diffusion of two solutes.

A comparison can be done with the free diffusion coefficients of NaCl and NH$_4$Cl in water and it is reasonable to compare the data at the same total ionic concentration (0.6 equiv/l.); in fact, although the concentration of Na$^+$ and that of NH$_4^+$ change from 0.6 to 0 through the exchange boundary, the ionic medium is at constant concentration. In Table I, columns 6 and 7, the available data for diffusion in a simple salt solution are given. It can be seen that the NaCl exchange diffusion coefficients are about 3% higher than the corresponding coefficients of free diffusion and the NH$_4$Cl exchange diffusion coefficients are correspondingly about 3% lower.

The agreement between free diffusion and exchange dif-

TABLE II

	C, equiv/l.		*D*, equiv/l.	
	NaCl	NH₄Cl	NaCl	NH₄Cl
Upper solution concentration	0.25	0.42	0.33	0.20
Lower solution concentration	0.35	0.18	0.27	0.40
Average concentration	0.30	0.30	0.30	0.30
$J_{lower} - J_{upper}$		$\simeq -60$		$\simeq +60$

TABLE III: Thermodynamic and Mobility Data at 25° and 0.6 equiv/l. (Mobility in cm² sec⁻¹ × 10⁵)

Salt	$y_{\pm}{}^a$	th.t.[b]	M^c	$t_+{}^d$	$M_-{}^e$	$M_+{}^e$	D^{*f}	$(M)_{exc}{}^g$
NaCl (1)	0.6694	0.9418	1.55	0.37	2.10	1.23	1.30	1.46
NH₄Cl (2)	0.6474	0.8710	2.15	0.49	2.19	2.11	1.87	1.84

[a] Mean ionic activity coefficient on the concentration scale: (1) NaCl aqueous solution from equations given in ref 11; (2) NH₄Cl aqueous solution from the $\gamma_{\pm}$ data of ref 22: $y_{\pm} = 0.99707 m\gamma_{\pm}/c$. A relationship between molality and molarity was obtained by using the densities given by eq 2: $m/c = 1.0053 + 0.0184c + 0.0200c^2 \pm 0.0021$. [b] Thermodynamic factor: $1 + (d \ln y_{\pm}/d \ln c) = c/m[1 + (d \ln \gamma_{\pm}/d \ln m)] = $ th.t. (1) NaCl aqueous solution from ref 11; (2) NH₄Cl aqueous solution,[22] graphical plotting of $\ln \gamma_{\pm}$ vs. $\ln m$. [c] Mobility factor of NaCl and NH₄Cl in aqueous solution: $M = D^0/(\text{th.t.})$. [d] Transport number of Na⁺ [11,23] and NH₄⁺ [24] in their chloride aqueous solution. [e] Single ion mobilities: $M_+ = M/2t_-$, $M_- = M/2t_+$. [f] Sodium[25] and ammonium[26] self-diffusion coefficients in their chloride aqueous solutions. [g] Exchange diffusion mobilities from exchange diffusion coefficients of Table I and thermodynamic factor of eq 11.
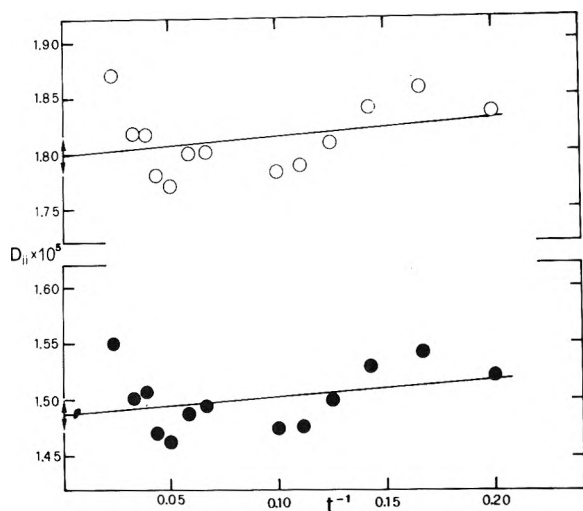

Figure 5. Exchange diffusion run of NaCl–NH₄Cl at 25°: (●) NaCl, D_{11} and (○) NH₄Cl, D_{22} diffusion coefficients plotted as a function of time⁻¹ (min⁻¹).

fusion coefficients and the small reciprocal effect between Na⁺ and NH₄⁺ ions is surprising, but it is probably fortuitous. The diffusion process corresponds, in fact, to an effective transport of Na⁺ and NH₄⁺ ions across the diffusion boundary, but it corresponds only to a redistribution of chloride ions inside the boundary, necessary to keep electroneutrality.

Longsworth[16] showed that for ions of similar mobility the exchange diffusion coefficient is almost equal to the self-diffusion coefficient.

In our case the Na⁺ ion mobility is much lower than that of the NH₄⁺ ion so that a mutual interaction must be expected, with a consequent motion of negative ions inside the boundary, as found experimentally. A change of the activity coefficient of positive ions going from one solution to the other must also affect their exchange mobility. A simple correlation neither with self-diffusion coefficients nor with single ion mobilities can be expected in our case.

It might be worth while to compare ionic mobilities, self-diffusion coefficients and exchange mobilities of NaCl and NH₄Cl. The available data at 25° are collected in Table III.

To give a reasonable value to the thermodynamic factor for the exchange diffusion case the following expression was used (see Table III)

$$1 + \frac{d \ln y_{\pm}}{d \ln c} \simeq 1 + \frac{c\Delta y_{\pm}}{(y)_{av}\Delta c} = 1 \pm \frac{0.0221}{0.6584} =$$
$$1 \pm 0.0336 \quad (11)$$

where $c = 0.6$ equiv/l., $\Delta c = 0.6$, and the mean activity coefficient $y_{\pm}$ was assumed to be that of the salt present in excess, so that the plus sign is given to Na⁺ → NH₄Cl and the minus sign to NH₄⁺ → NaCl solution.

From the data collected in Table III one can see that the self-diffusion coefficient is in both cases between the single ion mobility and the exchange mobility. The acceleration of the Na⁺ ions due to the motion of the faster NH₄⁺ is greater than the slowing down of NH₄⁺ due to Na⁺. This might be due to the contribution of the fast chloride ion the mobility of which is very nearly to that of NH₄⁺; the exchange mobility of NH₄Cl is in fact not very different from the self-diffusion coefficient of NH₄⁺ in NH₄Cl aqueous solution.

The NaPA–NH₄PA System. Table IV collects the results of the exchange diffusion experiments taken on this system. Figure 6 is an example of a graph of $J = f(x)$ with both experimental and computed values.

This system gave less reliable results than the NaCl–NH₄Cl system, and the mean square errors on ΔJ are much higher (see Figure 6). We may attribute this fact to several reasons. (1) The assumption of a linear relationship between refractive index and concentration through the boundary is a poor one, as shown in Figure 2. (2) Some gravitational instability due to development of reverse density layers within the diffusion boundary may have arisen, in this case, as suggested by the much larger difference in the fringe number between maximum and minimum of the $J = f(x)$ curve ($J_{max} - J_{min}$ is about 40, as compared with 7 in the NaCl–NH₄Cl system), this fact is probably responsible for some microconvective motions. These motions were not directly detected during the runs, but some small changes on the J_m values during the runs were observed on reading the photographic plates and they may be attributed to convection. Furthermore the values obtained from diffusion do

TABLE IV: Exchange Diffusion Data for the System NaPA–NH₄PA (0.6 equiv/l.)[a]

Temp, °C	15	25
J_1^{0} [b]	516	504
J_m [c]	-2.50 ± 1.10	-0.62 ± 2.56
D_{11} [d]	2.97 ± 0.04	4.08 ± 0.11
D_{22}	4.12 ± 0.07	5.61 ± 0.20
ϵ_J [e]	1.40	1.53
D_{11} [f]	2.66 ± 0.10	3.66 ± 0.14
D_{12}	0.096 ± 0.022	0.140 ± 0.048
D_{21}	0.096 ± 0.022	0.141 ± 0.049
D_{22}	3.70 ± 0.14	5.04 ± 0.25
ϵ_J [g]	0.95	1.01
D_1^{0} [h]		3.94

[a] Diffusion coefficients are in cm² sec⁻¹ × 10⁶; the data are average data of two sets of ten photographs. [b] The J_1^{0} value at 25° was obtained by integration of some interferometric data (unpublished results), as done for NaCl. The value at 15° was computed by assuming a J_1^{0} increment proportional to that for NaCl. [c] Average experimental J_m; as written in the text the J_m values are not constant during the run and, at 25° they do not even correspond to the refractometric value given in Figure 2. [d] Diffusion coefficients obtained from eq 9 and 10; $D_{12} = D_{21} = 0$. [e] Mean square error of $J = f(x)$ computed with the aid of eq 8. [f] Diffusion coefficients giving the best fit of experimental J's with those computed with eq 7. [g] Mean square error of $J = f(x)$ computed with the aid of eq 7. [h] Free diffusion coefficient of 0.6 N NaPA measured with a Gouy diffusiometer (unpublished results).
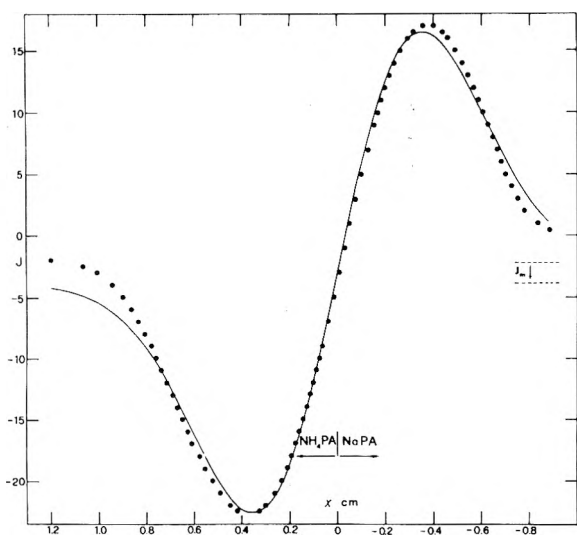

Figure 6. NaPA–NH₄PA at 25°, $t = 248.7$ min. Experimental and computed J values (through eq 7): $J_m = -1.64$; $A = -2.23$; $D_{11} = 0.352 \times 10^{-5}$; $D_{22} = 0.482 \times 10^{-5}$, $D_{12} = D_{21} = 0.016 \times 10^{-5}$ cm² sec⁻¹; $\epsilon_J = 0.99$. By assuming $D_{12} = D_{21} = 0$ and using eq 8; $D_{11} = 0.393 \times 10^{-5}$, $D_{22} = 0.541 \times 10^{-5}$, and $\epsilon_J = 1.63$.

not correspond to the refractometric value shown in Figure 2. The experimental J_m values read on each photograph were used for solving eq 8. (3) In diffusion processes involving polyelectrolyte systems the cross terms D_{ik} must be expected quite different from zero.[6]

An attempt to compute D_{12} and D_{21}, as previously sug-

gested, was done and a better agreement was found between experimental and computed J's, as shown in Table IV and Figure 6. However we do not believe that our experimental arrangement is good for computing cross diffusion terms. We believe that for this purpose it is much better to devise experiments where the non-Gaussian distribution of the concentration gradients inside the boundary is mainly due to the effect of cross terms, as in the experiments conducted by Fujita and Gosting.[17,27]

References and Notes

(1) This research was supported by the Italian CNR.
(2) M. Brakke, *Arch. Biochem. Biophys.*, **55**, 175 (1955).
(3) R. P. Wendt, *J. Phys. Chem.*, **66**, 1740 (1962).
(4) Y. Oishi, *J. Chem. Phys.*, **43**, 1611 (1965).
(5) V. Vitagliano, A. Zagari, R. Sartorio, and M. Corcione, *J. Phys. Chem.*, **76**, 2050 (1972).
(6) V. Vitagliano, R. Laurentino, and L. Costantino, *J. Phys. Chem.*, **73**, 2456 (1969).
(7) "International Critical Tables," Vol. III, Dow Chemical Co., Midland, Mich., p 79.
(8) J. Timmermann, "Physico Chemical Constants of Binary Systems," Vol. 4, Interscience, New York, N.Y., 1960, p 588.
(9) Reference 7, Vol. 7, p 13 Table 2.
(10) V. Vitagliano and P. A. Lyons, *J. Amer. Chem. Soc.*, **78**, 1549 (1956).
(11) V. Vitagliano, *Gazz. Chim. Ital.*, **90**, 1847 (1960).
(12) Reference 8, Vol. 4, p 590.
(13) J. S. Philpot, *Nature (London)*, **141**, 283 (1938).
(14) M. Bier, "Electrophoresis," Academic Press, New York, N.Y., 1959, p 145.
(15) L. G. Longsworth, *J. Amer. Chem. Soc.*, **74**, 4155 (1952).
(16) L. G. Longsworth, *J. Phys. Chem.*, **61**, 244 (1957).
(17) H. Fujita and L. J. Gosting, *J. Amer. Chem. Soc.*, **78**, 1099 (1956).
(18) Both in eq 7 and 8 the Integration constant A is zero if the x origin is set where $|dJ/dx|$ is maximum, according to the boundary conditions. Since the value of the integration constant does not change the shape of the $J = f(x)$ function, A was left as an adjustable parameter for best fitting the experimental data.
(19) In terms of the four diffusion coefficients

$$\Delta = [(D_{22} - D_{11})^2 - 4D_{12}D_{21}]^{1/2}$$

$$K_2^{+} = [(D_{22} - D_{11} + \Delta)J_1^{0} - 2D_{12}J_2^{0}]/4\Delta$$

$$K_1^{-} = -[(D_{22} - D_{11} - \Delta)J_1^{0} - 2D_{12}J_2^{0}]/4\Delta$$

Expressions for K_2^{+} and K_2^{-} are obtained from K_1^{+} and K_1^{-}, respectively, simply by interchanging subscripts 1 and 2 throughout.

$$\sigma_{+} = \frac{1}{2} \frac{(D_{22} + D_{11}) + [(D_{22} - D_{11})^2 + 4D_{12}D_{21}]^{1/2}}{D_{11}D_{22} - D_{12}D_{21}}$$

$$\sigma_{-} = \frac{1}{2} \frac{(D_{22} + D_{11}) - [(D_{22} - D_{11})^2 + 4D_{12}D_{21}]^{1/2}}{D_{11}D_{22} - D_{12}D_{21}}$$

where J_1^{0} and J_2^{0} are the total number of fringes of sodium and ammonium salts with respect to pure water, and $J_m = J_2^{0} - J_1^{0}$. This assumption was found correct for NH₄Cl aqueous solutions (eq 5) and it may also be accepted in the case of cation interchange at constant total concentration. Furthermore

$$y = x/2t^{1/2}$$

and

$$\Phi(q) = (2/\sqrt{\pi})\int_0^{q} e^{-q^2} dq$$

(20) The mean square error on D_{ii} ($\simeq 1\%$) is somehow higher than that generally obtained with Rayleigh or Gouy techniques in single salt solution, but this is not essential for the reliability of our experimental results; furthermore we took a single run at each temperature. Accuracy could certainly be improved if a set of runs were to be executed under the same experimental conditions.
(21) J. R. Hall, B. F. Wishaw, and R. H. Stokes, *J. Amer. Chem. Soc.*, **75**, 1556 (1953).
(22) B. F. Wishaw and R. H. Stokes, *Trans. Faraday Soc.*, **49**, 27 (1953).
(23) R. Caramazza, *Gazz. Chim. Ital.*, **90**, 1839 (1960).
(24) L. G. Longsworth, *J. Amer. Chem. Soc.*, **57**, 1185 (1935).
(25) J. H. Wang and S. Miller, *ibid.*, **74**, 1611 (1952).
(26) K. Tanaka and T. Hashitani, *Trans. Faraday Soc.*, **67**, 2314 (1971).
(27) H. Fujita and L. J. Gosting, *J. Phys. Chem.*, **64**, 1256 (1960).

Extension of the Chromatographic Broadening Method of Measuring Diffusion Coefficients to Liquid Systems. I. Diffusion Coefficients of Some Alkylbenzenes in Chloroform

Eli Grushka* and Edward J. Kikta, Jr.

Department of Chemistry, State University of New York at Buffalo, Buffalo, New York 14214　(Received April 1, 1974)

The chromatographic broadening method of measuring diffusion coefficients, which until recently was used with gaseous mixtures, is shown to be useful for liquid mixtures. In this method, a small amount of solute (component 1) is injected into a flowing stream of a solvent (component 2). From the width of the eluted peak, the diffusion coefficient is measured. The constraints due to the liquid system, as well as possible sources of errors, are discussed. It is shown that with a well-designed injection port, a small-volume detector cell, narrow tubing, and low flow rate, good diffusion data can be easily obtained. Since the method is a dynamic one, the accumulation of the data is rapid, especially if a multiple-injection technique is used. The method was utilized to measure the diffusion coefficients of several alkylbenzenes in chloroform. It was found that as the side chain of the molecule lengthens, the diffusion decreases. The effect of molecular geometry was also investigated by observing the diffusion coefficients of structural isomers. The results seem to indicate that the more branched the molecule is, the faster the diffusion. The ramifications of these findings are discussed.

Binary diffusion in nonelectrolyte liquid mixtures is an important transport phenomenon which plays a major role in many areas of science. Many separation techniques, pollution problems, and chemical reactions, to name but a few, depend to a large extent on some species diffusing in liquid media. There is quite a volume of literature dealing both with theoretical and with experimental aspects of diffusion in liquid systems.

In general, the measurement of binary diffusion coefficients is not trivial and it may take a long time (about 24 hr or so). Different values are often obtained in different laboratories even when using similar measuring techniques. In addition, agreement between theoretical and experimental values are frequently not so close as one might wish. General reviews on diffusion in liquids can be found in many reports.[1-4]

Most methods of measuring diffusion coefficients in liquids are static in nature. Taylor,[5,6] however, indicated that a dynamic method, based on the dispersion of one component in a flowing stream of a second one, can also be used. In the case of gaseous mixtures, such methods have been used, and in particular a method known as "chromatographic broadening technique" (CBT) has been quite successful. Originated in the early 1960's independently by Giddings and Seager[7] and by Boheman and Purnell,[8] the technique was since used by many other workers. Although neither partitioning nor adsorption is needed for diffusion determination, the method was developed using chromatographic equipment and some of its terminology, hence the name CBT. Recently, Grushka and Maynard[9] have shown that high-precision data can indeed be obtained by using chromatographic instrumentation. In liquid systems, however, the chromatographic broadening method has not been utilized with the exception of the recent work by Ouano.[10] He, however, failed to mention the similarity of his experiments to those used in gaseous diffusion measurements. Nonetheless, his paper attempts to measure diffusion coefficients using a flowing system. More recently Pratt, *et*

al.,[11] have measured diffusion of gases in liquids using this method. Balenovic, Myers, and Giddings[12] have used the CBT for obtaining diffusion coefficients in dense gases. In the present paper, we shall further demonstrate the utility of the method by (a) describing a better experimental design and (b) giving some diffusion data for a homologous family and discussing the trends observed.

The problem of solute dispersion in a fully developed laminar flow of a Newtonian liquid was discussed by many scientists, notably Taylor,[5,6] Aris,[13] and Gill and coworkers (see ref 14 and references therein). While most workers were interested in the concentration profile of the dispersed solute, here one is more interested in the broadening of the solute zone as it passes through the column. For straight tubes of circular cross section, it can be shown[9,10,15] that under certain conditions the variance of the solute concentration profile as it exits the column is given by

$$\sigma^2 = \frac{2D_m L}{U} + \frac{R^2 U L}{24 D_m} \tag{1}$$

where D_m is the diffusion coefficient of the solute in the flowing solvent and U is the solvent (or mobile-phase) velocity and is obtained from the column length divided by the time that the solute resided in it. L is the column length, and R is the tube radius. The condition for eq 1 to hold is that $(D_{eff}/UL) \ll 0.1$, where D_{eff} is the effective dispersion coefficient. In chromatographic theories the plate height is defined as

$$H = \sigma^2/L \tag{2}$$

and hence for a solute dispersing in a flowing mobile phase

$$H = \frac{2D_m}{U} + \frac{R^2 U}{24 D_m} \tag{3}$$

This equation can also be obtained from Golay's[16] treatment for open tubular columns with no stationary phase.

The plate height H is related to the peak width, the residence time in the column, and the column length via the relation[17]

$$H = \frac{L W_{1/2}^2}{5.54 t_R^2} \qquad (4)$$

t_R is the residence time of the solute in the column and $W_{1/2}$ is the width at half the solute peak height. This relationship holds true for a gaussian peak only. Equation 3 can be rearranged to give

$$D_m = \frac{U}{4}[H \pm \sqrt{H^2 - R^2/3}] \qquad (5)$$

Since all the parameters on the right-hand side of eq 5 can be obtained experimentally, the diffusion coefficient can be calculated. The various ramifications of eq 5 are discussed elsewhere.[18,19] The physically significant root of eq 5 depends upon the mobile-phase (or solvent) velocity. When the solvent velocity is less than that which minimizes eq 3, the positive root is used. At higher velocities, the negative root is the relevant one. In the case of gaseous mixtures, the positive root is most commonly obtained. In liquid mixtures, or dense gases,[12] however, the velocity that minimizes eq 3 is about 10^{-3} cm/sec and it is thus more advantageous to obtain the negative roots, i.e., use velocities which are greater than 10^{-3} cm/sec. On the other hand, as will be discussed shortly, too fast velocities cannot be usefully employed.

In liquid mixtures, due to the low diffusion coefficients, eq 3 simply reduces to

$$H = \frac{R^2 U}{24 D_m} \left(D_m = \frac{R^2 U}{24 H} \right) \qquad (6)$$

Which is the so-called Taylor diffusion term. It is also equivalent, albeit written differently, to eq 13 or 14 in Ouano's paper[10] or eq 5a in ref 11. Although derived in a somewhat different manner, both Ouano's approach and ours depend upon the condition, mentioned previously, of $(D_{eff}/UL) \ll 0.1$. Alternatively, the condition

$$\frac{R^2 U}{D_m L} \lll 1 \quad \left(\frac{R^2 u}{D_m L} \longrightarrow 0 \right)$$

must be obeyed. Equation 6, then, can be utilized in measuring diffusion coefficients. This technique is facilitated by the use of modern liquid chromatography equipment.

Experimental Section

Apparatus. The chromatographic system consisted of the following. The diffusion tubing was 9189.36 cm long having an internal radius of 0.0390 ± 0.0001 cm. The solvent delivery system was made of about 4570 cm long × 1/4 in. o.d. copper tubing reservoir connected via a pressure regulator to an N_2 tank. This system provided at least 6 hr (at 100 cm^3/hr) of pulseless and bubble-free flow of the mobile phase. Usually after delivering 360 cm^3 of the mobile phase, the reservoir was depressurized and refilled. This procedure and system produced a good flow rate stability (after a short equilibration period) and a steady detector base line.

The detector used was a LDC uv monitor operating at 254 nm. The detector cell volume was 8 μl. A Hewlett-Packard Model 7123A chart recorder was used to display the detector signal. The injection port was made from a Swagelock T union as shown in Figure 1. The two needle guides, made of Teflon, insured on column injections.

The coiled column was in a water bath controlled by a Fisher proportional temperature controller. The bath temperature was kept at 23 ± 0.01 or 23.9 ± 0.01°.

Reagents. Four different solvents (or mobile phases) were used: $CHCl_3$, n-hexane, n-heptane, and cyclohexane. These were either Spectro or reagent grade bought from various vendors. The chloroform was passed through a column of silica gel and molecular sieve to remove traces of ethanol. The solutes used were all reagent grade.

Procedure. With the solvent (mobile phase) flowing through the diffusion tubing 10 μl of solute was injected into the flowing stream using a Glenco syringe. It is important that the tip of the syringe be inserted directly into the column inlet. The flow of the mobile phase was controlled with the gas regulator connected to the N_2 tank. Mobile-phase flow rates were changed by changing the N_2 pressure at the reservoir head. For most measurements duplicate runs were made. In one case, at very slow velocity, several injections of the solute were made all during one run. Care was taken to make sure that the time interval between injections was greater than the time it took the whole peak width to elute. In this manner, the solute's peaks do not overlap and more than one measurement can be made.

The diffusion coefficients were calculated using eq 4 and 6. To get H, peak width at half-height was measured.

Results and Discussion

Possible Sources of Errors. Before describing the measured data, possible sources of errors should be discussed. To begin with, most of the mathematical models described here apply strictly to straight tubes. The experimental work described was done in a coiled tubing. Thus, the effect of the secondary flow phenomenon must be taken into account, since it might lead to an incorrect diffusion coefficient. Many papers cover the secondary flow phenomenon and its effects on solute dispersion in laminar flow.[20-23] It is generally recognized that secondary flow, due to lateral mass transport, can narrow the zone. Tijssen and Wittebrood[22] maintained that in liquid systems coiling an empty tubing, such as in capillary work, might diminish zone spreading even at low flow rate. Nunge, Lin, and Gill[23] developed an expression, however, showing that at low Reynolds numbers and for Schmidt numbers exceeding 0.124, the curvature of the tubing may actually increase zone dispersion over and above the which would have occurred in a straight tube. No experimental data are given, however, to substantiate either Tijssen's[22] or Gill's[23] theoretical work. Ouano in his work[10] considered the problem of coiled tubing and secondary flow and he maintained that if the coil diameter to tube diameter ratio is large and if the flow is slow, the effects are minimal. Pratt, et al.,[11] also indicated that secondary flow can be neglected at low flow. The present result seem to agree with this conclusion.

The length of the injection plug is rather important since it can contribute excessively to the zone broadening. In order to see whether our injection technique was suitable, the following examination was made. Ten-microliter samples of 25, 50, and 100 μg of benzene in $CHCl_3$ were injected into the chloroform mobile phase. At velocities of less than 1 cm/sec, the D_m values for benzene in chloroform, irrespective of concentration, were constant within experimental errors. At high velocity (around 2.9 cm/sec) the diffusion coefficient decreased by about 6% in going from 100 to 25 μg/10 μl of solution. The amounts injected were also varied from 1 to 10 μl with no noticeable effect on the resul-
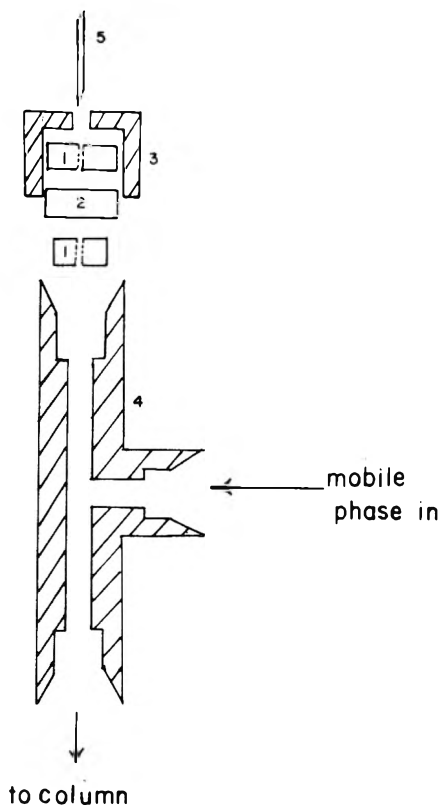
Figure 1. Injection head utilized in this study: (1) Teflon guide, (2) septum, (3) $\frac{1}{16}$-in. brass Swagelok nut, (4) $\frac{1}{16}$-in. brass Swagelok T union, (5) syringe needle.

Figure 2. Diffusion coefficients $\times 10^5$ vs. mobile-phase velocity: (1) $\triangle$, toluene in $CHCl_3$, $23°$, $D_m = 2.01 \times 16^{-5}$ cm^2/sec; (2) $\square$, isobutylbenzene in $CHCl_3$, $23°$, $D_m = 1.51 \times 10^{-5}$ cm^2/sec; (3) O, toluene in cyclohexane, $23.90°$, $D_m = 1.63 \times 10^{-5}$ cm^2/sec.

tant D_m values. Therefore 10-μl amounts of the solute were injected throughout the rest of the study so as to minimize detection problems. This amount occupied about 2 cm of the tubing (about 2.2×10^{-4}th fraction of the total length). As mentioned, one could conceivably inject a large volume whose variance would contribute excessively to the variance due to the actual dispersion process. This, of course, is undesirable and the volume injected should be much smaller than the volume the solute occupies upon leaving the column. This constraint, unfortunately, means that most likely only diffusion coefficients at infinite diffusion can be measured by this method using the formulation given here.

The actual injection process is also of prime importance. Initially, our injection port consisted of the Swagelock T union without the needle guides. Frequently, the needle did not penetrate the column itself. The dead volume in the T union acted as a mixing chamber which caused an increase in the measured H value. The calculated diffusion coefficients of test solutes were lower than those reported in the literature. However, once the needle guides were inserted as shown in Figure 1, this problem essentially disappeared.

Another potential problem spot lies in the detector. If the total peak width, in volume units, is smaller than that of the detector cell, the latter can act as a mixing chamber. In this study, the detector cell had a volume of 8 μl. Typical peak widths were between about 2.5 and 4.5 cm^3 depending upon the velocity of the solvent. Hence the detector did not introduce any measurable error to the data.

Velocity Dependence of the Diffusion Coefficient. As mentioned previously, the negative root of eq 5 is most suitable for diffusion measurements in liquid systems. The diffusion coefficient should, of course, be independent of
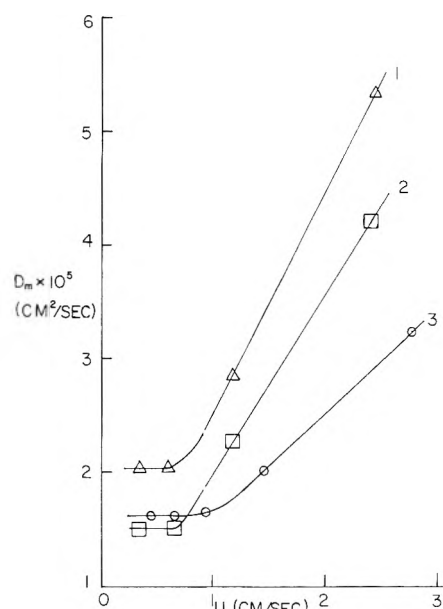
the solvent velocity. However, at high velocities the measured diffusion coefficients of all solutes were somewhat larger than expected. For example, in the case of toluene diffusing in the cyclohexane mobile phase, increasing the velocity about sixfold from 0.447 to 2.78 cm/sec doubled D_m from 1.63×10^{-5} to 3.24×10^{-5} cm^2/sec. At low velocities the solute peaks were symmetrical. The symmetry was determined by bisecting the peak and measuring, at the intersection of peak tangents and the base line, the width of the halves. When expressed as the difference between the two widths divided by the average of the two, the symmetry was usually about 0.002. A better measurement of the peak symmetry can be obtained by using the third central statistical moment. The present system does not have digitization capabilities and the moments could not be easily measured. For the purpose of this study the above method of determining the symmetry is sufficient. In future studies a system such as the one described previously by us[9] will be utilized. At high velocities the tops of concentration profiles were flattened, although at the base line symmetry was still observed. The zone dispersion can be affected by (a) the velocity profile of the mobile phase, (b) secondary flow effects and (c) asymmetric axial velocity distribution in coiled (or curved) tubes.[23] Of these, only secondary flow can logically decrease the solute-zone dispersion or cause the apparent (or measured) D_m values to be higher than they should be. It might be expected that at high flow rates, the solute molecules would not reside long enough in the column to "sample" all the streamlines of the velocity profile, thus producing a more dispersed zone. Stated differently, at high velocity the previously mentioned condition of R^2U/D_mL is not obeyed. Indeed, we found that the dispersivity, as measured by H, increased with the velocity. This was true for all solutes. The important quantity, on the other hand, is the ratio U/H (see eq 6). H does not increase faster than the velocity. At this point, since the change in D_m is not large, we tend to speculate that at high velocities both flow profile and secondary flow phenomena influence simultaneously the dispersion of the zone, largely

TABLE I: Diffusion of Benzene and Toluene in Various Solvents at 23.90°

Solute	Solvent	$10^5 D_m$, cm^2/sec	Lit. value[a]
Benzene	n-Hexane	4.39	4.747[24]
Benzene	n-Heptane	3.53	3.915[25] 3.871[24]
Benzene	Cyclohexane	1.86	1.896[25]
Benzene	Chloroform	2.10	2.30[26] 2.01[10]
Toluene	n-Hexane	4.06	4.21[2]
Toluene	n-Heptane	3.24	3.72[2]
Toluene	Cyclohexane	1.63	1.569[25]
Toluene	Chloroform	2.01	

[a] Superscript numbers indicate references. All the literature values, except that for benzene–chloroform, were obtained at 25°. The benzene–chloroform D_m was at 23°.

TABLE II: Diffusion Coefficients of Alkylbenzenes in CHCl$_3$ at 23°

Compd	$10^5 D_m$, cm^2/sec	Other reported data[a]
Benzene	2.10	2.30[26] 2.01[10]
Toluene	2.01	
Ethylbenzene	1.80	1.59[10]
Propylbenzene	1.58	
Isopropylbenzene	1.66	
Butylbenzene	1.46	
Isobutylbenzene	1.51	
sec-Butylbenzene	1.54	
tert-Butylbenzene	1.58	

[a] Superscript numbers indicate references.

negating the effect of one another. However, since the measured diffusion coefficients seem to increase somewhat at high velocities for all solutes and solvents studied here, it can be assumed that secondary flow effects predominate slightly at such velocities.

Figure 2 shows graphically the effect of the velocity on the observed diffusion coefficient for several compounds. As the velocity decreases, the diffusion coefficient becomes constant, independent of the velocity. It is interesting, perhaps, to compare Figure 2 with a similar plot from Ouano's work (Figure 3 of ref 10). He plotted the observed D value vs. Q/DL where Q is the flow rate. His plots were straight lines, having positive slopes, which he extrapolated to zero flow to obtain the actual diffusion coefficient of the mixtures which he studied.

Diffusion Data. To assess the reliability of the technique, some data were obtained and compared with some available values in the literature.[2,10,24–26] The results are shown in Table I. Considering the magnitude of the diffusion coefficients and the fact that most of the literature data were obtained at 25°, and agreement is very good. Indeed, considering the fact that most of the referenced values in Table I were obtained with a diaphragm cell, the agreement is most satisfying.

The precision of our system is estimated to be at about 1%. We usually ran duplicates of each data point and the results agreed to within 1%. The agreement in the retention time was usually less that 1% which indicated good flow control. Undoubtedly part of the error in the precision was due to manual data handling. As mentioned previously, we wanted to see if at low velocity we could make several injections of the solute at the appropriate time intervals. The results were excellent. For example, at $U = 0.612$ cm/sec, toluene was injected four times into the diffusion tubing. The measured diffusion coefficients in chloroform were

2.12 × 10^{-5} cm^2/sec for the first injection and 2.05 × 10^{-5} cm^2/sec for the other three. The first injection was done before the system reached flow equilibrium and hence the slightly high D_m value. The agreement in the rest of the values demonstrates that indeed repeated injections can be made, with the net result of being able to collect a large amount of data in a relatively short time period (6–8 hr). Moreover, several different solutes can be introduced sequentially to the diffusion apparatus.

In the near future, the precision, and presumably the accuracy, of the method will be substantially improved by computerization, in similarity to our work with gaseous systems.[9]

Table II shows diffusion coefficients of several alkylbenzenes in chloroform at 23°. Most of the data in Table II are, to our knowledge, new. The data for benzene agree well with other reported values. The review of Johnson and Babb[1] shows a value of 2.51 × 10^{-5} at 15°. Our value for ethylbenzene does not agree with that of Ouano.[10] The general trend of the diffusion data is as expected. The larger the solute molecule, the smaller is the diffusion in chloroform. The trend of decreasing diffusion with increasing molecule size is well known. However, few systematic studies have been done in that direction. There have been some attempts[27,28] to utilize Kirkwood's[29,30] models of hydrodynamic fractional force acting on a chain molecule and Doan and Brunet's[31] extension of the theory of corresponding states to correlate the chain length to the diffusion coefficient. These treatments are usually limited to linear alkanes. Part of the difficulty with more complicated molecules lies simply in the lack of systematic studies with such solutes. Hopefully, the data presented here would allow the calculation of hydrodynamic frictional forces and of other potential parameters of such moieties as benzene rings when they are part of the diffusing species.

More interesting, perhaps, is the effect of molecular branching. The larger the degree of branching, the larger is the diffusion coefficient. This is in agreement with branching effects observed in gaseous diffusion coefficients.[9,32] Not much work has been done on the effect of molecular structure on the diffusion. This is somewhat surprising. In 1956, Johnson and Babb[1] essentially indicated that the relationship between molecular size and shape and the diffusion coefficient is not known. They suggested a diffusion coefficient equation of the form

$$D = \psi(RT/N\eta)(1 + \partial \ln \gamma_1/\partial \ln N_1) \quad (7)$$

T is the absolute temperature, R is the gas constant, η is the solvent viscosity, N is Avogadro's number, γ_1 is the activity coefficient of the solute, N_1 is the mole fraction of the solute, and ψ is a parameter which depends on molecular size and shape. The fact that branching seems to increase the diffusion coefficient should be investigated carefully as it can help to elucidate the parameter ψ. Looking at the data, limited as they are, one is tempted to speculate that a shielding mechanism, as suggested by Fuller, Ensley, and Giddings,[33] is operative in liquid mixtures. This speculation should be further investigated since the mechanism of diffusion is different in gases and in liquids. The manifestation of the geometrical structure is extremely important as it can shed light on molecular collision. This phenomenon is now being looked at in greater detail.

Figure 3 is a graphical representation of the data in Table II. The four data points for species with linear side chains (i.e., toluene, ethylbenzene, propylbenzene, and but-
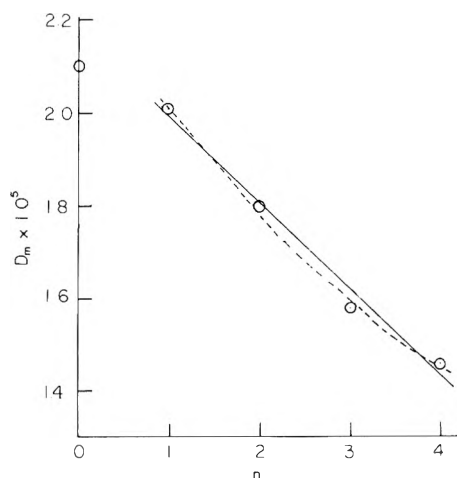
Figure 3. Diffusion coefficients for $C_6H_5(CH_2)_{n-1}CH_3$ vs. n (side chain length): linear fit, $10^5D_m = A + Bn$ where $A = 2.18$ and $B = -0.187$; hyperbolic fit, $10^5D_m = 1/(A + Bn)$ where $A = 0.433$ and $B = 6.4 \times 10^{-2}$. The point at $n = 0$ is for benzene; it is not included in the fit.

ylbenzene) were least-squares fitted to a straight line and to a hyperbolic function. The correlation coefficient of the latter was slightly better (0.995 as compared to 0.985). It is not yet clear, however, if these relationships have any significance.

Conclusions

The dynamic method, or the chromatographic broadening technique, can be utilized to measure with ease the diffusion coefficients of binary solutions. Being a dynamic method, the measurement time can be shortened as compared with static techniques. In this connection, multiple solute injections, at the correct time intervals, allow rapid accumulation of precise (and hopefully accurate) data. This eliminates the need for either simultaneous measurement in several diffusion cells or repeated determination with the same unit in a sequential manner. Moreover, the system described here does not need any calibration such as required when using a diaphragm cell. Actual calculation of the coefficient from the data is rather simple. It can easily be computerized in the manner recently discussed by us[9,32] for the case of gaseous mixtures.

The instrumentation involved is rather simple. In the case of non-uv absorbing species a refractive index detector can be used. The diffusion tubing can be thermostated and

the temperature dependence of D_m can be easily determined. Reid and Sherwood in their text[2] indicated that there is a lack in experimental data concerning this dependence. Since the system described here allows such a study to be made, this topic is now being pursued. In addition, by using a mobile phase made of more than one solvent, mass transport in multicomponent systems can be measured.

The data presented here show that with alkylbenzenes diffusing in chloroform the diffusion coefficient decreases as the alkyl side chain increases. More importantly, in the case of structural isomers, the more branched molecules diffuse more rapidly.

References and Notes

(1) P. A. Johnson and A. L. Babb, *Chem. Rev.*, **56**, 387 (1956).
(2) R. C. Reid and T. K. Sherwood, "The Properties of Gases and Liquids," 2nd ed, McGraw-Hill, New York, N. Y., 1966.
(3) R. K. Ghai, H. Ertl, and F. A. L. Dullien, *AIChE. J.*, **19**, 881 (1973).
(4) R. K. Ghai, H. Ertl, and F. A. L. Dullien, *AIChE J.*, **20**, 1 (1974).
(5) G. Taylor, *Proc. Roy. Soc., Ser. A*, **219**, 186 (1953).
(6) G. Taylor, *Proc. Roy. Soc., Ser. A*, **225**, 473 (1954).
(7) J. C. Giddings and S. L. Seager, *J. Chem. Phys.*, **33**, 1579 (1960).
(8) J. Boheman and H. J. Purnell, *J. Chem. Soc.*, 360 (1961).
(9) E. Grushka and V. R. Maynard, *J. Phys. Chem.*, **77**, 1437 (1973).
(10) A. C. Ouano, *Ind. Eng. Chem., Fundam.*, **11**, 268 (1972).
(11) K. C. Pratt, O. H. Slater, and W. A. Wakehem, *Chem. Eng. Sci.*, **28**, 1901 (1973).
(12) R. Aris, *Proc. Roy. Soc., Ser. A*, **235**, 67 (1956).
(13) Z. Balenovic, M. N. Myers, and J. C. Giddings, *J. Chem. Phys.*, **52**, 915 (1970).
(14) R. Sankarasubrauanian and W. N. Gill, *Proc. Roy. Soc., Ser. A*, **329**, 479 (1972).
(15) O. Levenspiel and W. K. Smith, *Chem. Eng. Sci.*, **6**, 227 (1957).
(16) M. J. E. Golay, "Gas Chromatography," D. H. Desty, Ed., Academic Press, New York, N. Y., 1958.
(17) Derivation of this equation can be found in any standard chromatography text.
(18) J. C. Giddings and S. L. Seager, *Ind. Eng. Chem., Fundam.*, **1**, 277 (1963).
(19) E. Grushka and V. Maynard, *J. Chem. Educ.*, **49**, 565 (1972).
(20) J. A. Koutsky and R. J. Adler, *Can. J. Chem. Eng.*, **43**, 239 1964.
(21) R. Tijssen, *Chromatographia*, **3**, 525 (1970).
(22) R. Tijssen and R. T. Wittebrood, *Chromatographia*, **5**, 286 (1972).
(23) R. J. Nunge, T. S. Lin, and W. N. Gill, *J. Fluid Mech.*, **51**, 363 (1972).
(24) K. R. Harris, C. K. N. Pua, and P. J. Dunlop, *J. Phys. Chem.*, **74**, 3518 (1970).
(25) S. A. Sanni, C. P. D. Fell, and H. P. Hutchinson, *J. Chem. Eng. Data*, **16**, 424 (1971).
(26) J. Timmermans, "Physico-Chemical Constants of Binary Systems," Vol. 1, Interscience, New York, N. Y., 1959.
(27) R. D. Burkhart and J. C. Merrill, *J. Chem. Phys.* **46**, 4985 (1967).
(28) D. V. S. Jain and K. K. Tewari, *Chem. Phys. Lett.*, **10**, 487 (1971).
(29) J. G. Kirkwood, *J. Polym. Sci.*, **12**, 1 (1954).
(30) J. G. Kirkwood and J. Riseman, *J. Chem. Phys.*, **16**, 565 (1948).
(31) M. H. Doan and J. Brunet, *Ind. Eng. Chem., Fundam.*, **11**, 356 (1972).
(32) E. Grushka and P. Schnipelsky, **78**, 1428 (1974).
(33) E. N. Fuller, K. Ensley, and J. C. Giddings, *J. Phys. Chem.*, **73**, 3679 (1969).

Nonequilibrium Thermodynamic Studies of Electrokinetic Effects. V. Onsager's Reciprocity Relations

R. L. Blokhra* and T. C. Singhal

Chemistry Department, Himachal Pradesh University, Simla 171001, India (Received May 10, 1974)

Onsager's reciprocity relations have been verified from studies on electroosmosis and the streaming potential of aqueous methanol, potassium chloride solution in water, and potassium chloride solution in dimethylformamide through a sintered Pyrex glass disk.

The thermodynamic theory of irreversible processes is essentially based on three conditions, viz., (i) linear phenomenological laws, (ii) the validity of Onsager's reciprocity relations, and (iii) phenomenological constants may be treated as constants, of course, in addition to the validity of Gibb's formula for entropy production. In most physical processes the above assumptions are not true in general. Rastogi and coworkers[1-5] and Blokhra and coworkers[6-10] have shown that linear relations between forces and fluxes do not hold beyond a certain magnitude of the force used to generate the flux. These workers have also proved that the phenomenological constants should not be treated as constants because these coefficients vary when the force exceeds a certain magnitude and the above mentioned conditions hold only in a limited region. The purpose of this short note is to test Onsager's reciprocity relations through studies on electroosmosis and the streaming potential of aqueous methanol (25 and 75% by volume), 10^{-5} M KCl solution in conductivity water, and 10^{-6} M KCl solution in dimethylformamide through a sintered Pyrex glass disk.

Experimental Section

Analar grade potassium chloride was used for preparing solutions. Potassium chloride solutions of 10^{-6} and 10^{-5} M were prepared by diluting 0.01 M solutions. Dilution was carried out by using a calibrated buret. Water of specific conductance 10^{-6} ohm^{-1} cm^{-1} was used for making aqueous solutions and aqueous mixtures of methanol. Methyl alcohol used was purified by the method described elsewhere.[11]

The apparatus used and the experimental procedure for studying electroosmosis were similar to those described earlier.[6-10] For streaming potential measurements, a constant pressure head was maintained with a reservoir and the liquid was allowed to flow freely through the Pyrex sintered glass. The pressure difference was measured with a travelling telescope. The streaming potential was measured with an electrometer supplied by the Electronic Corp. of India.

Results and Discussion

According to the thermodynamic theory of irreversible processes, the phenomenological equations for describing the volume flow and current flow in case of electrokinetic effects are written as[12]

$$I = L_{11}\frac{\Delta\phi}{T} + L_{12}\frac{\Delta P}{T} \tag{1}$$

$$J = L_{21}\frac{\Delta\phi}{T} + L_{22}\frac{\Delta P}{T} \tag{2}$$

where the L's are the phenomenological coefficients with $L_{12} = L_{21}$ according to Onsager's theorem. L_{11} is related to resistance while L_{22} is related to the permeability of the liquid. The coefficients L_{12} and L_{21} are the cross-phenomenological coefficients and other symbols have their usual significance.

Now, Onsager's reciprocity relation is

$$L_{21} = L_{12} \tag{3}$$

For verification of (3), evaluation of L_{12} and L_{21} is required and these are evaluated by different methods. The evaluation of L_{12} is carried out through streaming potential measurements. At $I = 0$, (1) becomes

$$(\Delta\phi/\Delta P)_{I=0} = L_{12}/L_{11} \tag{4}$$

Also at $\Delta P = 0$, (1) becomes

$$I = (L_{11}/T)\Delta\phi \tag{5}$$

On comparing (5) with Ohm's law we find that

$$L_{11} = 1/RT \tag{6}$$

where R is the resistance of the electroosmotic cell and T is the temperature in degrees Kelvin. On substituting (6) into (4), we obtain

$$(\Delta\phi/\Delta P)_{I=0} = L_{12}/RT \tag{7}$$

Values of $\Delta\phi$ corresponding to different values of the pressure difference, ΔP, across the disk were measured with an electrometer. The resistance of the system was determined with Toshniwal conductivity bridge. The right-hand side of (7) was estimated from the slope of the straight line plots of $\Delta\phi$ vs. ΔP for different systems and, on substituting the value of R, L_{12}/T was estimated.

The phenomenological coefficient L_{21}/T was estimated from the electroosmosis experiment by the method described by Blokhra, et al.[6] The values of L_{12}/T and L_{21}/T for different systems are given in Table I.

TABLE I: Values of Cross-Phenomenological Coefficients L_{12}/T and L_{21}/T for Different Systems at 25°

System	$(L_{12}/T)10^4$, cm^3 A J^{-1}	$(L_{21}/T)10^4$, cm^3 A J^{-1}
25% methanol	6.90	7.05
75% methanol	8.94	8.88
10^{-6} M KCl in DMF	4.50	4.41
10^{-5} M KCl in H$_2$O	8.38	8.40

Table I shows that L_{12}/T is in excellent agreement with L_{21}/T. This proves that Onsager's reciprocity relations hold for electrokinetic effects in the systems reported here.

References and Notes

(1) R. P. Rastogi, R. L. Blokhra, and R. K. Aggarwal, Trans. Faraday Soc., 60, 1386 (1964).
(2) R. P. Rastogi and R. C. Srivastava, Physica, 27, 265 (1961).
(3) R. P. Rastogi and K. M. Jha, J. Phys. Chem., 70, 1017 (1966).
(4) R. P. Rastogi, K. Singh, and M. L. Srivastava, J. Phys. Chem., 73, 46 (1969).
(5) R. P. Rastogi and K. M. Jha, Trans. Faraday Soc., 62, 585 (1966).
(6) R. L. Blokhra, C. I. Kaul, B. R. Soni, and S. K. Jalota, Electrochim. Acta, 12, 773 (1967).
(7) R. L. Blokhra and T. C. Singhal, J. Electroanal. Chem., 48, 353 (1973).
(8) R. L. Blokhra and T. C. Singhal, Electrochim. Acta, submitted for publication.
(9) R. L. Blokhra and T. C. Singhal, J. Electroanal. Chem., accepted for publication.
(10) R. L. Blokhra and M. L. Parmar, Aust. J. Chem., submitted for publication.
(11) D. D. Perrin, W. L. F. Armarego, and D. R. Perrin, "Purification of Laboratory Chemicals," Pergamon Press, London, 1966, p 349.
(12) I. Prigogine, "Introduction to Thermodynamics of Irreversible Processes," Charles C Thomas, Springfield, Ill., 1955.

COMMUNICATIONS TO THE EDITOR

Intermediate Oxygen Species of Homomolecular Oxygen Exchange and the Oxidation of Carbon Monoxide over Zinc Oxide under Illumination

Sir: In recent years, three forms of adsorbed oxygen species, O^-, O_2^-, and O_3^-, have been detected on various oxides by using esr techniques,[1] and now interests are focussing on the reactivity and/or the selectivity of these species in catalytic oxidation reactions. The higher reactivity of adsorbed O^- compared to O_2^-, in reactions with CO, H_2, O_2, CH_4, C_2H_4, and C_3H_6, has been reported on various oxides such as MgO,[2] ZnO,[3,4] and vanadium oxide and molybdenum oxide supported on silica,[5] but partially oxidized products such as aldehydes and acroleine formed on V_2O_5/SiO_2 seem to be responsible for the reaction of C_3H_6 with O_2^-.[6] A photopromoting effect on the oxygen exchange reaction on ZnO was observed by Barry and Stone,[7] however, the intermediate oxygen species and the mechanism of this simple reaction have not been settled. The oxygen exchange reaction on TiO_2 is also markedly accelerated by illumination,[8] but the adsorbed O_2^- species undergoes little isotopic mixing upon illumination. This result suggests that any mechanism having an O_2^- intermediate is unfavorable, and O_3^- formed with O^- and O_2 is proposed as the most plausible intermediate of the oxygen exchange reaction over illuminated TiO_2. On the other hand, illumination substantially changes the kinetics and the activity of the oxidation of CO on ZnO,[4] and the slow step of the oxidation under illumination has been suggested to be the formation of the O^- species. This communication presents results showing how the oxygen species O_2^-, O^-, and O_3^- are related to the exchange reaction and to the oxidation of carbon monoxide over illuminated ZnO.

A 0.434-g sample of ZnO (Kadox-25 from New Jersey Zinc. Co.) was added to a Pyrex glass reactor and evacuated at ca. 420° for more than 12 hr. The evacuated ZnO was cooled to room temperature *in vacuo* and was allowed to adsorb oxygen. A medium-pressure mercury lamp (Toshiba H-400-P) was used for illumination of the reactor at room temperature. The reactor was shaken during illumination so that the ZnO powder could be exposed to light homogeneously. $^{18}O_2$ (90 atom % oxygen-18) and $^{16}O_2$ were mixed and adsorbed on ZnO at a total pressure of ca. 2 mm for 8.5 hr at room temperature. The ratio of $^{18}O^{16}O/(^{18}O_2 +$

$^{18}O^{16}O)$ did not change after 8.5 hr contact, indicating that no detectable exchange proceeded on ZnO in the dark.

When the catalyst was exposed to illumination, the isotopic exchange of gas-phase oxygen was conspicuously accelerated so that equilibrium was attained within 3 min as shown in Figure 1, in which the broken lines indicate the equilibrium compositions and the solid lines the experimentally observed compositions. After 3 min of illumination, the gas phase was removed by 30 min of evacuation at room temperature, and an isotopic analysis of desorbed oxygen was made by connecting the reactor to a mass spectrometer and heating the reactor. Oxygen desorption having a maximum at around 180° has been assigned to O_2^- by esr.[4] The factor of oxygen-18 in desorbed oxygen is constant throughout the temperature range and the isotopic compositions are apparently far from equilibrium. It is seen, however, that oxygen desorbed at the lower temperatures is closer to isotopic equilibrium than that desorbed at the higher temperatures. This tendency is quite similar to observations on illuminated TiO_2.[8] Such apparent progress of the isotopic equilibration of oxygen desorbed at the lower temperatures could be well explained by a replacement process of O_2^- and gas-phase oxygen which involves no isotopic scramble. $*O_2^- + O_2 \rightleftharpoons *O_2 + O_2^-$. Evidence for such a process was more firmly established by contacting 1 mm of $^{18}O_2$ with $^{16}O_2$ preadsorbed ZnO at room temperature for 5 min in the dark. The analysis of the desorbed oxygen is shown in Figure 2. The desorbed oxygen at the lower temperatures contains more $^{18}O_2$ but the values of $^{18}O^{16}O/(^{18}O_2 + ^{18}O^{16}O)$, a measure of isotopic
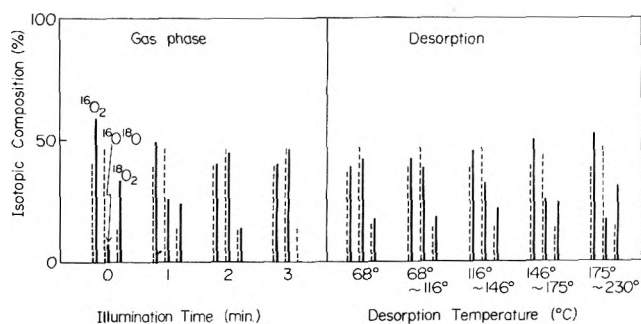

Figure 1. Photocatalytic isotopic mixing of oxygen on ZnO under illumination and the isotopic scramble of adsorbed O_2^- during the exchange reaction. The broken lines are the equilibrium compositions and the solid lines are the observed one.
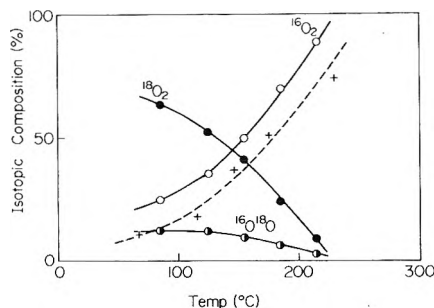
Figure 2. Replacement of adsorbed $^{16}O_2{}^-$ with $^{18}O_2$ from the gas phase in the dark. Crosses are values calculated from Figure 1 by assuming replacement with isotopically equilibrated gas-phase oxygen.
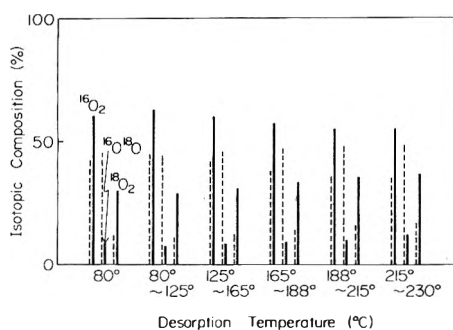

Figure 3. Illumination effect on the isotopic mixing of adsorbed $O_2{}^-$.

scramble, are approximately constant in the whole temperature range, indicating that the replacement of $^{16}O_2{}^-$ and $^{18}O_2$ takes place with no isotopic scramble. If the oxygen equilibrated under illumination is assumed to perturb the composition of adsorbed oxygen with the same trend as that shown in Figure 2, the dotted line on Figure 2 is obtained for $^{16}O_2$ from the data shown in Figure 1. Taking account of the difference of contact time with gas-phase oxygen in the two cases, this parallel change may allow us to conclude that the apparent progress of the isotopic equilibration at lower temperatures results from a replacement process involving oxygen equilibrated by illumination. In order to verify the inactivity of $O_2{}^-$ on the illuminated ZnO, a mixture of $^{18}O_2$ and $^{16}O_2$ was adsorbed at room temperature for 5 hr, the gas phase was then removed by 30 min of evacuation and was exposed to illumination for 3 min. The isotopic composition of oxygen desorbed from the illuminated ZnO is shown in Figure 3, which clearly indicates that $O_2{}^-$ species and neutral adsorbed species if present are inactive in the isotopic exchange reaction under illumination. These results support the conclusion that both the dissociative mechanism, $O_2{}^- \rightleftharpoons 2O^-$, and the associative mechanism, $O_2{}^- + O_2 \rightleftharpoons O_4{}^-$, including the $O_2{}^-$ species are unfavorable for the isotopic exchange reaction over illuminated ZnO.

$O_3{}^-$ species have been directly detected by Tench and Lawson[9] and by Wong and Lunsford[10] over uv irradiated MgO. They found that $O_3{}^-$ on uv irradiated MgO is less active for the isotopic exchange reaction. Kazansky, et al.,[5] however, have suggested that $O_3{}^-$ is the intermediate in the exchange reaction on vanadium oxide supported on silica by reason of the unstability of the $O_3{}^-$ species in this case. The results of the present work suggest that the $O_3{}^-$ species formed by the reaction of O^- with O_2 over illuminated ZnO is the most plausible intermediate in the ex-
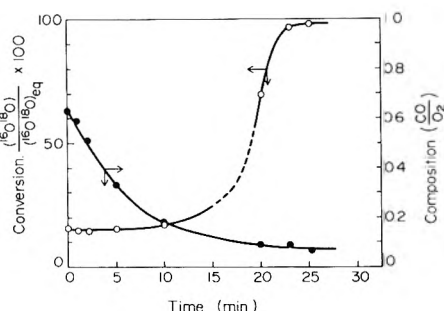
Figure 4. Retardation effect of CO on the oxygen exchange reaction over ZnO under illumination at room temperature.

change reaction, as has been proposed for the reaction on illuminated TiO_2.[8]

On the other hand, it has been found that the formation of O^- on illuminated ZnO is the slow step in the photocatalytic oxidation reaction of carbon monoxide.[4] Accordingly, it is interesting to see how the CO oxidation and oxygen exchange reactions compete over ZnO under illumination. A mixture of CO, $^{18}O_2$, and $^{16}O_2$ at a total pressure of about 6 mm was submitted to the reactor and illumination applied at room temperature. The ratio of CO/O_2 and the isotopic compositions of oxygen were followed by mass spectrometric analysis. As shown in Figure 4, the ratio of CO/O_2 decreases with reaction time under illumination, indicating the oxidation of CO proceeds on ZnO under illumination at room temperature. The exchange reaction of oxygen retarded by the addition of CO is abruptly accelerated when gas-phase CO has been consumed as shown in Figure 4. The sequence of adsorption strength may be in the order of $CO < CO_2$ and $CO < O_2{}^- < O^-$ as inferred from desorption temperatures.[4] The amount of CO_2 adsorbed should increase with illumination time, but appreciable inhibition of CO_2 formation is not observed as a result. This is quite consistent with the results of no retardation of CO_2 formation with time in the photocatalytic oxidation of CO.[4] Accordingly, the inhibiting effect of CO on the oxygen exchange reaction is not caused by the competitive adsorption of CO and oxygen, but by the competitive reaction of CO and O_2 with the common intermediate species of O^-, that is, the formation of $O_3{}^-$ by the reaction of O^- with O_2 is competitively retarded by the reaction of CO with O^-, because the reactivity of CO with O^- is much higher than that of O_2 with O^-.

References and Notes

(1) J. H. Lunsford, *Catal. Rev.*, **8**, 135 (1973).
(2) C. Naccache, *Chem. Phys. Lett.*, **11**, 1323 (1971).
(3) K. M. Sancier, *J. Catal.*, **9**, 331 (1967).
(4) K. Tanaka and G. Blyholder, *J. Phys. Chem.*, **76**, 1807, 3184 (1972); *Chem. Commun.*, **736**, 1343 (1971); K. Tanaka and K. Miyahara, *ibid.*, 877 (1973).
(5) V. A. Shvets and V. B. Kazansky, *J. Catal.*, **25**, 123 (1972); V. B. Kazansky, *et al.*, *Proc. Int. Congr. Catal., 5th*, 104 (1972).
(6) S. Yoshida, T. Matsuzaki, T. Kashiwazaki, K. Mori, and K. Tarama, *Bull. Chem. Soc. Jap.*, **47**, 1564 (1974).
(7) T. I. Barry and F. S. Stone, *Proc. Roy. Soc., Ser. A*, **335**, 124 (1960).
(8) K. Tanaka, *J. Phys. Chem.*, **78**, 555 (1974).
(9) A. J. Tench and T. Lawson, *Chem. Phys. Lett.*, **7**, 457 (1970).
(10) N. B. Wong and J. H. Lunsford, *J. Chem. Phys.*, **56**, 2664 (1972).

Research Institute for Catalysis   **Ken-ichi Tanaka***
Hokkaido University   **Koshiro Miyahara**
Sapporo, Japan 060

An Acoustical Technique for Measuring the Temperature of Maximum Density of Dilute Aqueous Solutions

Sir: The temperature of maximum density, the TMD, is a thermodynamic parameter of an aqueous solution which is unusually sensitive to solute-induced modifications in the structure of water.[1-6] We observe that sound transients produced in aqueous solutions by pulses of microwave energy can be used to measure this parameter rapidly and accurately. These sound transients result directly from thermal expansion of the heated regions of fluid; they have an amplitude proportional to the thermal expansion coefficient, α, and they vanish at the TMD.

To illustrate, suppose that the free surface of a fluid is uniformly irradiated by a pulse of electromagnetic radiation of duration τ and power density I_0. If the surface area of the fluid is sufficiently large to allow a one-dimensional analysis, and if R_0, the depth of penetration of the radiation, is sufficiently small, it can be shown that positive and negative pressure transients, corresponding to the leading and trailing edges of the pulse, will propagate away from the surface where the energy is absorbed. The peak pressure amplitude is given by[7]

$$P_{max} = \frac{\alpha I_0 ct}{2C_p J}[1 - \exp(-c\tau/R_0)]$$

where t is the fraction of incident energy absorbed by the fluid (the remaining energy being reflected), c is the velocity of sound in the fluid, C_p is the fluid heat capacity at constant pressure, R_0 is the distance from the surface at which the absorbed power is reduced by a factor e, and J is the mechanical equivalent of heat. Effects of viscosity and thermal conduction are assumed to be negligible in this first-order result, and the maximum fluid particle velocity is assumed to be much less than c. If τ is sufficiently long that $c\tau/R_0 \gg 1$, P_{max} is independent of R_0. Under these conditions, a value of $tI_0 = 1.0$ W/cm^2 would make $P_{max} = 4.6$ dyn/cm^2 for water at 25°. These thermally generated acoustic pressures are four orders of magnitude more intense than electromagnetically generated pressure transients resulting from radiation pressure or electrostrictive forces,[8] and should provide a convenient means of measuring α and the TMD.

To test this method, we performed measurements on distilled water and on dilute solutions of sodium chloride. The sample container consisted of a cylindrical polystyrene foam cylinder, 9 cm i.d. and 18.5 cm high, placed over the open end of a section of vertically oriented cylindrical waveguide. Pulses of 2450-MHz radiation, 27 μsec long, were coupled to the waveguide from an Applied Microwave Laboratories generator (Model PH-40). Incident and reflected power was monitored with a Hewlett-Packard Model 432A power meter. The reflection coefficient $(1 - t)$ was approximately 0.50, and did not change observably with solution temperature or conductivity for the salt concentrations examined in this study. For distilled water, $c\tau/R_0$ is greater than 4 for these pulses.

Sound transients were measured with a large 4 cm diameter hydrophone (U. S. Navy Type H-56) immersed in the sample. Figure 1 shows the peak hydrophone output for a sample of distilled water vs. the literature value of α for water at several temperatures.[9] An oscilloscope tracing,
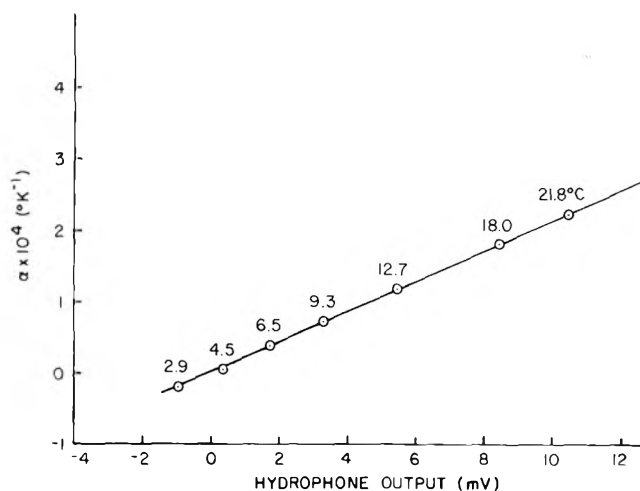

Figure 1. The peak hydrophone output for a sample of distilled water, plotted vs. the literature value of the volume thermal expansion coefficient, α, at several different temperatures. The hydrophone (U. S. Navy Model H-56) was immersed in the sample, which was in a cylindrical polystyrene foam container placed on top of a section of cylindrical waveguide. The incident electromagnetic energy consisted of 27-μsec pulses of 2450-MHz microwave energy, with an incident intensity of approximately 10 W/cm^2 at the bottom of the sample. The hydrophone output was amplified by a simple integrated circuit preamplifier, filtered by a Kron-Hite active bandpass filter (bandwidth 1–60 kHz), and displayed on a Tektronix oscilloscope (Model 475); the hydrophone noise was approximately 0.1 mV peak-to-peak.
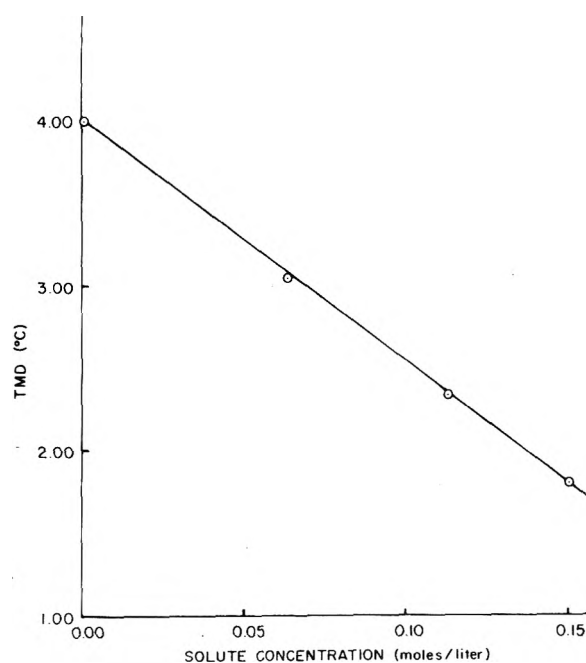

Figure 2. The observed temperature of maximum density, TMD, for dilute solutions of sodium chloride vs. the salt concentration. The solid line was calculated from ref 11. The TMD was experimentally determined as the temperature at which the microwave-induced sound transients vanished. The peak hydrophone output was measured at several temperatures within 2° of the estimated TMD, and a linear regression analysis was performed to obtain the data points shown in this figure.

showing a typical hydrophone signal, has been published elsewhere.[10] The observed signal is clearly proportional to α; it vanishes at 4°, the TMD for pure water. The dependence of the temperature at which the signal vanishes upon

salt concentration is shown in Figure 2. The peak hydrophone output was measured at several temperatures within 2° of the estimated TMD, and a linear regression analysis was performed to obtain the data points shown in Figure 2. The results are in excellent agreement with the TMD calculated from literature values of the partial specific volume of sodium chloride determined by a conventional technique.[11]

In this study, microwave irradiation and hydrophone detection were employed because the equipment was available in our laboratory. We made no attempt to minimize the sample volume or to employ signal averaging techniques. The accuracy of our measurements was limited primarily by the signal-to-noise ratio of our hydrophone, which was acceptable at higher temperatures ($\sim$100:1 at 20°) but became very low near the TMD. This acoustical technique probably cannot be used for precise ($<2\%$ uncertainty) measurements of α, for two reasons. The first is the instrumental difficulty of accurately measuring the amplitude of the sound transients, and of ensuring that the absorbed energy density, tI_0, remains constant as experimental conditions are changed. The second is the need to correct for possible solute-induced changes in C_p and c. This second limitation does not apply to the measurement of the TMD, which should easily be measurable to 0.01° using this technique. Specific applications might find other irradiation and detection techniques useful; for example, it appears possible to use a small piezoelectric ceramic shell as both sample holder and acoustic detector, and to use a pulsed infrared laser to produce the sound transients.

This investigation has shown the feasibility of using radiation-induced pressure transients to measure the TMD of dilute aqueous solutions. For some purposes, this technique might also be used to measure the thermal expansion coefficient. This method is inherently much faster than conventional densitometry, and should be applicable to samples whose properties are changing with time, or to substances such as gels and biological materials which are not easily examined by conventional techniques.

References and Notes

(1) F. Franks and B. Watson, *Trans. Faraday Soc.*, **63**, 329 (1967).
(2) J. E. Garrod and T. M. Herrington, *J. Phys. Chem.*, **74**, 363 (1970).
(3) J. L. Neal and D. A. I. Goring, *J. Phys. Chem.*, **74**, 658 (1970).
(4) G. Wada and S. Umeda, *Bull. Chem. Soc. Jap.*, **35**, 646 (1962).
(5) G. Wada and S. Umeda, *Bull. Chem. Soc. Jap.*, **35**, 1797 (1962).
(6) A. J. Darnell and J. Greyson, *J. Phys. Chem.*, **72**, 3021 (1968).
(7) L. S. Gournay, *J. Acoust. Soc. Amer.*, **40**, 1322 (1966). The quantity α is the volume coefficient of thermal expansion, not the linear coefficient as stated by Gournay. This can be shown by an independent derivation of the fundamental differential equation for thermally driven pressure waves in fluids, eq 9 of this reference, from the first-order acoustic equations for a fluid. See F. A. Firestone in "The American Institute of Physics Handbook" D. E. Gray, Ed., McGraw-Hill, New York, N.Y., 1957, p 3-44.
(8) J. A. Stratton, "Electromagnetic Theory," McGraw-Hill, New York, N.Y., 1941, p 151.
(9) G. S. Kell, *J. Chem. Eng. Data*, **12**, 67 (1967).
(10) K. R. Foster and E. D. Finch, *Science*, **185**, 256 (1974).
(11) F. J. Millero, *J. Phys. Chem.*, **74**, 356 (1970).
(12) From the Bureau of Medicine and Surgery, Navy Department Research Subtask MR 041.03.01.0101B7LX. The opinions and statements contained herein are the private ones of the writers and are not to be construed as official or reflecting the views of the Navy Department or of the Naval Service at large.

Biophysics Division   **Kenneth R. Foster*[12]**
Naval Medical Research Institute   **Edward D. Finch**
Bethesda, Maryland 20014

Structure of the Triiodide Ion in Solution. Raman Evidence for the Existence of Higher Polyiodide Species

Sir: Several reports of the Raman spectrum of the I_3^- ion have appeared in the recent literature claiming that the structure of the ion in aqueous and alcoholic solutions is linear but asymmetric.[1-3] The basis for this conclusion has been the observation of two polarized bands in the spectrum where only one would be expected for a symmetric structure. However, this observation alone is insufficient to establish structural asymmetry as the possibility of Fermi resonance between the ν_1 symmetric stretching mode and the second overtone, $2\nu_2$, of the bending mode seems to have been overlooked. This interaction could cause an apparent splitting of the ν_1 band into a doublet similar to that first observed in the Raman spectrum of CO_2.[4]

Because the actual structure of I_3^- is of some importance in bonding schemes of polyhalide ions, as well as in understanding the exchange kinetics of the iodide ion with the I_3^- ion,[5] a closer examination of the problem appeared warranted. In addition, other studies have been reported on iodide–iodine systems which indicated the existence of higher polyiodide ions with increasing iodide concentration.[6,7]

We have studied aqueous $KI-I_2$ solutions over the following concentration ranges: $0.2\ M \leq [I^-] \leq 4.0\ M$, $0.01\ M \leq [I_3^-] \leq 0.5\ M$, the $[I_3^-]$ being determined by its absorbance at 3530 Å on a Cary 14 spectrometer.[7] Raman spectra obtained with a Spectra-Physics 125 He–Ne laser on a Jarrell-Ash 25-300 spectrometer showed two peaks at 114 and 155 cm^{-1} in good agreement with previous studies. Strong scattering observed from the broad Rayleigh line prevented us from observing any bands below 100 cm^{-1}. The relative intensities and positions of the peaks were independent of the nature of the cation, as measurements with Li^+, Na^+, and Cs^+ cations showed, but a marked dependence of the spectrum upon the I^- concentration was observed (Figure 1). The two peaks must then be due to different species rather than asymmetry in I_3^-; the strongest band at 114 cm^{-1} is attributed to I_3^-, while the band at 155 cm^{-1} indicates the presence of a higher polyiodide.

Several studies of the visible and ultraviolet spectra of iodide solutions have noted that the apparent molar absorptivity of I_3^- varies with iodide concentration; these results have been interpreted as evidence for the formation of I_4^{2-},[6] I_5^-,[7] or I_6^{2-}.[8] Although these species are all expected to have several Raman active vibrations, we found only one additional band in our spectra, the others are assumed to be buried beneath the 114-cm^{-1} band or the Rayleigh wing. We are unable to establish the nature of the higher polyiodide, or its structure, on the basis of our observations. However, we do believe that our data demonstrate the existence of an additional species present in the concentration range where most vibrational spectra have been obtained to date.

Under the influence of strong anisotropic dipolar forces the I_3^- ion can be distorted into an asymmetric form in the solid state as several crystallographic[9] and spectroscopic[10] studies have shown. In dilute solutions the ion should experience a more isotropic environment and assume its unperturbed shape. Our results indicate that this is the linear symmetric configuration.
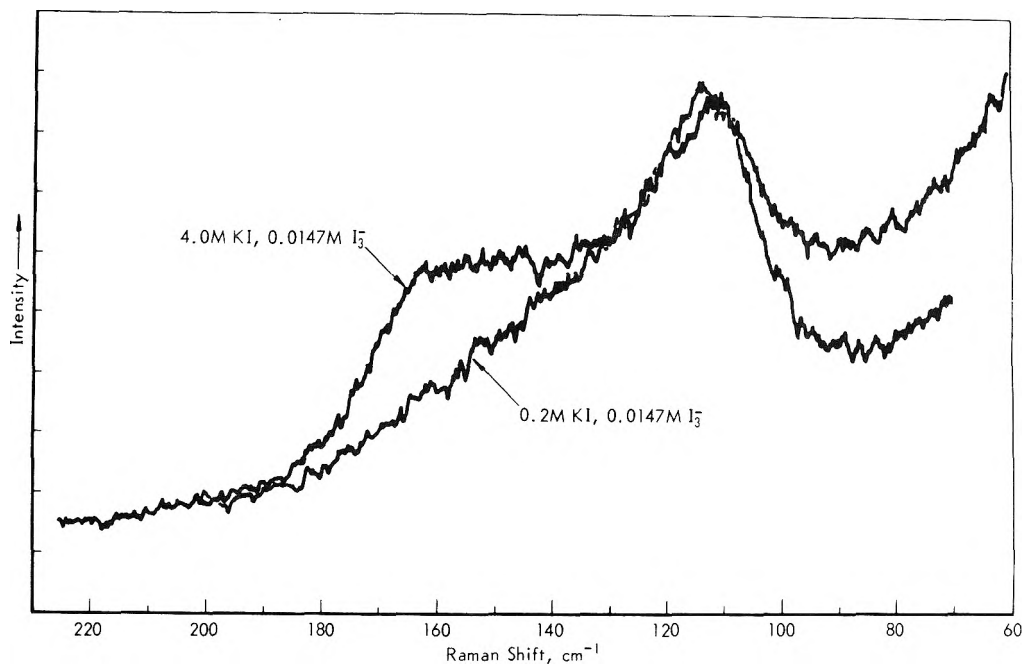
Figure 1. Raman spectra of I_3^- solutions.

References and Notes

(1) M. E. Heyde, L. Rimai, R. G. Kilponen, and D. Gill, *J. Amer. Chem. Soc.*, **94**, 5222 (1972).
(2) K. Kaya, N. Mikami, Y. Udagawa, and M. Ito, *Chem. Phys. Lett.*, **16**, 151 (1972).
(3) W. Kiefer and H. J. Bernstein, *Chem. Phys. Lett.*, **16**, 5 (1972).
(4) E. Fermi, *Z. Phys.*, **71**, 250 (1931).
(5) E. E. Genser and R. E. Connick, *J. Chem. Phys.*, **58**, 990 (1973).
(6) D. A. French and J. A. Effenberger, Abstracts of Papers, 140th National Meeting of the American Chemical Society, Chicago, Ill., Sept 1961, Abstract 25T.
(7) R. W. Ramette and R. W. Sanford, Jr., *J. Amer. Chem. Soc.*, **87**, 5001 (1965).
(8) M. Davies and E. Gwynne, *J. Amer. Chem. Soc.*, **74**, 2748 (1952).
(9) R. C. L. Mooney Slater, *Acta Crystallogr.*, **12**, 187 (1959).
(10) W. Gabes, D. J. Stufkens, and H. Gerding, *J. Mol. Struct.* **17**, 329 (1973).

Shell Development Company   **K. R. Loos***
P. O. Box 481   **A. C. Jones**
Houston, Texas 77001

Self-Diffusion in Liquid Binary Solutions

Sir: Investigations of the self-diffusion of binary organic solutions have furnished valuable information as to the inner structure solutions and molecular interactions. However, a description of the relationship between the structure of liquids and the diffusion rate is hardly possible.

We have determined the dependence of the tracer diffusion coefficient of the components of a liquid mixture on the system composition, taking benzene–toluene as an example of an ideal system and benzene–cyclohexane as a nonideal one.

We used the capillary-cell method[1] and determined tracer diffusion coefficients for benzene-^{14}C (D_B), toluene-^{14}C (D_T), and cyclohexane-^{14}C (D_C) at $25.00 \pm 0.05°$. The

chemical composition of the radioactive solution in capillaries and the nonradioactive solution surrounding the capillaries was the same. Reagent grade chemicals (POCh, Poland) were purified by double distillation with metallic sodium. We used benzene-^{14}C (CEA, France), toluene-^{14}C (Isocomerz, G.D.R.), and cyclohexane-^{14}C (Amersham, England) for the preparation of radioactive solutions. The radioactivity of the tracers was determined in a toluene solution of 2,5-diphenyloxazole (PPO), 4 g/l. and p-bis[2(5-phenyloxazolyl)]benzene (POPOP), 0.3 g/l. with a liquid scintillation counter (USB, Poland) connected to a scaler (PEL-5, ZWN-25, Poland). The diffusion times, varying within the range 16–25 hr, were adjusted to result in diffusion of an amount corresponding to half of the initial radioactivity of the solution in capillaries. The tracer diffusion coefficients were calculated as mean values from more than nine experiments. We determined them from the equation

$$\frac{A}{A_0} = \frac{8}{\pi^2} \exp\left[-\frac{\pi^2 D t}{4 l^2}\right] \tag{1}$$

where A_0 and A are the radioactivities of solutions in capillaries before and after diffusion, respectively; l is the capillary length, determined by the mercury method and verified by the self-diffusion coefficient of benzene-^{14}C, $D_B{}^0 = 2.18$ cm^2/sec.[2]

Figure 1 shows the dependence of diffusion coefficients D_B and D_T for the benzene–toluene system on the mole fraction of toluene x_T and Figure 2 shows the dependence of D_B and D_C on the mole fraction of cyclohexane x_C.[3] We have found that the tracer diffusion coefficient of benzene-^{14}C is equal to the tracer diffusion coefficient of toluene-^{14}C for all solution compositions. The dependence on the mole fraction of toluene is described by the equation

$$D_B = D_T = D_B{}^0 - (D_B{}^0 - D_T{}^0)x_T \tag{2}$$
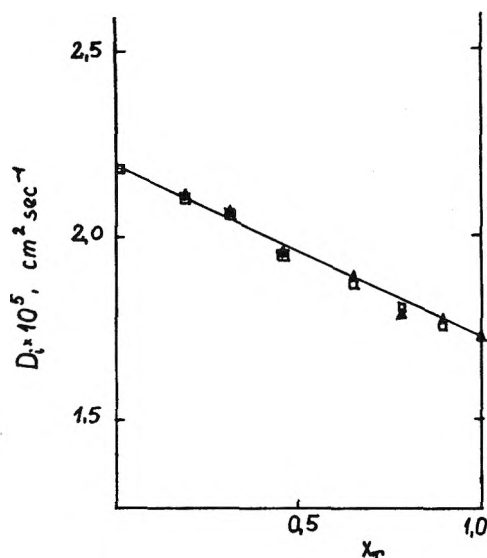
or

$$D_B = D_T = D_B{}^0 x_B + D_T{}^0 x_T$$

Figure 1. Benzene-^{14}C (□) and toluene-^{14}C (▲) diffusion coefficients as a function of mole fraction of toluene at 25.0°.

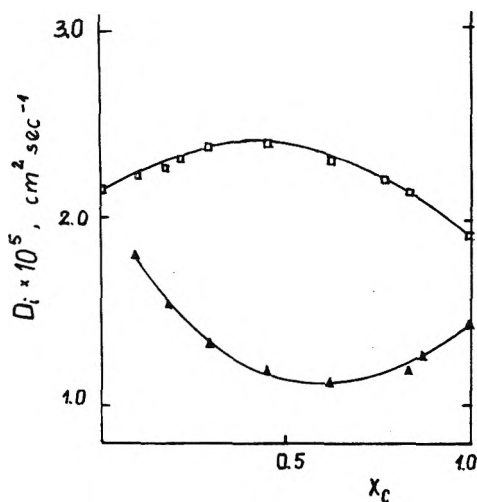**Figure 2.** Benzene-^{14}C (□) and cyclohexane-^{14}C (▲) diffusion coefficients as a function of mole fraction of cyclohexane at 25.0°.

where D_B^0 and D_T^0 are the self-diffusion coefficients of benzene and toluene, respectively, and $x_B = 1 - x_T$. The relationships between D_B and D_C and the composition of the benzene–cyclohexane system are parabolical, and D_B

vs. mole fraction of cyclohexane shows maximum for $x_C = 0.4$ but D_C shows a minimum for $x_C = 0.6$. In the range of $x_C = 0.4$–0.6 this system reveals the largest deviation from ideality.

We tested the product of the tracer diffusion coefficient and the viscosity of the solution, $D_i\eta$, and found that in the benzene–toluene system this product changes with the composition for both components of the solution. In benzene–cyclohexane solutions the product of the viscosity and benzene-^{14}C diffusion coefficient $(D_B\eta)$ was constant for all mole fraction of cyclohexane, but the cyclohexane-^{14}C diffusion coefficient fulfills the equation

$$D_C\eta/(d \ln a_C/d \ln x_C) = \text{constant} \qquad (3)$$

where $(d \ln a_C/d \ln x_C)$ is the thermodynamic factor representing the systems deviation from ideality.

These experimental data show that the inner structure of the solution is very complex. The molecules probably form aggregates and the diffusion process is related to the transfer of these species rather than to single molecules. The size and structure of the aggregates vary with the composition of liquids.

More accurate information about the inner structure of solution will probably be obtained by the examination of the temperature dependence of the tracer diffusion coefficient. Such studies are in progress in our laboratory.

References and Notes

(1) S. Anderson and J. K. Saddington, *J. Chem. Soc.*, S 381 (1949).
(2) R. R. Irani and A. W. Adamson, *J. Phys. Chem.*, **62**, 1517 (1958).
(3) See paragraph at end of text regarding supplementary material.

Insitute of Radiation Chemistry   **W. Reimschussel***
Lódź, Poland   **E. Hawlicka**

Directory of Graduate Research

1973
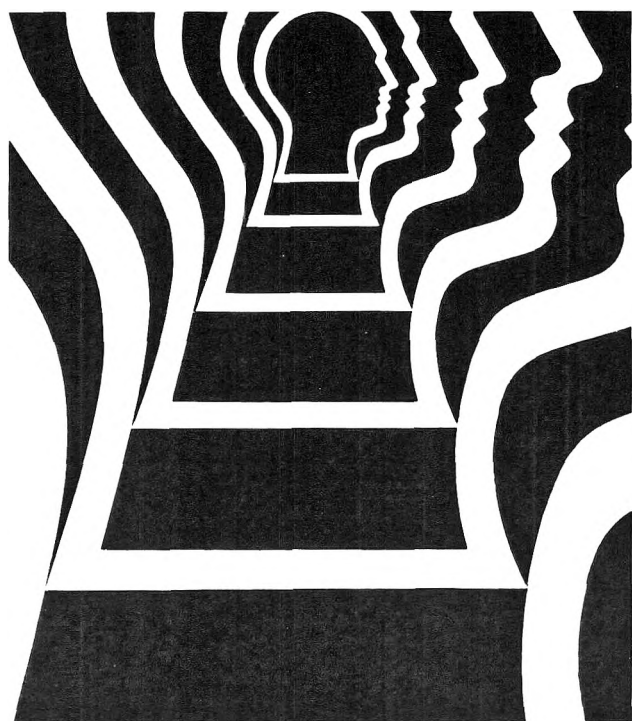
A valuable guide to graduate schools, research, and personnel in the universities and colleges in the United States and Canada offering an organized curriculum leading to the doctoral degree in chemistry, biochemistry, chemical engineering, and pharmaceutical or medicinal chemistry.

Covers

211 Departments of Chemistry
158 Departments of Biochemistry
104 Departments of Chemical Engineering
 32 Departments of Pharmaceutical or Medicinal Chemistry

Listings include 8,480 full- and part-time staff members, each with outline of career, teaching and research specialties, and publications for the past two years; interdisciplinary programs and doctoral theses; and statistical data on departments featuring graduate enrollment, number of staff members, number of Ph.D. degrees conferred during the past two years, and number of postdoctoral appointments.

Prepared by the ACS Committee on Professional Training.

880 pages including index of names.
Paperbound (1974) $20.00 postpaid in U.S., plus 50¢ in Canada and PUAS, 75¢ foreign.

Order from:
Special Issues Sales
American Chemical Society
1155 Sixteenth St., N.W.
Washington, D.C. 20036

1 2 N.W. 251**